Spaceborne SAR Systems with Digital Beamforming and Reflector Antenna

Zur Erlangung des akademischen Grades eines

DOKTOR-INGENIEURS

von der Fakultät für
Elektrotechnik und Informationstechnik
des Karlsruher Instituts für Technologie (KIT)

genehmigte

DISSERTATION

von

Dipl.-Ing. Sigurd Huber
geb. in Augsburg

Tag der mündlichen Prüfung:	25.02.2014
Hauptreferent:	Prof. Dr.-Ing. habil. Alberto Moreira
Korreferent:	Prof. Dr.-Ing. Dr. h.c. Dr.-Ing. E.h. Werner Wiesbeck
Korreferent:	Univ.-Prof. Dr.-Ing. Jürgen Detlefsen

Vorwort

Die vorliegende Dissertation entstand im Zuge meiner Tätigkeit als wissenschaftlicher Mitarbeiter am Institut für Hochfrequenztechnik und Radarsysteme des Deutschen Zentrums für Luft- und Raumfahrt (DLR). Mein Dank gilt daher insbesondere Herrn Prof. Dr.-Ing. Alberto Moreira, für die freundliche Aufnahme an seinem Institut und die wissenschaftliche Betreuung, die wesentlich zum Erfolg dieser Arbeit beigetragen hat. Ferner möchte ich mich bei Herrn Prof. Dr.-Ing. Werner Wiesbeck sowie Herrn Prof. Dr.-Ing. Jürgen Detlefsen für die Übernahme der Koreferate bedanken.
Inspiriert war diese Forschungsarbeit durch Voruntersuchungen zu einer gemeinsamen internationalen Satelliten-SAR-Mission zwischen dem Jet Propulsion Laboratory (JPL) der NASA und dem DLR, die unter dem Arbeitsnamen Tandem-L lief. Hierbei fokussierten sich meine Analysen auf Konzepte, die an der Schnittstelle zwischen Antennenhardware und digitaler Signalverarbeitung angesiedelt war. In diesem Forschungsumfeld konnte ich nicht nur auf zahlreichen Konferenzen sowie mit Partnern aus der Raumfahrtindustrie neue Erfahrungen und Anregungen sammeln, sondern insbesondere auch in der Zusammenarbeit mit meinen Kollegen am Institut. Hervorheben und danken möchte ich Herrn Dr.-Ing. Gerhard Krieger, Leiter der Abteilung Radarkonzepte, der durch seinen Ideenreichtum und sein tiefes fachliches Verständnis die vorliegende Arbeit maßgeblich mitgeprägt hat. Ebenso gilt mein Dank Herrn Dr.-Ing. Marwan Younis, Leiter der Gruppe SAR-Techniken, der mich in fachlichen Diskussionen immer konstruktiv unterstützt hat.
An dieser Stelle möchte ich es nicht versäumen, meiner Familie und meinen Freunden für ihre Unterstützung auch jenseits der Ingenieursarbeit zu danken.

Oberpfaffenhofen, im Januar 2014

Sigurd Huber

Zusammenfassung

Kontaktlose Informationsgewinnung mittels elektromagnetischer Wellen spielt für den wissenschaftlichen und industriellen Fortschritt eine immer wichtigere Rolle. Insbesondere das Prinzip des Radars mit synthetische Apertur (SAR), das zu den bildgebenden Verfahren zählt, gehört heute zum Standardrepertoire ziviler und militärischer Erdbeobachtung. Zukünftige SAR-Systeme, deren Leistungsfähigkeit signifikant von der verwendeten Hardware sowie der Datenverarbeitung abhängt, sollen immer größere Gebiete in immer kürzeren zeitlichen Abständen erfassen können. Die vorliegende Arbeit beschäftigt sich mit der Sensorik, dessen beide Hauptbestandteile die Antennentechnik sowie die nachfolgende analoge und digitale Signalverarbeitung umfasst. Der Fokus liegt hierbei auf digitalen Strahlformungstechniken, die es erlauben, den SAR-Sensor besonders effizient zu betreiben. Hierzu werden raum-zeit-adaptive Algorithmen abgeleitet, die geeignet sind, das Systemrauschen des Sensors zu minimieren sowie räumliche Interferenzen zu unterdrücken. Diese Algorithmen werden anhand eines satelliten-getragenen SAR-Systems simuliert, bei dem das innovative Konzept einer großen entfaltbaren Reflektorantenne in Kombination mit einem digitalen Speisearray zum Einsatz kommt. Sinn dieses Radartyps ist es, das elektromagnetische Signal möglichst kurz nach dem Empfänger zu digitalisieren, um eine maximale Flexibilität des SAR-Systems zu erreichen und gleichzeitig Kosten für teure analoge Elektronik zu sparen. Der zweite Schwerpunkt der Arbeit behandelt Optimierungsaspekte, wobei unter anderem eine neue Methode aufgezeigt wird, die es erlaubt, eine inhärente Problematik solcher Reflektor-Speisearray-Konstellationen abzumildern. Da bei Ausfall eines oder mehrerer Elemente des Speisearrays ein blinder Bereich im Aufnahmefeld entsteht, wird zur Lösung ein defokussiertes Reflektorantennen-Konzept vorgeschlagen, das den Vorzug planarer Arrayantennen, nämlich der Erhaltung der Funktionsfähigkeit bei Ausfall eines Antennenelements, mit dem Vorteil entfaltbarer Reflektorantennen, nämlich der Bereitstellung großer Aperturen, kombiniert.

Abstract

Contactless information retrieval using electromagnetic waves plays an increasingly important role for scientific and industrial progress. In particular the synthetic aperture radar (SAR) principle, numbered among the imaging techniques, nowadays belongs to the standard-repertoire of civil and military Earth observation. Future SAR systems, whose performance significantly depends on the employed hardware as well as the data processing, shall map increasingly

large areas in shorter and shorter time intervals. The work at hand deals with sensor systems, whose two main parts encompass antenna techniques, as well as the subsequent analog and digital signal processing. Here, the focus lies on digital beamforming techniques, enabling an efficient operation of the SAR sensor. For this, space-time adaptive algorithms are derived, which are suitable to minimize the system noise of the sensor and to suppress spatial interference. These algorithms are simulated using the example of a spaceborne SAR system, where the innovative concept of a large unfoldable reflector in combination with a digital feed array is employed. The purpose of such a radar type is to digitize the electromagnetic signal almost immediately after the receiver, in order to ensure the maximal flexibility of the SAR system and to save costs for expensive analog electronics at the same time. The second emphasis of this work deals with optimization aspects, where amongst others a new method is proposed, which allows to mitigate an inherent problematic of such reflector-feed-array constellations. Since in the event of a failure of a single or multiple elements of the feed array a blind spot in the field of view is generated, as solution a defocused reflector antenna concept is proposed. Such an antenna concept combines the merit of planar array antennas, namely the preservation of the functionality in case of an antenna element failure, with the advantage of unfurlable reflector antennas, which is the realization of large apertures.

Contents

Acronyms and Symbols

Mathematical Notations and Symbols

symbol	description
$\cdot$	multiplication symbol, scalar product
$\times$	multiplication symbol, cross product
$*$	convolution symbol
$\star$	correlation symbol
$\wedge$	logic AND operator
$\hat{=}$	correspond symbol
$\circ\!\!-\!\!\bullet$	Fourier pair
$\lvert . \rvert$	absolute value (modulus) $\lvert z \rvert = \sqrt{z^* z},\ z \in \mathbb{C}$
$\lVert . \rVert$	Euclidean norm $\lVert \boldsymbol{x} \rVert = \sqrt{\boldsymbol{x}^\mathsf{T} \boldsymbol{x}},\ \boldsymbol{x} \in \mathbb{R}^n$
$\{.\}^*$	conjugate complex
$\{.\}^\mathsf{H}$	conjugate transpose (Hermitian)
$\{.\}^\mathsf{T}$	transpose
$\lceil . \rceil$	ceiling operator
∇	Nabla operator $\left[\partial/\partial x \quad \partial/\partial y \quad \partial/\partial z\right]^\mathsf{T}$, gradient
Δ	Laplace operator $\nabla^2 = \partial^2/\partial x^2 + \partial^2/\partial y^2 + \partial^2/\partial z^2$
$\Box$	D'Alembert operator $\epsilon_0 \mu_0 \partial^2/\partial t^2 - \Delta$
$\mathbb{C}$	set of complex numbers
$\delta(.)$	Dirac-Delta distribution
det	determinant
arg{.}	argument (angle) of a complex quantity
$\mathcal{E}\{.\}$	expectation value operator
$f(.)$	function
$\dot{f}(t)$	temporal derivative $\mathrm{d}f(t)/\mathrm{d}t$
$\mathcal{F}_x\{.\}$	Fourier transform with respect to variable x
$\mathcal{F}_x^{-1}\{.\}$	inverse Fourier transform with respect to variable x
$\mathcal{H}\{.\}$	Hilbert transform
Im{.}	imaginary part of a complex number
lg	logarithm to base ten $\lg(x) = \ln(x)/\ln 10$
$\mathcal{L}\{.\}$	linear differential operator
lim	limes
$\max_x\{.\}$	maximizer with respect to variable x

$\mathbb{N}$	set of natural numbers
nint{.}	nearest integer operator
$\mathcal{Q}${.}	quantization operator
$\mathbb{R}$	set of real numbers
Re{.}	real part of a complex number
rect	boxcar function
sgn	signum function
sinc	sinus cardinalis function $\mathrm{sinc}(x) = \sin(x)/x$
$\mathbb{Z}$	set of integer numbers

Acronyms

acronym	description
2-D	two-dimensional
3-D	three-dimensional
ADC	analog-to-digital converter
ASIC	application specific integrated circuit
AWGN	additive white Gaussian noise
CW	continuous wave
DBF	digital beamforming
DEM	digital elevation model
DOA	direction of arrival
EM	electromagnetic
FFT	fast Fourier transform
FIR	finite impulse response
FPGA	field programmable gate array
GEO	geostationary Earth orbit
HPA	high power amplifier
HRWS	high-resolution wide-swath
IF	intermediate frequency
IFFT	inverse fast Fourier transform
IIR	infinite impulse response
ISTFT	inverse short-time Fourier transform
LCMV	linear constraint minimum variance
LEO	low Earth orbit
LO	local oscillator
LTI	linear time invariant
MEO	medium Earth orbit
MTI	moving target indication
MVDR	minimum variance distortionless response

MUSIC	multiple signal classification
OFDM	orthogonal frequency-division multiplexing
PDF	probability density function
PDN	power distribution network
PT	point target
RF	radio frequency
Radar	radio detection and ranging
RCS	radar cross section
Rx	receive
SAR	synthetic aperture radar
SCORE	scan-on-receive
SLAR	side-looking airborne radar
STAP	space-time adaptive processing
STFT	short-time Fourier transform
TRM	transmit/receive module
Tx	transmit
UAV	uninhabited aerial vehicle

Lower Case Symbols

symbol	unit	description
a	m	length of an array element
a	-	complex-valued antenna far field pattern belonging to an individual element/channel
$\boldsymbol{a}$	-	embedded array manifold
$\widehat{\boldsymbol{a}}$	-	measured (erroneous) array manifold
a_f	-	element amplitude pattern model
b	m	width of an array element
$\boldsymbol{c}$	-	constraint vector
d	m	array element spacing
dc	-	pulse duty cycle
e	$\sqrt{\mathrm{W}}$	spatio-temporal interference
f	Hz	frequency
f_c	Hz	carrier/center frequency
f_g	Hz	3 dB cut-off frequency
f_D	Hz	Doppler frequency
f_s	Hz	temporal sampling frequency
f_y	Hz	azimuth (Doppler) frequency
g	-	Green's function
$h, \overline{h}$	-	filter impulse response function

$\boldsymbol{h}$	-	vectorial filter impulse response function
h_s	m	orbit height
i	-	count variable for channels / spatial interferers
k	m^{-1}	wavenumber / magnitude of the wavevector
$\boldsymbol{k}$, $\boldsymbol{k}_\mathrm{SAR}$	m^{-1}	wavenumber vector
k_c	m^{-1}	center wavenumber
$k_{y\mathrm{s}}$	m^{-1}	azimuth sampling wavenumber
k_x, k_y, k_z	m^{-1}	wavenumber domain variables
l	-	count variable for range ambiguities
m	-	count variable for grating lobes / FIR filter subbands / azimuth ambiguities
n	-	count variable for array elements / integer power
n, n'	s	discrete time variable
$\boldsymbol{n}_\mathrm{a}$	-	unit antenna normal vector
$\boldsymbol{n}_\mathrm{s}$	-	unit surface normal vector
o	-	backscatter/reflectivity function
$\overline{o}$	-	reconstructed reflectivity function
$\hat{o}$	-	complex backscatter coefficient of a point target
p	-	probability density function
p	$\sqrt{\mathrm{W}}$	transmitted waveform
q	$\sqrt{\mathrm{W}}$	quantization noise
r	-	receive antenna element pattern function
r	m	slant range distance
$\boldsymbol{r}$, $\boldsymbol{r}'$, $\boldsymbol{r}''$	m	spatial coordinate in Euclidean space
$\boldsymbol{r}_\mathrm{f}$	m	feed position vector
$\boldsymbol{r}_\mathrm{s}$	m	position vector of the SAR sensor
$\boldsymbol{r}_\mathrm{r}$	m	parametrization of the reflector surface
s	$\sqrt{\mathrm{W}}$	noise free SAR raw data signal
s	-	coefficient of the scattering matrix
t, t', t''	s	continuous time variable
t	-	transmit antenna element pattern function
u	$\sqrt{\mathrm{W}}$	SAR raw data signal
$\boldsymbol{u}$	$\sqrt{\mathrm{W}}$	vectorial SAR raw data signal
v_y	ms^{-1}	relative sensor velocity (in azimuth)
$\boldsymbol{v}_\mathrm{s}$	ms^{-1}	sensor velocity vector
v	$\sqrt{\mathrm{W}}$	additive white Gaussian noise (AWGN)
w	-	complex weight/excitation coefficient
$\boldsymbol{w}$	-	complex weight vector
x	$\sqrt{\mathrm{W}}$	(input) signal
x, y, z	m	spatial variables

x', y', z'	m	local antenna coordinates
$x_\mathrm{f}, y_\mathrm{f}, z_\mathrm{f}$	m	feed array coordinates
y	$\sqrt{\mathrm{W}}$	(output) signal
y, y'	m	spatial azimuth coordinate

Capital Symbols

symbol	unit	description
A	m^2	(projected) aperture area
A	-	wavenumber representation of the complex antenna pattern function a
$\boldsymbol{A}, \overline{\boldsymbol{A}}, A$	-	array response matrix
A_cell	m^2	cross section of a resolution cell
$\boldsymbol{A}_\mathrm{e}$	Vsm^{-1}	electric vector potential
A_eff	m^2	effective antenna aperture area
$\boldsymbol{A}_\mathrm{m}$	Asm^{-1}	magnetic vector potential
A_r	m^2	reflector surface
$AASR$	-	azimuth ambiguity-to-signal ratio
ASR	-	integrated ambiguity-to-signal ratio
$\boldsymbol{B}$	Vsm^{-2}	magnetic flux density
B	Hz	signal bandwidth
$\overline{B}$	Hz	FIR filter bank bandwidth
B_y	Hz	processed azimuth Doppler bandwidth
D	m	antenna diameter in elevation or azimuth / total length of a linear array antenna
$\boldsymbol{D}$	Asm^{-2}	electric displacement density
$\boldsymbol{E}, \boldsymbol{E}_0, \underline{\boldsymbol{E}}$	Vm^{-1}	electric field intensity vector
E	Vm^{-1}	component of the electric field intensity vector
$E_\mathrm{g}, E_\mathrm{h}$	-	energy of a kernel / filter
EWL	s	echo window length
F, F_x, F_y	m	focal length
G	-	wavenumber spectrum of the Green's function / antenna gain pattern
G_f	-	feed element gain pattern
$\boldsymbol{H}$	Am^{-1}	magnetic field intensity vector
H	-	spatial / temporal filter transfer function
$HPBW$	rad	half power beamwidth
I	A	integral current
$ISLR$	-	integrated sidelobe ratio
$\boldsymbol{J}, \boldsymbol{J}_\mathrm{e}$	Am^{-2}	electric current density

$\boldsymbol{J}_\mathrm{m}$	Vm^{-2}	magnetic current density
K_y	m^{-1}	azimuth sampling wavenumber
K_y'	m^{-1}	processed azimuth wavenumber domain / high azimuth sampling wavenumber
L_p	-	losses induced by long pulses
M	-	number of FIR filter subbands / azimuth ambiguities / highly-sampled azimuth signal samples
N	-	number of undersampled azimuth signal samples
N_act	-	number of activated channels
N_b	-	number of bits
N_c	-	number of channels
N_coef	-	number of FIR filter coefficients
N_dir	-	number of directions
N_p	-	number of samples per pulse
N_x	-	number of feed elements in elevation
N_y	-	number of feed elements in azimuth
O	m	reflector antenna offset
P	W	(signal) power
P	$\sqrt{\mathrm{W}}\mathrm{Hz}^{-1}$	spectrum of the transmitted waveform
PRF	Hz	pulse repetition frequency
PRI	s	pulse repetition interval
$PSLR$	-	peak-sidelobe ratio
$\boldsymbol{Q}$	-	vectorial source function
R	s^{-1}	data rate
$\boldsymbol{R}$	-	matrix of receive antenna element pattern functions
R_0	m	zero-Doppler distance sensor-target
$\boldsymbol{R_a}$	W	antenna element covariance matrix
$\boldsymbol{R_u}$	W	raw data channel covariance matrix
$\boldsymbol{R_v}$, $\boldsymbol{R_{v'}}$	W	noise channel covariance matrix
$RASR$	-	range ambiguity-to-signal ratio
S	$\sqrt{\mathrm{W}}\mathrm{Hz}^{-1}$	signal transfer function
$\boldsymbol{S}$	Wm^2	Poynting vector
$\boldsymbol{S}$	-	scattering matrix
SIR	-	signal-to-interference ratio
$\widehat{SIR}$	-	erroneous signal-to-interference ratio
SNR	-	signal-to-noise ratio
$\widehat{SNR}$	-	erroneous signal-to-noise ratio
T	s	clock period / time interval
$\boldsymbol{T}$	-	matrix of transmit antenna element pattern functions
U	$\sqrt{\mathrm{W}}\mathrm{Hz}^{-1}$	SAR raw data spectrum

U	V	integral voltage
$\boldsymbol{U}, \boldsymbol{U}'$	$\sqrt{\text{W}}$	matrix of SAR raw data signals
$\boldsymbol{V}$	-	eigenvector matrix / vector field
$\boldsymbol{V}, \boldsymbol{V}'$	$\sqrt{\text{W}}$	matrix of noise signals
X	m	swath width (arc length for spherical Earth model)
X	$\sqrt{\text{W}}\text{Hz}^{-1}$	(input) signal spectrum
X_f	m	feed length in elevation
XPI	-	cross polarization isolation
Y	m	processed azimuth aperture length
Y_f	m	feed length in azimuth
Z	-	set of activated channels

Greek Symbols

symbol	unit	description
α	-	real numbered factor
α_f	-	focal ratio
$\gamma, \overline{\gamma}$	-	Gaussian integration kernel
Δa	-	antenna pattern measurement uncertainty
$\Delta AASR$	-	relative azimuth ambiguity-to-signal ratio
Δf	Hz	frequency resolution / bandwidth
$\Delta \boldsymbol{k}$	m^{-1}	wavenumber vector uncertainty
$\Delta k_x, \Delta k_y, \Delta k_z$	m^{-1}	wavenumber resolution / bandwidth / sample spacing
Δr	m	slant range resolution / difference
Δr_g	m	ground range resolution
ΔSNR	-	relative signal-to-noise ratio
Δt	s	temporal resolution / interval
$\Delta \vartheta$	rad	angular uncertainty
$\Delta x, \Delta y, \Delta y', \Delta z$	m	spatial resolution / interval / sample spacing
Δx_f	m	feed element spacing in elevation
Δy_f	m	feed element spacing in azimuth
ϵ	$\text{AsV}^{-1}\text{m}^{-1}$	permittivity
η_a	-	total efficiency
η_ap	-	aperture efficiency
η_s	-	spillover efficiency
η_t	-	taper efficiency
ϑ, ϑ'	rad	spherical coordinate
ϑ_s	rad	angular stop band
ϑ_t	rad	angular target band

θ	rad	angle referring to the reflector geometry
θ_{bore}	rad	boresight angle with respect to nadir
θ_{i}	rad	incident angle with respect to surface normal
θ_{f}	rad	feed tilt angle
θ_{l}	rad	look angle with respect to nadir
Θ_{3dB}	rad	half-power beamwidth
λ	m	wavelength
λ	-	eigenvalue
$\boldsymbol{\lambda}$	-	vector of Lagrangian multipliers
$\boldsymbol{\Lambda}$, $\overline{\boldsymbol{\Lambda}}$	-	eigenvalue matrix / Lagrange function
μ	-	expectation value / real valued parameter
μ	$\text{VsA}^{-1}\text{m}^{-1}$	permeability
Ω	-	normalized angular frequency
Ω_{c}	-	cut-off frequency for FIR filter subbands
ρ, ρ_{e}	Asm^{-3}	electric volume charge density
ρ_{m}	Vsm^{-3}	magnetic volume charge density
σ	-	standard deviation
σ_0	-	normalized backscatter coefficient
σ_o^2	m^2	variance / RCS of a point target
σ_v^2	W	variance / power of a zero-mean noise process
τ	s	delay time
τ_{p}	s	pulse duration
φ, φ'	rad	spherical coordinate
Ψ	-	MUSIC spectrum
ω	$\text{rad}\cdot\text{s}^{-1}$	pulsatance (angular frequency)

Superscripts and Subscripts

symbol	description
$\{.\}_{\text{aa}}$	azimuth ambiguity
$\{.\}_{\text{az}}$	quantity refers to azimuth
$\{.\}_{\text{co}}$	co-polar component
$\{.\}_{\text{cx}}$	cross-polar component
$\{.\}_{\text{eff}}$	effective
$\{.\}_{\text{el}}$	quantity refers to elevation
$\{.\}_{\text{h}}$	horizontal polarization
$\{.\}_{\text{i}}$, $\{.\}^{\text{i}}$	incident
$\{.\}_{\text{in}}$	input quantity
$\{.\}_{\text{max}}$	maximal value of the quantity
$\{.\}_{\text{min}}$	minimal value of the quantity

$\{.\}_{\mathrm{ML}}$	mainlobe
$\{.\}_{\mathrm{out}}$	output quantity
$\{.\}_{\mathrm{ra}}$	range ambiguity
$\{.\}_{\mathrm{rc}}$	range compressed
$\{.\}_{\mathrm{ref}}$	reference value / function
$\{.\}_{\mathrm{Rx}}$	quantity refers to receive case
$\{.\}^{\mathrm{s}}$	scattered
$\{.\}_{\mathrm{sep}}$	separate
$\{.\}_{\mathrm{SL}}$	sidelobe
$\{.\}_{\mathrm{tot}}$	total
$\{.\}_{\mathrm{Tx}}$	quantity refers to transmit case
$\{.\}_{\mathrm{v}}$	vertical polarization

Constants and Numbers

symbol	value	unit	description
$\mathbf{0}$	all zero	-	zero-vector
$\mathbf{1}$	all one	-	ones-vector
c	299792458	ms^{-1}	speed of light
e	2.71828	-	Euler number
ϵ_0	$8.8541878 \times 10^{-12}$	$\mathrm{AsV}^{-1}\mathrm{m}^{-1}$	vacuum permittivity
$\mathbf{I}$	diagonal ones	-	identity matrix
j	$\sqrt{-1}$	-	imaginary number
μ_0	$4\pi \times 10^{-7}$	$\mathrm{VsA}^{-1}\mathrm{m}^{-1}$	vacuum permeability
π	3.14159	-	mathematical constant
r_{e}	6378137	m	WGS84 Earth radius at equator

1 Introduction

Synthetic Aperture Radar (SAR) has entered a new era of technological evolution. Imaging radars nowadays find application in various fields of natural sciences, military surveillance, security services and commercial products. One way to characterize such SAR systems is by their distance to the objects to be imaged. Basically three classes of distance can be identified. The first class covers systems operating over distances in the order of a few centimeters to several meters. Those systems are often referred to as near field imaging radars. Potential areas of applications are, for example, passenger scanners at airport security terminals, hand-held scanners for finding the armoring in concrete walls or mine detectors. Apparently, these systems aim to detect small structures in the order of millimeters to a few centimeters and therefore operate in the regime of higher frequencies, like W-band and above. The second class of imaging radars is separated some hundred meters to a few kilometers from the targets. Those radar systems are usually mounted on aircrafts or drones and are therefore referred to as *airborne* SAR systems. Here, the resolutions typically are in the centimeter to meter range. Typical frequency bands of interest range from P-band to Ka-band. The use of such SAR systems is mainly in scientific fields as well as military applications with *uninhabited aerial vehicles* (UAV). The last category is represented by *spaceborne* SAR systems. Here, the SAR sensor is integrated into a satellite. Those systems have unlocked several new fields of applications ranging from the generation of digital elevation models (DEM), using interferometric SAR data acquisitions, to the systematic observation of Earth system dynamics or disaster monitoring. Depending on the application, the used frequency bands, as well as the desired resolutions, are comparable to the airborne case. The exploitation of new SAR imaging modes is attended by new technology developments.

The term beamforming is related to the shaping of the antenna beam which is used to scan the object, or in case of spaceborne sensors, the swath. Beamforming is a scientific field by its own, and various techniques exist to shape a beam under certain constraints. Although beamforming often is associated with antenna arrays where the array coefficients are subject to optimization, also antennas with special geometries fall under this category. Examples are conformal antennas, which are integrated in all kinds of chassis. Classically, beamforming is performed with analog signals, that means the individual radiators, which constitute the array antenna, are connected to delay elements and attenuators

and finally summed up. Shaping an antenna beam using special geometries must be regarded as analog beamforming in this context. With the availability of fast *analog-to-digital converters* (ADC) the relatively new concept of *digital beamforming* (DBF) is of increasing interest. Here, the idea is to form a beam by means of digital software or hardware based signal processors.

1.1 A Brief Historical Review

The foundation of the electromagnetic theory was laid by James Clerk Maxwell, when he published his famous set of partial differential equations [82] in 1865, which are known as Maxwell's equations. About twenty years later, Heinrich Hertz gave, with the *hertzsche Oszillator*, an experimental proof of Maxwell's electromagnetic theory [39]. In his experiments Hertz was the first being able to transmit and receive electromagnetic waves. Inspired by Hertz' results, Guglielmo Marconi established a telegraphical link in the Swiss Alps over a distance of 1.5 km in 1895. Later he patented his *Gerät zur Aufspürung und Registrierung elektrischer Schwingungen*, which could be translated as *device for retrieval and detection of electromagnetic waves*, in Great Britain [79]. Christian Hülsmeyer, also interested in the research of Heinrich Hertz, finally had the groundbreaking idea which led to the development of the radar. Radar is the acronym for *radio detection and ranging* and Hülsmeyer was especially interested in the detection of ships. Eventually, his invention, which he called *Telemobiloskop*, found its way in two patents [40, 41]. However, when he demonstrated his invention in 1904 in Cologne, the reaction on side of the public as well as the navy was marginal. Later during the 1930s, the importance of detection and positioning of air- and sea-targets was recognized in different European countries independently and led nearly simultaneously to the development of radar techniques. In Germany the development essentially was pushed by Rudolf Kühnhold, Director of the communication experiment department of the German Reichsmarine. With his system, which he tested in the Kiel harbor, he could not only detect ships but also aircraft flying above the harbor. In 1934 commercial production of radar systems was started by companies like GEMA, Telefunken, Siemens or Blaupunkt.

After World War II a new radar concept was developed. The *side-looking airborne radar* (SLAR), constructed for military applications in the early 1950s, is an imaging radar, utilized to map terrain from airborne platforms. This real aperture radar type offered imagery with angular resolution proportional to the beamwidth of the antenna in flight direction [112]. A further advancement of the imaging radar principle is the *synthetic aperture radar*, which has been patented in 1954 [131]. Here, for the first time the Doppler frequency effect,

predicted by Christian Doppler already in 1842, was utilized to map terrain from airborne platforms with high angular resolution. With this invention the path was opened to a completely new field of research in technology as well as natural sciences.

1.2 State-of-the-art and Motivation

Since the first civilian SAR Earth observation mission Seasat [53], launched in 1978, advances in the development of SAR antennas have been made. The Seasat SAR antenna was a classical passive phased array antenna with microstrip radiators. The array is fed by a central radio frequency (RF) source, a traveling wave tube. This allowed to map swathes on planetary surfaces in the so called *stripmap mode*, where the sensor images the region on ground using a fixed beam both on transmit and receive. The space shuttle mounted SAR sensors for the radar missions SIR-A [15] and SIR-B [16] were based on planar arrays with microstrip technology as well.

An innovation in planar SAR antenna technology was introduced with the use of slotted waveguides as basic antenna elements. This type of radiator is potentially able to transmit more power compared to its microstrip based pendant and allows, due to a denser packing of orthogonally polarized waveguides, a simpler realization of polarimetric SAR antennas. Slotted waveguide arrays are a mature technology and have heritage within various SAR missions, like the Russian ALMAZ-1 [126], the European ERS-1 [98] and ERS-2 [101], the Japanese JERS-1 [89], the US/German SRTM [130], the Canadian Radarsat-1 [132], as well as X-SAR [129], realized in a cooperation between the US, Italy and Germany.

A further improvement emerged with the miniaturization of RF sources. With so called *transmit/receive modules* (TRM) each individual antenna element can be supplied with its own power source. What followed up was a new generation of SAR satellites, with active phased array antennas, as the European ENVISAT ASAR [76], the Japanese ALOS PalSAR [102], the Canadian Radarsat-2 [7] and the German Earth observation satellite TerraSAR-X [10] with its add-on TanDEM-X [85]. These new generation SAR systems offered full polarimetric capability, with the exception of ENVISAT, that operated with a dual-polarized mode. New operational imaging modes like *scanSAR* or the high resolution mode *spotlight*, which has been implemented on TerraSAR-X, TanDEM-X, Radarsat-2 and the Italian COSMO-SkyMed [74], became available.

Almost in parallel with the conception of SAR missions with sensors based on planar array technology, a SAR development has been brought forward, which relies on reflector antennas. This technology was lent from military communi-

cation satellite developments, kicked off at the end of the 1950s. In one of the first conceptual assessments of geostationary communication satellites already *inflatable paraboloidal antennas* [2] have been mentioned. In the field of imaging radars, the first reflector SAR experiments were the Soviet space explorer missions Venera 15 and 16 [126] with the goal to map Venus. Here, for the only time cylindrical reflector antennas have been utilized. Later SAR missions, like the Magellan mission [128] and the Cassini-Huygens mission [71] employed parabolic reflector antennas. Another example for military reflector based SAR systems is the German SAR Lupe constellation [59], comprising five satellites.

Recent SAR system developments are driven by new applications like Earth system dynamics monitoring [70], where short revisit times are required, which in turn rises the need of large swath widths. At the same time operators and investigators are interested in a high information content of the SAR signal. This is traditionally achieved by increasing the signal bandwidth resulting in a higher resolution of the SAR images. Large swath widths and high azimuth resolutions are contradicting requirements for conventional SAR systems. Since spaceborne SAR systems demand a very high isolation between the transmit- and receive-channel, they cannot be implemented as *continuous wave* (CW) radars on a single platform. This technical constraint leaves as only option pulsed radar systems, which are subject to a stringent timing of transmit and receive events. Aiming at high azimuth resolutions a broad antenna footprint or, respectively, a broad beam is required. In order to sample the received signal adequately a sufficiently high *pulse repetition frequency* (*PRF*) has to be used. The high *PRF* in turn limits the swath width.

One possibility to overcome this restriction is to transmit a signal using a broad beam and to record with multiple receivers. These individual receiver signals are then processed in order to reconstruct the high-resolution image. Classical approaches employ planar array antennas where the aperture is split on receive into several subapertures [18, 134]. This so called *high-resolution wide-swath* (HRWS) concept has been investigated by means of hardware demonstrators in [24, 25, 38] and [56, 104]. In this context innovative digital beamforming concepts and optimization strategies have been developed in [30, 68].

The performance for a spaceborne SAR system consisting of several formation-flying small satellites and the implications on signal processing have been investigated in [73]. The novel concept of combining a reflector antenna with a feed array, where the signal is digitized almost immediately after the receiver, was first proposed in [68] and further investigated in [28, 45–47, 69, 135]. It was demonstrated that such systems have the potential to outperform conventional planar SAR systems. Reflector antenna based systems are already a mature technique for communication satellites. Generally, reflector antennas inherently generate a shaped beam due to the mechanical molding of the reflector

dish. That means for any given feed position only a certain solid angle can be illuminated. Therefore, a set of multiple feed elements is required in order to cover the complete region of interest. By moving the analog-to-digital converters closer to the *radio frequency* (RF) front-end, it is possible to form beams by means of digital signal processing avoiding a costly analog receiver chain. In that context several space agencies started research activities, as the European Space Agency (ESA) with a feasibility study about Ka-band reflector antenna based SAR systems with digital beamforming [77]. One of NASA's space centers, the Jet Propulsion Laboratory (JPL), began concept studies of SAR systems with large deployable mesh reflectors [12, 52] in the context of a dedicated spaceborne Earth observation mission. In the frame of a collaboration with JPL the German Aerospace Center (DLR) proposed the dual SAR satellite interferometer mission Tandem-L [62,87], where this innovative reflector hardware concept with digital feed array is considered as baseline to deal with the challenges of this mission. Only in brief it shall be mentioned that digital beamforming SAR systems are of course constrained with respect to their data rate and quality by key hardware components like analog-to-digital converters. A survey of the state-of-the-art and future trends in ADC technology can be found for instance in [88] and references therein.

Considering all these technological advancements, this work is motivated by the fact, that in the field of spaceborne SAR missions, based on reflector antenna technology, new and powerful digital beamforming concepts are required, in order to guarantee the maximum surplus of future SAR missions in terms of scientific output.

1.3 Scope of the Work

Being a contribution in the field of synthetic aperture radar, this work is confined to antenna hardware concepts and signal processing aspects of SAR systems with digital beamforming. In the chain of SAR imagery production, starting with the SAR instrument transmitting an electromagnetic wave, which is scattered on the ground and received by the same or other SAR instruments, this work treats innovative hardware concepts and sophisticated digital signal processing techniques, related to the processing of multi-channel SAR raw data. Insofar the final step of SAR image generation, the so called SAR image focusing, and beyond that, the scientific interpretation of SAR image content, is not subject of this thesis. It is the objective of this work to present a detailed analysis of the innovative hardware concept of combining a reflector antenna with a digital feed array in the context of SAR and to discuss the performance of such systems. Emphasis is laid on digital beamforming procedures which improve

or balance the system performance.

Remote sensing in general, and SAR imaging in particular, is a discipline settled in the field of electromagnetic scattering. It is therefore vital to review the basic electromagnetic theory in chapter 2 with emphasis on wavenumber descriptions of point-like scatterers. This wavenumber notation provides the natural mathematical formalism to describe scattering problems as well as beamforming concepts in a compact way. Above that the basic performance figures characterizing SAR systems are introduced based on a SAR signal model. Chapter 3 discusses trade-offs of conventional SAR systems with respect to wide-swath high-resolution operation. A brief antenna theoretical comparison between planar array antennas and array-fed reflector antennas finally leads to the limitations of conventional SAR systems without digital beamforming. The body of work is concentrated in chapter 4, where array-fed reflector SAR systems are generalized to multi-channel reflector SAR systems. Here, dedicated digital beamforming strategies are introduced and discussed in a general way for SAR systems with multiple receive channels. In view of real reflector based SAR missions the more general beamforming approach is split in realtime capable processing concepts in elevation and azimuth. Moreover, these beamforming techniques are extended to polarimetric SAR applications. It is important to emphasize that the decoupling of SAR specific processing steps, like the SAR image formation and beamforming methods, which are related to the SAR antenna, allows to transfer these beamforming principles to multi-channel SAR systems with any kind of SAR antenna. The performance of reflector SAR systems is demonstrated by means of a design example in chapter 5 with numerical simulations. The analysis of array-fed reflector SAR systems shows that feed elements failures can significantly impact the performance of such systems. Chapter 6 is dedicated to the optimization of reflector SAR systems in terms of beam stability. For this, basically two approaches are investigated, the first aiming at an improvement of the digital beamforming itself, while the second approach is based on a novel reflector antenna concept. Finally, in chapter 7 selected beamforming concepts are verified by means of a ground based multi-channel radar demonstrator. The work is concluded with an outlook to future developments of spaceborne SAR systems in chapter 8.

In this context the novel contributions of this thesis can be summarized as follows: Induced by the investigation of large unfoldable mesh reflector antennas, a further limitation of large antennas in conjunction with long duration pulses has been identified in chapter 3. In the next chapter digital beamforming with SAR systems is approached in a general way, where the SAR data space is expanded such that individual scatterers can be discriminated and existing beamforming techniques can be applied. For this, compact equations are derived which describe the mapping between the SAR data space and the indi-

vidual antenna patterns defined in a local coordinate system. Based on this general framework a dedicated beamforming concept in elevation has been developed, which combines frequency adaptive filtering techniques with time-variant beamforming concepts, allowing to resolve the afore mentioned limitation. In azimuth a new algorithm is introduced, which allows to process SAR azimuth data such that the signal-to-noise ratio is optimized and ambiguities are suppressed simultaneously. These dedicated beamforming principles have been published in several conference and journal contributions [48, 135]. Further, the previously introduced concepts are expanded to a new processing scheme for polarimetric applications, where the problem of channel coupling via the cross polarized patterns is dealt with. In chapter 5 for the first time a compact set of equations has been derived which enables to design an array-fed reflector antenna for a SAR imaging scenario taking into account swath width, azimuth resolution and other parameters. A final contribution regards the problem of feed element failure with array-fed reflector SAR systems. Here, the novel idea of compensating the gain loss of a one-dimensionally defocused reflector antenna using digital beamforming techniques is introduced. This concept has been published in [43] and is currently in a patenting process [44].

2 Theoretical Background

This chapter is meant to provide the necessary fundamentals, required for the beamforming concepts presented in chapter 4. At this point the SAR principles shall be introduced in a very general way without presuming specific imaging geometries. The high altitude imaging case will be introduced in chapter 3, when the constraints and limitations of spaceborne SAR systems are discussed.

2.1 Radar Scattering

There are possibly two ways to approach synthetic aperture radar imaging, in which the first would be a purely field theoretical perspective and the second being the system theoretical perspective. Clearly the system theoretical approach is a result of electromagnetic theory. These two approaches differ insofar, that in the electromagnetic view one deals with differential, or field quantities, that are the electric field intensity vector $\boldsymbol{E}(\boldsymbol{r},t)$ and the magnetic field intensity vector $\boldsymbol{H}(\boldsymbol{r},t)$ as function of the four-dimensional space-time continuum $(\boldsymbol{r},t)$. The system theoretical approach mainly deals with integral quantities, that are voltages $U(t)$ and currents $I(t)$. Digital beamforming operates on signals and the problem arises how field quantities and integral quantities are linked. Naturally in any radar system the antenna represents the interface between field quantities and signals which can be processed. Therefore, it is important to review the formalism finally leading to the SAR imaging equation, which in turn is the basis for beamforming algorithms with multi-channel systems. Maxwell's equations represent the fundamental theory of electromagnetics in classical physics and write

$$\nabla \times \boldsymbol{E}(\boldsymbol{r},t) = -\frac{\partial \boldsymbol{B}(\boldsymbol{r},t)}{\partial t}\,, \tag{2.1}$$

$$\nabla \times \boldsymbol{H}(\boldsymbol{r},t) = \frac{\partial \boldsymbol{D}(\boldsymbol{r},t)}{\partial t} + \boldsymbol{J}(\boldsymbol{r},t)\,, \tag{2.2}$$

$$\nabla \cdot \boldsymbol{D}(\boldsymbol{r},t) = \rho(\boldsymbol{r},t)\,, \tag{2.3}$$

$$\nabla \cdot \boldsymbol{B}(\boldsymbol{r},t) = 0\,. \tag{2.4}$$

The first equation (2.1) is called Faraday's law of induction, with the magnetic flux density $\boldsymbol{B}(\boldsymbol{r},t)$, and the second equation (2.2) is Ampère's law, with the elec-

tric displacement density $\boldsymbol{D}(\boldsymbol{r},t)$ and the electric current density $\boldsymbol{J}(\boldsymbol{r},t)$. Equations (2.3) and (2.4) are Gauss' laws for the electric and magnetic fields, with the volume charge density $\rho(\boldsymbol{r},t)$. For isotropic media the flux densities and the field intensities are connected via the material equations

$$\boldsymbol{D}(\boldsymbol{r},t) = \epsilon(\boldsymbol{r},t)\boldsymbol{E}(\boldsymbol{r},t)\ , \tag{2.5}$$

$$\boldsymbol{B}(\boldsymbol{r},t) = \mu(\boldsymbol{r},t)\boldsymbol{H}(\boldsymbol{r},t)\ , \tag{2.6}$$

where $\epsilon(\boldsymbol{r},t)$ is the permittivity and $\mu(\boldsymbol{r},t)$ is the permeability. Charge conservation is governed by the *continuity equation*

$$\nabla\cdot\boldsymbol{J}(\boldsymbol{r},t) = -\frac{\partial\rho(\boldsymbol{r},t)}{\partial t}\ , \tag{2.7}$$

which is obtained by taking the divergence of equation (2.2) and substituting equation (2.3).

Radar imaging is settled in the field of scattering, with the goal to find the scattering sources responsible for the measured electromagnetic fields. These scatterers are characterized by the material parameters $\epsilon(\boldsymbol{r}')$ and $\mu(\boldsymbol{r}')$, as presented in Fig. 2.1. In scattering theory it is common practice to decompose the total field in an incident field $(\boldsymbol{E}^{\mathrm{i}},\boldsymbol{H}^{\mathrm{i}})$ and a scattered field $(\boldsymbol{E}^{\mathrm{s}},\boldsymbol{H}^{\mathrm{s}})$

$$\boldsymbol{E} = \boldsymbol{E}^{\mathrm{i}} + \boldsymbol{E}^{\mathrm{s}}\ , \tag{2.8}$$

$$\boldsymbol{H} = \boldsymbol{H}^{\mathrm{i}} + \boldsymbol{H}^{\mathrm{s}}\ . \tag{2.9}$$

With this approach it is possible to write the Maxwell equations in terms of the scattered electric and magnetic field, (A.5) and (A.6), respectively. The analytic solution for the electric scattered field (A.28) in time domain may be written in compact notation according to

$$\boldsymbol{E}^{\mathrm{s}}(\boldsymbol{r},t) = \int_{t'}\iiint_{\boldsymbol{r}'}\mathcal{L}(\epsilon(\boldsymbol{r}'),\mu(\boldsymbol{r}'),\boldsymbol{E}(\boldsymbol{r}',t'),\boldsymbol{H}(\boldsymbol{r}',t'))\Big\{\frac{\delta(t-\|\boldsymbol{r}-\boldsymbol{r}'\|/c-t')}{4\pi\|\boldsymbol{r}-\boldsymbol{r}'\|}\Big\}\mathrm{d}\boldsymbol{r}'\mathrm{d}t'\ , \tag{2.10}$$

where $\mathcal{L}(\epsilon(\boldsymbol{r}'),\mu(\boldsymbol{r}'),\boldsymbol{E}(\boldsymbol{r}',t'),\boldsymbol{H}(\boldsymbol{r}',t'))$ represents a linear differential operator as function of the material parameters and the total fields, applied to an integration kernel. This equation already exhibits the fundamental structure of the SAR imaging equation, with the *Green's function* $\delta(t-\|\boldsymbol{r}-\boldsymbol{r}'\|/c-t')/(4\pi\|\boldsymbol{r}-\boldsymbol{r}'\|)$ describing the wave propagation from the source to the observation point in space and time. For a detailed derivation the interested reader is referred to appendix A. Note, in the following, for duality reasons, the discussion shall be carried out at the example of the electric field. Nevertheless, it is important to

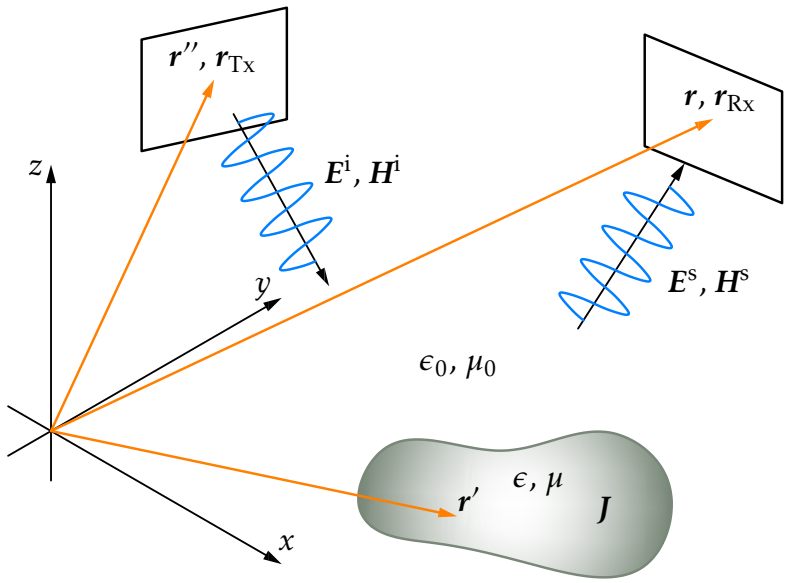

Figure 2.1: Scattering scenario with incident $(\boldsymbol{E}^{\mathrm{i}}, \boldsymbol{H}^{\mathrm{i}})$ and scattered field $(\boldsymbol{E}^{\mathrm{s}}, \boldsymbol{H}^{\mathrm{s}})$ in a bistatic observation configuration. Here, $\boldsymbol{r}_{\mathrm{Tx}}$ and $\boldsymbol{r}_{\mathrm{Rx}}$ represent the point-like phase centers of the transmit and receive antenna, respectively, while $\boldsymbol{r}''$ and $\boldsymbol{r}$ describe the geometrical structure of the corresponding antennas, indicated by the rectangular shapes. The scatterer is characterized by the position vector $\boldsymbol{r}'$, the permittivity ϵ and the permeability μ, as well as the induced current density $\boldsymbol{J}$.

mention that the recorded signals in a radar instrument, which are voltages and currents, are a result of both, the electric and the magnetic field. A simplification to this integral equation (*Lippmann-Schwinger equation*) can be introduced, if the weak scatterer approximation, also known as *Born approximation* [124], is applied. This implies that the currents on the sources are only induced by the incident field. In case of a conglomerate scatterer the individual scatterers do not interact among each other. Then equation (2.10) reduces to

$$\boldsymbol{E}^{\mathrm{s}}(\boldsymbol{r}, t) = \int_{t'} \iiint_{\boldsymbol{r}'} \mathcal{L}(\epsilon(\boldsymbol{r}'), \mu(\boldsymbol{r}'), \boldsymbol{E}^{\mathrm{i}}(\boldsymbol{r}', t'), \boldsymbol{H}^{\mathrm{i}}(\boldsymbol{r}', t')) \left\{ \frac{\delta(t - \|\boldsymbol{r} - \boldsymbol{r}'\|/c - t')}{4\pi\|\boldsymbol{r} - \boldsymbol{r}'\|} \right\} \mathrm{d}\boldsymbol{r}' \mathrm{d}t' \,. \tag{2.11}$$

With equation (2.11) an analytic expression is given, which allows to describe the scattered fields as function of the incident fields, as illustrated in Fig. 2.1.

2.1.1 The SAR Imaging Equation

Since this work is concerned with digital beamforming techniques, the main problem to be faced here is the introduction of complex-valued antenna pattern functions, which will become important later when specific beamforming concepts are discussed. At this stage it is necessary to make several approximations to the fields, fulfilling Maxwell's equations, in order to arrive at a more system-theoretical model of radar scattering, the so called SAR imaging equation. A first approximation regards the differential operator $\mathcal{L}$ in equation (2.11). Clearly this operator links the material functions $\epsilon(\boldsymbol{r}')$, $\mu(\boldsymbol{r}')$ and the incident fields $\boldsymbol{E}^{\mathrm{i}}(\boldsymbol{r}', t')$, $\boldsymbol{H}^{\mathrm{i}}(\boldsymbol{r}', t')$ with the Green's function in a complicated way, as can be seen from equations (A.28) and (A.29). In the frame of radar imaging the interaction of the incident wave with the scatterers is typically represented as the product of the incident field with a so called *object function*, or *reflectivity function* $o(\boldsymbol{r}')$[1] [13]. The incident field $\boldsymbol{E}^{\mathrm{i}}(\boldsymbol{r}', t')$ at the position of the scatterer $\boldsymbol{r}'$ is generated by a current distribution on the transmitting antenna at position $\boldsymbol{r}''$, as shown in Fig. 2.1, and can therefore be written as the solution (A.20) of the wave equation according to

$$\boldsymbol{E}^{\mathrm{i}}(\boldsymbol{r}', t') = \int_{t''} \iiint_{\boldsymbol{r}''} \boldsymbol{Q}(\boldsymbol{r}'', t'') \frac{\delta(t' - \|\boldsymbol{r}' - \boldsymbol{r}''\|/c - t'')}{4\pi\|\boldsymbol{r}' - \boldsymbol{r}''\|} \mathrm{d}\boldsymbol{r}'' \mathrm{d}t'' \tag{2.12}$$

$$\approx \boldsymbol{a}_{\mathrm{Tx}}(\boldsymbol{r}') \int_{t''} p(t'') \mathrm{e}^{\mathrm{j}2\pi f_{\mathrm{c}} t''} \frac{\delta(t' - \|\boldsymbol{r}' - \boldsymbol{r}_{\mathrm{Tx}}\|/c - t'')}{4\pi\|\boldsymbol{r}' - \boldsymbol{r}_{\mathrm{Tx}}\|} \mathrm{d}t'' \,, \tag{2.13}$$

where $\boldsymbol{Q}$ denotes the source term. Here, the transmit antenna is represented by a normalized vectorial complex far field pattern function $\boldsymbol{a}_{\mathrm{Tx}}$ with its phase center at position $\boldsymbol{r}_{\mathrm{Tx}}$, $\boldsymbol{r}'' \mapsto \boldsymbol{r}_{\mathrm{Tx}}$, which shall have no time dependence for the moment in order to avoid a too complicated discussion. Further, the temporal structure of the incident field shall be characterized by the transmitted waveform $p(t)$ of bandwidth B, modulated with a carrier signal at frequency f_{c}. Based

[1] In the frame of polarimetric imaging this object function would be an entry in a 2-by-2 matrix, depending on the polarization combination of incident wave and received wave.

on these assumptions the scattered field (2.11) takes the form

$$\begin{aligned}
\boldsymbol{E}^{\mathrm{s}}(\boldsymbol{r},t) &\approx \int_{t'}\iiint_{\boldsymbol{r}'} o(\boldsymbol{r}')\boldsymbol{E}^{\mathrm{i}}(\boldsymbol{r}',t')\frac{\delta(t-\|\boldsymbol{r}-\boldsymbol{r}'\|/c-t')}{4\pi\|\boldsymbol{r}-\boldsymbol{r}'\|}\mathrm{d}\boldsymbol{r}'\mathrm{d}t' \\
&= \int_{t'}\iiint_{\boldsymbol{r}'} o(\boldsymbol{r}')\boldsymbol{a}_{\mathrm{Tx}}(\boldsymbol{r}')\int_{t''} p(t'')\mathrm{e}^{\mathrm{j}2\pi f_{\mathrm{c}}t''}\frac{\delta(t'-\|\boldsymbol{r}'-\boldsymbol{r}_{\mathrm{Tx}}\|/c-t'')}{4\pi\|\boldsymbol{r}'-\boldsymbol{r}_{\mathrm{Tx}}\|}\mathrm{d}t'' \\
&\quad\cdot\frac{\delta(t-\|\boldsymbol{r}-\boldsymbol{r}'\|/c-t')}{4\pi\|\boldsymbol{r}-\boldsymbol{r}'\|}\mathrm{d}\boldsymbol{r}'\mathrm{d}t' \\
&= \iiint_{\boldsymbol{r}'} o(\boldsymbol{r}')\boldsymbol{a}_{\mathrm{Tx}}(\boldsymbol{r}')p(t-\|\boldsymbol{r}-\boldsymbol{r}'\|/c-\|\boldsymbol{r}'-\boldsymbol{r}_{\mathrm{Tx}}\|/c) \\
&\quad\cdot\frac{\mathrm{e}^{\mathrm{j}2\pi f_{\mathrm{c}}(t-\|\boldsymbol{r}-\boldsymbol{r}'\|/c-\|\boldsymbol{r}'-\boldsymbol{r}_{\mathrm{Tx}}\|/c)}}{4\pi\|\boldsymbol{r}'-\boldsymbol{r}_{\mathrm{Tx}}\|\cdot 4\pi\|\boldsymbol{r}-\boldsymbol{r}'\|}\mathrm{d}\boldsymbol{r}' \,. \qquad (2.14)
\end{aligned}$$

In turn this electromagnetic field induces an electric current I_{Rx} on the receiving antenna structure $\boldsymbol{r}$, according to Maxwell equation (2.2) in integral notation

$$I_{\mathrm{Rx}}(t) = \oint_{\partial A}\boldsymbol{H}^{\mathrm{s}}(\boldsymbol{r},t)\cdot\mathrm{d}\boldsymbol{r} - \frac{\partial}{\partial t}\iint_{A}\epsilon(\boldsymbol{r})\boldsymbol{E}^{\mathrm{s}}(\boldsymbol{r},t)\cdot\mathrm{d}\boldsymbol{A} \,, \qquad (2.15)$$

where A represents the aperture area of the receiving antenna. With a similar reasoning as before, the integration of the scattered field over the receive aperture can be interpreted as weighting of the field with a complex amplitude pattern function $\boldsymbol{a}_{\mathrm{Rx}}$ with phase center at $\boldsymbol{r}_{\mathrm{Rx}}$, $\boldsymbol{r}\mapsto\boldsymbol{r}_{\mathrm{Rx}}$. Because spaceborne SAR imaging typically takes place in the far field, the vectorial pattern functions $\boldsymbol{a}_{\mathrm{Tx}}$ and $\boldsymbol{a}_{\mathrm{Rx}}$ shall be replaced by scalar functions, representing the co- or cross-polar pattern components. Then with the above results, neglecting all constant terms, the received so called *SAR raw signal* u can be cast in the form

$$u(\boldsymbol{r}_{\mathrm{Rx}},t) = \iiint_{\boldsymbol{r}'} o(\boldsymbol{r}')a_{\mathrm{Tx}}(\boldsymbol{r}')a_{\mathrm{Rx}}(\boldsymbol{r}')p(t-\tau)\frac{\mathrm{e}^{\mathrm{j}2\pi f_{\mathrm{c}}(t-\tau)}}{4\pi\|\boldsymbol{r}'-\boldsymbol{r}_{\mathrm{Tx}}\|\cdot 4\pi\|\boldsymbol{r}_{\mathrm{Rx}}-\boldsymbol{r}'\|}\mathrm{d}\boldsymbol{r}' \,, \qquad (2.16)$$

where the delay time τ between transmitter, object and receiver is

$$\tau = \|\boldsymbol{r}'-\boldsymbol{r}_{\mathrm{Tx}}\|/c + \|\boldsymbol{r}_{\mathrm{Rx}}-\boldsymbol{r}'\|/c \,. \qquad (2.17)$$

The raw data signal is written as function of the receiver position $\boldsymbol{r}_{\mathrm{Rx}}$, to indicate the SAR operation where the sensor stays not at a fixed position, but moves along a certain trajectory.

2.2 Spectral Representation of Point Targets

Of fundamental interest for SAR imaging systems is the response of so called *point targets*. From the spectral analysis of point targets SAR specific digital

beamforming concepts can be derived as well as a consistent description of spatial resolution in SAR imagery. Mathematically, point targets are described by Dirac distributions of the form

$$o(\boldsymbol{r}') = \hat{o} \cdot \delta(\boldsymbol{r}') \,. \tag{2.18}$$

Understanding the reflectivity function $o(\boldsymbol{r}')$ as a zero mean complex random process, the radar cross section (RCS) of a point target[2] would correspond to the variance $\sigma_o^2(\boldsymbol{r}') = \mathcal{E}\{|o(\boldsymbol{r}')|^2\}$. The point target reflectivity function (2.18) inserted into the SAR imaging equation (2.16) yields for the raw data signal

$$u(\boldsymbol{r}_{\mathrm{Rx}}, t) = \hat{o} \cdot a_{\mathrm{Tx}}(\boldsymbol{r}') a_{\mathrm{Rx}}(\boldsymbol{r}') p(t-\tau) \frac{\mathrm{e}^{\mathrm{j}2\pi f_{\mathrm{c}}(t-\tau)}}{4\pi\|\boldsymbol{r}' - \boldsymbol{r}_{\mathrm{Tx}}\| \cdot 4\pi\|\boldsymbol{r}_{\mathrm{Rx}} - \boldsymbol{r}'\|} \,. \tag{2.19}$$

Up to now, the temporal-frequency transfer characteristics of the antenna pattern functions have been assumed to be constant. However, this frequency dependency is of special interest for reflector antennas and will be considered later in chapter 4.4.1. In time domain this results in a convolution operation ($*$) between the individual temporal impulse response functions of the transmitted waveform, the propagation paths and the pattern functions

$$\begin{aligned} u(\boldsymbol{r}_{\mathrm{Rx}}, t) = \{[(p(t)\mathrm{e}^{\mathrm{j}2\pi f_{\mathrm{c}} t} * a_{\mathrm{Tx}}(\boldsymbol{r}', t)) * \delta(t - \|\boldsymbol{r}' - \boldsymbol{r}_{\mathrm{Tx}}\|/c)] \cdot \hat{o} * \delta(t - \|\boldsymbol{r}_{\mathrm{Rx}} - \boldsymbol{r}'\|/c)\} \\ * a_{\mathrm{Rx}}(\boldsymbol{r}', t) \cdot (4\pi\|\boldsymbol{r}' - \boldsymbol{r}_{\mathrm{Tx}}\| \cdot 4\pi\|\boldsymbol{r}_{\mathrm{Rx}} - \boldsymbol{r}'\|)^{-1} \,. \end{aligned} \tag{2.20}$$

Then the temporal spectrum of this signal is found via the Fourier transform with respect to the variable t

$$\begin{aligned} u(\boldsymbol{r}_{\mathrm{Rx}}, f) &= \int_t u(\boldsymbol{r}_{\mathrm{Rx}}, t) \mathrm{e}^{-\mathrm{j}2\pi f t} \mathrm{d}t \\ &= \hat{o} \cdot P(f - f_{\mathrm{c}}) a_{\mathrm{Tx}}(\boldsymbol{r}', f) a_{\mathrm{Rx}}(\boldsymbol{r}', f) \frac{\mathrm{e}^{-\mathrm{j}k\|\boldsymbol{r}' - \boldsymbol{r}_{\mathrm{Tx}}\|}}{4\pi\|\boldsymbol{r}' - \boldsymbol{r}_{\mathrm{Tx}}\|} \frac{\mathrm{e}^{-\mathrm{j}k\|\boldsymbol{r}_{\mathrm{Rx}} - \boldsymbol{r}'\|}}{4\pi\|\boldsymbol{r}_{\mathrm{Rx}} - \boldsymbol{r}'\|} \,. \end{aligned} \tag{2.21}$$

Note, the correspondence between the wavenumber k and the frequency f is $k = 2\pi f/c$. An analytic representation of SAR raw data in the spatial frequency domain, or wavenumber domain $\boldsymbol{k} = [k_x \; k_y \; k_z]^{\mathsf{T}}$, is not easily obtained. A first consideration is required with respect to the antenna pattern functions, which shall describe the range-normalized far fields. These far field patterns expressed in terms of wavenumbers can be shown to be the spatial Fourier transforms of

[2] Note, the classical definition of the RCS for SAR systems, which is equivalent to the one given here, is the product of the normalized backscatter coefficient σ_0 and the resolution cell A_{cell} (cf. equation (4.94)).

the current distributions on the antenna structures [4,109]. With the wavenumber and spatial descriptions in spherical coordinates

$$\boldsymbol{k} = \begin{bmatrix} k_x \\ k_y \\ k_z \end{bmatrix} = k \begin{bmatrix} \sin\vartheta\cos\varphi \\ \sin\vartheta\sin\varphi \\ \cos\vartheta \end{bmatrix}, \quad \boldsymbol{r} = \begin{bmatrix} x \\ y \\ z \end{bmatrix} = r \begin{bmatrix} \sin\vartheta\cos\varphi \\ \sin\vartheta\sin\varphi \\ \cos\vartheta \end{bmatrix} \tag{2.22}$$

it turns out, that the representation of far field patterns in spatial and in wavenumber domain are equivalent [109]

$$A_{\mathrm{Tx,Rx}}(\boldsymbol{k},k) \hat{=} a_{\mathrm{Tx,Rx}}(\boldsymbol{r},k) \,, \tag{2.23}$$

when $\boldsymbol{r}$ is replaced by $\boldsymbol{k}$. What remains is the spatial Fourier analysis of the Green's function

$$g(\boldsymbol{r},k) = \frac{\mathrm{e}^{-\mathrm{j}k\|\boldsymbol{r}\|}}{4\pi\|\boldsymbol{r}\|} \,. \tag{2.24}$$

This function is a solution of the scalar wave equation [21]

$$-\Delta g(\boldsymbol{r},k) - k^2 g(\boldsymbol{r},k) = \delta(\boldsymbol{r}) \,, \tag{2.25}$$

under the homogeneous Dirichlet boundary condition, at which the fields vanish for $\|\boldsymbol{r}\|$ approaching infinity. Consequently, the wavenumber domain function is found by Fourier transforming the wave equation resulting in

$$-(-k_x^2 - k_y^2 - k_z^2 + k^2) G(\boldsymbol{k},k) = 1 \,. \tag{2.26}$$

Solving for $G(\boldsymbol{k})$ gives

$$G(\boldsymbol{k},k) = -\frac{1}{k^2 - k_x^2 - k_y^2 - k_z^2} \,. \tag{2.27}$$

This function becomes singular for $k^2 = k_x^2 + k_y^2 + k_z^2$, which is the mathematical description of a sphere with radius k. With the well known Fourier theory relation

$$g(\boldsymbol{r} - \boldsymbol{r}') = \mathcal{F}_{\boldsymbol{k}}^{-1} \left\{ G(\boldsymbol{k}) \mathrm{e}^{\mathrm{j}\boldsymbol{k}\cdot\boldsymbol{r}'} \right\} \,, \tag{2.28}$$

the Fourier pair of the freespace Green's function is given in closed form as

$$\frac{\mathrm{e}^{-\mathrm{j}k\|\boldsymbol{r}-\boldsymbol{r}'\|}}{4\pi\|\boldsymbol{r}-\boldsymbol{r}'\|} \circ\!\!-\!\!\bullet -\frac{\mathrm{e}^{\mathrm{j}\boldsymbol{k}\cdot\boldsymbol{r}'}}{k^2 - k_x^2 - k_y^2 - k_z^2} \,. \tag{2.29}$$

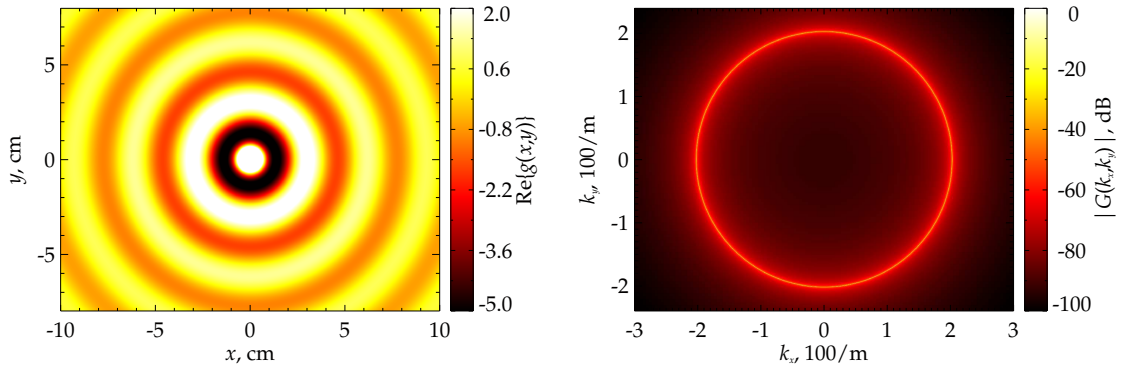

(a) (b)

Figure 2.2: (a) Real part of the Green's function (2.24) for a X-band wavenumber $k = 202.25\,\mathrm{m}^{-1}$, corresponding to a frequency of 9.65 GHz and (b) its Fourier transform according to equation (2.27).

Figures 2.2a and 2.2b show the real part of the Green's function and its Fourier transform in two dimensions, respectively, for a wavelength of 3.1 cm. Considering now the product of the pattern function with a Green's functions in wavenumber domain $A_{\mathrm{Tx,Rx}}(\boldsymbol{k},k)\cdot G(\boldsymbol{r}',\boldsymbol{k},k)$ against the background of spaceborne SAR imaging, it becomes clear that only a small segment of the spectrum of the Green's function is visible. This is because the antenna pattern can be interpreted as a spatial filter, masking the spectrum of the Green's function (2.27). In the spaceborne case the angular support of the main beam is in the order of some fractions of a degree to a few degrees.

A final difficulty arises from the fact that inside the SAR imaging equation two Green's functions appear, one describing the propagation path between transmitter and target and another related to the propagation path between target and receiver. An elegant way to deal with this problem shall be introduced in the next section.

2.2.1 Ewald Sphere Constructions

A comfortable way to describe SAR data in the wavenumber domain is by means of Ewald Sphere constructions. This method, originally developed in the field of X-ray crystallography [23], allows to construct and interpret SAR data without complicated mathematics. The basic concept is to assign each, the incident and scattered field, a wavevector. Here, the convention according to Fig. 2.3 is used, where the incident wavevector $\boldsymbol{k}_{\mathrm{Tx}}$ and the scattered wavevector $\boldsymbol{k}_{\mathrm{Rx}}$ both point in an object centered coordinate system [19] from the point target in the

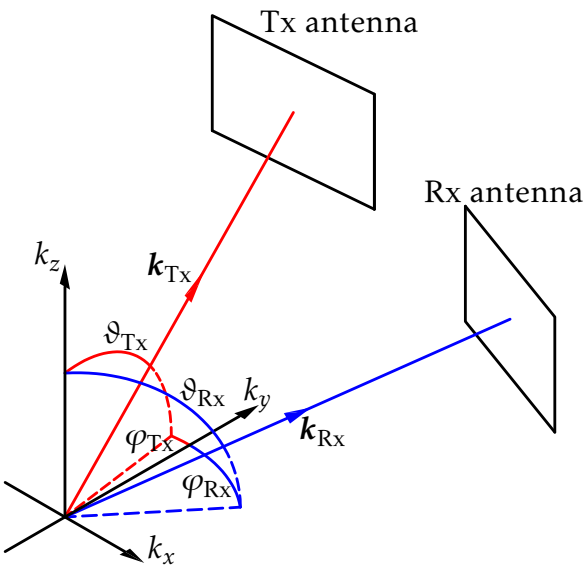

Figure 2.3: Wavevectors $\boldsymbol{k}_{\mathrm{Tx}}$ and $\boldsymbol{k}_{\mathrm{Rx}}$ in object centered coordinates.

origin to the phase centers of the transmit and receive antenna, respectively. The part of the wavenumber domain $\boldsymbol{k}_{\mathrm{SAR}}$, occupied by the SAR data, is then geometrically constructed by summing the incident and scattered wavevectors

$$\boldsymbol{k}_{\mathrm{SAR}} = \boldsymbol{k}_{\mathrm{Tx}} + \boldsymbol{k}_{\mathrm{Rx}} \,. \tag{2.30}$$

Since antenna patterns are usually defined in spherical coordinates it is convenient to apply the same notation to the wavevectors yielding

$$\begin{bmatrix} k_x \\ k_y \\ k_z \end{bmatrix}_{\mathrm{SAR}} = k \begin{bmatrix} \sin\vartheta_{\mathrm{Tx}} \cos\varphi_{\mathrm{Tx}} \\ \sin\vartheta_{\mathrm{Tx}} \sin\varphi_{\mathrm{Tx}} \\ \cos\vartheta_{\mathrm{Tx}} \end{bmatrix} + k \begin{bmatrix} \sin\vartheta_{\mathrm{Rx}} \cos\varphi_{\mathrm{Rx}} \\ \sin\vartheta_{\mathrm{Rx}} \sin\varphi_{\mathrm{Rx}} \\ \cos\vartheta_{\mathrm{Rx}} \end{bmatrix} . \tag{2.31}$$

Throughout this thesis the beamforming concepts shall be demonstrated with *monostatic* SAR sensor configurations, this means transmitter and receiver are collocated $\boldsymbol{r}_{\mathrm{Tx}} = \boldsymbol{r}_{\mathrm{Rx}} = \boldsymbol{r}_{\mathrm{s}}$. This allows to rewrite the bistatic wavevector (2.31) as

$$\begin{bmatrix} k_x \\ k_y \\ k_z \end{bmatrix}_{\mathrm{SAR}} = 2k \begin{bmatrix} \sin\vartheta \cos\varphi \\ \sin\vartheta \sin\varphi \\ \cos\vartheta \end{bmatrix} , \tag{2.32}$$

with $\varphi_{\mathrm{Tx}} = \varphi_{\mathrm{Rx}} = \varphi$ and $\vartheta_{\mathrm{Tx}} = \vartheta_{\mathrm{Rx}} = \vartheta$. Later the variables ϑ and φ shall refer to the local antenna coordinate system of the SAR sensor. Figure 2.4a shows an example of SAR data in wavenumber domain in a *bistatic* configuration, where

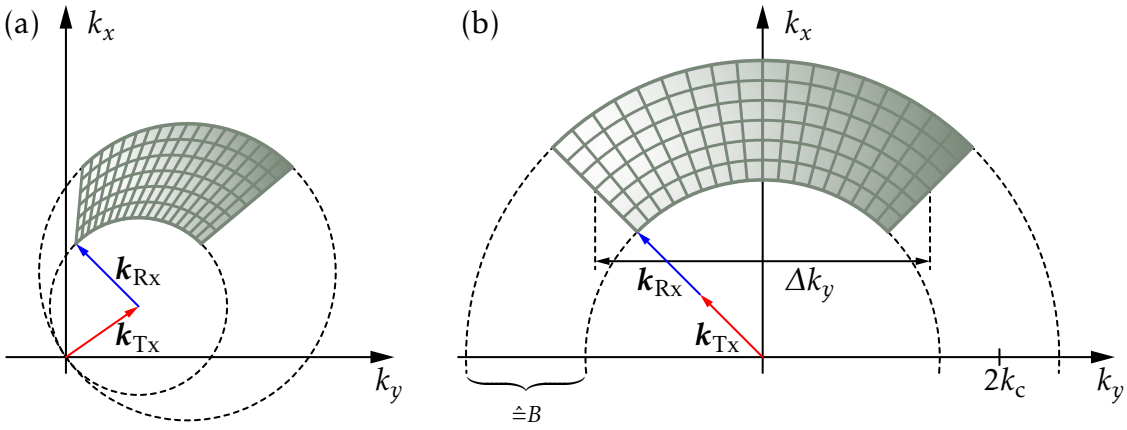

Figure 2.4: (a) Example of bistatic SAR data in wavenumber domain and (b) monostatic SAR data in wavenumber domain with spatial Doppler bandwidth Δk_y. $\boldsymbol{k}_{\mathrm{Tx}}$ and $\boldsymbol{k}_{\mathrm{Rx}}$ are the incident and scattered wavevectors, respectively.

the incident wavevector is kept constant at 35 ° with respect to the k_y-axis and the scattered wavevector is swept in the interval ±45 °. In Fig. 2.4b monostatic wavenumber data are presented, with both wavevectors swept between ±45 °. The variable Δk_y shall denote the Doppler wavenumber bandwidth of the SAR data taken at the center wavenumber k_c. The width of the ring exactly corresponds to the bandwidth B of the transmitted waveform. Comparing both cases it is evident that the Ewald construction with the largest extent is reached in the monostatic case, since here the wavevectors are parallel. Note that for spaceborne SAR systems the illuminated wavenumber domain is typically much smaller, as for example for the TerraSAR-X satellite [113] with a 3 dB beamwidth in azimuth of approximately 0.33 °.

With this framework it is possible to formulate beamforming concepts for SAR systems in a general and efficient way. Although this derivation is based on point targets the generalization to distributed targets is valid, because any scattering object or even a whole SAR scene of several hundred kilometers in size can be understood as aggregation of an infinite number of point targets under the first Born approximation.

2.2.2 SAR Systems and Resolution

Certainly one of the SAR system parameters of major interest is the achievable resolution. Without going into the technical details and restrictions of SAR systems the concept of resolution can be explained with the help of the Ewald sphere representation of SAR data. Generally, resolution is the capability of

discriminating physical quantities of the same dimension. One quantity of interest for a SAR system is the spatial resolution. The azimuth resolution of a SAR system is constant over range and only dependent on the angular domain illuminated by the antenna and the transmit frequency. This is in contrast to real aperture radar systems, where the angular resolution is constant. The concept of resolution is covered by the time-bandwidth product, first formulated by Karl Küpfmüller in 1924 [60]

$$\Delta t \cdot \Delta f \geq 1 \,, \tag{2.33}$$

which prohibits time resolution Δt and frequency resolution Δf to be measured arbitrarily accurate at the same time. This relation is also known as Küpfmüller uncertainty principle. This principle transferred to space-wavenumber quantities can be stated accordingly as

$$\Delta i \cdot \Delta k_i \geq 2\pi \,, \quad i \in [x, y, z] \,, \tag{2.34}$$

with $\Delta k_i = 2\pi \Delta f_i / v_i$ and $\Delta i = v_i \Delta t_i$. It shall be mentioned that this relation represents a physical law, which cannot be overcome. In practice resolution depends also on the waveform $p(t)$ itself. The equality sign holds only for Gaussian waveforms [55].

For monostatic SAR systems the spatial resolution in cartesian coordinates can be given by substituting equation (2.32) into the uncertainty principle (2.34). The resolution is then for example in y-direction in the limit of the equality sign

$$\Delta y = \frac{2\pi}{\Delta k_y} = \frac{2\pi}{2k_1 \sin\vartheta_1 \sin\varphi_1 - 2k_2 \sin\vartheta_2 \sin\varphi_2} \,, \tag{2.35}$$

where $(k_1, \vartheta_1, \varphi_1)$ and $(k_2, \vartheta_2, \varphi_2)$ denote the extents of the illuminated wavenumber domain. In lateral dimensions, that are azimuth and elevation, this domain is usually defined by the 3 dB beamwidth of the antenna pattern and the transmitted center wavenumber $k_1 = k_2 = k_\mathrm{c}$, as indicated in Fig. 2.4b. It is important to underline, that in general each point target in the scene to be imaged occupies a different space in the wavenumber domain, so that the lateral resolutions for the individual scatterers might deviate from each other. Clearly, this consideration is not relevant for instance for stripmap imaging, where only the targets at the start and at the end of the swath have a degraded resolution. The range resolution Δr of a SAR system is typically defined via the signal bandwidth B and is computed from (2.34) according to

$$\Delta r = \frac{2\pi}{\Delta k_r} = \frac{2\pi}{2k_\mathrm{max} - 2k_\mathrm{min}} = \frac{c}{2B} \,, \tag{2.36}$$

where $k_{\min}$ and $k_{\max}$ are the minimal and maximal wavenumbers, respectively. This definition, however, is only meaningful for monostatic SAR systems. Taking as example the bistatic wavenumber domain in Fig. 2.4a directions with vanishing range resolution can also occur.

Although an academical case, the maximal achievable resolution with a SAR system is reached, when the whole diameter of the Ewald sphere is occupied. The maximum monostatic resolution is then

$$\Delta i = \frac{2\pi}{4k_{\max}} = \frac{\lambda_{\max}}{4} \ , \ i \in [x, y, z] \ . \tag{2.37}$$

2.2.3 SAR Signal Sampling

A topic directly related to resolution is the sampling of SAR signals. The received SAR signal $u(\boldsymbol{r}_s, t)$ is a function of time and digitized at some point in the receiver hardware by means of analog-to-digital converters. The sampling frequency f_s must obey the Nyquist-Shannon sampling theorem

$$f_s \geq 2 f_g \ , \tag{2.38}$$

where f_g denotes the highest occurring frequency, which usually is the 3 dB cutoff frequency of a real signal spectrum. This means, the time domain signal in baseband has to be sampled with a frequency equal or larger than the signal bandwidth B.

When SAR data $u(\boldsymbol{r}_s, t)$ are collected on a one-dimensional flight trajectory, the dimension associated with delay time t is called *range* and the dimension along the track is *azimuth*[3] $\boldsymbol{r}_s$. Due to the reception of the radar echoes at different spatial locations the SAR signal in azimuth is inherently discrete. In analogy to (2.38) the sampling law can be formulated for spatial baseband signals according to

$$k_{is} \geq k_{\max} - k_{\min} = \Delta k_i \ , \ i \in [x, y, z] \ . \tag{2.39}$$

Here, the difference between the maximal wavenumber $k_{\max}$ and the minimal wavenumber $k_{\min}$ is taken, because SAR signals often have bandpass character, as for example in squinted SAR acquisitions. It is important to mention that this minimum and maximum wavenumbers are related to all observed scatterers within a scene or footprint. This means, if azimuth is associated with the

[3] In tomographic SAR applications the third dimension is often called elevation. Here, in the frame of digital beamforming with spaceborne SAR systems, elevation is addressed in a similar way and associated with the range dimension, since there is a unique relation between delay time, or range, respectively, and elevation angle.

k_y-dimension in Fig. 2.4b, in order to avoid aliasing effects, the wavenumber sampling rate should be at least

$$k_{ys} \geq 2k_c(\sin\vartheta_1 \sin\varphi_1 - \sin\vartheta_2 \sin\varphi_2) = \Delta k_y \,. \tag{2.40}$$

It is worth to establish a connection between the sampling wavenumber k_{ys} and the pulse repetition frequency PRF, which is more common in airborne or spaceborne SAR literature. The Doppler frequencies f_D, observed by a SAR system, are defined as the rate of change of the phase terms in equation (2.21) normalized to 2π. In the monostatic case this is expressed as

$$f_D(t) = -\frac{2k}{2\pi} \cdot \frac{\partial \|\boldsymbol{r} - \boldsymbol{r}_s\|}{\partial t} = -\frac{2k}{2\pi} \cdot \frac{(\boldsymbol{r} - \boldsymbol{r}_s)^T(\dot{\boldsymbol{r}} - \dot{\boldsymbol{r}}_s)}{\|\boldsymbol{r} - \boldsymbol{r}_s\|} \,, \tag{2.41}$$

where $\boldsymbol{r}$ and $\boldsymbol{r}_s$ represent the target and the sensor location, respectively, and the dot above the vectors indicates its component-wise time derivative. For linear flight trajectories it is possible to find a simple relation between the wavenumbers and Doppler frequencies. If for example the azimuth direction is associated with the y-dimension in cartesian coordinates, as shown in Fig. 4.3, and the sensor moves with a velocity v_y in this direction, then the Doppler frequencies measured are

$$f_D(t) = -\frac{2k}{2\pi} \cdot \frac{y \cdot v_y}{\|\boldsymbol{r} - \boldsymbol{r}_s\|} \,. \tag{2.42}$$

Rearranging this equation according to

$$\frac{2\pi f_D}{v_y} = -2k \cdot \frac{y}{\|\boldsymbol{r} - \boldsymbol{r}_s\|} \tag{2.43}$$

reveals the similarity, except the minus sign, to the y-wavenumber in equation (2.32) for $\varphi = 0\,°$

$$k_y = 2k \sin\vartheta \,. \tag{2.44}$$

Consequently, for linear flight paths the simple relationship

$$k_y = \frac{2\pi f_D}{v_y} \tag{2.45}$$

between wavenumbers and Doppler frequencies can be established. The relation between the PRF and the azimuth sampling wavenumber is then given as

$$k_{ys} = \frac{2\pi(f_{D,max} - f_{D,min})}{v_y} = \frac{2\pi PRF}{v_y} \,. \tag{2.46}$$

Since azimuth SAR signals naturally are discrete signals, the consequences of finite sampling, and in a wider sense, the impact of spatio-temporal ambiguities on SAR signals, shall be discussed in the next section.

2.3 SAR Signals and Ambiguities

In SAR imagery principally two sources of ambiguities can be identified. The first one, resulting from undersampling the SAR signal in azimuth, is known as *azimuth ambiguity*. Azimuth ambiguities are electromagnetic signal power typically collected with the sidelobes of the SAR antenna and folded back into the signal domain. A performance measure, quantifying the amount of ambiguous signal power with respect to the signal power of interest, is the azimuth ambiguity-to-signal ratio (*AASR*) [17]. In the focused SAR image $\overline{o}(y,r)$ azimuth ambiguities can be observed as range- and azimuth-shifted replicas of the main image. Therefore, a very basic definition is given by[4]

$$AASR \equiv \frac{\sum\limits_{m\in\mathbb{Z}\setminus\{0\}} \int_{r_m}\int_{y_m} |\overline{o}(y,r)|^2 \mathrm{d}y_m \mathrm{d}r_m}{\int_r \int_y |\overline{o}(y,r)|^2 \mathrm{d}y \mathrm{d}r}\,, \tag{2.47}$$

where y_m and r_m denote the discrete relative positions of the azimuth ambiguities in azimuth and slant range, respectively. These positions can be derived, assuming a linear flight path, from the wavenumber history (2.43) substituting equation (2.45), by adding integer multiples of the sampling wavenumber on the left side

$$k_y + mk_{y\mathrm{s}} = -2k \cdot \frac{y_m}{\sqrt{R_0^2 + y_m^2}}\,, \tag{2.48}$$

and solving for y_m, yielding

$$y_m = \pm R_0 \left(\left(\frac{2k}{k_y + mk_{y\mathrm{s}}} \right)^2 - 1 \right)^{-\frac{1}{2}}\,, \tag{2.49}$$

with R_0 the distance of closest approach between target and sensor. Similarly, the range shift is found to be

$$r_m = R_0 \left(\left(1 - \left(\frac{k_y + mk_{y\mathrm{s}}}{2k} \right)^2 \right)^{-\frac{1}{2}} - 1 \right). \tag{2.50}$$

[4] In this context the integration over the positions of the azimuth ambiguities (y_m, r_m) and the signal (y,r) must be interpreted as integration over the mainlobe regions of the ambiguities as well as the signal. These regions can be of different size. For instance azimuth ambiguities can be defocused due to range cell migration effects and therefore smeared over a wider domain.

In the case of spaceborne SAR missions, as for example the TanDEM-X mission [85], this range shift is in the order of 10 to 25 m for a *PRF* range between 3000 and 4000 Hz. The corresponding angular shifts lie then between 0.0011 and 0.0019 ° and can therefore be safely neglected in any further considerations. Finally, important for beamforming, the relation between the sampling wavenumber and its corresponding ambiguous directions is described by

$$k_y + mk_{y\mathrm{s}} = 2k \sin \vartheta_m \,. \tag{2.51}$$

The *AASR* formulation with equation (2.47) involves in principle all processing steps, including digital beamforming as well as SAR focusing and is therefore not easily evaluated. Instead, a formulation of the *AASR* in terms of antenna patterns would be quite intuitive, because DBF techniques aim at a manipulation of the shapes of the patterns. A major goal of the work is to improve the *AASR* by means of sophisticated DBF concepts. However, at this stage the *AASR* shall be specified in the more general form in terms of the SAR raw data $U(k_y)$ in the Doppler-range domain and the SAR azimuth processing filter $H_{\mathrm{az}}(k_y)$ as

$$AASR = \frac{\sum\limits_{m \in \mathbb{Z}\setminus\{0\}} \int\limits_{-\Delta k_y/2}^{\Delta k_y/2} \left| U(k_y + mk_{y\mathrm{s}}) H_{\mathrm{az}}(k_y) \right|^2 \mathrm{d}k_y}{\int\limits_{-\Delta k_y/2}^{\Delta k_y/2} \left| U(k_y) H_{\mathrm{az}}(k_y) \right|^2 \mathrm{d}k_y} \,. \tag{2.52}$$

$U(k_y)$ is found by Fourier transforming the signal (2.21) with respect to the azimuth variable y. Since the distances to the signal and the ambiguities, accounted for via the Green's functions, are roughly in the same order, the *AASR* is mainly determined by the product of the transmit pattern $a_{\mathrm{Tx}}(k_y)$ and the receive pattern $a_{\mathrm{Rx}}(k_y)$. This *AASR* formula shall serve as basis for multi-channel systems in chapter 4.

The second source of ambiguities, so called *range ambiguities*, relates to signal energy from preceding and succeeding pulse echoes arriving at the same time at the sensor as the signal of interest. This means that further echo terms on the right side of equation (2.16) appear, assuming monostatic data acquisition, of the form

$$u_l(\boldsymbol{r}_{\mathrm{s}}, t) = \iiint_{\boldsymbol{r}_l} o(\boldsymbol{r}_l) a_{\mathrm{Tx}}(\boldsymbol{r}_l) a_{\mathrm{Rx}}(\boldsymbol{r}_l) p(t - \tau_l) \frac{\mathrm{e}^{\mathrm{j}2\pi f_{\mathrm{c}}(t-\tau_l)}}{(4\pi)^2 \|\boldsymbol{r}_{\mathrm{s}} - \boldsymbol{r}_l\|^2} \mathrm{d}\boldsymbol{r}_l \,, \tag{2.53}$$

with $\tau_l = \|\boldsymbol{r}_{\mathrm{s}} - \boldsymbol{r}_l\|/c$. The condition for this can be expressed in terms of the distance between the sensor $\boldsymbol{r}_{\mathrm{s}}$ and the position of the lth range ambiguity $\boldsymbol{r}_l$

through

$$\|\boldsymbol{r}_\mathrm{s} - \boldsymbol{r}_l\| = \|\boldsymbol{r}_\mathrm{s} - \boldsymbol{r}\| + l\frac{c}{2PRF}\,. \tag{2.54}$$

The range ambiguity-to-signal ratio (*RASR*) is best assessed in time domain, or equivalently in slant range domain r ($t = 2r/c$)

$$RASR(t) = \frac{\sum\limits_{l\in\mathbb{Z}\setminus\{0\}} \int\limits_{t'=t}^{t+\tau_\mathrm{p}} |u_l(t')|^2 \mathrm{d}t'}{\int\limits_{t'=t}^{t+\tau_\mathrm{p}} |u(t')|^2 \mathrm{d}t'}\,, \tag{2.55}$$

where a range processing filter of rectangular shape is assumed. As in the azimuth case, this formula will be adapted in chapter 4 in the frame of digital beamforming.

2.4 Signal-to-Noise Ratio

A fundamental measure of the sensitivity of a radar system is the signal-to-noise ratio *SNR*. The *SNR* for SAR systems has always been discussed controversially. An issue raised in this context is, for example, the question if point targets and distributed targets should be treated differently [17]. Different interpretations of the SAR signal itself exist. In [99] the author uses a physical approach where the SAR signal is modeled as a noise process and the SAR signal processing is consequently characterized as *detection of noise within noise*. It is concluded, that there can't be coherent processing gain. Later this conclusion is discarded in [100], where the authors explicitly derive formulas for the SAR processing gain. Another thorough analysis of the SAR *SNR* problem can be found in [80] with particular emphasis on the treatment of noise distributions. The above mentioned publications deal with single-channel systems and are therefore limited in their validity. The trend in future SAR systems is clearly towards multi-channel systems and therefore it is an important aspect to expand existing SAR *SNR* models. Generally, the *SNR* in a SAR image

$$SNR(y,r) = \frac{P_s(y,r)}{P_v(y,r)} = \frac{\mathcal{E}\{|s(y,r) * h(y,r)|^2\}}{\mathcal{E}\{|v(r) * h(y,r)|^2\}}\,, \tag{2.56}$$

can be expressed in terms of the noise-free SAR raw data signal $s(y,r)$, the noise signal $v(r)$ and the SAR processing filter $h(y,r)$, assuming uncorrelated signal and noise. Here, $\mathcal{E}\{.\}$ denotes the expectation value. This formula is based on a

simplified SAR focusing, described by the two-dimensional convolution operator $*$ with respect to slant range r and azimuth y. Again, this *SNR* model will be refined in the context of digital beamforming in chapter 4.

3 Conventional SAR Systems

Due to the increasing spectrum of SAR applications, radar systems undergo an evolution in terms of hardware complexity and flexibility. In the chain of technological advancement the term *conventional* shall refer to all kinds of non-digital beamforming systems. This means, a characteristic of such systems is that they collect electromagnetic energy with a single beam and channel at a time-instance. Beams can either be created by mechanical adjustment of the SAR antenna, or, as presented in Fig. 3.1, via electrical beam-steering. For example on receive, indicated by the blue signal path, the phase and amplitude are controlled within the transmit/receive modules such that the beam points at the desired direction. On transmit, the beam is typically generated by phase-only synthesis, in order to radiate the maximum available power. The signal is then combined in the *power distribution network* (PDN), down converted with the *local oscillator* (LO) signal and finally analog-to-digital converted. At this

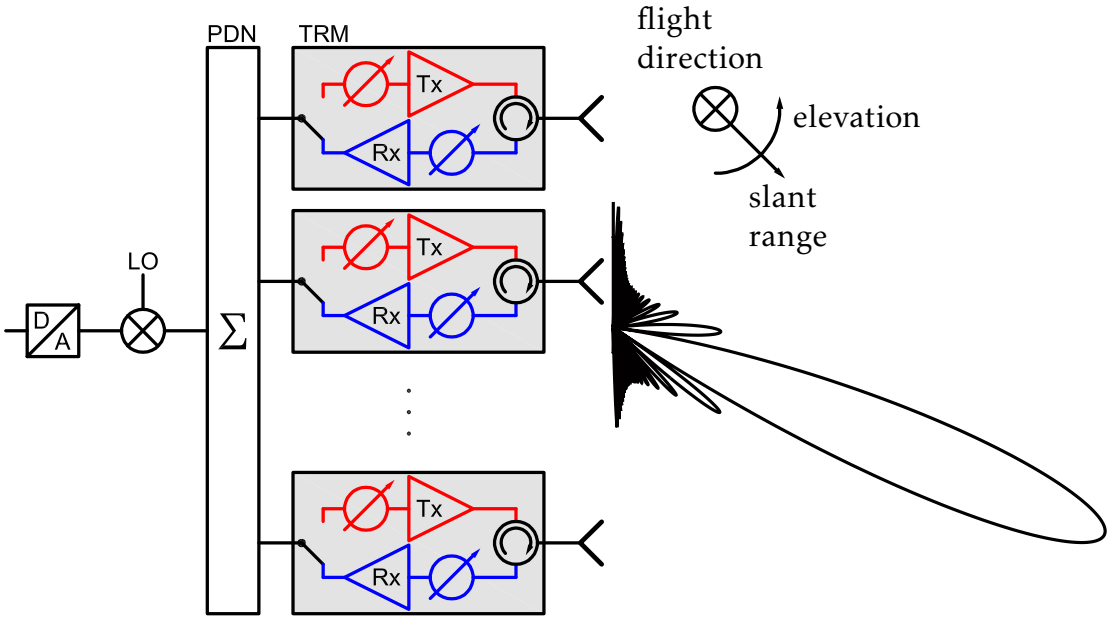

Figure 3.1: Basic conventional SAR system architecture with transmit- and receive-chain, operated in a side-looking configuration. To maintain a clear representation hardware components like limiters, amplifiers or filters have been omitted.

stage the SAR raw data signal is in principle available for digital signal processing routines.

Generally, spaceborne SAR systems are flown in a side-looking geometry, that means the antenna boresight points laterally and orthogonal to the flight direction to the Earth surface. The SAR data are consequently collected in the coordinates azimuth, associated with the flight direction, and slant range. Later also elevation is used to label slant range. This is useful, as long as there exists a unique relationship between the elevation angle and slant range, because beamforming is conveniently described in antenna- or wavenumber-coordinates, respectively.

Hardware components in the transmit and receive path of a SAR system, like mixers, filters or amplifiers alter the signal in some way. However, these contributions differ, when comparing different SAR systems, only in terms of magnitude. In contrast, the SAR antenna has a major impact on the way how to operate a SAR system, on the signal processing and on the performance in general. Insofar the introduction of reflector antennas to SAR systems shall be motivated by a comparison to their planar counterparts in the next sections.

3.1 Comparison: Planar versus Reflector Antenna SAR System

The radar antenna, being the interface between electromagnetic waves and electric signals inside the receiver hardware, requires careful design, since it defines the observation space within the wavenumber domain. Two major standards for SAR antennas can be identified, one referring to the time-domain behavior and the other concerning the spatial-domain characteristics. In the far field of an antenna, the observation space is spanned be the triple (k, φ, ϑ) defining the wavenumber domain (2.32). Desirable is an antenna design where these variables are independent, which is in general not the case. Interpreting the antenna pattern as space-time filter, the pattern should be constant in the passband with a high slew rate. In the following, the conventional antenna type for SAR systems, the planar array antenna, shall be contrasted with the array-fed reflector antenna.

3.1.1 Planar Array Antennas

The most widely used antenna types for SAR sensors are planar array antennas. The electromagnetic theory for these antennas is well established and can be found in various books [1, 37, 78, 84, 109, 114]. A commonly used antenna gain

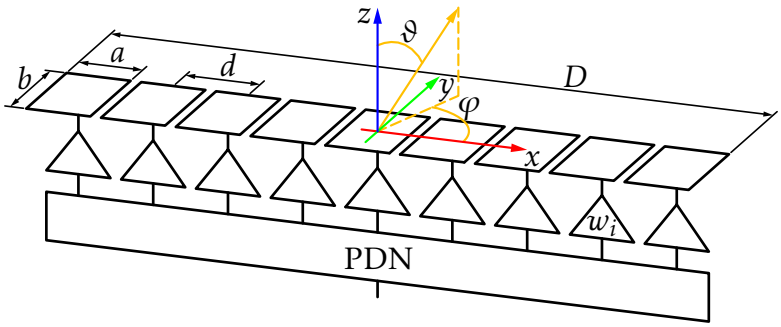

Figure 3.2: Linear planar array antenna with rectangular elements of dimensions a and b. The antenna excitation coefficients are given by the complex weights w_i.

pattern model [32] in the far field for a linear equi-spaced array takes the form

$$G(k,\varphi,\vartheta) = \eta_\mathrm{a} \frac{\left|\sum_{i=0}^{N_\mathrm{c}-1} w_i \cdot a_{\mathrm{f},i}(k,\varphi,\vartheta) \cdot \mathrm{e}^{\mathrm{j}ikd\sin\vartheta\cos\varphi}\right|^2}{\sum_{i=0}^{N_\mathrm{c}-1} |w_i|^2}\,, \tag{3.1}$$

where η_a is the total efficiency of an array antenna. In the usual antenna terminology, the denominator in model (3.1) would represent the total radiated electromagnetic power, while the numerator resembles the directional power. As indicated in the antenna example in Fig. 3.2 the array is aligned with the x-axis and its elements are spaced d apart. The number of elements is denoted with N_c. Later this variable will be used for the number of digital channels, which is not necessarily the same as the number of elements in an array. The function a_f represents a model for the individual element patterns in the array. A most rudimentary model for rectangular apertures, assuming a constant aperture current distribution, could be [1] [114]

$$a_\mathrm{f}(k,\varphi,\vartheta) = k\sqrt{ab/\pi} \cdot \mathrm{sinc}(ka/2\sin\vartheta\cos\varphi) \cdot \mathrm{sinc}(kb/2\sin\vartheta\sin\varphi)\,, \tag{3.2}$$

with the dimensions of the aperture in x and y of a and b, respectively. In the pattern model (3.1) the individual channels are multiplied with so called complex weights w_i (excitation coefficients). Each weight can be associated with the phase and amplitude control in a TRM, likewise on transmit or receive (see Fig. 3.1). In the context of beamforming these weights are dimensionless. However, in practice these quantities carry the power transmitted or received by the antenna.

[1] The term $k\sqrt{ab/\pi}$ is the square-root of the aperture gain using the effective area $a \cdot b$ and substituting $2\pi/k$ for λ.

From equations (3.1) and (3.2), assuming constant weights w_i, several important parameters can be derived. An equi-spaced array, consisting of isotropic radiators, generates so called *grating lobes*, depending on the element spacing d and the wavelength λ, at angles

$$\vartheta_m = \arcsin\left(\frac{m\lambda}{d}\right), \quad m \in \mathbb{Z} \setminus \{0\}, \tag{3.3}$$

with respect to the principal mainlobe, in the x-z-plane ($\varphi = 0°$). Note, in the special case $a = d$ and constant weights the zeros of the element patterns (3.2) eliminate these grating lobes. Between any two mainlobes exist $N_c - 2$, $N_c \geq 2$, sidelobes, the first being approximately 13.26 dB below the mainlobe for large N_c. The 3 dB beamwidth for aperture antennas with constant weights can be approximated with

$$\Theta_{3\text{dB}} \approx 0.89\frac{\lambda}{D}, \tag{3.4}$$

where $D = (N_c - 1) \cdot d + a$ describes the total aperture length.

3.1.2 Array-fed Reflector Antennas

The concept of reflector antennas is to radiate electromagnetic energy not directly from the feeding element, short *feed*, but via a scattering surface, the reflector, as presented in Fig. 3.3. This means, for a spaceborne reflector SAR system, the feed faces the reflector, which directs the transmitted electromagnetic wave to the Earth surface. Classical reflectors are built in various designs ranging from cylindrical-, corner- to the well known parabolic shapes [111]. Parabolic reflectors, for example, which shall serve as basis for the investigations throughout this thesis, have the property to focus a plane wave, incoming antiparallel to the rotational axis of the paraboloid, after scattering at the reflector, in the so called focal point, short *focus*. Geometrically, parabolic reflectors can be described in Cartesian coordinates with the equation

$$z = \frac{1}{4F}\left(x^2 + y^2\right), \tag{3.5}$$

where $(x, y, z) = (0, 0, F)$ is the location of the focal point. Consequently, in order to collect the electromagnetic energy, the feed is placed in the focus at the place of the highest field strength. However, if the plane wave impinges the reflector under a slightly different angle, the field strength at the focus drops rapidly and so does the antenna gain. Insofar the position of the feed is of great importance, since it determines the solid angle where electromagnetic energy is radiated

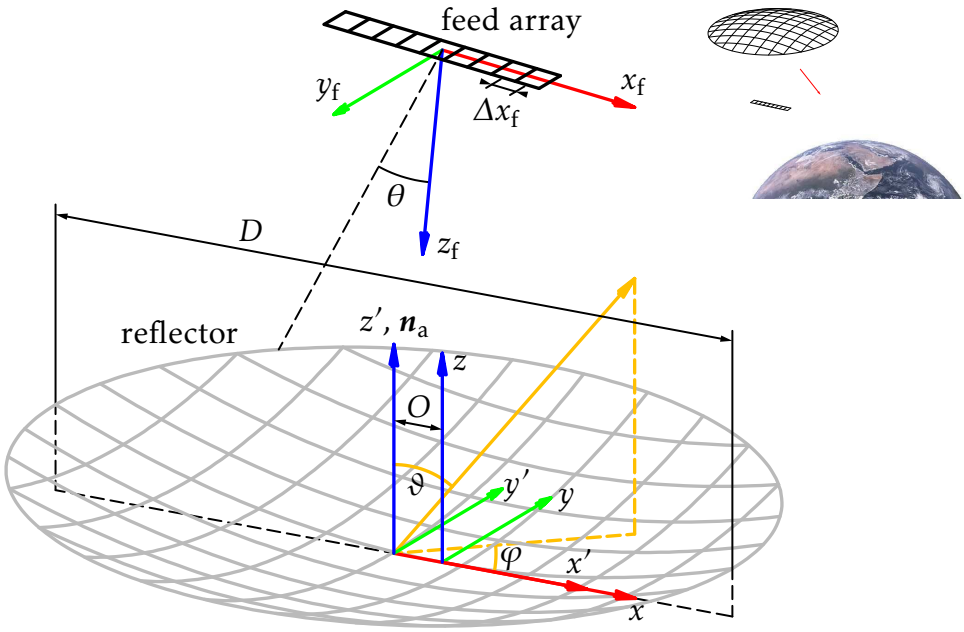

Figure 3.3: Reflector and feed array geometry, with different coordinate systems for the feed (x_f, y_f, z_f), the reflector (x, y, z) and the far field (x', y', z'). The reflector and the far field coordinate system coincide for non-offset configurations. The small sketch in the top right shows how the array-fed reflector is oriented in space.

or received. Therefore, in order to cover a whole continuum of solid angles, an array of feed elements is required, each illuminating a small essentially disjunct domain. Feed array design might be even more challenging than the conception of a planar array antenna, since feed arrays are usually more compact in size and effects from coupling and multipath propagation need careful attention. Since this work is focused on beamforming techniques, in the subsequent analysis these effects are neglected.

The conceptual design of a reflector antenna with planar feed array is presented in a perspective view in Fig. 3.3. The linear feed array is defined in coordinates (x_f, y_f, z_f), with the origin in the center of the array. This point coincides with the afore mentioned focal point. Here, the individual feed elements are oriented in the z_f-direction. However, for large feed arrays the reflector illumination might be improved by tilting each feed element individually towards the reflector's center. The parabolic reflector according to equation (3.5) is defined in (x, y, z)-coordinates, where the z-axis serves as rotational axis for the parabola. In so called *offset*-reflector configurations it is useful to introduce a new coordinate system (x', y', z'), where the far field in terms of the spherical

parameter	symbol	value
frequency	f	9.65 GHz
diameter	D	7 m
focal length	F	4.9 m
offset	O	0.5 m
elevation feed element spacing	Δx_f	0.6λ
number of elevation feed elements	N_x	27

Table 3.1: Reflector and feed array parameters for the simulation shown in Figs. 3.4 and 3.5.

angles (φ, ϑ) is defined. This coordinate system shall be called local antenna coordinate system. The boresight direction is aligned with the direction of the antenna normal vector $\boldsymbol{n}_\mathrm{a}$. Here, the offset O is defined as perpendicular distance between the coordinate axes z and z' (see Fig. 3.3). A reflector with circular aperture is defined such, that the orthogonal projection of the reflector rim, in a plane z = constant, results in a circle. The diameter D of a reflector therefore refers to the diameter of this circle. For the application with SAR systems it often proofs useful to design reflectors with elliptical aperture areas, with different diameters in azimuth D_az and elevation D_el (see Fig. 5.2). With such designs the shapes of the beams in azimuth and elevation can be controlled almost independently.

A clear disadvantage in the theoretical treatment of reflector antennas is the difficulty to derive a compact analytical expression for the antenna gain pattern, comparable to (3.1). Here, the term 'pattern' refers to the radiation characteristic after scattering at the reflector, also known as *secondary pattern* [1, 84] in the reflector antenna literature. A typical way to find the fields is to solve equations (A.30) and (A.31) under the *physical optics approximation* [1]. In this case the integration is performed over the reflector surface. For a reflector antenna design example, with the parameters listed in Table 3.1, the far field patterns have been simulated using the EM-simulation software TICRA GRASP9 [118]. Figure 3.4a shows a reflector gain pattern, when all elements are active, as function of elevation and azimuth. These coordinates are related to the spherical coordinates (φ, ϑ) according to

$$\text{elevation} = \vartheta \cos\varphi \,, \tag{3.6}$$

$$\text{azimuth} = \vartheta \sin\varphi \,. \tag{3.7}$$

This means, the principal azimuth cut is defined at $\varphi = 90°$ and the principal elevation cut at $\varphi = 0°$. Figure 3.4a makes clear, that in the SAR application, it is necessary to activate all feed elements in order to illuminate a large solid

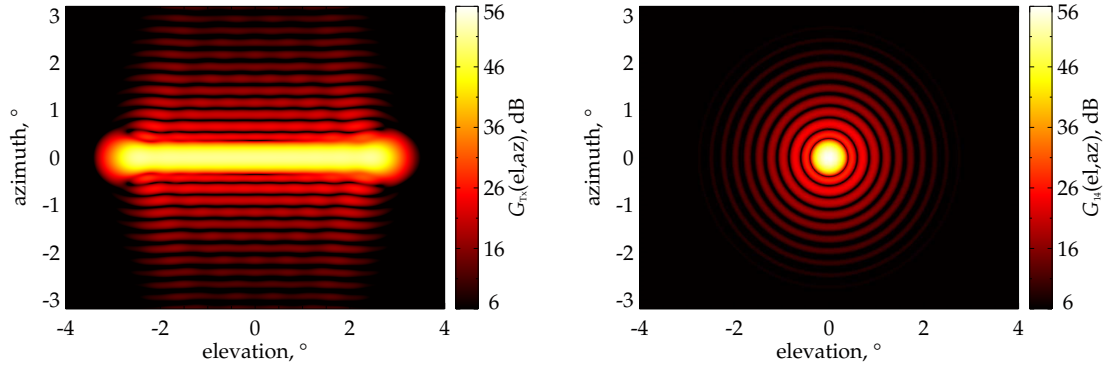

Figure 3.4: (a) 2-D gain pattern with all elements active and (b) gain pattern for element 14 in the center of the feed array in elevation-azimuth coordinates.

angle or swath, respectively. In contrast, the gain pattern for a single feed element in the center of the array is depicted in Fig. 3.4b. The sidelobes differ from those of a planar array antenna of rectangular shape insofar that they appear as concentric rings around the mainlobe. The shape of the pattern might be characterized by rotationally symmetric Bessel functions [49]. However, this model is at best reliable for center fed reflectors and small offsets. Insightful is the pattern cut plot in Fig. 3.5. Here, the bandpass character of the individual patterns becomes evident. This is in contrast to direct radiating arrays, where each element basically illuminates the same angular domain. The overlap between adjacent patterns is mainly determined by the feed spacing Δx_f. A too large spacing results in a larger separation of the individual patterns and in an increased risk of loosing a part of the wavenumber domain in case of an element failure.

The combination of a reflecting surface with a feed does not come without any losses, which can be expressed in terms of the so called *aperture efficiency* η_{ap} [1]. Among other contributions, the two major effects reducing the total efficiency are the *spillover efficiency* [1, 84], quantifying the amount of electromagnetic en-

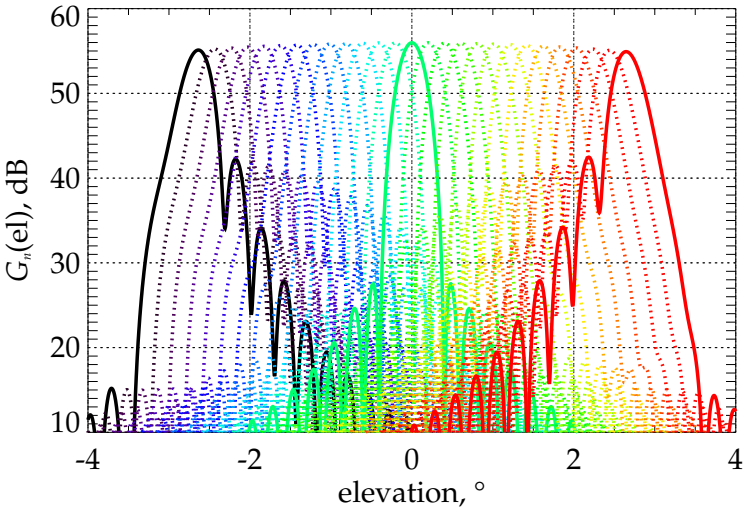

Figure 3.5: Individual reflector gain patterns in the principal elevation cut.

ergy radiated from the feeds past the reflector,

$$\eta_s = \frac{\int_k \int_0^{2\pi} \int_0^{\theta(\varphi_f)} G_f(k,\varphi_f,\vartheta_f) \sin\vartheta_f \mathrm{d}\vartheta_f \mathrm{d}\varphi_f \mathrm{d}k}{\int_k \int_0^{2\pi} \int_0^{\pi} G_f(k,\varphi_f,\vartheta_f) \sin\vartheta_f \mathrm{d}\vartheta_f \mathrm{d}\varphi_f \mathrm{d}k} \quad \in [0,1]\,, \tag{3.8}$$

and the *taper efficiency* [1, 84]

$$\eta_t = \frac{\left(\int_k \iint_A \sqrt{G_f(k,A)} r^{-1}(A) \mathrm{d}A \mathrm{d}k \right)^2}{A \cdot \int_k \iint_A G_f(k,A) r^{-2}(A) \mathrm{d}A \mathrm{d}k} \quad \in [0,1]\,, \tag{3.9}$$

measuring the tapered aperture field distribution with respect to a uniform aperture field distribution. Note, in equation (3.8) the spherical angles (φ_f, ϑ_f) refer to a local feed element coordinate system. G_f is the feed gain pattern and $\theta(\varphi_f)$ denotes the angle between the boresight pointing vector of a feed element and the vector pointing from the feed element's phase center to the reflector rim, as shown for the center feed element in Fig. 3.3. In equation (3.9) A is the projected aperture area of the reflector and $r(A)$ denotes the distance between a feed element's phase center and a point on this reflector aperture area. These

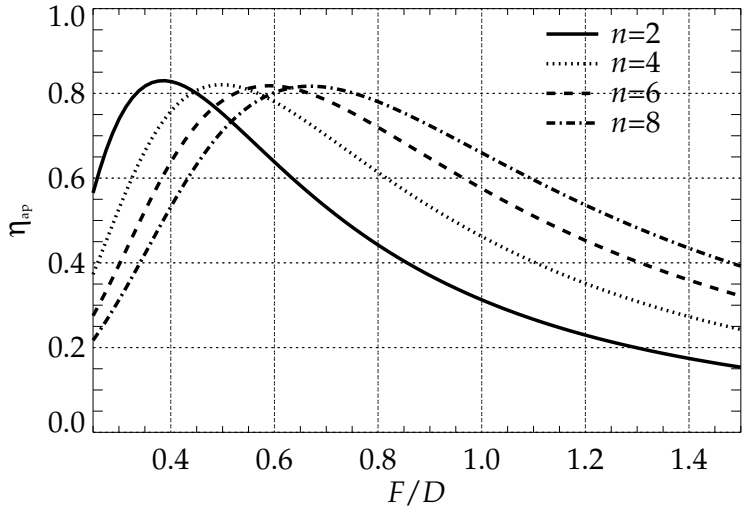

Figure 3.6: Aperture efficiency η_{ap} for a center fed parabolic reflector antenna with circular aperture for cosine feed pattern models according to equation (3.10) as function of the F-over-D ratio and the exponential value n of the cosine function.

formulas have been modified with respect to those given in [1, 84], as the integration over the transmit wavenumber band has been introduced. For a cosine feed pattern model, first introduced by Silver [1, 109]

$$G_f(\vartheta_f) = \begin{cases} G_0^{(n)} \cos^n \vartheta_f & , \quad 0 \le \vartheta_f \le \pi/2 \\ 0 & , \quad \pi/2 < \vartheta_f \le \pi \end{cases} \tag{3.10}$$

the aperture efficiency is plotted in Fig. 3.6 for different powers n versus the F-over-D ratio. In this model G_0 is a constant for a given power n. In case of a center fed parabolic reflector with circular aperture the F-over-D ratio is related to the constant angle θ via

$$\tan\theta = \frac{8F/D}{16(F/D)^2 - 1} \,. \tag{3.11}$$

Since the spillover efficiency and the taper efficiency behave in the opposite way, the aperture efficiency $\eta_{ap} = \eta_s \cdot \eta_t$ has an optimum, depending on the feed pattern model in the order of 80 %. These two efficiency components do not occur with planar array antennas, as long as no taper is applied. This means, reflector antennas have an inherently reduced gain of about 1 dB compared to direct radiating arrays of the same aperture size. This gain loss is potentially even higher

characteristic	**planar array**	**array-fed reflector**
boresight *HPBW*	$\sim 0.89\lambda/D$	$\sim 1.22\lambda/D$
total efficiency	η_a	$\sim 0.8\eta_a$
grating lobes	$\vartheta_m = \arcsin(m\lambda/d)$	-
scan angle domain	limited by grating lobes	limited due to defocusing
beam characteristic[2]	lowpass	bandpass
beam overlap	fully overlapping	partially overlapping
blockage	-	gain loss ~ 0.1 dB [112]
frequency response	determined by k in equations (3.1) & (3.2)	influenced by blockage and multipath
antenna weight	heavy	light
realizable aperture	medium	large

Table 3.2: Comparison between planar array antenna and reflector antenna. The beam characteristic as well as the beam overlap refer to a single element.

for off-focus feeding, in case of a suboptimal illumination of the reflector, and limits in principle the region where feed elements can be placed. Consequently, the 3 dB beamwidth of the secondary pattern is strongly influenced by the feed pattern shape as well as the position of the feed relative to the reflector. A useful approximation for center fed parabolic reflectors is [84]

$$\Theta_{3\text{dB}} \approx 1.22\frac{\lambda}{D}\,. \tag{3.12}$$

The broadening of the beam is accompanied by an improved sidelobe level in the order of -27 dB for center fed reflectors. With off-focus feeding an effect called *coma lobes* [84] occurs. This effect is related to the asymmetric levels of the first sidelobes next to the mainlobe. Here, typically one sidelobe rises its level disproportionately high, depending on the distance of the feed element from the focus $(0, 0, F)$. This can be observed, for example, on the most left or most right pattern in Fig. 3.5.

Table 3.2 summarizes the key aspects of array-fed reflector antennas in comparison to planar array antennas. In the context of multi-element antennas, the beam characteristic and the beam overlap refer to the individual antenna element patterns, which are the secondary patterns, associated with the feed elements, in case of a reflector antenna. Blockage and related to this phenomenon, multipath effects, which can evolve from an interaction of the radiated wave

[2]Here, the terminology common in system theory and filter design is adopted. The characteristic refers to the spatial transfer function.

with the feed array but also the satellite bus or the boom connecting reflector and satellite, are a peculiarity of array-fed reflector antennas, which impact their frequency response. In [96, 97] the dependency of the antenna pattern on the transmitted frequency has been investigated. A solution to mitigate this effect to a certain degree is to use offset reflector configurations. Another consequence of multipath effects, which is well known for multi-scattering scenarios on ground [51], manifests in so called ghost images which are time delayed and possibly distorted versions of the direct path image. Also for this problem offset configurations might provide a benefit. Direct radiating arrays experience an increase in gain with higher frequencies (see equation (3.2)) and a scanning of the beam, determined by the term $k \cdot d$ in equation (3.1). Nevertheless, in general the frequency response of planar antennas is much smoother than that of array-fed reflector antennas, where gain variations in X-band of up to 8 dB have been observed [97].

Besides the electrical characteristics of SAR antennas also mechanical aspects need careful attention. Especially spaceborne SAR systems are constrained with respect to the mass budget as well as the overall size of the SAR satellite to be stowed in the fairing. Also quite challenging and different from a planar array SAR system is the flight dynamics of such a distributed mass, as in the case of a reflector SAR system. In this context deployable mesh reflectors [33,50,92,117], already a mature technique for communication satellites, offer the opportunity to realize high gain antennas at a relatively low weight compared to planar array antennas.

3.2 Wide-Swath SAR System Operation

Spaceborne SAR systems acquire backscatter data in a side-looking geometry in order to avoid ambiguous signal overlap in range. The electromagnetic energy is directed via the transmit beam to the Earth surface. The region on ground illuminated by the 3 dB extent of the Tx beam is called footprint. Typically this 3 dB extent in elevation, or range, defines the swath width X (see Fig. 3.7 and 3.8). The sensor moves in azimuth direction, and successively transmits radar pulses. These radar pulses are scattered at the Earth surface and a part of the signal, called the echo, is reflected back to the sensor, where the signal is received and coherently recorded.

A SAR imaging mode, where a receive beam moves over the swath in accordance with the direction of reflection using analog beam-steering, was first suggested in [3] for an array of linear feeds and further developed in [29, 115, 116] with the innovation of digital receiver hardware. This operation principle, today known as Scan-On-Receive (SCORE), offers the opportunity to map swaths

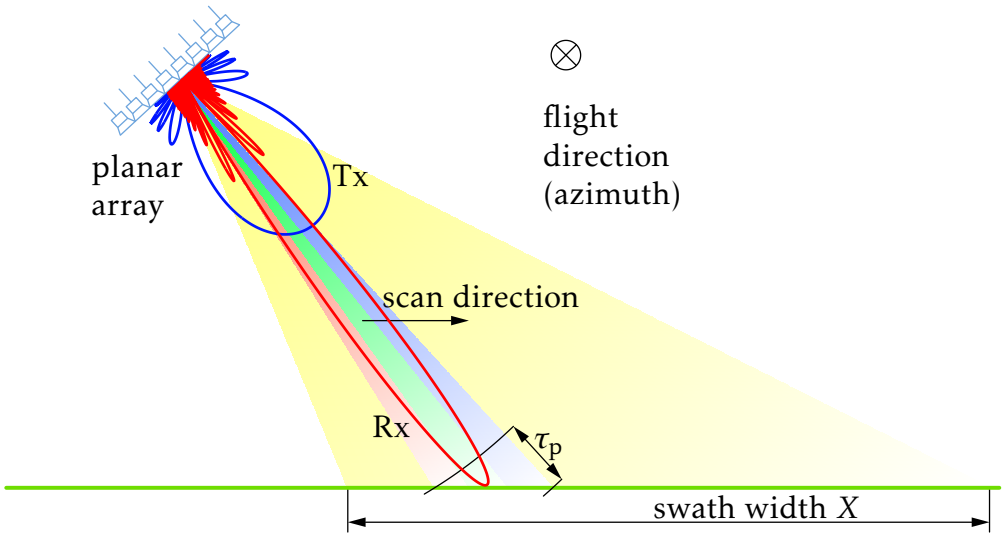

Figure 3.7: Planar array system operation with Tx beam illuminating the swath and Rx beam following the pulse on ground.

with very large widths. Considering the planar array SAR system in Fig. 3.7, on transmit a broad beam, indicated by yellow color, is generated in order to cover the entire swath. This low gain beam will require phase only pattern synthesis methods [8, 9, 121, 122], with all antenna elements active, in order to maintain the maximum amount of transmit power. When the transmitted waveform reaches the ground it moves from the near to the far end of the swath. On receive a high gain beam, symbolized by the red-green-blue color scheme in Fig. 3.7, with a half-power beamwidth approximated by equation 3.4, is steered electronically over the swath in order to follow the pulse on ground. Here, again all antenna elements are active. The coloring of the receive beam is related to the frequency properties of the transmitted waveform, which is usually a chirp signal. This means that different spectral parts, within the pulse duration τ_p, will arrive at different time instances at the sensor. This peculiarity motivates elevation beamforming techniques, where not only spatial beamforming methods but also temporal beamforming approaches have to be taken into account. This will be elaborated in detail in chapter 4.4.1.

The SCORE principle has been extended to analog reflector SAR systems by [54], dedicated to the improvement of the performances of SAR systems in terms of 'edge losses' and 'range ambiguities'. In the frame of ultra-wide-swath imaging a reflector SAR system employing a digital feed array is presented for the first time in [68] and further investigated in [28,63]. The SCORE operation principle of reflector-based SAR systems with linear digital feed arrays is sketched in Fig. 3.8. The waveform is transmitted with all feed elements active simulta-

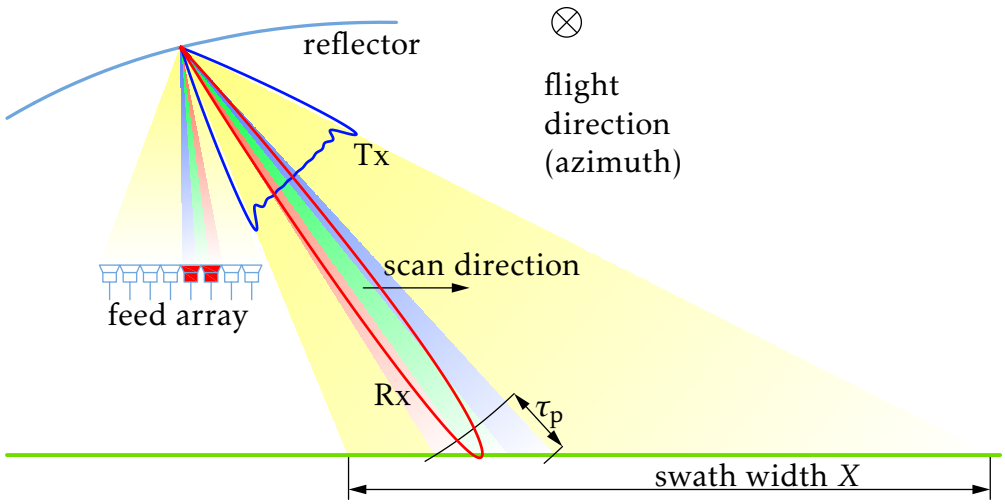

Figure 3.8: Reflector system operation with Tx beam illuminating the swath and Rx beam following the pulse on ground. The Rx beam is steered by activating sets of consecutive feed elements.

neously, again indicated by the yellow pattern. The coverable region on ground depends on the reflector geometry and the size of the feed array. After deflection by the reflector the pulse impinges the ground and moves from the near to the far end of the swath. The signal returning from the ground is again scattered by the reflector and successively collected by different parts of the feed array, indicated by the red feed elements. This circumstance can be made clear by having a look at the power distribution in the feed plane $z_f = 0$ (see Fig. 3.3). For this, a plane wave, impinging the reflector under an angle of 2 ° with respect to the z'-axis in the x'-z'-plane, has been simulated. The plane wave generates, after deflection by the reflector, a power distribution characterized by the Poynting vector

$$\boldsymbol{S} = \boldsymbol{E} \times \boldsymbol{H}\,, \tag{3.13}$$

in the region near the focus. The normalized z-component of the Poynting vector S_z is shown in Fig. 3.9. As expected, the power is concentrated in a small region, which in this case requires three feed elements, symbolized by the black squares, in order to collect most of the electromagnetic power. The power P_i entering the ith feed element is the power flux received by the effective feed element aperture $A_{i,\mathrm{eff}}$ [109]

$$P_i = A_{i,\mathrm{eff}} \cdot S_z\,. \tag{3.14}$$

Note that in Fig. 3.8 the receive beam on the feed array moves exactly the opposite direction as the receive beam on ground. That means the most right feed

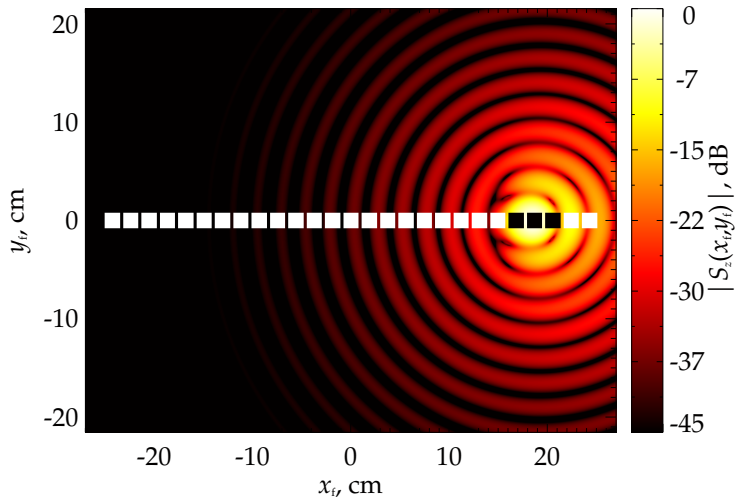

Figure 3.9: Normalized z-component of the Poynting vector in the plane $z_f = 0$. The active feed elements are indicated by the black patches.

element 'sees' the near end of the swath.

Figure 3.10a gives another view on the issue of feed selection in the scan process, where the individual channel gain patterns $G_i(t)$ are plotted in a projection onto the time axis. Here, basically two channel selection laws are of interest. The first is simply choosing a fixed number of feed elements N_{act} at a time instance. The second approach uses a threshold above which a certain channel is activated

$$G_i(t) \geq \alpha \cdot G_{\max}\,, \quad \alpha \in [0,1]\,. \tag{3.15}$$

Here, $G_{\max}$ represents the maximum gain. Figure 3.10b shows the activated channels versus time in black color for an α of 0.2. This law seems to be more reasonable from a physical point of view, but allows for discontinuities in the on-time of feed elements, as can be observed at channels 1, 26 and 27 in Fig. 3.10b. A more sophisticated channel selection law foresees the activation of a set of channels $Z(t)$, such that the linear combination of the complex amplitude patterns a_i ($G_i = |a_i|^2$) produces the largest gain

$$G(t) = \max_{N_{\text{act}}}\{|\sum_{i\in Z(t)} a_i|^2\} \geq \alpha \cdot G_{\max}\,, \quad \alpha \in [0,1] \tag{3.16}$$

for a given time instance. Note, so far the temporal extension of the transmitted pulse has been neglected in this channel activation concept. In chapter 4.4.1 a refined version of the channel activation procedure will be introduced.

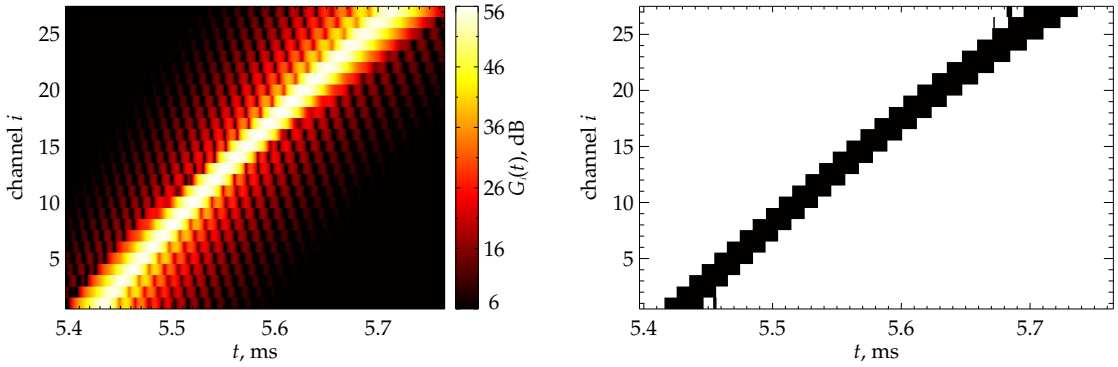

(a) (b)

Figure 3.10: (a) Individual feed element gain patterns projected onto the time axis, assuming a spherical Earth model and an orbit height of 745 km. (b) Corresponding channel selection using a gain threshold.

3.3 Limitations

Conventional pulsed SAR systems, specifically single-channel systems, are inherently restricted with respect to their imaging capability. With these systems it is impossible to map broad swaths with simultaneously high azimuth resolutions [27]. Pulsed SAR systems receive the radar echoes within the so called *echo window length* (*EWL*), which must not exceed the time interval between two succeeding pulses

$$\frac{1-dc}{PRF} \geq EWL = \frac{2}{c}(r_{\max} - r_{\min}) + \tau_{\mathrm{p}} = \frac{2}{c}\Delta r + \tau_{\mathrm{p}} \,. \tag{3.17}$$

Here, *dc* stands for *duty cycle*, which is a measure for the pulse length relative to the pulse period. The slant range difference Δr is the difference between the maximum distance $r_{\max}$ and the minimum distance $r_{\min}$ (see Fig. 3.11). The additional pulse duration τ_{p} in the echo window length is required to ensure that the far range echo completely enters the receiver, as indicated in Fig. 3.11. Substituting the pulse length

$$\tau_{\mathrm{p}} = \frac{dc}{PRF} \,, \tag{3.18}$$

equation (3.17) can be rewritten according to

$$\frac{1}{PRF} \geq \frac{2\Delta r}{c(1-2dc)} \,. \tag{3.19}$$

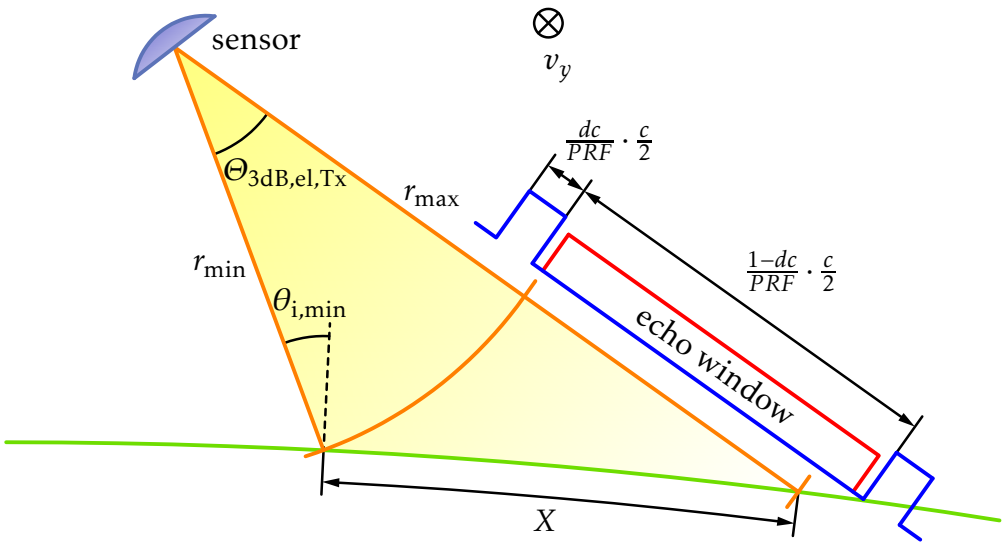

Figure 3.11: Side-looking sensor geometry showing the relation between swath width and *PRF*. Decreasing the *PRF* enables to acquire larger swath widths at the cost of a reduced azimuth resolution.

For a spherical Earth model the relation between the slant range difference Δr and the swath width X is found to be

$$\Delta r = X \cdot \frac{\sin(X/(2r_e) + \Theta_{3dB,el,Tx}/2 + \theta_{i,min})}{\cos(\Theta_{3dB,el,Tx}/2)} , \tag{3.20}$$

with the Earth radius r_e, the minimum incident angle $\theta_{i,min}$ and the half-power beamwidth of the transmit beam in elevation $\Theta_{3dB,el,Tx}$. Note that the swath width X in a spherical model is an arc length (see Fig. 3.11). The azimuth resolution Δy, however, depends inversely on the processed azimuth Doppler bandwidth B_y, which might approach the *PRF* in the limit

$$\Delta y = \frac{v_y}{B_y} \geq \frac{v_y}{PRF} , \tag{3.21}$$

where v_y is the relative velocity between sensor and Earth surface. Eliminating the *PRF* by combining inequalities (3.19) and (3.21) one finds

$$\frac{\Delta y}{\Delta r} \geq \frac{2v_y}{c(1-2dc)} . \tag{3.22}$$

If one considers the right side of inequality (3.22) as a constant for a given imaging geometry and instrument setting, then resolution can be traded for a larger swath width, which is proportional to the slant range difference Δr, and vice

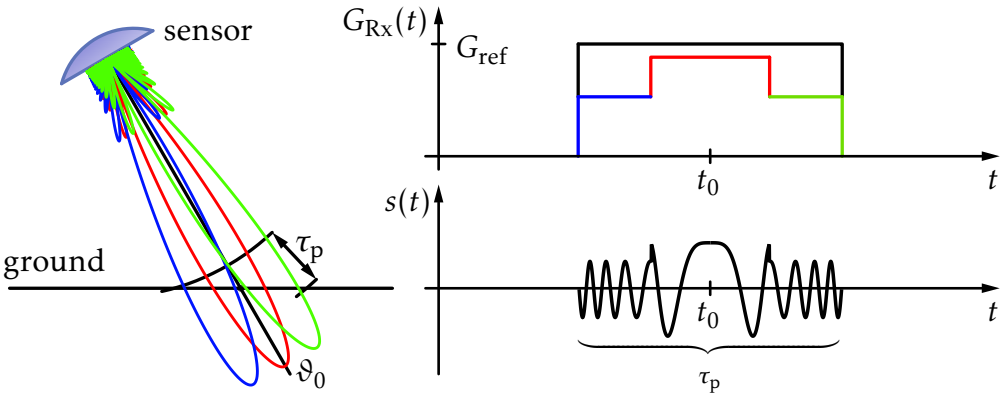

Figure 3.12: SCORE operation with narrow Rx beam conflicts with long duration pulses (left). The waveform is modulated in the SCORE process (right top) resulting in a loss of signal energy (right bottom).

versa. Improving both quantities at the same time is not possible for conventional SAR systems. Strategies to overcome this limitation, based on digital beamforming techniques in azimuth, will be presented in chapter 4.4.2.

Conventional SAR systems with high gain antennas suffer from another trade-off. This trade-off exists between the pulse duration τ_p and the elevation half-power beamwidth on receive $\Theta_{3dB,el,Rx}$. In order to keep a constant average power on transmit the pulse duration is coupled to the *PRF* via equation (3.18), however, in general a long pulse length is preferred in order to emit enough electromagnetic energy. With long pulses the sensitivity of a SAR system can be increased, allowing to relax the requirements on costly hardware components, like high power amplifiers (HPA). Figure 3.12 shows a SAR sensor, which receives an echo from a target under a scan angle ϑ_0, corresponding to the time instance t_0. During SCORE operation, different beams, starting with the blue one over red to green, are switched in order to follow the pulse backscattering movement on ground. The beams are controlled such that at time instance t_0 the red beam covers the center of the waveform. As indicated on the right side of Fig. 3.12 the switching of the beams results in an unwanted modulation of the received chirp signal proportional to the receive gain variation $G_{Rx}(t)$. In the worst case, that is for very narrow Rx beams compared to the pulse length, spectral parts are lost involving a degraded range resolution. Additionally, the loss of signal energy in combination with the modulation results in a reduced SAR image *SNR*. One option to mitigate this effect is to use a broader Rx pattern, which covers the complete pulse projected on ground. This requires the half-power beamwidth of the Rx beam $\Theta_{3dB,el,Rx}$ to coincide at least with the

angular domain covered by the pulse projected on ground

$$\Theta_{3\mathrm{dB,el,Rx}} \gtrsim 2 \arctan\left(\frac{c\tau_\mathrm{p}}{4r\tan\theta_\mathrm{i}}\right). \tag{3.23}$$

The drawback of this solution is that a broader pattern involves a gain loss and consequently a loss in *SNR*. This means, the benefit of a high gain antenna is eaten up to a certain degree by losses of signal energy. A performance figure measuring this loss can be defined in time domain according to [135]

$$L_\mathrm{p}(t_0) = \frac{1}{G_\mathrm{ref}(t)\cdot\tau_\mathrm{p}} \int_{t_0-\tau_\mathrm{p}/2}^{t_0+\tau_\mathrm{p}/2} G_\mathrm{Rx}(t)\mathrm{d}t\,. \tag{3.24}$$

Here, the reference gain G_ref could in principle be any gain besides the maximum SCORE gain in direction ϑ_0, if one is interested in the relative performance of different beamforming techniques. Important to note is, that in the loss definition (3.24) a coherent combination of signal energy is assumed. In general however, the modulation will alter the range compressed waveform in a non-trivial way. Then the loss must be computed after range processing with a filter h

$$L_\mathrm{p}(t_0) = \frac{\mathcal{E}\{|[a_\mathrm{Rx}(t)\cdot s(t-t_0+\tau_\mathrm{p}/2)]*h(t)|^2\}}{\mathcal{E}\{|[a_\mathrm{ref}(t_0)\cdot s(t-t_0+\tau_\mathrm{p}/2)]*h(t)|^2\}}\,, \tag{3.25}$$

with $*$ denoting time domain convolution. Here, the lowercase letters in the gain functions refer to the complex amplitudes of the patterns.

To allow a flexible SAR system operation, processing concepts in elevation in combination with innovative digital beamforming methods are discussed in chapter 4.4.1. These concepts aim at a preservation of the waveform itself and an optimization of the gain at the same time.

4 Multi-Channel Reflector SAR Systems

In chapter 3.3 the limitations of conventional SAR systems have been discussed. These restrictions exist in a trade-off between swath width and azimuth resolution as well as signal energy and antenna gain. Insofar the motivation of multi-channel SAR systems is to overcome these restrictions. However, this is not the only reason to deal with multi-channel systems. One could argue, a single-channel system can map an area several times, each covering a different Doppler sub-band, with a low *PRF* in order to cover a large swath. These multiple acquisitions could then be combined to a single high azimuth resolution image. Evidently, this acquisition concept is prone to temporal decorrelation, especially in vegetated areas and moreover it is time consuming. A far more powerful and flexible way to collect SAR data is to use a multi-channel system, realized on a single platform or via multiple platform transmitters and receivers. Here, the term *channel* refers to digital signal channels, available as individual data streams, for a digital signal processor. In contrast to conventional SAR systems, arbitrarily many beams can be realized at a single time instance, as sketched in Fig. 4.1. The key idea of digital beamforming systems is to move the A/D converter closer to the RF frontend. The individual digital channel signals can then either be downlinked to a ground station or directly processed on board the satellite in the digital beamforming unit, as indicated in Fig. 4.1.

Physically a channel is characterized by its spatial and temporal behavior. A system employing several channels has special requirements on the individual channels. One is called *spatial diversity*. This is expressed with spatially displaced pattern functions $a_i(k, \vartheta, \varphi) \sim E_i(k, \vartheta, \varphi)$[1] (see equation (2.13)), which are in general vector quantities with two entries describing the far field. However, for the moment these pattern functions shall be treated as scalar functions referring for instance to the co-polar electric far field component. Later in chapter 4.4.3 this concept is expanded to polarimetric applications, where co- and cross-polar field components need to be considered. Note that with reflector antenna based SAR systems the patterns a_i refer to the far field after deflection at the reflector, not to be mixed up with the feed patterns. Here, in general a_i describes the two-way pattern, taking into account the receive pattern $a_{\mathrm{Rx},i}$ as well as the transmit pattern a_{Tx}, as given in equation (4.3). This will be important later in the performance evaluation in chapter 5. However, when it comes to the deriva-

[1] In the context of digital beamforming these patterns shall represent so called *embedded* patterns, incorporating effects from coupling

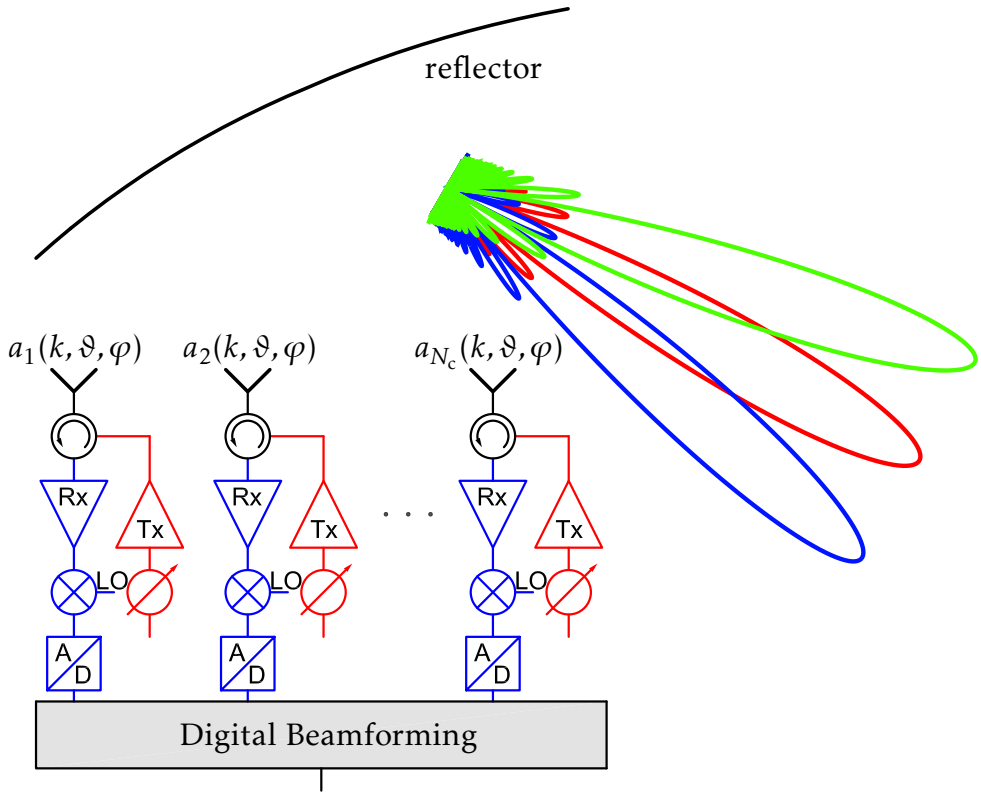

Figure 4.1: Hardware concept of a multi-channel reflector SAR system. The A/D-converters are close to the front end.

tion of dedicated beamformers, the pattern function a_i shall refer to the receive characteristic $a_{\mathrm{Rx},i}$ only, rather than the two-way pattern. This approach is motivated by the fact that with beamforming-on-receive techniques a single transmit pattern is optimized for a whole continuum of directions, while on receive an individual pattern is formed digitally for every direction. Insofar the problem of computing proper patterns on transmit and receive can be treated separately. Besides spatial diversity for radar systems other diversity schemes play a role, like *temporal diversity*, *spectral diversity* and *polarization diversity*. The patterns a_i can be conveniently represented with the so called *array manifold*

$$\boldsymbol{a}(k,\vartheta,\varphi) = \begin{bmatrix} a_1(k,\vartheta,\varphi) & a_2(k,\vartheta,\varphi) & \cdots & a_{N_c}(k,\vartheta,\varphi) \end{bmatrix}^{\mathsf{T}} . \tag{4.1}$$

The abstraction of a real SAR imaging process is done via a system theoretical model. Such a model should formalize the complete signal path, starting from the transmit chain in the SAR instrument via the atmosphere, the scattering on the ground and back through the receive path of the SAR sensor. The sys-

tem model is based on the physical equations, describing the electromagnetic scattering mechanics. In the simplest case the SAR sensor is modeled as a receiver with a certain gain and certain noise contributions in each channel. In chapter 5.3 this simple model is expanded in order to differentiate additional error sources, like quantization noise and calibration errors. In system theoretical terms a SAR with a single transmitting antenna and multiple receiving antennas is called a single-input multiple-output (SIMO) system.

In this work the multi-channel SAR image formation process is divided into two steps. Each digital channel generates a unique SAR raw data set. The task of digital beamforming is to combine these raw data sets to a single SAR raw data set such that conventional SAR focusing routines can be applied.

4.1 Multi-Channel Reflector SAR System Model

The multi-channel expansion of the SAR imaging equation (2.16), taking into account range ambiguous signal returns (2.53), can be cast in the form

$$\begin{aligned} u_i(\boldsymbol{r}_{\mathrm{s},i}, t) = &\iiint_{\boldsymbol{r}} o(\boldsymbol{r}) a_i(k, \vartheta, \varphi) g(\boldsymbol{r}_{\mathrm{s},i}, \boldsymbol{r}, t) \mathrm{d}\boldsymbol{r} \\ &+ \sum_l \iiint_{\mathbf{r}_l} o(\mathbf{r}_l) a_i(k, \vartheta_l, \varphi_l) g(\mathbf{r}_{\mathrm{s},i}, \mathbf{r}_l, t) \mathrm{d}\mathbf{r}_l + v_i(t) \,, \end{aligned} \tag{4.2}$$

$$a_i(k, \vartheta, \varphi) = a_{\mathrm{Tx}}(k, \vartheta, \varphi) \cdot a_{\mathrm{Rx},i}(k, \vartheta, \varphi) \,, \tag{4.3}$$

$$g(\boldsymbol{r}_{\mathrm{s},i}, \boldsymbol{r}, t) = \underbrace{\mathrm{rect}\left(\frac{t - \tau_i - \tau_\mathrm{p}/2}{\tau_\mathrm{p}}\right) \mathrm{e}^{\mathrm{j}\pi(B/\tau_\mathrm{p})(t-\tau_i-\tau_\mathrm{p}/2)^2}}_{\text{transmitted waveform, } p(t)} \cdot \underbrace{\frac{\mathrm{e}^{\mathrm{j}2\pi f_\mathrm{c}(t-\tau_i)}}{(4\pi)^2 \|\boldsymbol{r}_{\mathrm{s},i} - \boldsymbol{r}\|^2}}_{\text{Green's function}} \,. \tag{4.4}$$

Compared to (2.16) equation (4.2) has been complemented by the sum term describing range ambiguous returns and thermal receiver noise v_i. The distance of the target position $\boldsymbol{r}$ to the ith sensor position $\boldsymbol{r}_{\mathrm{s},i}$ results in a specific monostatic time delay

$$\tau_i = 2\|\boldsymbol{r}_{\mathrm{s},i} - \boldsymbol{r}\|/c \,. \tag{4.5}$$

Note, in this model all constant terms have been omitted for the ease of discussion. Figure 4.2 shows the system theoretical implementation of equation set (4.2) - (4.4). After reception of the SAR echoes, symbolized by the orange colored rays, the signal is weighted with the individual channel patterns and superimposed by thermal receiver noise. The digital beamforming stage contains all SAR specific array processing routines, which will be derived and explained in detail in the subsequent chapters. In the most rudimentary case the raw data

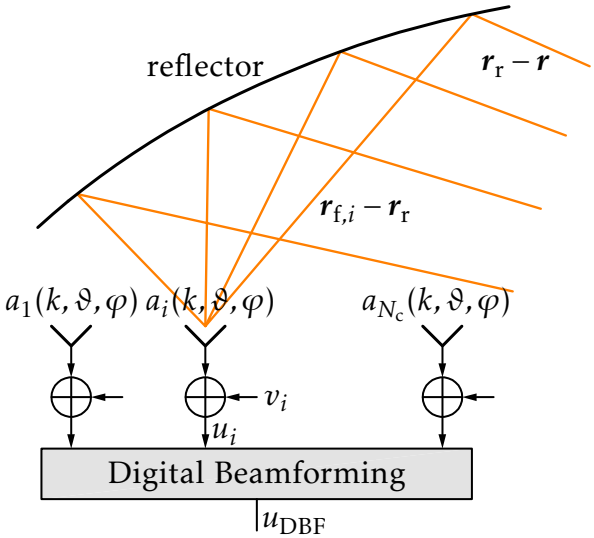

Figure 4.2: Basic multi-channel system model for a reflector SAR on receive.

output u_DBF, to be processed by conventional SAR focusing routines, is simply formed by a linear combination of complex weights w_i with the individual raw data channel signals u_i

$$u_\mathrm{DBF} = \boldsymbol{w}^\mathsf{T}\boldsymbol{u}\,, \quad \boldsymbol{u} = \begin{bmatrix} u_1 & \dots & u_i & \dots & u_{N_\mathrm{c}} \end{bmatrix}^\mathsf{T}\,. \tag{4.6}$$

However, in the frame of digital beamforming with SAR systems, this basic operation will usually be embedded in more sophisticated algorithms, as shown later. It is important to mention that the alignment of the feed antennas in Fig. 4.2 at this point can be related to azimuth or elevation or, quite generally, to any other geometrical feed array configuration. An essential question in this context is whether beamforming concepts, accounting for these individual time delays τ_i, are required. This problematic is connected to the term *narrowband sources* and shall be discussed for reflector antenna systems in the following section.

4.1.1 The Narrowband Approximation

The narrowband approximation for an array of antennas states that the difference between the time delays τ_i, when a plane wave passes the first antenna of the array and enters the most distant antenna, has to be much smaller than the inverse of the signal bandwidth B [123]

$$\max\{\tau_i\} - \min\{\tau_i\} \ll \frac{1}{B}\,. \tag{4.7}$$

If this inequality is violated, beamforming needs to be realized via true-time-delay elements. In the frame of SAR it makes sense to rewrite this inequality in terms of the resolution cell size in slant range $c/(2B)$ yielding

$$\frac{c}{2}(\max\{\tau_i\} - \min\{\tau_i\}) \ll \frac{c}{2B} \,. \tag{4.8}$$

Typically the slant range shift, corresponding to the left side of inequality (4.8), should be less than 10 % of a resolution cell, otherwise too much resolution is lost. The reason for this is a mismatch between the waveform after beamforming and the pulse compression filter. For planar arrays the narrowband statement can be easily formulated using the antenna dimensions. In the case of reflector antennas one deals with the difficulty that the delays τ_i are continuous functions due to the interaction of the incident plane wave with the reflector (see Fig. 4.2). One possibility to define a delay for a reflector-feed-array configuration could be the mean delay time

$$\overline{\tau}_i \equiv \frac{2}{c} \cdot \frac{\iint_{A_\mathrm{r}} (\|\boldsymbol{r}_\mathrm{r} - \boldsymbol{r}\| + \|\boldsymbol{r}_{\mathrm{f},i} - \boldsymbol{r}_\mathrm{r}\|) \mathrm{d}A_\mathrm{r}}{\iint_{A_\mathrm{r}} \mathrm{d}A_\mathrm{r}} \,, \tag{4.9}$$

where the individual vectors

$$\boldsymbol{r} = \begin{bmatrix} r\sin\vartheta\cos\varphi \\ r\sin\vartheta\sin\varphi \\ r\cos\vartheta \end{bmatrix} \,,\; \boldsymbol{r}_{\mathrm{f},i} = \begin{bmatrix} x_{\mathrm{f},i} \\ y_{\mathrm{f},i} \\ z_{\mathrm{f},i} \end{bmatrix} \,,\; \boldsymbol{r}_\mathrm{r} = \begin{bmatrix} x \\ y \\ (x^2+y^2)/(4F) \end{bmatrix} \tag{4.10}$$

denote a point in the far field of the reflector, the phase center of the ith feed element and the parametrization of the reflector surface $\boldsymbol{r}_\mathrm{r} \in A_\mathrm{r}$, respectively. With definition (4.9) substituted into (4.8) for τ_i a parabolic reflector antenna, as specified for example in Table 3.1, with the area element

$$\mathrm{d}A_\mathrm{r} = \sqrt{\frac{1}{4F^2}(x^2+y^2)+1}\,\mathrm{d}x\mathrm{d}y \,, \quad \sqrt{(x-O)^2+y^2} \leq \frac{D}{2} \,, \tag{4.11}$$

is suitable for signal bandwidths of up to 2.54 GHz, assuming a plane wave incident under the angles $(\vartheta, \varphi) = (10\,°, 0\,°)$. Since the signal bandwidths of current spaceborne SAR systems are roughly one order of magnitude smaller, the individual time delay τ_i can be neglected in the digital beamforming. Insofar equations (4.2) - (4.5) simplify with the substitutions $\tau_i \mapsto \tau$ and $\boldsymbol{r}_{\mathrm{s},i} \mapsto \boldsymbol{r}_\mathrm{s}$. In case of planar array antennas a single delay τ is specified, which refers typically to the antenna phase center. Consequently for reflector antennas this reference point is chosen to be in the origin of the local antenna coordinate system, as presented in Fig. 3.3, since the patterns a_i are computed with respect to this coordinate system.

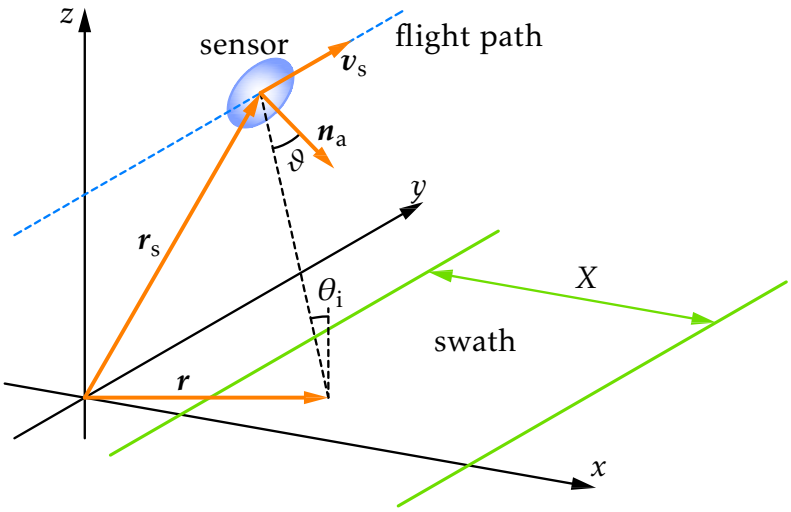

Figure 4.3: Imaging geometry for a spaceborne reflector SAR system.

4.2 Digital Beamforming for Side-Looking SAR Systems

In the most general case a multi-channel SAR system produces N_c data sets u_i. In this work two-dimensional data sets are considered with the time coordinate t, corresponding to slant range and the azimuth coordinate y, which coincides with the flight direction of the SAR sensor, as depicted in Fig. 4.3. Important is that there exists a unique functional relationship between the position of the target on ground $\boldsymbol{r}$, the spherical antenna coordinates (ϑ, φ) and the delay time τ. The target coordinates are related to the antenna angles according to

$$\cos\vartheta = \frac{\boldsymbol{n}_a^T(\boldsymbol{r}-\boldsymbol{r}_s)}{\|\boldsymbol{n}_a\| \cdot \|\boldsymbol{r}-\boldsymbol{r}_s\|} \,. \tag{4.12}$$

The angle φ is best assessed in the local antenna coordinate system, as defined in Fig. 3.3, by transforming the vector $\boldsymbol{r}-\boldsymbol{r}_s$ to this coordinate system and projection into the x'-y'-plane. The delay time τ is related to the target coordinates $\boldsymbol{r}$ for a monostatic setup via

$$\tau = 2\|\boldsymbol{r}_s - \boldsymbol{r}\|/c \,, \tag{4.13}$$

with c the velocity of light. Finally, a waveform specific relation between time t and frequency f can be derived from the phase term of equation (4.4) according to

$$f = \frac{B}{\tau_p}(t-\tau-\tau_p/2)\left(1-\frac{\partial\tau}{\partial t}\right) + f_c\left(1-\frac{\partial\tau}{\partial t}\right), \quad \tau \le t \le \tau+\tau_p \,, \tag{4.14}$$

which equals at zero-Doppler position ($\partial\tau/\partial t = 0$)

$$f = (B/\tau_\mathrm{p})(t - \tau - \tau_\mathrm{p}/2) + f_\mathrm{c}\,. \tag{4.15}$$

Generally DBF algorithms require knowledge about the position of the target $\boldsymbol{r}$, or equivalently, the direction of arrival (DOA) (ϑ, φ) of the incoming plane wave. For the purpose of the derivation of the beamforming algorithms the direction of arrival is assumed to be known. The impact of imprecise DOA knowledge on the beamformer performance is investigated in chapter 5.3. An investigation of the DOA estimation problem for spaceborne SAR systems employing SCORE techniques can be found in [5].

4.2.1 Digital Beamforming and Extended Pulses

As outlined in chapter 3.3 long duration pulses suffer from an unwanted modulation during the scan process. A preliminary solution was to increase the pattern beamwidth on receive, with the consequence of a gain loss. More sophisticated beamforming techniques exploit the information on the complex antenna pattern functions (4.3) in such a way, that each raw data pixel is weighted with a unique corresponding sample of these pattern functions. In this context a problem arises, which has to do with the fact that radar pulses are not Dirac-like but have a certain duration. Consider the ith channel of a SAR system in Fig. 4.4b, plotted versus time t. Here, the individual echoes resulting from two point targets at different slant ranges are plotted. Due to the specific SAR imaging geometry different slant ranges correspond to different DOAs, according to equations (4.12), (4.13) and (4.15), and therefore each point target echo is weighted with a different part of the ith complex channel pattern as sketched in Fig. 4.4a. Evidently, in the overlap domain, for instance at $t = 6\,\mathrm{ms}$ it is not possible to apply a weight, corresponding to the pattern at $t = 6\,\mathrm{ms}$, since this wouldn't match either of the echo DOAs. It is even more problematic that the weight at $t = 6\,\mathrm{ms}$ should match the two point targets at the same time and in the general case of distributed targets a beamformer theoretically must fit to infinite many directions at the same time.

Although short pulses might not require special processing, in general the pulse length cannot be neglected. Basically two approaches to deal with this problem shall be discussed in the subsequent sections. These two concepts shall serve as theoretical basis for realtime capable beamforming strategies to be implemented on board a SAR sensor, as well as beamforming methods applicable to ground based processors.

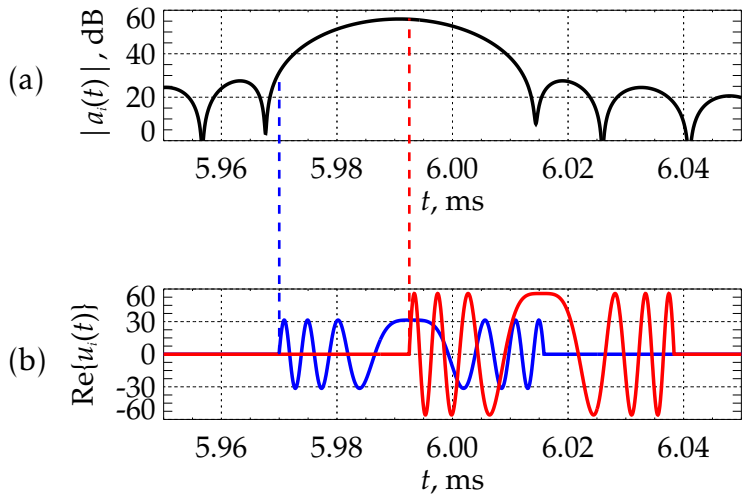

Figure 4.4: (a) Magnitude of the ith complex antenna pattern projected onto the time axis. (b) Baseband raw data signal of two point targets at different slant range positions, weighted with the corresponding parts of the antenna pattern. Note that for the purpose of illustration the individual chirp signals are displayed instead of the superposition of the chirps.

4.2.2 Digital Beamforming with Range Compressed Data

An essential step in the SAR image formation process is the so called *range compression*. In time domain this requires the ith SAR raw data channel u_i to be convolved with a range compression filter $h_{\mathrm{rc}}(t)$ to yield the range compressed raw data signal

$$u_{\mathrm{rc},i}(y,t) = \int_{t'} u_i(y, t-t') h_{\mathrm{rc}}(t') \mathrm{d}t' \,. \tag{4.16}$$

The range compression filter is a matched filter and derived from the transmitted waveform as (see equation (4.4))

$$h_{\mathrm{rc}}(t) = p^*(-t) \,. \tag{4.17}$$

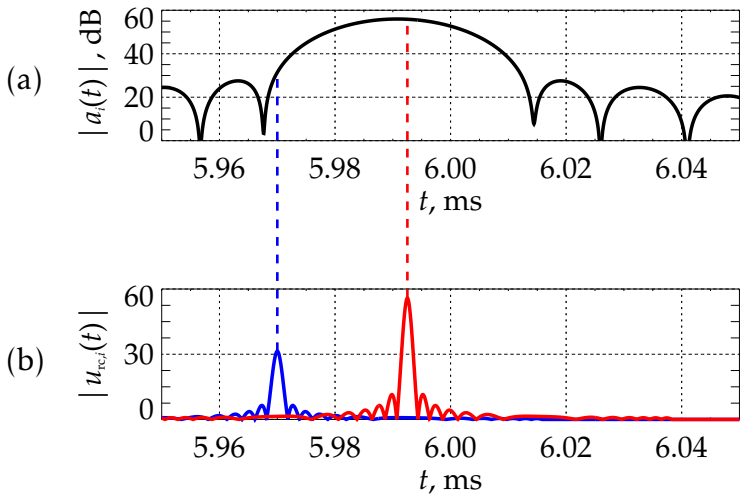

Figure 4.5: (a) Magnitude of the ith complex antenna pattern projected onto the time axis. (b) Range compressed SAR signal comprising two point targets, which can now be weighted with the corresponding patterns.

Inserting equation (4.2) into the convolution expression (4.16) yields a closed form solution (see appendix C for a derivation of matched filtered chirp signals)

$$u_{\mathrm{rc},i}(y,t) = \iiint_{\boldsymbol{r}} o(\boldsymbol{r}) \cdot a_i(k,\vartheta,\varphi) \cdot \frac{\mathrm{e}^{-\mathrm{j}2\pi f_c \tau}}{(4\pi)^2 \|\boldsymbol{r}_\mathrm{s} - \boldsymbol{r}\|^2} \cdot (\tau_\mathrm{p} - |t-\tau|) \cdot \operatorname{sinc}\left(\pi \frac{B}{\tau_\mathrm{p}}(t-\tau)(\tau_\mathrm{p} - |t-\tau|)\right) \cdot \operatorname{rect}\left(\frac{t-\tau}{2\tau_\mathrm{p}}\right) \mathrm{d}\boldsymbol{r} + \ldots \tag{4.18}$$

Here, indicated by the dots, for clarity reasons the range ambiguity term as well as the noise contribution in equation (4.2) have been omitted. This matched filter operation causes most of the signal energy to be concentrated within one ground range resolution cell of size (see equation (2.36))

$$\Delta r_\mathrm{g} = \frac{c}{2B \sin\theta_\mathrm{i}}\,, \tag{4.19}$$

with the local incident angle θ_i. Obviously for spaceborne SAR systems the antenna patterns can be assumed constant within the angular extent of such resolution cell sizes, which are typically in the order of a few meters. The benefit from this approach is that now the individual targets in elevation are clearly differentiated and a unique weight can be applied to every sample of the range

compressed data set, resulting in the beamformer output analogous to equation (4.6)

$$u_{\mathrm{DBF}}(y,t) = \boldsymbol{w}^{\mathsf{T}}(t)\boldsymbol{u}_{\mathrm{rc}}(y,t)\,. \tag{4.20}$$

This is demonstrated in Fig. 4.5, where again for the purpose of illustration, the individual SAR impulse response functions are shown. The drawback is that the range compression needs to be implemented in realtime on board the SAR satellite by means of field programmable gate array (FPGA) or application specific integrated circuit (ASIC) technology. Taking for instance a SAR with a pulse length in the order of 50 µs and bandwidth of up to 100 MHz would already result in filter lengths of 5000 taps.

An even more severe handicap of range compressing the raw data prior to beamforming is that any frequency dependent behavior of the channel patterns cannot be accounted for. This is especially important for reflector SAR systems, where multipath effects can deteriorate the channel transfer function even within small bandwidths.

4.2.3 Digital Beamforming in the Time-Wavenumber Domain

One possible solution to this problem is to expand the raw data signal $u_i(t)$ into the time-frequency domain, or time-wavenumber domain, respectively. This could be done via a *short-time Fourier transform* (STFT) defined for a temporal signal $x(t)$ as

$$X(t,f) = \int_{-\infty}^{\infty} x(t')\gamma^*(t'-t)\mathrm{e}^{-\mathrm{j}2\pi f t'}\mathrm{d}t'\,, \tag{4.21}$$

Substituting the frequency variable f with the wavenumber $k = 2\pi f/c$, the equivalent time-wavenumber representation of the ith raw data channel $u_i(t)$ is given as

$$U_i(y,t,k) = \int_{-\infty}^{\infty} u_i(y,t')\gamma^*(t'-t)\mathrm{e}^{-\mathrm{j}kct'}\mathrm{d}t'\,. \tag{4.22}$$

Figure 4.6 shows an example of a short time Fourier pair for a raw data signal with two distinct targets. For the computation of the spectrogram in Fig. 4.6b a Gaussian integration kernel

$$\gamma(t) = \left(\frac{\alpha}{\pi}\right)^{\frac{1}{4}} \mathrm{e}^{-\frac{\alpha}{2}t^2} \tag{4.23}$$

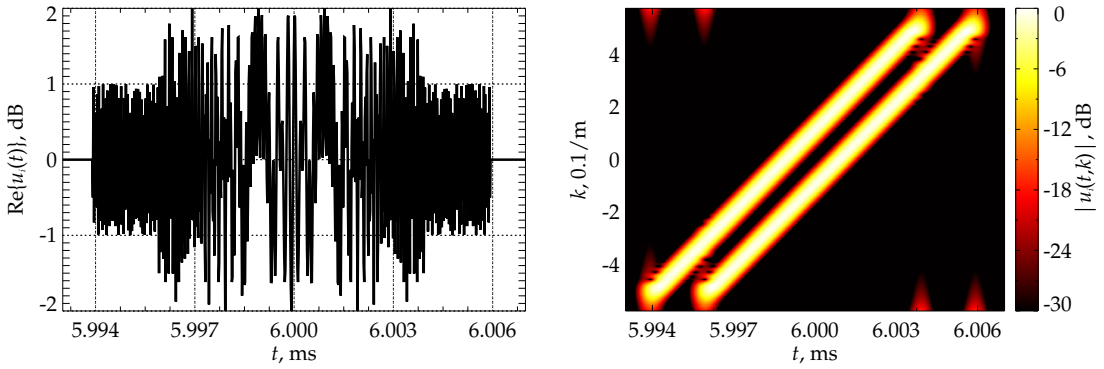

(a) (b)

Figure 4.6: (a) Superposition of two 50 MHz chirp signals with a pulse duration of 10 µs in time domain. (b) Spectrogram of the two chirps. In the upper left and the lower right corner artifacts from the adjacent ambiguous spectra can be observed (sampling frequency $f_s = 55\,\text{MHz}$, $\alpha = 1.286 \times 10^{13}$).

has been used, with the parameter α controlling the width of the kernel. For Gaussian waveforms the effective duration Δt_{eff} and the effective bandwidth Δf_{eff} are related to the parameter α via [55]

$$\Delta t_{\text{eff}} = \sqrt{\frac{2\pi}{\alpha}}\,, \tag{4.24}$$

$$\Delta f_{\text{eff}} = \sqrt{\frac{\alpha}{2\pi}}\,, \tag{4.25}$$

fulfilling the uncertainty principle (2.33) with the equality sign. This means, with large parameters α wavenumbers k can be resolved well, while with small parameters α the position of wavenumbers in time t can be determined more accurately. After applying the STFT to each raw data channel it is now possible to take the transfer characteristics of the individual channels into account by applying weights, which additionally depend on the wavenumber k compared to equation (4.20)

$$U_{\text{DBF}}(y,t,k) = \boldsymbol{w}^{\mathsf{T}}(t,k)\boldsymbol{U}(y,t,k)\,. \tag{4.26}$$

Here, one advantage of linearly frequency modulated waveforms becomes apparent, that is the time-frequency resolution of the integration kernel can be kept constant. For other waveforms the so called *wavelet transform* [36], which

allows to scale the kernel length adaptively, might be more appropriate. The concept of expanding the raw data stream into the time-wavenumber domain shall serve as basis for beamforming techniques, which can be realized onboard a satellite with moderate hardware effort, using filter-bank structures. This will be elaborated in detail in chapter 4.4.1.

4.2.4 Digital Beamforming in 3-D Time-Wavenumber Space

Not considered yet in the beamforming process is the azimuth dimension. The azimuth dimension is generated by moving the SAR platform on an essentially arbitrary but known trajectory. Spaceborne SAR systems acquire data by orbiting the Earth on a trajectory, which can be assumed to be locally linear. Here, this linear flight path is parameterized with the azimuth variable y. From the beamforming perspective the question arises, whether a combination of raw data channels can be performed in the spatial domain or not. This is clearly not the case, since targets spatially displaced in azimuth direction will respond with different wavenumbers for a single azimuth position of the SAR sensor. This means, the SAR data need to be transformed into the azimuth wavenumber domain before beamforming. Taking the spatial Fourier transform of equation (4.22) with respect to y the azimuth wavenumber representation of the SAR raw data is given as

$$\begin{aligned} U_i(k_y,t,k) &= \int_y U_i(y,t,k)\mathrm{e}^{-\mathrm{j}k_y y}\mathrm{d}y \\ &= \int_y \int_{t'} u_i(y,t')\gamma^*(t'-t)\mathrm{e}^{-\mathrm{j}kct'}\mathrm{d}t'\mathrm{e}^{-\mathrm{j}k_y y}\mathrm{d}y\,. \end{aligned} \tag{4.27}$$

In Fig. 4.7 these integral transformations are illustrated graphically for a set of two point scatterers. Starting with the ith raw data set $u_i(y,t)$ in Fig. 4.7a it becomes evident that the zero-Doppler positions of the two targets differ, which prevents beamforming. Remember that the different zero-Doppler positions have to correspond to the same wavenumber k_y. This is illustrated in Fig. 4.8a and 4.8b, where two examples of sensor trajectories with translationally invariant antenna pointings are depicted. If this is not the case, as shown in Fig. 4.8c, the most general expansion of the raw data would be given by a 2-D STFT with respect to the variables t and y yielding

$$U_i(y,k_y,t,k) = \int_{y'} \int_{t'} u_i(y',t')\gamma^*(y'-y,t'-t)\mathrm{e}^{-\mathrm{j}kct'}\mathrm{e}^{-\mathrm{j}k_y y'}\mathrm{d}t'\mathrm{d}y'\,. \tag{4.28}$$

For spaceborne SAR systems, however, it can be safely assumed that the imaging geometry and the pointing of the antenna is at least locally translationally

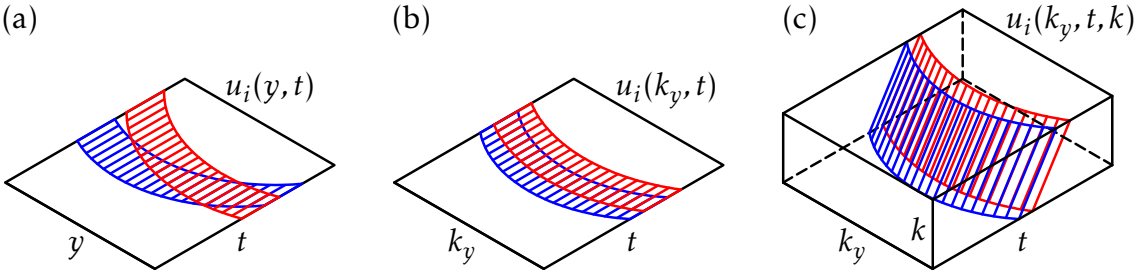

Figure 4.7: Time-wavenumber domain beamforming: (a) SAR raw data for two point targets in SAR coordinates azimuth y and range t. (b) Fourier transform with respect to azimuth coordinate. (c) Raw data after short-time Fourier transform of range dimension allowing a full separation of individual targets.

invariant with respect to the azimuth coordinate. Insofar it is sufficient to take equation (4.27) as basis for any further considerations.

Transforming the data sets in Fig. 4.7a into the azimuth wavenumber domain (k_y) aligns the target signals as can be observed in Fig. 4.7b. Here, the target signals still overlap in time domain. The full separation of the target signals is achieved after applying a STFT in the range time domain as depicted in Fig. 4.7c. With this, the beamforming operation in the 3-D time-wavenumber domain can be stated according to

$$U_{\mathrm{DBF}}(k_y,t,k) = \boldsymbol{w}^{\mathsf{T}}(k_y,t,k)\boldsymbol{U}(k_y,t,k)\,. \tag{4.29}$$

The raw data signal after digital beamforming transformed back into radar co-

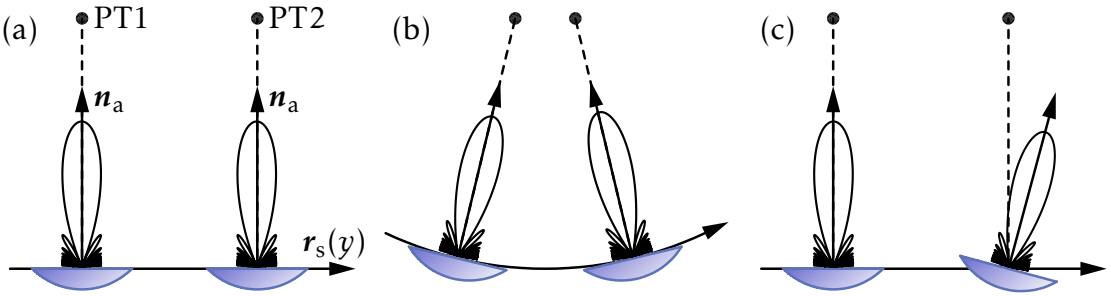

Figure 4.8: Two examples of translationally invariant imaging geometries, with linear (a) and circular (b) sensor trajectories, respectively, where the zero-Doppler positions are 'seen' with the same pattern. (c) Translationally variant imaging geometry where the second point target is 'seen' with a different pattern, compared to point target 1, at zero-Doppler position.

ordinates (y,t) is given by the inverse operation [55]

$$u_{\mathrm{DBF}}(y,t) = \int_{k_y}\int_{k}\int_{t'} U_{\mathrm{DBF}}(k_y,t',k)\overline{\gamma}(t-t')\mathrm{e}^{\mathrm{j}kct}\mathrm{d}t'\mathrm{d}k\cdot\mathrm{e}^{\mathrm{j}k_y y}\mathrm{d}k_y\ . \tag{4.30}$$

Hereby the inner integrations over t' and k resemble an *inverse short-time Fourier transform* (ISTFT). The kernels in the STFT and the ISTFT are connected via the relation [55]

$$\int_{-\infty}^{\infty}\gamma^*(t)\overline{\gamma}(t)\mathrm{d}t = 1\ , \tag{4.31}$$

which is fulfilled, for instance, for Gaussian kernels as given in equation (4.23). In that case $\gamma(t) = \overline{\gamma}(t)$. However, since the functions u_i and U_{DBF} in the STFT (4.27) and in the ISTFT (4.30), respectively, differ due to the beamforming operation, relation (4.31) does not apply in the strict sense.

To recall this again - for the purpose of the derivation of the beamforming algorithms the position of the target is assumed to be known. In that case every sample in the 3-D raw data space (k_y,t,k) can be associated with a unique point in the wavenumber space (k,φ,ϑ) on the basis of equations (4.12), (4.13), (4.15) and (2.32).

4.3 Optimal Beamforming Techniques

Up to now the digital beamforming operation (4.29) is described as a linear combination of channel weights $\boldsymbol{w}(k_y,t,k)$ with the corresponding raw data sets $\boldsymbol{U}(k_y,t,k)$. A major goal in this thesis is to separate SAR specific processing steps, as given in equation (4.27), from the problem of finding meaningful weights. Moreover the weights w_i shall not be derived for any specific antenna type, like reflector antennas, or planar array antennas, but in a general form with

$$w_i = f\left(\boldsymbol{a}(k,\varphi,\vartheta),\boldsymbol{R}_{\boldsymbol{v}}\right)\ , \tag{4.32}$$

being a function of the array manifold $\boldsymbol{a}(k,\varphi,\vartheta)$ and the so called *channel covariance matrix* $\boldsymbol{R}_{\boldsymbol{v}}$ [123] of the thermal noise (see equation 4.2)

$$\boldsymbol{R}_{\boldsymbol{v}} = \mathcal{E}\left\{\boldsymbol{v}\boldsymbol{v}^{\mathrm{H}}\right\}\ . \tag{4.33}$$

This offers the advantage to assign these beamforming concepts to SAR systems independently from their antenna architectures. Finding a weight vector $\boldsymbol{w}\in\mathbb{C}^{N_{\mathrm{c}}}$ is an optimization problem in multiple dimensions. In the frame of pure antenna pattern optimization this is commonly referred to as *pattern synthesis* problem in the literature. In the context of RF systems the cost function

often includes a model of error sources in the system, like thermal receiver noise $v_i(t)$ as given in equation (4.2). Possibly one of the most widely used approaches to design a beamformer is to optimize the signal-to-noise ratio generated by a given SAR system. More sophisticated beamforming methods incorporate additional conditions, addressing for example the suppression of spatial interference. Insofar a first step is to derive a SAR specific cost function based on the *SNR* and constraints resulting from ambiguities.

4.3.1 Cost Function and Constraints

Principally two approaches to assess the *SNR* can be distinguished, the first being introduced in equation (2.56). In this case the *SNR* expression incorporates the SAR focusing kernel. Clearly this would not allow much insight in the mechanics of digital beamforming, since the *SNR* could only be stated using complicated integral expressions with no analytic solution.

In a second approach, without loosing generality, the *SNR* in compact form can be derived by inserting the point target hypothesis (2.18) into equation (4.2), yielding

$$u_i(y,t) = o(\boldsymbol{r})a_i(k,\vartheta,\varphi)g(y,t,\boldsymbol{r}) + \sum_l o(\boldsymbol{r}_l)a_i(k,\vartheta_l,\varphi_l)g(y,t,\mathbf{r}_l) + v_i(y,t)\,. \tag{4.34}$$

This raw data signal expanded into the time-wavenumber domain using the transform relation (4.27) results in

$$\begin{aligned} U_i(k_y,t,k) = o(\boldsymbol{r})a_i(k,\varphi,\vartheta)g(k_y,t,k,\boldsymbol{r}) + \sum_l o(\boldsymbol{r}_l)a_i(k,\vartheta_l,\varphi_l)g(k_y,t,k,\mathbf{r}_l) \\ + v_i(k_y,t,k)\,. \end{aligned} \tag{4.35}$$

Remember, here the complex antenna patterns a_i are far field patterns, obeying relation (2.23), assumed to be slowly varying in y, compared to the rapidly

oscillating function g, and therefore drawn in front of the Fourier integral.

$$\begin{aligned} U_i(k_y,t,k) &= \int_y \int_{t'} \Big[o(\boldsymbol{r}) a_i(k,\vartheta,\varphi) g(y,t,\mathbf{r}) + \sum_l o(\boldsymbol{r}_l) a_i(k,\vartheta_l,\varphi_l) g(y,t,\mathbf{r}_l) \\ &\quad + v_i(y,t) \Big] \gamma^*(t'-t) \mathrm{e}^{-\mathrm{j}kct'} \mathrm{d}t' \mathrm{e}^{-\mathrm{j}k_y y} \mathrm{d}y \qquad (4.36) \\ &= \int_y \Big[o(\boldsymbol{r}) a_i(k,\vartheta,\varphi) g(y,t,k,\mathbf{r}) + \sum_l o(\boldsymbol{r}_l) a_i(k,\vartheta_l,\varphi_l) g(y,t,k,\mathbf{r}_l) \\ &\quad + v_i(y,t,k) \Big] \mathrm{e}^{-\mathrm{j}k_y y} \mathrm{d}y \qquad (4.37) \\ &\approx o(\boldsymbol{r}) a_i(k,\vartheta,\varphi) \int_y g(y,t,k,\mathbf{r}) \mathrm{e}^{-\mathrm{j}k_y y} \mathrm{d}y \\ &\quad + \sum_l o(\boldsymbol{r}_l) a_i(k,\vartheta_l,\varphi_l) \int_y g(y,t,k,\mathbf{r}_l) \mathrm{e}^{-\mathrm{j}k_y y} \mathrm{d}y + v_i(k_y,t,k) \,. \qquad (4.38) \end{aligned}$$

Note, the relation between the azimuth wavenumber variable k_y and the antenna variables (k,ϑ,φ) is given by equations (2.32). The beamformer output U_{DBF} is then the linear combination of the individual 3-D raw data sets $U_i(k_y,t,k)$ by means of complex weights w_i and equals

$$\begin{aligned} U_{\mathrm{DBF}}(k_y,t,k) = \boldsymbol{w}^{\mathsf{T}}(k_y,t,k) \Big[& o(\boldsymbol{r}) \boldsymbol{a}(k,\vartheta,\varphi) g(k_y,t,k,\boldsymbol{r}) \\ & + \sum_l o(\boldsymbol{r}_l) \boldsymbol{a}(k,\vartheta_l,\varphi_l) g(k_y,t,k,\boldsymbol{r}_l) + \boldsymbol{v}(k_y,t,k) \Big] \,, \end{aligned} \qquad (4.39)$$

with the unique mapping $(k,\vartheta,\varphi) \mapsto (k_y,t,k)$. To better recognize the structure of this equation, the arguments shall be dropped in the following derivations, giving

$$U_{\mathrm{DBF}} = \boldsymbol{w}^{\mathsf{T}} [o g \cdot \boldsymbol{a} + \sum_l o_l g_l \cdot \boldsymbol{a}_l + \boldsymbol{v}] \,. \qquad (4.40)$$

Hence a power expression of the beamformer output can be derived according to

$$\begin{aligned} P_{U_{\mathrm{DBF}}} &= \mathcal{E} \left\{ |U_{\mathrm{DBF}}|^2 \right\} \\ &= P_s + P_{\mathrm{ra}} + P_v \\ &= \mathcal{E} \left\{ |o|^2 \right\} |g \cdot \boldsymbol{w}^{\mathsf{T}} \boldsymbol{a}|^2 + \sum_l \mathcal{E} \left\{ |o_l|^2 \right\} |g_l \cdot \boldsymbol{w}^{\mathsf{T}} \boldsymbol{a}_l|^2 + \boldsymbol{w}^{\mathsf{T}} \mathcal{E} \left\{ \boldsymbol{v} \boldsymbol{v}^{\mathsf{H}} \right\} \boldsymbol{w}^* \\ &= \sigma_o^2 |g \cdot \boldsymbol{w}^{\mathsf{T}} \boldsymbol{a}|^2 + \sum_l \sigma_{o,l}^2 |g_l \cdot \boldsymbol{w}^{\mathsf{T}} \boldsymbol{a}_l|^2 + \boldsymbol{w}^{\mathsf{T}} \boldsymbol{R}_{\boldsymbol{v}} \boldsymbol{w}^* \,. \end{aligned} \qquad (4.41)$$

Here, it is assumed that signal, range ambiguities and noise are statistically independent, so that individual terms for the signal power P_s, the power of the range ambiguities P_{ra} and the noise power P_v can be found. With this, a compact raw data *SNR* expression for multi-channel SAR systems can be stated according to

$$SNR(k_y, t, k, \boldsymbol{r}) = \frac{P_s(k_y, t, k, \boldsymbol{r})}{P_v(k_y, t, k)} = \frac{\sigma_o^2 \left| g \cdot \boldsymbol{w}^{\mathsf{T}} \boldsymbol{a} \right|^2}{\boldsymbol{w}^{\mathsf{T}} \boldsymbol{R_v} \boldsymbol{w}^*} \,. \tag{4.42}$$

The variable $\boldsymbol{r}$ shall indicate that this expression is a function of the target position on ground. In order to define cost functions as well as constraints, a good strategy is to formulate an optimization problem for each pixel of the afore mentioned 3-D raw data space (k_y, t, k) separately. The task is now to find weight vectors $\boldsymbol{w}(k_y, t, k)$ which optimize, or more precisely, maximize the *SNR* in an individual raw data cell. This optimization problem can be formulated as a convex problem, where the noise power P_v is minimized under certain constraints. The cost function, taken from the above *SNR* equation, is then

$$P_v(k_y, t, k) = \boldsymbol{w}^{\mathsf{T}}(k_y, t, k) \boldsymbol{R_v}(k_y, t, k) \boldsymbol{w}^*(k_y, t, k) \,, \quad \boldsymbol{R_v} \in \mathbb{C}^{N_{\mathrm{act}} \times N_{\mathrm{act}}} \,. \tag{4.43}$$

In order to avoid the trivial solution of the weight vector, that is the null vector $\boldsymbol{w} = \boldsymbol{0}$, constraints have to be formulated. These shall be discussed in the next sections for three specific beamforming methods.

Most important in terms of constraints for SAR systems are range and azimuth ambiguities. Here again, for the purpose of finding appropriate weight vectors, the range and azimuth ambiguity ratios are written as function of their respective variables in the 3-D raw data space (k_y, t, k). These performance parameters, stated in chapter 2 for single-channel systems, can be extended to multi-channel systems based on the previous derivations. The azimuth ambiguity-to-signal ratio, given by equation (2.52) for conventional SAR systems, writes then in the multi-channel case by inserting the signal power term from equation (4.41) as

$$\begin{aligned} AASR(k_y, \boldsymbol{r}) &= \frac{\sum\limits_{m \in \mathbb{Z} \setminus \{0\}} P_s(k_y + m k_{y\mathrm{s}}, \boldsymbol{r}_m)}{P_s(k_y, \boldsymbol{r})} \\ &= \frac{\sum\limits_{m \in \mathbb{Z} \setminus \{0\}} \left| g(k_y + m k_{y\mathrm{s}}, \boldsymbol{r}_m) \cdot \boldsymbol{w}^{\mathsf{T}} \boldsymbol{a}(k, \varphi_m, \vartheta_m) \right|^2}{\left| g(k_y, \boldsymbol{r}) \cdot \boldsymbol{w}^{\mathsf{T}} \boldsymbol{a}(k, \varphi, \vartheta) \right|^2} \,, \end{aligned} \tag{4.44}$$

assuming a constant azimuth compression filter $H_{\mathrm{az}}(k_y)$. To emphasize this again, the above *AASR* expression refers to the raw data domain in contrast

to equation (2.52), where the *AASR* in the final SAR image via the integration over k_y is described. The only purpose of this notation must be seen in the context of finding solutions for the weight vectors. Similarly, the single-channel range ambiguity-to-signal ratio from equation (2.55) can be extended based on equation (4.41) according to

$$\begin{aligned} RASR(t,k,\boldsymbol{r}) &= \frac{\sum\limits_{l\in\mathbb{Z}\setminus\{0\}} P_{\mathrm{ra}}(t,k,\boldsymbol{r}_l)}{P_s(t,k,\boldsymbol{r})} \\ &= \frac{\sum\limits_{l\in\mathbb{Z}\setminus\{0\}} \sigma_o^2(\boldsymbol{r}_l)\left|g(t,k,\boldsymbol{r}_l)\cdot\boldsymbol{w}^{\mathsf{T}}\boldsymbol{a}(k,\varphi_l,\vartheta_l)\right|^2}{\sigma_o^2(\boldsymbol{r})\left|g(t,k,\boldsymbol{r})\cdot\boldsymbol{w}^{\mathsf{T}}\boldsymbol{a}(k,\varphi,\vartheta)\right|^2} . \end{aligned} \tag{4.45}$$

In the *AASR* formula (4.44) azimuth ambiguities originating from the range ambiguous signal returns have been neglected. Being insignificant for rectangular SAR antennas, in some cases a joint treatment of range and azimuth ambiguities could make sense. The so called *integrated ambiguity-to-signal ratio* (*ASR*), incorporating both types of ambiguities can then be written for multi-channel SAR systems according to

$$ASR(k_y,t,k,\boldsymbol{r}) = \frac{\sum\limits_{m,l\in\mathbb{Z}\setminus\{0\}} \sigma_o^2(\boldsymbol{r}_l)\left|g(k_y+mk_{ys},t,k,\boldsymbol{r}_{m,l})\cdot\boldsymbol{w}^{\mathsf{T}}\boldsymbol{a}(k,\varphi_{m,l},\vartheta_{m,l})\right|^2}{\sigma_o^2(\boldsymbol{r})\left|g(k_y,t,k,\boldsymbol{r})\cdot\boldsymbol{w}^{\mathsf{T}}\boldsymbol{a}(k,\varphi,\vartheta)\right|^2} \tag{4.46}$$

This means, the integrated ambiguity-to-signal ratio is usually larger than range and azimuth ambiguities computed individually

$$ASR \geq AASR + RASR . \tag{4.47}$$

A major task of the following beamforming concepts will be to minimize the influence of range and azimuth ambiguities while maintaining the best possible *SNR*.

4.3.2 Beamforming by Channel Switching

A most rudimentary beamforming concept to be implemented with reflector SAR systems has been suggested in [68]. As introduced in chapter 3.2, in the frame of SCORE operation, a certain subset of feed elements is activated in order to receive the echo signal power. Although a time-variant procedure, here no information about antenna and channel characteristics are adopted, respectively. Instead simply an integer number of feed elements is activated at a time

instance. Hence no specific constraints in terms of a mathematical optimization problem need to be formulated. A typical weight vector takes the form

$$\boldsymbol{w} = \begin{bmatrix} 0 & 1 & 1 & 1 & 0 & \dots & 0 \end{bmatrix}^{\mathsf{T}} , \tag{4.48}$$

with '1' indicating active channels, which in this example totals to $N_{\text{act}} = 3$. As can be seen from Fig. 3.10b such a weight vector configuration discontinuously changes over time depending on the activated channels. Throughout this work this beamforming approach shall be referred to as *unity* beamforming. To demonstrate the principal behavior of such a beamforming concept, the channel noise shall be mutually uncorrelated and of equal power $\boldsymbol{R}_{\boldsymbol{v}}(k_y, t, k) = \sigma_v^2(k_y, t, k)\mathbf{I}$, with $\mathbf{I}$ the identity matrix. It becomes clear that the raw data *SNR* (4.42) for this beamformer drops proportional to the number of activated channels

$$SNR(k_y, t, k, \boldsymbol{r}) = \frac{\sigma_o^2 \left| g \cdot \boldsymbol{w}^{\mathsf{T}} \boldsymbol{a} \right|^2}{N_{\text{act}} \sigma_v^2} . \tag{4.49}$$

This is due to the fact that most channels in a reflector SAR system contribute only with noise on receive for a given direction, as can be observed in Fig. 3.9. Here, the optimal number of activated channels is in the order of three, assuming short pulses. Note, this *SNR* loss does not occur with direct radiating arrays, since all channels contain signal plus noise power. Another drawback is that in the SAR image formation process, where basically the reflectivity function $o(\boldsymbol{r})$ is to be retrieved, a careful calibration, taking into account the inverse of the pattern magnitude function $|\boldsymbol{w}^{\mathsf{T}}\boldsymbol{a}|$, is required. Nevertheless this beamformer is justified by the fact that it is technically easy and cost effective to implement. Moreover this beamformer is robust in terms of coefficient stability, because no weights incorporating knowledge of the complex antenna amplitude pattern $\boldsymbol{a}(k, \varphi, \vartheta)$ is required.

This type of beamformer is not dedicated to suppress spatial interferences. However, the number of active channels is chosen such that only those channels with the highest signal amplitude contribute for a specific direction. Consequently, due to the inherent focusing capability of reflector antennas, ambiguities are damped very effectively. However, in situations with very low pulse repetition frequencies, where azimuth ambiguities become dominant, or with large *PRF*s, when range ambiguities are of importance, more advanced beamforming concepts are required. Clearly the unity DBF concept would not be applicable to direct radiating arrays.

4.3.3 Minimum Variance Distortionless Response Beamforming

A second beamforming method is the *minimum variance distortionless response* (MVDR) beamformer [123]. This beamformer belongs to the class of optimal beamformers, where the term *distortionless* refers to the fact that the signal is to be estimated undisturbed, or, in other words, the signal magnitude is kept constant. This can be achieved by defining a constraint, taken from the numerator of equation (4.42), with the vector product between the weight vector and the array manifold equal to one

$$\boldsymbol{w}^{\mathsf{T}}(k_y, t, k)\boldsymbol{a}(k, \varphi, \vartheta) = 1 \; . \tag{4.50}$$

The consequence of this approach is clearly that the noise power spectral density after beamforming is no longer constant. This means, the initially white noise spectrum becomes colored. The optimization problem can then be stated according to

$$\text{minimize} \quad \boldsymbol{w}^{\mathsf{T}}\boldsymbol{R}_{\boldsymbol{v}}\boldsymbol{w}^{*} \tag{4.51}$$

$$\text{subject to} \quad \boldsymbol{w}^{\mathsf{T}}\boldsymbol{a} = 1 \; . \tag{4.52}$$

The solution for the conjugate complex weight vector $\boldsymbol{w}^{*}$ can be given in closed form as (see appendix D)

$$\boldsymbol{w}^{*} = \frac{\boldsymbol{R}_{\boldsymbol{v}}^{-1}\boldsymbol{a}}{\boldsymbol{a}^{\mathsf{H}}\boldsymbol{R}_{\boldsymbol{v}}^{-1}\boldsymbol{a}} \; . \tag{4.53}$$

Usually the noise covariance matrix $\boldsymbol{R}_{\boldsymbol{v}}$ is unknown and therefore needs to be estimated from recently received time domain data [75]

$$\boldsymbol{R}_{\boldsymbol{u}}(t) = \frac{1}{T} \int_{t'=t-T}^{t} \boldsymbol{u}(t')\boldsymbol{u}^{\mathsf{H}}(t')\mathrm{d}t' \quad \in \mathbb{C}^{N_{\mathrm{act}} \times N_{\mathrm{act}}} \; . \tag{4.54}$$

Using the estimate $\boldsymbol{R}_{\boldsymbol{u}}$ instead of the noise covariance matrix $\boldsymbol{R}_{\boldsymbol{v}}$ is a concept originally developed by Capon [11]. The consistent expansion of this covariance matrix estimator to the time-wavenumber domain could take the following form

$$\boldsymbol{R}_{\boldsymbol{u}}(t, k) = \frac{1}{\sqrt{E_\gamma}} \int_{t'} \boldsymbol{u}(t')\boldsymbol{u}^{\mathsf{H}}(t')\gamma^{*}(t' - t)\mathrm{e}^{-\mathrm{j}kct'}\mathrm{d}t' \; , \quad E_\gamma = \int_{t} |\gamma(t)|^2 \mathrm{d}t \; , \tag{4.55}$$

where the STFT principle has been exploited. Two preconditions for this concept to work are the noise process $\boldsymbol{v}(t)$ being stationary within the length of the

kernel γ and the power of the underlying reflectivity function $o(\boldsymbol{r})$, which can be modeled as complex random process, being small compared to the thermal noise power. Otherwise the estimate is biased. Another option is to use an a-priori characterization of the channels as estimate for $\boldsymbol{R}_v$. Nevertheless, this approach might become challenging if effects like temperature induced instrument drift are taken into account.

Inserting the weight vector (4.53) into the *SNR* equation (4.42), yielding

$$SNR(k_y, t, k, \boldsymbol{r}) = \frac{\sigma_o^2 |g|^2}{(\boldsymbol{a}^{\mathsf{H}} \boldsymbol{R}_v^{-1} \boldsymbol{a})^{-1}} \,, \tag{4.56}$$

clarifies the principle of the MVDR beamformer. Clearly, this beamformer can be interpreted as *SNR* maximizer for each cell (k_y, t, k) in the 3-D raw data space. The signal is preserved undistorted, while the noise power spectral density is proportional to the inverse of the antenna gain pattern $\boldsymbol{a}^{\mathsf{H}} \boldsymbol{R}_v^{-1} \boldsymbol{a}$. Compared to the unity beamformer, the MVDR beamformer has the advantage that all available channels can be activated simultaneously. Those channels contributing predominantly with noise are quasi nulled with small magnitude weights, as can be seen from the power density distribution in Fig. 3.9. However, in contrast to planar array antennas, it is advisable to restrict the activated feed elements to those where the complex amplitude pattern is accurately known. Otherwise mismatch will degrade the *SNR*.

Just as the unity beamformer the MVDR beamformer is not dedicated to suppress spatial interference. In the denominator of the *ASR* expression (4.46) the signal power would reduce to

$$\sigma_o^2(\boldsymbol{r}) |g(k_y, t, k, \boldsymbol{r})|^2 \,, \tag{4.57}$$

while the ambiguous signal power depends on the sidelobe levels. Nevertheless also this beamforming concept benefits from the focusing capability of reflector antennas and insofar the ambiguous power can be expected to be in the same order as for the unity beamformer for most relevant *PRF*s.

4.3.4 Linear Constraint Minimum Variance Beamforming

A major aspect of digital beamforming in the context of SAR applications has not been considered yet, that is the suppression of spatial interference. While the purpose of MVDR beamformers is to maximize the sensitivity of a SAR for a specific direction, or wavenumber, respectively, another class of beamformers allows to optimize the sensitivity for the direction of interest and to suppress certain other directions, where interference is expected, at the same time. This

method is called *linear constraint minimum variance* (LCMV) [123] beamforming. The optimization problem can be formulated in analogy to equations (4.51) and (4.52) according to

$$\text{minimize} \quad \boldsymbol{w}^{\mathsf{T}} \boldsymbol{R}_v \boldsymbol{w}^* \tag{4.58}$$

$$\text{subject to} \quad \boldsymbol{A}^{\mathsf{T}} \boldsymbol{w} = \boldsymbol{c} \,, \tag{4.59}$$

with the cost function (4.58) being identical to the one of the MVDR beamformer. Here, a set of linear constraints is defined via equations (4.59), where the matrix

$$\boldsymbol{A} = \left[\boldsymbol{a}(k, \varphi_1, \vartheta_1) \quad \boldsymbol{a}(k, \varphi_2, \vartheta_2) \quad \dots \quad \boldsymbol{a}(k, \varphi_{N_{\text{dir}}}, \vartheta_{N_{\text{dir}}}) \right] \in \mathbb{C}^{N_{\text{act}} \times N_{\text{dir}}} \,, \tag{4.60}$$

consists of the array manifold vectors with N_{act} active feed elements for N_{dir} different directions. Here, the first column could correspond to the signal of interest, given for instance in the denominator of equation (4.46), while all further columns might correspond to the m,lth ambiguity collected in the sum term in the numerator. Of course the same consideration applies to the *AASR* (4.44) and the *RASR* (4.45) individually. A closed form solution can be derived (see appendix D) resulting in

$$\boldsymbol{w}^* = \boldsymbol{R}_v^{-1} \boldsymbol{A} (\boldsymbol{A}^{\mathsf{H}} \boldsymbol{R}_v^{-1} \boldsymbol{A})^{-1} \boldsymbol{c}^* \,. \tag{4.61}$$

The constraint vector $\boldsymbol{c}$ can in principle be chosen freely. A meaningful constraint vector could for example take the form

$$\boldsymbol{c} = \left[1 \quad 0 \quad \dots \quad 0 \right]^{\mathsf{T}} \,, \tag{4.62}$$

where the '1' corresponds to the direction of the signal of interest and a zero is placed in directions to be suppressed [2]. Inserting equations (4.62) and (4.61) into (4.42) gives

$$SNR(k_y, t, k, \boldsymbol{r}) = \frac{\sigma_o^2 \left| g \cdot \boldsymbol{w}^{\mathsf{T}} \boldsymbol{a} \right|^2}{\boldsymbol{c}^{\mathsf{T}} (\boldsymbol{A}^{\mathsf{H}} \boldsymbol{R}_v^{-1} \boldsymbol{A})^{-1} \boldsymbol{c}^*} \,. \tag{4.63}$$

Under certain circumstances the term $\boldsymbol{w}^{\mathsf{T}} \boldsymbol{a}$ in the numerator is equal to one. This is the case if

$$\overline{\boldsymbol{A}}^{\mathsf{H}} \boldsymbol{R}_v^{-1} \boldsymbol{a} = \boldsymbol{0} \,, \tag{4.64}$$

[2] Wide-swath SAR acquisitions may require multiple signal directions simultaneously. In those cases simply another array manifold vector is added to the matrix $\boldsymbol{A}$ in equation (4.60) and in the constraint vector $\boldsymbol{c}$ another '1' is placed at the corresponding position.

with the definition

$$\boldsymbol{a} = \boldsymbol{a}(k, \varphi_1, \vartheta_1) \text{ and } \overline{\boldsymbol{A}} = \left[\boldsymbol{a}(k, \varphi_2, \vartheta_2) \quad \dots \quad \boldsymbol{a}(k, \varphi_{N_{\text{dir}}}, \vartheta_{N_{\text{dir}}})\right]. \tag{4.65}$$

This means, the array manifold with the wavenumber of interest must be orthogonal to the array manifold for all other wavenumbers, under consideration of the noise channel covariance matrix $\boldsymbol{R}_v$.

The key step in the numerical evaluation of the LCMV beamformer (4.61) is the computation of the inverse of $\boldsymbol{A}^{\mathsf{H}}\boldsymbol{R}_v^{-1}\boldsymbol{A}$. Even if the channels are well balanced $\boldsymbol{R}_v \sim \mathbf{I}$, with $\mathbf{I}$ the identity matrix, this matrix can become ill posed quickly [123]. The reason for this is again the focusing ability, characteristic for reflector antennas. If for instance a single or multiple wavenumbers to be suppressed are outside the swath to be illuminated, the corresponding array manifold vectors in (4.60) will contain only small magnitude numbers compared to the signal vector. This means, the condition number, which is the ratio of the largest to the smallest eigenvalue, of the matrix $\boldsymbol{A}^{\mathsf{H}}\boldsymbol{R}_v^{-1}\boldsymbol{A}$ will be large. In the worst case this matrix will become rank deficient and no solution can be obtained. The same problem arises from very close wavenumbers. In this case the corresponding array manifold vectors become linearly dependent, with the same consequence of rank deficiency. In that sense, from a purely beamforming perspective, two requirements for the design of an antenna can be formulated, that are mutually independent array manifold vectors and a small condition number.

A dedicated method to improve the robustness of such beamformers is *eigenvalue thresholding* [75], or *diagonal loading* [72, 127]. Assuming that $\boldsymbol{R}_v^{-1}$ exists,

$$\boldsymbol{A}^{\mathsf{H}}\boldsymbol{R}_v^{-1}\boldsymbol{A} = \boldsymbol{V}\boldsymbol{\Lambda}\boldsymbol{V}^{\mathsf{H}} \tag{4.66}$$

can be decomposed into an eigenvalue matrix

$$\boldsymbol{\Lambda} = \begin{bmatrix} \lambda_1 & & \\ & \ddots & \\ & & \lambda_{N_{\text{act}}} \end{bmatrix}, \tag{4.67}$$

and the corresponding eigenvector matrices $\boldsymbol{V}$. A modified eigenvalue matrix can now be constructed of the form

$$\overline{\boldsymbol{\Lambda}} = \begin{bmatrix} \max\{\mu\lambda_{\max}, \lambda_1\} & & \\ & \ddots & \\ & & \max\{\mu\lambda_{\max}, \lambda_{N_{\text{act}}}\} \end{bmatrix}, \tag{4.68}$$

with $\lambda_{\max} = \max\{\lambda_1, \dots, \lambda_{N_{\text{act}}}\}$, $\mu \in [0, 1]$ and replace the former eigenvalue matrix $\boldsymbol{\Lambda}$. The effect of this method can best be described as 'detuning' of the

beamformer. In the worst case this can result, with an improper selection of the parameter μ, in an insufficient suppression of spatial interference or even a deterioration of the mainlobe.

The main motivation for the introduction of the LCMV beamformer in SAR applications is to minimize spatial interference in the ambiguity-to-signal ratio expression (4.46). If the array response matrix (4.60) is well posed, zeros can be placed in the directions to be suppressed. A fundamental limit of this concept to work is of course when spatial interference enters the main beam. An expression of the half-power beamwidth for center fed reflector antennas was given in equation (3.12). However, in practice the array response matrix is usually not a square matrix, so that the LCMV beamformer must be understood as least square solution of a quadratic program. This means, some directions might not be suppressed as efficiently as others. The LCMV beamformer shows its best performance when interference needs to be damped in the region of a few sidelobes next to the mainlobe. This will be a major motivation to use the LCMV concept with azimuth processing techniques.

In summary, LCMV beamforming is a technique which optimizes the *SNR* and the ambiguity-to-signal ratio at the same time. The signal of interest is preserved via the constraint '1' with the best possible *SNR*, while ambiguities are suppressed by placing $N_{\mathrm{dir}} - 1$ zeros[3] in the constraint vector.

4.4 Beamforming with Spaceborne Reflector SAR Sensors

The beamforming concepts in the chapters before represent a general approach to the optimal processing of multi-channel SAR data. For the purpose of clarity continuous time and wavenumber domain variables have been used. In real SAR applications, however, one deals with time and value discrete data. This means, in practice the downlink capacity between a SAR sensor and the ground station sets a stringent constraint to this data volume. The data rate in bits per second of SAR system with complex demodulation of N_{c} digital channels can be estimated according to

$$R = N_{\mathrm{c}} \cdot 2 \cdot f_{\mathrm{s}} \cdot N_{\mathrm{b}} \cdot EWL \cdot PRF \,. \tag{4.69}$$

The factor 2 accounts for in-phase and quadrature channel, N_{b} is the number of bits per sample, *EWL* is the echo window length given by equations (3.17) and (3.20). The sampling frequency f_{s} is typically chosen in the order of 10 %

[3] In principle also constraint vectors can be constructed where the ambiguities are not 'nulled', but damped with small numbers as for example -20 dB. Such a choice of constraints might be meaningful in the presence of other additive distortions like thermal receiver noise. Moreover, the robustness of such a beamformer might be improved.

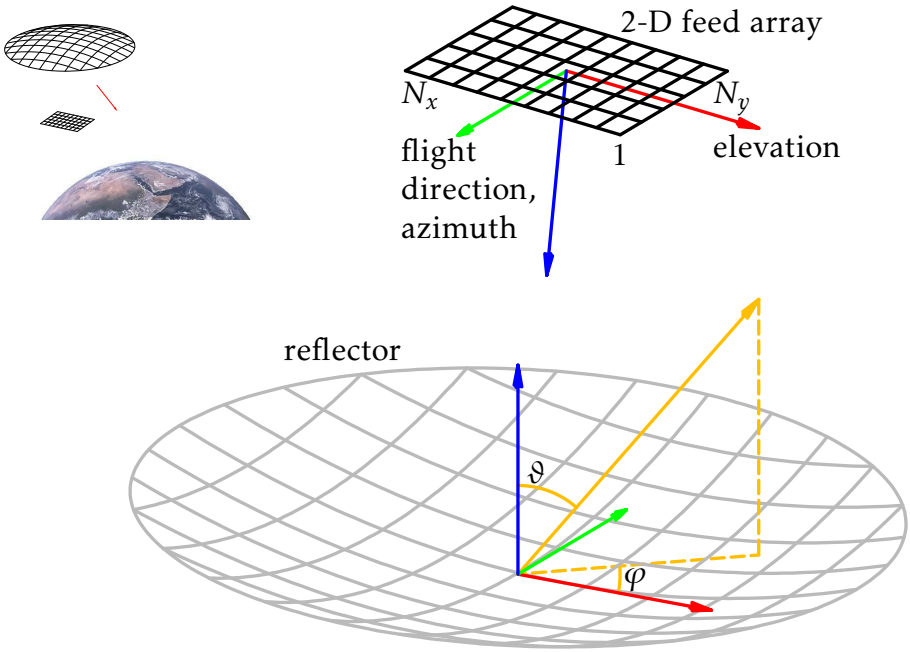

Figure 4.9: Reflector antenna with two-dimensional feed array. The number of channels in azimuth N_y determines the Doppler domain to be covered and with this the azimuth resolution. The number of channels in elevation N_x defines the illuminated swath width. In the top left the orientation of the reflector with respect to the Earth is shown.

larger than the signal bandwidth B. From a SAR mission design perspective the EWL must be considered rather as a fixed parameter, since a digital beamforming SAR system should be able to acquire the maximal possible swath width. The number of bits N_b depends on the data compression scheme used, as well as on the expected SAR data SNR. The number of digital channels N_c is a design parameter. Due to the imaging geometry it is common practice to separate the design of a spaceborne SAR system into azimuth and elevation, or slant range, respectively. Consequently the feed array is constructed with N_x feed elements, which is equivalent to digital channels, in elevation and N_y feed elements in azimuth, resembling a two-dimensional array with $N_\mathrm{c} = N_x N_y$ channels. With this, it is possible to perform digital beamforming in realtime onboard the spacecraft and downlink only N_y azimuth channels, effectively reducing the data rate R by a factor of N_x. Figure 4.9 illustrates the antenna hardware concept of a reflector antenna based digital beamforming SAR system using a two-dimensional feed array. Here, a linear placement of the feed elements is chosen, however, also hexagonal element arrangements are feasible. Important is that enough distinct phase centers are available in both the azimuth and ele-

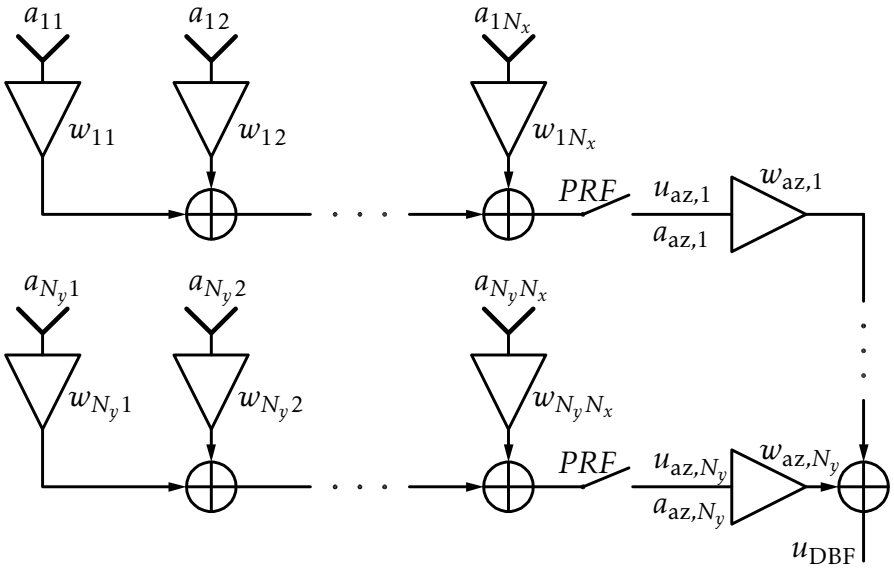

Figure 4.10: Separation of DBF processing in elevation and azimuth. The block diagram is drastically simplified in order to demonstrate the formation of the individual weights in the signal paths.

vation dimension to apply beamforming techniques efficiently.

The processing schemes, to be introduced in the following sections, in elevation and azimuth are based on the unity (4.48), MVDR (4.53) and LCMV (4.61) beamformers. Nevertheless, before discussing dedicated beamforming strategies, the implications of this afore mentioned separation in elevation and azimuth on the performance shall be discussed. Beamforming in elevation is carried out onboard the satellite, giving N_y azimuth raw data signals

$$\boldsymbol{u}_{\mathrm{az}} = \begin{bmatrix} u_{\mathrm{az},1} \\ \vdots \\ u_{\mathrm{az},N_y} \end{bmatrix} = \begin{bmatrix} \boldsymbol{w}_{1,\mathrm{el}}^{\mathsf{T}} \boldsymbol{u}_{1,\mathrm{el}} \\ \vdots \\ \boldsymbol{w}_{N_y,\mathrm{el}}^{\mathsf{T}} \boldsymbol{u}_{N_y,\mathrm{el}} \end{bmatrix} \text{ and } \boldsymbol{a}_{az}(k,\varphi,\vartheta) = \begin{bmatrix} \boldsymbol{w}_{1,\mathrm{el}}^{\mathsf{T}} \boldsymbol{a}_{1,\mathrm{el}} \\ \vdots \\ \boldsymbol{w}_{N_y,\mathrm{el}}^{\mathsf{T}} \boldsymbol{a}_{N_y,\mathrm{el}} \end{bmatrix} \tag{4.70}$$

new azimuth patterns. The final output after digital beamforming in azimuth is

$$u_{\mathrm{DBF}} = \boldsymbol{w}_{\mathrm{az}}^{\mathsf{T}} \boldsymbol{u}_{\mathrm{az}} \text{ , with } \boldsymbol{w}_{\mathrm{az}} = f(\boldsymbol{a}_{az}) \,. \tag{4.71}$$

By substituting equation (4.70) into equation (4.71), it becomes evident that beamforming with separation in elevation and azimuth is an iterative procedure. This is graphically illustrated in Fig. 4.10. Here, all further signal processing steps, like STFTs have been omitted, in order to demonstrate the formation of the weight vectors in equations (4.70) and (4.71). In principle different

beamformers could be combined, for example in elevation MVDR beamforming for maximum gain and then in azimuth LCMV beamforming to suppress azimuth ambiguities.

If one intends to stick with a single beamforming scheme a loss in *SNR* might be inevitable. The unity beamformer (4.48) clearly is a linear processor, and insofar the *SNR* after iterative beamforming in elevation and azimuth leads to the same *SNR* as in the case when all channels are available at the same time. This is in general not true for pure MVDR beamforming. As long as the cross correlation terms in the noise channel covariance matrix $\boldsymbol{R_v}$ are not equal to zero, the separate beamforming approach will generate a lower *SNR* than the DBF approach using all channels. In the special case when $\boldsymbol{R_v} \sim \mathbf{I}$ it can be shown for MVDR beamforming that

$$SNR_{\text{sep}} = \sum_{i=1}^{N_y} SNR_{\text{az},i} = SNR_{\text{tot}} \,, \tag{4.72}$$

where SNR_{sep} refers to the separate approach and SNR_{tot} denotes the approach utilizing all channels at a time. The individual $SNR_{\text{az},i}$ are measured before applying the weights $w_{\text{az},i}$ in Fig. 4.10. The LCMV beamformer will principally generate different *SNR* values, comparing the approach where subsets of feed channels are used to the case when all channels are employed simultaneously, since LCMV beamforming (4.61) utilizes combinations of channel patterns through the matrix $\boldsymbol{A}^{\mathrm{H}}\boldsymbol{R_v}^{-1}\boldsymbol{A}$. In terms of ambiguity suppression the performance should not be affected, as long as the phase centers in elevation are aligned as depicted in Fig. 4.9.

In the following two sections dedicated processing strategies in elevation and in azimuth are discussed [48], which essentially are based upon equation (4.27).

4.4.1 Digital Beamforming in Elevation

For pulsed radar systems the time interval between two succeeding pulses is $PRI = PRF^{-1}$. Consequently, all digital signal processing in elevation takes place in a time smaller than this interval, which is in the order of several hundred microseconds for spaceborne SAR systems. Even for simple beamforming algorithms the computational power required may exceed those of software based processors. Therefore, signal processing strategies are required which incorporate the concepts derived in the previous chapters, but offer enough simplicity to be realized on hardware signal processors implemented on FPGAs or ASICs.

For clarity reasons, in the following derivations the azimuth variable y shall be dropped. Formally, the beamforming operation in elevation can be stated by

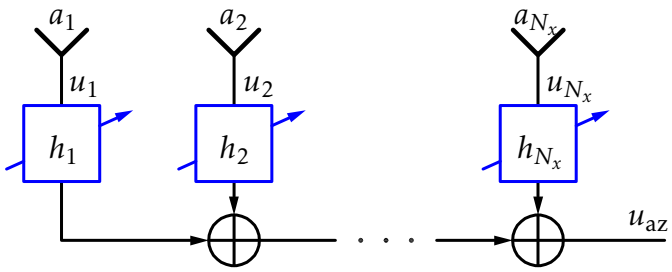

Figure 4.11: Block diagram illustrating the time-variant processing scheme (4.74) in an individual elevation branch. The output signals u_{az} serve then as input for an azimuth beamforming processor.

inserting equations (4.27) and (4.29) into equation (4.30) according to

$$u_{\mathrm{az}}(t) = \int_k \int_{t''} \boldsymbol{w}^{\mathsf{T}}(t'',k) \int_{t'} \boldsymbol{u}(t')\gamma^*(t'-t'')\mathrm{e}^{-\mathrm{j}kct'}\mathrm{d}t' \cdot \overline{\gamma}(t-t'')\mathrm{e}^{\mathrm{j}kct}\mathrm{d}t''\mathrm{d}k \,. \tag{4.73}$$

The subscript 'az' refers to the individual beamformer outputs in elevation as sketched in Fig. 4.10. This equation describes in general the beamforming operation using the STFT principle and its inverse. Rearranging this integral and carrying out the integration over the wavenumber k gives

$$\begin{aligned} u_{\mathrm{az}}(t) &= \int_{t'} \boldsymbol{u}^{\mathsf{T}}(t') \int_{t''} \boldsymbol{w}(t'',t-t')\gamma^*(t'-t'')\overline{\gamma}(t-t'')\mathrm{d}t''\mathrm{d}t' \\ &= \int_{t'} \boldsymbol{u}^{\mathsf{T}}(t')\boldsymbol{h}(t,t-t')\mathrm{d}t' \\ &= \int_{t'} \boldsymbol{u}^{\mathsf{T}}(t-t')\boldsymbol{h}(t,t')\mathrm{d}t' \,, \end{aligned} \tag{4.74}$$

with

$$\boldsymbol{h}(t,t') = \int_{t''} \boldsymbol{w}(t'',t-t')\gamma^*(t'-t'')\overline{\gamma}(t-t'')\mathrm{d}t'' \,. \tag{4.75}$$

With this result two observations, concerning the structure of the filter vector $\boldsymbol{h}$, can be made. First, the filter is time-variant, or more precisely, the weight vector $\boldsymbol{w}$ is time-variant, since it is adapted to different directions as the pulse travels over ground. The wavenumber dependency is translated into a temporal variable. This is, because different spectral parts of the chirp waveform arrive at different times (see equation (4.15)). Second, the filter requires a scalar kernel, which is basically time-invariant. This kernel is responsible for the discrimination of different spectral parts of the chirp. Figure 4.11 shows the realization

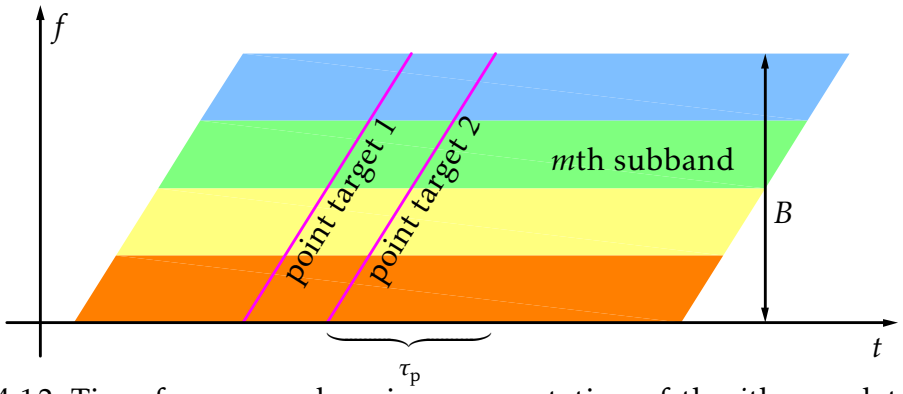

Figure 4.12: Time-frequency domain representation of the ith raw data signal u_i, where the signal bandwidth B is divided into M subbands. This approach is the discrete version of the STFT principle demonstrated in Fig. 4.6b. Any frequency dependency of the antenna transfer function can be accounted for with proper weights.

of the elevation beamforming equation (4.74) in a block diagram. In total N_y output signals u_{az} are then further processed using DBF techniques in azimuth. Such multi-dimensional processing concepts are embraced under the umbrella term *space-time adaptive processing* (STAP) [58, 83, 108].

At this stage it is tempting to derive the vectorial filter impulse response function $\boldsymbol{h}(t,t')$ directly from equation (4.74). This however leads to a computationally expensive solution. The interested reader is referred to appendix F. Instead a solution is favored which requires filter lengths N_{coef} in the order of a few ten coefficients. The basic idea of the filtering approach is to decompose the received signal $u_i(n)$ into multiple frequency bands and to apply a specific filter on each of these individual subbands as sketched in Fig. 4.12, which shows the graphical interpretation of equation (4.15). To each subband a bandpass filter according to equation (4.82) and a weight is applied which is derived from its corresponding channel pattern. These individual bandpass filters are then combined to a single filter (4.77) as presented in Fig. 4.13.

For the purpose of filter design it is useful to turn back from wavenumbers to frequencies ($k = 2\pi f/c \mapsto f$). Then the time discrete ($t \mapsto n$) beamformer output (4.74) writes

$$u_{\mathrm{az}}(n) = \sum_{n'=0}^{N_{\mathrm{coef}}-1} \boldsymbol{u}^{\mathsf{T}}(n-n')\boldsymbol{h}(n,n')\,, \tag{4.76}$$

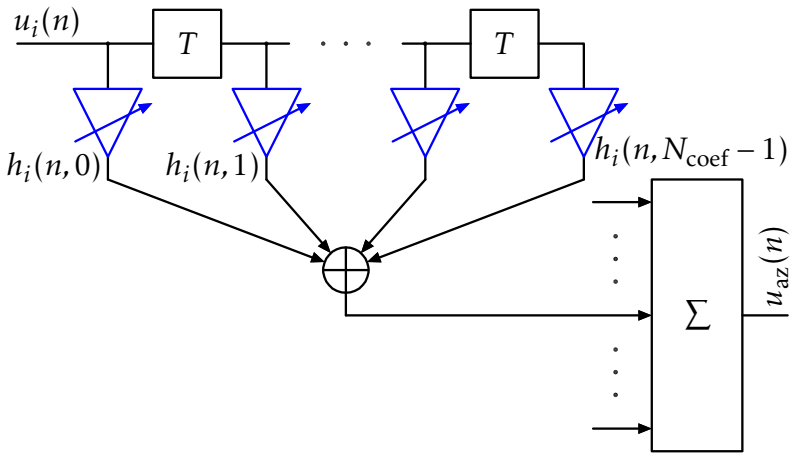

Figure 4.13: FIR filter with time-variant coefficients $h_i(n,n')$.

with the discrete version of (4.75)

$$\boldsymbol{h}(n,n') = \sum_{m=0}^{M-1} \boldsymbol{w}(n,m)\overline{h}(n',m)\,. \tag{4.77}$$

N_{coef} is the number of filter coefficients for a *finite impulse response* (FIR) filter of order $N_{\text{coef}}-1$ and M is the number of subbands. Note, as mentioned before, the frequency dependency enters the weights via the time variable m due to the linear time-frequency relation of chirp signals as described by equation (4.15). Figure 4.13 shows a block diagram of such a filter with delay elements denoted by the clock period $T = 1/f_{\text{s}}$. The filter design for $\overline{h}$ is based on a Fourier analysis of bandpass transfer functions of rectangular shape with cutoff frequencies $\Omega_{\text{c1},m}$ and $\Omega_{\text{c2},m}$. Then the Fourier series coefficients are

$$\overline{h}(n,m) = \frac{1}{2\pi}\int_{\Omega_{\text{c1},m}}^{\Omega_{\text{c2},m}} \mathrm{e}^{\mathrm{j}n\Omega}\mathrm{d}\Omega\,, \quad \Omega = 2\pi\frac{f}{f_{\text{s}}}\,, \tag{4.78}$$

resulting in

$$\overline{h}(n,m) = \frac{\Omega_{\text{c2},m}-\Omega_{\text{c1},m}}{2\pi}\cdot\operatorname{sinc}\left(n\frac{\Omega_{\text{c2},m}-\Omega_{\text{c1},m}}{2}\right)\cdot\mathrm{e}^{\mathrm{j}n(\Omega_{\text{c1},m}+\Omega_{\text{c2},m})/2}\,. \tag{4.79}$$

Dividing the design bandwidth $\overline{B}$ into M subbands of equal width, the cutoff frequencies are given as

$$\Omega_{\text{c1},m} = 2\pi\left(\frac{m}{M}-\frac{1}{2}\right)\frac{\overline{B}}{f_{\text{s}}}\,, \quad m\in[0,M-1]\,, \tag{4.80}$$

$$\Omega_{\text{c2},m} = 2\pi\left(\frac{m+1}{M}-\frac{1}{2}\right)\frac{\overline{B}}{f_{\text{s}}}\,, \quad m\in[0,M-1]\,. \tag{4.81}$$

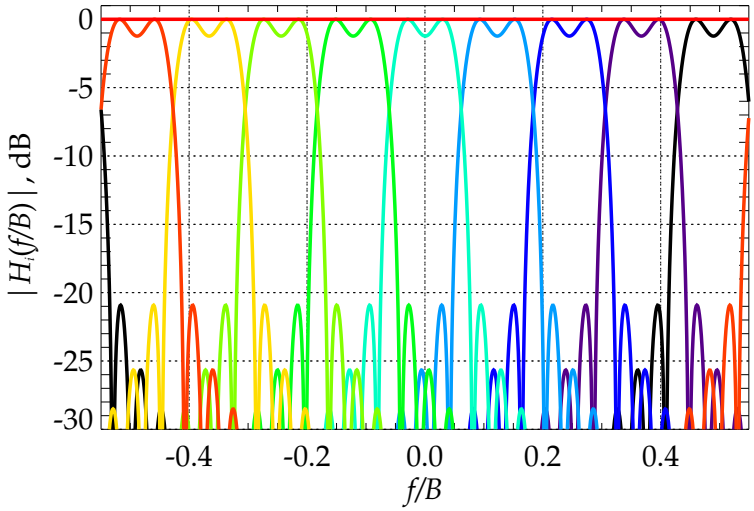

Figure 4.14: FIR filter bank with nine subbands and after ideal reconstruction (constant curve)

The resulting filter coefficients equate

$$\overline{h}(n,m) = \frac{\overline{B}}{M f_s} \cdot \mathrm{sinc}\left(n\pi \frac{\overline{B}}{M f_s}\right) \cdot \mathrm{e}^{\mathrm{j}n\pi((2m+1)/M-1)\overline{B}/f_s} \,. \tag{4.82}$$

For the filter bank design it has to be ensured that the signal after combining the single filter outputs reconstructs the input signal. From equation (4.77) with the above definitions it can be shown that

$$\sum_{m=0}^{M-1} w_i(n,m)\overline{h}(n,m) = \frac{\overline{B}}{f_s}\mathrm{sinc}\left(n\pi \frac{\overline{B}}{f_s}\right) , \tag{4.83}$$

assuming unity weights $w_i(n,m) = 1$. In order to avoid aliasing, the sampling frequency f_s must be equal or larger than the signal bandwidth B. Consequently, it would be sufficient to restrict the design bandwidth $\overline{B}$ to the signal bandwidth. However, setting $\overline{B}$ to f_s offers

$$\frac{\overline{B}}{f_s}\mathrm{sinc}\left(n\pi \frac{\overline{B}}{f_s}\right) = \mathrm{sinc}(n\pi) = \delta(n) \,. \tag{4.84}$$

From this result it can be concluded, that the reconstruction is ideal and independent from the number of filter coefficients N_{coef} for $w_i(n,m) = 1$. Figure 4.14 shows the transfer functions for a filter bank with nine subbands and 31

coefficients. The constant curve represents the transfer function after ideal reconstruction given by equation (4.84).

If the antenna patterns are constant over the transmitted signal bandwidth, no frequency dependent weights are required. In this case a simplified processing scheme can be implemented. Due to the linear time-frequency relationship of chirp signals every subspectrum enters a feed element at a defined time for a given direction. Since the chirp spectrum is divided into M subbands the time dependent weights are best taken at the center of each subspectrum. Introducing the subband specific delay n_m the weights in equation (4.77) can then be rewritten as

$$w_i(n,m) = w_i(n - n_m)\,, \quad m \in [0, M-1]\,. \tag{4.85}$$

where

$$n_m = \text{nint}\left\{\frac{2m+1}{2M}\tau_\text{p} f_\text{s}\right\}\,, \tag{4.86}$$

with nint{.} the nearest integer function.

An alternative way to implement the time-variant filter (4.77) on a SAR instrument with frequency invariant weights is by means of filter banks, as illustrated in Fig. 4.15. Each subband, distinguished by different colors as for instance in Fig. 4.12, is associated with a filter $\overline{h}$ and weighted with a time delayed weight as defined in equation (4.85). This concept offers the advantage to conveniently store the time-variant weights in a lookup table, instead of computing entire filter transfer functions in advance. Moreover, multirate processing techniques could be applied, where every subband filter $\overline{h}(n,m)$ is clocked with f_s/M. Of course also this processing scheme can be adapted to take frequency dependent weighting into account. Then a two-dimensional lookup table would be required, where each subband is weighted separately. This beamforming concept would be mathematically identical to the one presented in Fig. 4.13.

Finally, it is necessary to adapt the channel activation concept (3.15) to the case of temporally extended pulses. The on-time of an individual channel still obeys equation (3.15). However, at each time instance another pulse duration τ_p needs to be added in order to ensure that the echo pulses enter the receiver completely. This results in a prolongation of the on-time of each channel as presented for example in Fig. 3.10b by one pulse length.

With equations (4.76), (4.77) and (4.79) the entire signal processing procedure in elevation is characterized. As in the general 3-D beamforming approach, the beamformers in elevation shall be restricted to the concepts introduced in chapter 4.3, with equations (4.48) for unity beamforming, (4.53) for MVDR beamforming and (4.61) for LCMV beamforming. To judge the performance of these

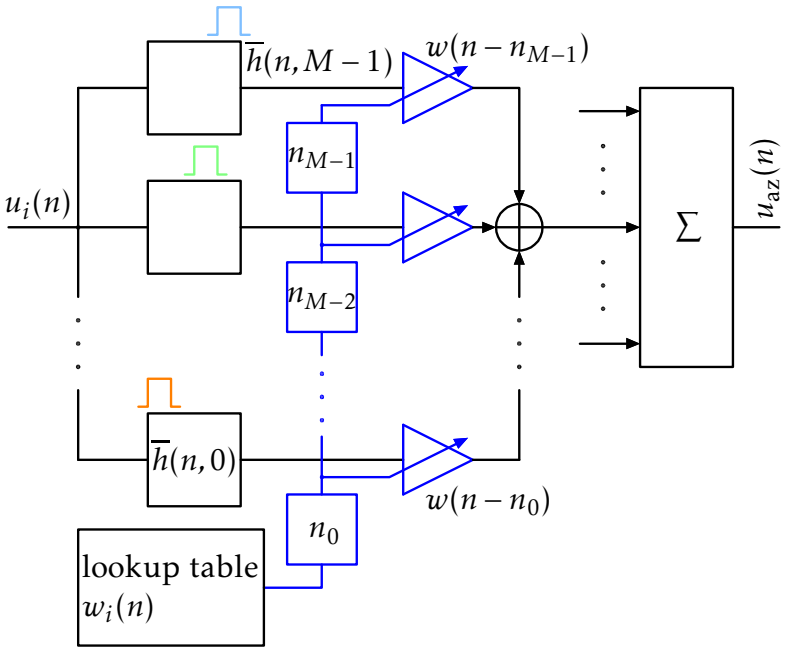

Figure 4.15: FIR filter bank realization of the filter coefficients $h_i(n, n')$ for frequency independent weighting.

beamformers in elevation, it is useful to derive performance figures, adapted from the raw data *SNR* expressions (4.49), (4.56) and (4.63), respectively. The performance in terms of range ambiguity suppression shall be evaluated on the basis of equation (4.45).

The *SNR* in elevation can be expressed, substituting the signal power (E.6) and the noise power (E.10) into equation (E.12), yielding

$$SNR(n) = \frac{\sigma_o^2(\vartheta)\left|\sum_n^{n+N_\mathrm{p}} |\boldsymbol{a}^\mathsf{T}(\vartheta)\sum_{n'} g(\vartheta, n-n')\boldsymbol{h}(n, n')|\right|^2}{\sum_n^{n+N_\mathrm{p}}\sum_{n'}\boldsymbol{h}^\mathsf{T}(n, n')\boldsymbol{R}_{\boldsymbol{v}}(n-n')\boldsymbol{h}^*(n, n')}\,, \tag{4.87}$$

where $N_\mathrm{p} = \mathrm{nint}\{\tau_\mathrm{p} f_\mathrm{s}\}$ is the number of samples per pulse. The above *SNR* formula (4.87) is the result of a treatment of digital beamforming in elevation as a one-dimensional problem. In the general two-dimensional case the integration over the azimuth variable, which is a coherent integration for the signal and an incoherent integral with respect to the noise, will result in the so called azimuth processing gain, similar to the range processing gain. Insofar the *SNR* expressions in elevation do not account for any azimuth processing. Nevertheless, in this context the relative performances of the individual beamforming concepts are of importance.

Considering, as special case, a filter with a single band ($M = 1$) the vectorial impulse response function $\boldsymbol{h}(n, n')$ is

$$\boldsymbol{h}(n, n') = \boldsymbol{w}(n)\delta(n') \,. \tag{4.88}$$

With this, the *SNR* simplifies to

$$SNR(n) = \frac{\sigma_o^2(\vartheta)\left|\sum_{N_\mathrm{p}} |g(\vartheta, n)\boldsymbol{a}^\mathsf{T}(\vartheta)\boldsymbol{w}(n)|\right|^2}{\sum_{N_\mathrm{p}} \boldsymbol{w}^\mathsf{T}(n)\boldsymbol{R}_{\boldsymbol{v}}(n)\boldsymbol{w}^*(n)} \,. \tag{4.89}$$

Only in the limit of infinite short pulses the *SNR* according to equations (4.87) and (4.89) are equal. Nevertheless, equation (4.89) adopted for the three beamforming concepts gives insight in the principal behavior of a specific beamformer.

Assuming $\boldsymbol{R}_{\boldsymbol{v}}(n) = \sigma_v^2(n)\mathbf{I}$, with $\mathbf{I}$ the identity matrix, the *SNR* for the unity beamformer (4.48) takes the form

$$SNR_\mathrm{unity}(n) = \frac{\sigma_o^2(\vartheta)\left|\sum_{N_\mathrm{p}} |g(\vartheta, n)\boldsymbol{a}^\mathsf{T}(\vartheta)\boldsymbol{w}(n)|\right|^2}{N_\mathrm{act}\sum_{N_\mathrm{p}} \sigma_v^2(n)} \,. \tag{4.90}$$

MVDR beamforming according to equation (4.53), implemented as a technique to combine elevation channels, results for single band filters ($M = 1$) and balanced noise channels $\boldsymbol{R}_{\boldsymbol{v}}(n) = \sigma_v^2(n)\mathbf{I}$ in

$$SNR_\mathrm{MVDR}(n) = \frac{\sigma_o^2(\vartheta)\left|\sum_{N_\mathrm{p}} |g(\vartheta, n)|\right|^2}{\sum_{N_\mathrm{p}} \sigma_v^2(n)(\boldsymbol{a}^\mathsf{H}\boldsymbol{a})^{-1}} \,. \tag{4.91}$$

Here, again the inverse shaping of the noise signal becomes apparent. If the antenna patterns $\boldsymbol{a}$ additionally depend on the transmit frequency f or wavenumber k, respectively, the noise spectrum will become colored.

Finally, the linear constraint minimum variance (LCMV) beamformer, given with equation (4.61), produces an *SNR* which is typically smaller than in the MVDR case

$$SNR_\mathrm{LCMV}(n) = \frac{\sigma_o^2(\vartheta)\left|\sum_{N_\mathrm{p}} |g(\vartheta, n)\boldsymbol{a}^\mathsf{T}(\vartheta)\boldsymbol{w}(n)|\right|^2}{\sum_{N_\mathrm{p}} \sigma_v^2(n)\boldsymbol{c}^\mathsf{T}(\boldsymbol{A}^\mathsf{H}\boldsymbol{A})^{-1}\boldsymbol{c}^*} \,, \tag{4.92}$$

again assuming $M = 1$ and $\boldsymbol{R}_{\boldsymbol{v}}(n) = \sigma_v^2(n)\mathbf{I}$. The motivation of LCMV beamforming in elevation is to suppress range ambiguities, contaminating the signal of

interest. Adopting the raw data *RASR* formula (4.45) to the elevation case one finds for the SAR image range ambiguity-to-signal ratio[4]

$$RASR(n) = \frac{\sum\limits_{l\in\mathbb{Z}\setminus\{0\}} \sigma_o^2(\vartheta_l) \sum_{N_\mathrm{p}} |g(\vartheta_l, n)\boldsymbol{a}^\mathsf{T}(\vartheta_l)\boldsymbol{w}(n)|^2}{\sigma_o^2(\vartheta) \sum_{N_\mathrm{p}} |g(\vartheta, n)\boldsymbol{a}^\mathsf{T}(\vartheta)\boldsymbol{w}(n)|^2} \,. \tag{4.93}$$

The variance of the reflectivity function σ_o^2 corresponds to the product of the normalized backscatter coefficient σ_0 and the resolution cell of size A_cell. Decomposing the resolution cell into ground range resolution Δr_g, modifying equation (2.36) with the sine of the incident angle θ_i, and azimuth resolution Δy, using equation (2.35), the RCS can be written

$$\sigma_o^2 = \sigma_0 \cdot A_\mathrm{cell} = \sigma_0 \cdot \Delta r_\mathrm{g} \cdot \Delta y = \sigma_0 \cdot \frac{c}{2B\sin\theta_\mathrm{i}} \cdot \frac{\lambda R_0}{2Y} \,, \tag{4.94}$$

where Y is the length of the processed azimuth aperture and R_0 denotes the zero-Doppler distance between sensor and target $\|\boldsymbol{r}_\mathrm{s} - \boldsymbol{r}\|$, or sensor and ambiguity $\|\boldsymbol{r}_\mathrm{s} - \boldsymbol{r}_l\|$, alternatively. Since the SAR focusing filter applies approximately in the same way to signal and ambiguity, respectively, it is allowed to drop the summation over the samples per pulse N_p in equation (4.93). Inserting equation (4.94) into (4.93) the *RASR* for a multi-channel SAR system can be compactly cast in the form

$$RASR(n) = \frac{\sum\limits_{l\in\mathbb{Z}\setminus\{0\}} \sigma_o^2(\boldsymbol{r}_l) \frac{|\boldsymbol{a}^\mathsf{T}(\vartheta_l)\boldsymbol{w}(n)|^2}{\|\boldsymbol{r}_\mathrm{s}-\boldsymbol{r}_l\|^3 \sin\theta_{\mathrm{i},l}}}{\sigma_o^2(\boldsymbol{r}) \frac{|\boldsymbol{a}^\mathsf{T}(\vartheta)\boldsymbol{w}(n)|^2}{\|\boldsymbol{r}_\mathrm{s}-\boldsymbol{r}\|^3 \sin\theta_\mathrm{i}}} \,, \tag{4.95}$$

where the distance from the sensor to the ambiguous regions $\boldsymbol{r}_l$ is

$$\|\boldsymbol{r}_\mathrm{s} - \boldsymbol{r}_l\| = \|\boldsymbol{r}_\mathrm{s} - \boldsymbol{r}\| + l\frac{c}{2PRF} \,. \tag{4.96}$$

Equation (4.95) is the multi-channel expansion of range ambiguity formulas given for example in [17]. Although this formula does not explicitly take into account the time-variant filter vector $\boldsymbol{h}(n, n')$, it gives nevertheless a good estimate of range ambiguous signal power. Of course this *RASR* expression applies not only to LCMV beamforming but also to any other beamforming method.

[4] In contrast to the *SNR* formulas the signal power as well as the range ambiguous power are summed up incoherently in the *RASR* expression (4.93). This is motivated by the fact, that especially the beamforming operation might lead to a modulation of the range ambiguous signal returns. The consequence is that these ambiguities will not be focused ideally but smeared over a certain domain. In that case range ambiguities behave rather like noise and their energy must be summed incoherently.

4.4.2 Digital Beamforming in Azimuth

As outlined in chapter 3.3 conventional pulsed SAR systems, specifically single-channel systems, are inherently restricted with respect to their imaging capability. With these systems it is not possible to achieve a large swath width X and a high azimuth resolution Δy at the same time [27]. A high resolution requires a broad beam, which needs a large PRF in order to sample adequately. The high PRF in turn limits the swath width. This relation is given in compact form with inequality (3.22).

One possibility to overcome this restriction is to transmit a signal using a broad beam and to collect the scattered signal with multiple receivers. The individual signals are then processed in order to reconstruct the high-resolution image. A simple way to implement such a system using a reflector antenna is to extend the digital feed array in the azimuth dimension [68, 69] as sketched in Fig. 4.9.

Concerning digital signal processing strategies, extensive work has been carried out to investigate this problem in the context of planar array SAR systems [31]. In contrast to reflector SAR systems with digital feed arrays, a peculiarity of planar array DBF systems lies in the fact that, depending on the PRF, the synthetic aperture is sampled non-uniformly. This is due to the fact, that the phase centers in azimuth are displaced, depending on the total antenna length and the number of azimuth channels. Based on a generalization of the sampling theorem [93], a concept was developed in order to form the output of a multi-azimuth-channel planar array SAR system [31].

The azimuth processing principle, introduced in this work, follows the schematic presented in Fig. 4.7. The basic operation is to transform the ith azimuth channel $u_{\mathrm{az},i}$ into the wavenumber domain. Dropping the elevation variables t and k, equation (4.27) writes for the ith azimuth channel

$$U_{\mathrm{az},i}(k_y) = \frac{1}{v_y} \int_{y=-\infty}^{\infty} u_{\mathrm{az},i}(y) \mathrm{e}^{-\mathrm{j}k_y y} \mathrm{d}y \; . \tag{4.97}$$

Since the azimuth signal is naturally a discrete signal, sampled with K_y or PRF, respectively, the problem of aliasing arises. As stated in chapter 3.3, it is the aim to achieve a high azimuth resolution and a large swath width simultaneously. Since with small PRFs large swath widths can be generated, K_y has to be chosen as low as possible. However, the minimum possible K_y is determined by what is called in [18] the diffraction limit of the antenna. This means that in the digital beamforming process a minimum beam width can be reconstructed which is determined by the physical length of the antenna and the transmitted frequency. For small azimuth half-power beamwidths according to equation (3.12)

the lower bound for K_y can be shown to be

$$K_y \geq 4k \sin\left(\frac{\Theta_{3\mathrm{dB,az}}}{2}\right) \approx 1.22 \frac{4\pi}{D_{\mathrm{az}}} , \tag{4.98}$$

with D_{az} the reflector antenna diameter in azimuth. Due to the pattern sidelobes, principally every azimuth channel is undersampled and therefore subject to aliasing. The azimuth processing approach can therefore be characterized as a two-stage process. First, in order to form the high-resolution image, the individual azimuth channels have to be reconstructed on a common grid with a high sampling rate K_y'. And secondly beamforming concepts have to be applied to suppress the aliased azimuth signal energy. The approach presented here is based on the discrete version of equation (4.97) over a finite domain[5]

$$U_{\mathrm{az},i}(m\Delta k_y) = \frac{\Delta y}{v_y} \sum_{n=0}^{N-1} u_{\mathrm{az},i}(y(n\Delta y)) \mathrm{e}^{-\mathrm{j}k_y(m\Delta k_y)y(n\Delta y)} , \tag{4.99}$$

with the wavenumber sampling increment Δk_y

$$\Delta k_y = \frac{2\pi}{Y} = \frac{2\pi}{M\Delta y'} = \frac{K_y'}{M} , \quad k_y \in \left[-\frac{K_y'}{2}, \frac{K_y'}{2}\right] , \tag{4.100}$$

and

$$N = \frac{Y}{\Delta y} , \quad M = \frac{Y}{\Delta y'} . \tag{4.101}$$

Here, Y is the complete integration path length. N is the number of samples of the undersampled channel signals and M is the number of samples of the high-resolution signal. Δy and $\Delta y'$ are the corresponding spatial sampling increments. Figure 4.16 illustrates the evaluation of equation (4.99). In Fig. 4.16a the magnitude of the ith azimuth signal $u_{\mathrm{az},i}(y)$ for a single point target is depicted. The shape is due to the two-way channel pattern described by equation (4.3). Note, in general the azimuth signal for distributed scatterers is dictated by the reflectivity distribution, so that the pattern like shape becomes visible only in the wavenumber domain. By taking the discrete Fourier transform according to (4.99) not only the principal interval, restricted to $\pm K_y/2$, becomes visible but also additional replicas of the spectrum beyond the baseband as can be observed in Fig. 4.16b. The green curve represents the corresponding signal spectrum of the ith azimuth channel, which could be interpreted as spatial

[5] Equation (4.99) is also applicable if the data $u_{\mathrm{az},i}$ are sampled non-uniformly. In that case the non-uniform sample spacing Δy would be drawn inside the sum.

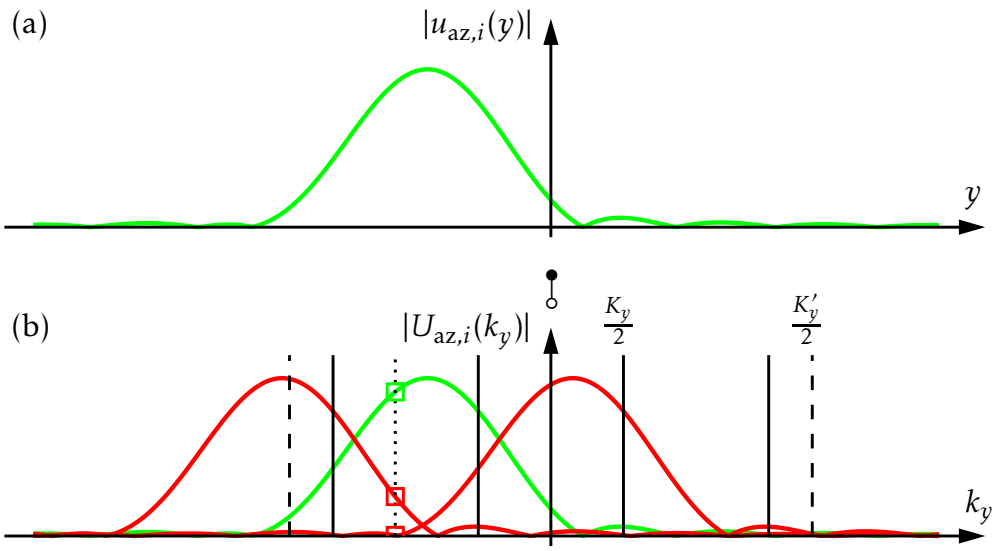

Figure 4.16: (a) ith azimuth signal for a single point target as function of the sensor position y. (b) Wavenumber domain representation of the corresponding azimuth signal with the two first ambiguous spectra drawn in red. For each wavenumber a new beam is formed digitally, with the goal to suppress these ambiguous wavenumbers, as indicated by the dotted vertical line.

bandpass filter. The first left and first right ambiguous spectrum is plotted in red. In fact, (4.99) is evaluated over the desired wavenumber domain $\pm K'_y/2$. Evidently, this procedure can be implemented in a computationally more efficient way by using the FFT, where the spectra are juxtaposed and limited to the bandwidth K'_y. From a information theoretical point of view it is enough to just use the principal Doppler band K_y, because no new information is generated.

The second step in the azimuth processing is the combination of the individual channel spectra $U_i(k_y)$ by means of weights as introduced with equation (4.71) according to

$$U_{\mathrm{DBF}}(k_y) = \boldsymbol{w}_{\mathrm{az}}^{\mathsf{T}}(k_y)\boldsymbol{U}_{\mathrm{az}}(k_y)\,. \tag{4.102}$$

As in the elevation case, an *SNR* expression shall be derived, which allows to measure the performance of different DBF approaches. On the basis of the raw data *SNR* according to equation (4.42), the SAR image signal-to-noise ratio in

azimuth writes[6]

$$SNR(\boldsymbol{r}) = \frac{\sigma_o^2 \left| \int_{K_y'} |g(k_y) \boldsymbol{w}_{\mathrm{az}}^{\mathsf{T}}(k_y) \boldsymbol{a}_{\mathrm{az}}(k_y)| \mathrm{d}k_y \right|^2}{\int_{K_y'} \boldsymbol{w}_{\mathrm{az}}^{\mathsf{T}}(k_y) \boldsymbol{R}_{\boldsymbol{v}}(k_y) \boldsymbol{w}_{\mathrm{az}}^{*}(k_y) \mathrm{d}k_y} \,. \tag{4.103}$$

The choice of the weight vector $\boldsymbol{w}_{\mathrm{az}}$ shall be restricted to the beamforming techniques already presented in chapter 4.3. The unity beamforming method according to equation (4.48) can be adapted to the azimuth case by putting a '1' to the channel of interest, which is basically the one providing the maximum power for a specific direction, or wavenumber, respectively, and setting every other channel to zero, giving for example

$$\boldsymbol{w}_{\mathrm{az}}(k_y) = \begin{bmatrix} 1 & 0 & \dots & 0 \end{bmatrix}^{\mathsf{T}} \,. \tag{4.104}$$

This is repeated for every azimuth wavenumber k_y. Consequently, the azimuth signal spectrum will be modulated proportional to the envelope of the azimuth patterns, as can be observed in Fig. 5.12. As indicated by the vertical dotted line in Fig. 4.16(b), the signal contribution, marked by the green square, might be heavily contaminated by ambiguous spectral parts, represented by the red squares, for low sampling rates K_y. In this case it is not advisable to use more than one channel per wavenumber. Still, for large enough sampling rates K_y, or *PRF*s, unity beamforming can be an option to process multi-channel azimuth SAR data, mainly for the reason of robustness.

The second method is the MVDR beamformer according to equation (4.53)

$$\boldsymbol{w}_{\mathrm{az}}^{*}(k_y) = \frac{\boldsymbol{R}_{\boldsymbol{v}}^{-1}(k_y) \boldsymbol{a}_{\mathrm{az}}(\vartheta)}{\boldsymbol{a}_{\mathrm{az}}^{\mathsf{H}}(\vartheta) \boldsymbol{R}_{\boldsymbol{v}}^{-1}(k_y) \boldsymbol{a}_{\mathrm{az}}(\vartheta)} \,. \tag{4.105}$$

This beamformer minimizes the additive noise contributions over the wavenumber spectrum generating therefore the optimal *SNR*. However, since this beamformer only considers the direction of interest, the ambiguous spectra are not suppressed. In the worst case they might even be amplified.

As mentioned above, at any wavenumber not only the signal of interest is present but also ambiguous signals (see Fig. 4.16b). The opportunity to suppress these ambiguities is offered by LCMV beamforming (4.61) as a function of wavenumbers

$$\boldsymbol{w}_{\mathrm{az}}^{*}(k_y) = \left(\boldsymbol{R}_{\boldsymbol{v}}^{-1} \boldsymbol{A} \left(\boldsymbol{A}^{\mathsf{H}} \boldsymbol{R}_{\boldsymbol{v}}^{-1} \boldsymbol{A} \right)^{-1} \boldsymbol{c}^{*} \right)(k_y) \quad . \tag{4.106}$$

[6] As in the elevation case the azimuth *SNR* formula (4.103) follows from a one-dimensional consideration. Insofar here the range processing gain is not present. However, as argued before, in the context of digital beamforming not the absolute but the relative performances are of interest.

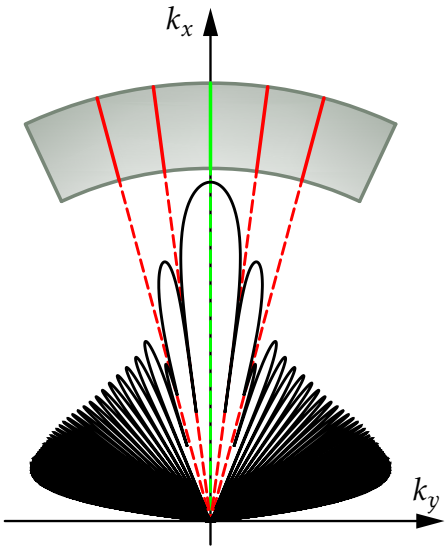

Figure 4.17: LCMV principle applied in the wavenumber domain. The LCMV beam is computed such that the signal of interest, indicated in green, is amplified, while ambiguous wavenumbers, marked in red, are damped.

The ambiguous directions ϑ_m are dictated by integer multiples of the sampling wavenumber K_y

$$k_y + mK_y = -2k \sin \vartheta_m \,, \quad m \in \mathbb{Z} \setminus \{0\} \,. \tag{4.107}$$

With this, the array response matrix $\boldsymbol{A}$ can be constructed according to

$$\boldsymbol{A} = \begin{bmatrix} \boldsymbol{a}_{\mathrm{az}}(k, \varphi_0, \vartheta_0) & \ldots & \boldsymbol{a}_{\mathrm{az}}(k, \varphi_m, \vartheta_m) & \ldots \end{bmatrix} \in \mathbb{C}^{N_y \times M+1} \,, \tag{4.108}$$

where M is the number of azimuth ambiguities to be suppressed. The LCMV principle applied in the azimuth wavenumber domain is illustrated in Fig. 4.17.

By definition MVDR beamforming preserves the signal undistorted. However, this is not true for unity and LCMV beamforming. The signal wavenumber spectrum after digital beamforming, $U_{\mathrm{DBF}}(k_y)$, will have a complex modulation due to the patterns. For unity beamforming this complex function takes the form

$$\boldsymbol{w}_{\mathrm{az}}^{\mathrm{T}}(k_y) \boldsymbol{a}_{\mathrm{az}}(k_y) = \max_{i,k_y} \{a_{\mathrm{az},i}(k_y)\} \,, \quad i \in [1, N_y] \,, \quad |k_y| \leq \frac{K_y'}{2} \,, \tag{4.109}$$

where $a_{\mathrm{az},i}$ is the azimuth antenna pattern with the maximum gain for each

wavenumber. Similarly the complex envelope with LCMV beamforming equates

$$\boldsymbol{w}_{\mathrm{az}}^{\mathsf{T}}(k_y)\boldsymbol{a}_{\mathrm{az}}(k_y) = \boldsymbol{c}^{\mathsf{T}}\left(\boldsymbol{A}^{\mathsf{H}}\boldsymbol{R}_{\boldsymbol{v}}^{-1}\boldsymbol{A}\right)^{-1\mathsf{H}}\boldsymbol{A}^{\mathsf{H}}\boldsymbol{R}_{\boldsymbol{v}}^{-1\mathsf{H}}\boldsymbol{a}_{\mathrm{az}}\,, \quad |k_y| \leq \frac{K_y'}{2}\,. \tag{4.110}$$

In order to achieve a flat signal spectrum one could define a filter which is inversely proportional to the pattern after beamforming

$$H_{\mathrm{DBF}}(k_y) = \frac{1}{\boldsymbol{w}_{\mathrm{az}}^{\mathsf{T}}(k_y)\boldsymbol{a}_{\mathrm{az}}(k_y)}\,. \tag{4.111}$$

The phase and amplitude corrected azimuth spectrum would then be

$$H_{\mathrm{DBF}}(k_y)\cdot U_{\mathrm{DBF}}(k_y) = \frac{\boldsymbol{w}_{\mathrm{az}}^{\mathsf{T}}(k_y)\boldsymbol{U}_{\mathrm{az}}(k_y)}{\boldsymbol{w}_{\mathrm{az}}^{\mathsf{T}}(k_y)\boldsymbol{a}_{\mathrm{az}}(k_y)}\,. \tag{4.112}$$

This filter operation is uncritical, since no zeros in the beamforming pattern exist within the wavenumber band of interest, which would generate singularities. From a pure beamforming perspective this filtering is not crucial but might be of interest if the preservation of an ideal sinc-like SAR impulse response function is intended. The drawback of this method is a slight increase of the noise level as well as a small rise of the ambiguities.

Finally, the SAR image azimuth ambiguity-to-signal ratio, according to equation (4.44) for a multi-channel SAR system, can be written as[7]

$$AASR(\boldsymbol{r}) = \frac{\sum\limits_{m\in\mathbb{Z}\setminus\{0\}}\int_{K_y'}|g(k_y+mK_y,\boldsymbol{r}_m)\cdot\boldsymbol{w}_{\mathrm{az}}^{\mathsf{T}}\boldsymbol{a}_{\mathrm{az}}(k,\varphi_m,\vartheta_m)|^2\mathrm{d}k_y}{\int_{K_y'}|g(k_y,\boldsymbol{r})\cdot\boldsymbol{w}_{\mathrm{az}}^{\mathsf{T}}\boldsymbol{a}_{\mathrm{az}}(k,\varphi,\vartheta)|^2\mathrm{d}k_y} \tag{4.113}$$

If a filter according to equation (4.111) is applied this needs of course to be accounted for in the above *AASR* formula as well as in the *SNR* expression (4.103). Often in the literature a version of the *AASR* is presented where the signal spectrum $\boldsymbol{s}(k_y)$ is replaced by the antenna pattern $\boldsymbol{a}(k_y)$ [17]. This can be done if the denominator in the Green's function of equation (4.4) is neglected. Therefore, this approximation is a worst case estimate for the *AASR* for a zero-Doppler imaging geometry.

The block diagram in Fig. 4.18 shows the processing flow, where multiple azimuth channels are combined to a single raw data signal $u_{\mathrm{DBF}}(y)$, which can be processed with conventional SAR focusing routines.

[7] With the same reasoning as for the *RASR* formula (4.93) the signal energies are integrated incoherently in the *AASR* equation (4.113). Digital beamforming over a large azimuth aperture introduces significant mismatch with the azimuth processing filter with the consequence of smeared azimuth ambiguities.

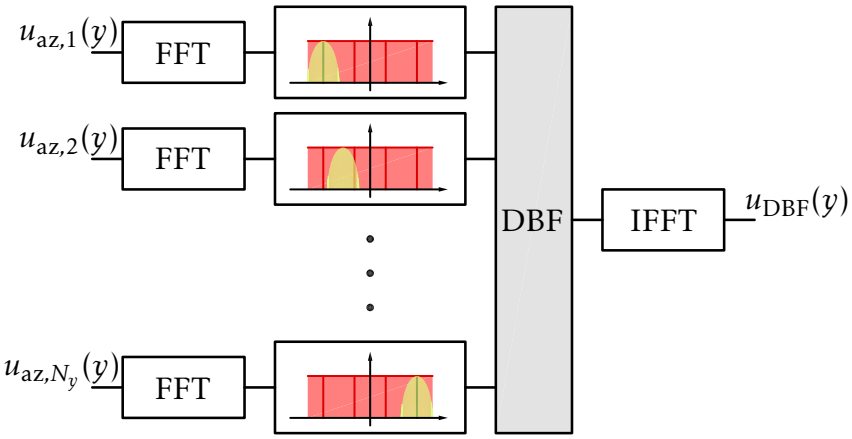

Figure 4.18: Block diagram showing the individual processing steps to form a single raw data signal $u_{\mathrm{DBF}}(y)$. The computation of the discrete Fourier transform according to equation (4.99) has been split up into two operations, that is after applying the FFT, the spectra of bandwidth K_y are juxtaposed and limited to the final bandwidth K_y'. After digital beamforming the signal in spatial domain is obtained by an inverse FFT.

4.4.3 Digital Beamforming for Polarimetric Applications

SAR systems with a single polarization channel are designed to retrieve the complex scattering coefficient $\hat{o}$ of a resolution cell. The polarization of an electromagnetic wave refers to the alignment of the electric field intensity vector $\boldsymbol{E}$ with respect to the direction of propagation. Commonly, SAR systems acquire data using linear or circular polarized waves, which are special cases of elliptically polarized waves. Since single polarization SAR systems do not provide any information about the vectorial character of the reflectivity function $\boldsymbol{o}(\boldsymbol{r})$, the conceptual idea of polarimetric SAR systems is to measure combinations of polarizations. These combinations are generated by accessing the SAR antenna via different polarization ports. A popular linear polarization basis consists of *horizontal* polarization, short 'h', and *vertical* polarization, short 'v'. A fundamental problem with real antennas is, if for instance the v-port of an antenna is switched, the actual electric field emitted by the antenna will not only have the desired v-component, but also an unwanted orthogonal h-component. In terms of antenna patterns the desired polarization would correspond to the co-polar pattern, while the unwanted component is determined by the cross-polar pattern. This means, polarimetric SAR data are always subject to contaminations from the cross-polar components of the antenna pattern. To mitigate the effects from those contaminations, polarimetric SAR data usually require cali-

bration [26]. SAR polarimetry, being already a mature technique for spaceborne SAR systems with planar antennas, has no heritage with reflector antenna based systems. Alone due to the geometrical conditions reflector antennas can be expected to produce larger cross-polar pattern components compared to direct radiating arrays. Moreover, depending on the technology, the feed array design might itself generate larger cross-polar patterns due to the dense packing of the feed elements. In the context of multi-channel reflector SAR systems therefore procedures shall be established, which allow to mitigate, or minimize, the effects of cross-polar patterns on the co-polar components.

Conceptually, polarimetry is covered by electromagnetic scattering theory. The basic equations in terms of the electric far field vectors can be stated according to [120]

$$\underline{\boldsymbol{E}}^{\mathrm{s}} = \frac{\mathrm{e}^{-\mathrm{j}kr}}{r}\boldsymbol{S}\underline{\boldsymbol{E}}^{\mathrm{i}} \,, \tag{4.114}$$

with superscripts 's' and 'i' denoting the scattered and the incident field, respectively. In order to distinguish field quantities, which are vector quantities, from matrices, using capital letters in both cases, the vector quantities are underlined. This equation is basically a simplified version of equation (2.14) for point targets in temporal frequency domain, where the pattern function $\boldsymbol{a}$ and the waveform p have been omitted in order to maintain a clear representation. The distance between sensor and target is r. $\boldsymbol{S}$ is the 2×2 complex scattering matrix , which can be written for the h-v-polarization basis as[8]

$$\boldsymbol{S} = \begin{bmatrix} s_{\mathrm{hh}} & s_{\mathrm{hv}} \\ s_{\mathrm{vh}} & s_{\mathrm{vv}} \end{bmatrix} . \tag{4.115}$$

This scattering principle applied to the ith transmit antenna would result in

$$\underline{\boldsymbol{E}}_{\mathrm{out},i} = \boldsymbol{T}_i \underline{\boldsymbol{E}}_{\mathrm{in},i} = \begin{bmatrix} E_{\mathrm{h}} \\ E_{\mathrm{v}} \end{bmatrix}_{\mathrm{out},i} = \begin{bmatrix} t_{\mathrm{co,h}} & t_{\mathrm{cx,v}} \\ t_{\mathrm{cx,h}} & t_{\mathrm{co,v}} \end{bmatrix}_i \begin{bmatrix} E_{\mathrm{h}} \\ E_{\mathrm{v}} \end{bmatrix}_{\mathrm{in},i} . \tag{4.116}$$

In this context $\underline{\boldsymbol{E}}_{\mathrm{in},i}$ should not be interpreted as electric field intensity vector, but rather as input voltage at the antenna terminals. In the following $\underline{\boldsymbol{E}}_{\mathrm{in},i}$ is treated as a vector of two dimensionless excitation quantities in order to keep the notation simple. The transmit antenna transfer function $\boldsymbol{T}_i$ contains four elements, where for example $t_{\mathrm{co,h}}$ refers to the co-polar pattern, with a stimulus in the h-polarization channel. That means, if for instance a h-polarized wave shall be emitted,

$$\underline{\boldsymbol{E}}_{\mathrm{in},i} = \begin{bmatrix} 1 & 0 \end{bmatrix}^{\mathsf{T}} \,, \tag{4.117}$$

[8] Following the notation in polarimetric literature the scattering coefficients are denoted with s, in contrast to equation (2.14) where the symbol o has been used.

then the actual radiated far field

$$\begin{bmatrix} E_{\mathrm{h}} \\ E_{\mathrm{v}} \end{bmatrix}_{\mathrm{out},i} = \begin{bmatrix} t_{\mathrm{co,h}} & t_{\mathrm{cx,v}} \\ t_{\mathrm{cx,h}} & t_{\mathrm{co,v}} \end{bmatrix}_i \begin{bmatrix} 1 \\ 0 \end{bmatrix} = \begin{bmatrix} t_{\mathrm{co,h}} \\ t_{\mathrm{cx,h}} \end{bmatrix}_i \tag{4.118}$$

contains a co-polar as well as a cross-polar field component. Expanding this principle to the complete transmit-receive chain, for all four polarization combinations, the ith channel of the multi-channel system equates

$$\boldsymbol{U}_i = g\boldsymbol{R}_i\boldsymbol{S}\boldsymbol{T}_i + \boldsymbol{V}_i \ . \tag{4.119}$$

This notation essentially is the polarimetric generalization of equation (4.34), with the kernel g defined via equation (4.4) and $\boldsymbol{V}_i$ describing the additive thermal noise contribution. In order to focus on the conceptual idea, range ambiguities are excluded in the following derivation. Generally, in polarimetric applications the matrices $\boldsymbol{T}_i$ and $\boldsymbol{R}_i$ represent the transfer functions of the entire transmit and receivepath, respectively. However, here in the beamforming context, these matrices shall exclusively refer to the transmit and receive characteristics of the antenna channels, represented by the corresponding patterns. Expanding equations (4.119) yields

$$\begin{bmatrix} u_{\mathrm{hh}} & u_{\mathrm{hv}} \\ u_{\mathrm{vh}} & u_{\mathrm{vv}} \end{bmatrix}_i = g \begin{bmatrix} r_{\mathrm{co,h}} & r_{\mathrm{cx,v}} \\ r_{\mathrm{cx,h}} & r_{\mathrm{co,v}} \end{bmatrix}_i \begin{bmatrix} s_{\mathrm{hh}} & s_{\mathrm{hv}} \\ s_{\mathrm{vh}} & s_{\mathrm{vv}} \end{bmatrix} \begin{bmatrix} t_{\mathrm{co,h}} & t_{\mathrm{cx,v}} \\ t_{\mathrm{cx,h}} & t_{\mathrm{co,v}} \end{bmatrix}_i + \begin{bmatrix} v_{\mathrm{h}} & v_{\mathrm{h}} \\ v_{\mathrm{v}} & v_{\mathrm{v}} \end{bmatrix}_i \ . \tag{4.120}$$

Computing for instance the raw data signal $u_{\mathrm{hh},i}$ in the ith h-polarization channel

$$\begin{aligned} u_{\mathrm{hh},i} = g(&r_{\mathrm{co,h}} s_{\mathrm{hh}} t_{\mathrm{co,h}} + r_{\mathrm{cx,v}} s_{\mathrm{vh}} t_{\mathrm{co,h}} \\ &+ r_{\mathrm{co,h}} s_{\mathrm{hv}} t_{\mathrm{cx,h}} + r_{\mathrm{cx,v}} s_{\mathrm{vv}} t_{\mathrm{cx,h}})_i + v_{\mathrm{h},i} \ , \end{aligned} \tag{4.121}$$

one can observe, that the scattering coefficients are coupled via the individual antenna patterns. Note, inside the brackets the index i shall refer to the antenna transfer functions only. Clearly, the individual scattering coefficients are retrieved undistorted, if the antenna exhibits no cross-polar pattern components. In this case the equations would simplify to

$$u_{\mathrm{hh},i} = g(r_{\mathrm{co,h}} s_{\mathrm{hh}} t_{\mathrm{co,h}})_i + v_{\mathrm{h},i} \ , \tag{4.122}$$

possessing essentially the same structure as given in equation (4.34), except the range ambiguity term. Insofar the task of digital beamforming in the context of polarimetric applications is, first, to decouple the scattering coefficients and second, to minimize the thermal noise contributions using the array manifold.

The decoupling of the scattering coefficients can be achieved by multiplying equations (4.119) from left and from right with the inverse pattern transfer functions $\boldsymbol{R}^{-1}$ and $\boldsymbol{T}^{-1}$, respectively, giving

$$\boldsymbol{U}_i' \equiv \boldsymbol{R}_i^{-1}\boldsymbol{U}_i\boldsymbol{T}_i^{-1} = g\boldsymbol{S} + \boldsymbol{R}_i^{-1}\boldsymbol{V}_i\boldsymbol{T}_i^{-1} = g\boldsymbol{S} + \boldsymbol{V}_i' \,, \tag{4.123}$$

with the inverse matrices

$$\boldsymbol{R}_i^{-1} = \frac{1}{\det \boldsymbol{R}_i}\begin{bmatrix} r_{\mathrm{co,v}} & -r_{\mathrm{cx,v}} \\ -r_{\mathrm{cx,h}} & r_{\mathrm{co,h}} \end{bmatrix}_i \,, \text{ and } \boldsymbol{T}_i^{-1} = \frac{1}{\det \boldsymbol{T}_i}\begin{bmatrix} t_{\mathrm{co,v}} & -t_{\mathrm{cx,v}} \\ -t_{\mathrm{cx,h}} & t_{\mathrm{co,h}} \end{bmatrix}_i \,. \tag{4.124}$$

Now the new hh-polarization channel raw data signal for the ith antenna element takes the form

$$\begin{aligned} u_{\mathrm{hh},i}' = g s_{\mathrm{hh}} + v_{\mathrm{h},i}' = g s_{\mathrm{hh}} + \frac{1}{\det \boldsymbol{R}_i} \cdot \frac{1}{\det \boldsymbol{T}_i} \cdot (r_{\mathrm{co,v}} v_{\mathrm{h}} t_{\mathrm{co,v}} \\ - r_{\mathrm{cx,v}} v_{\mathrm{v}} t_{\mathrm{co,v}} - r_{\mathrm{co,v}} v_{\mathrm{h}} t_{\mathrm{cx,h}} + r_{\mathrm{cx,v}} v_{\mathrm{v}} t_{\mathrm{cx,h}})_i \,. \end{aligned} \tag{4.125}$$

Comparing equations (4.121) and (4.125) it becomes clear that the coupling of the scattering coefficients effectively has been transferred into a coupling of the thermal noise contributions. Finally, the individual raw data signals $u_{\mathrm{hh},i}'$ can be combined in the usual vector notation according to

$$\boldsymbol{u}_{\mathrm{hh}}' = g s_{\mathrm{hh}} \mathbf{1} + \boldsymbol{v}_{\mathrm{h}}' \,, \tag{4.126}$$

where the vector $\mathbf{1}$ is given as

$$\mathbf{1} = \begin{bmatrix} 1 & 1 & \dots & 1 \end{bmatrix}^{\mathsf{T}} \in \mathbb{N}^{N_{\mathrm{c}} \times 1} \,, \tag{4.127}$$

with N_{c} the size of the array manifold. The beamforming operation in the hh-polarization is then the combination of the individual channels by means of weights

$$u_{\mathrm{DBF,hh}}' = \boldsymbol{w}_{\mathrm{hh}}^{\mathsf{T}} (g s_{\mathrm{hh}} \mathbf{1} + \boldsymbol{v}_{\mathrm{h}}') \,. \tag{4.128}$$

Using a beamforming approach, which minimizes the thermal noise contributions, the power expression of equation (4.128) is

$$\mathcal{E}\{u_{\mathrm{DBF,hh}}'\} = \mathcal{E}\{|s_{\mathrm{hh}}|^2\} |g \cdot \boldsymbol{w}_{\mathrm{hh}}^{\mathsf{T}} \mathbf{1}|^2 + \boldsymbol{w}_{\mathrm{hh}}^{\mathsf{T}} \mathcal{E}\{\boldsymbol{v}_{\mathrm{h}}' \boldsymbol{v}_{\mathrm{h}}'^{\mathsf{H}}\} \boldsymbol{w}_{\mathrm{hh}}^{*} \tag{4.129}$$

$$= \sigma_{s_{\mathrm{hh}}}^2 |g \cdot \boldsymbol{w}_{\mathrm{hh}}^{\mathsf{T}} \mathbf{1}|^2 + \boldsymbol{w}_{\mathrm{hh}}^{\mathsf{T}} \boldsymbol{R}_{\mathrm{hh},v'} \boldsymbol{w}_{\mathrm{hh}}^{*} \,. \tag{4.130}$$

With this, the problem of finding a weight vector is traced back to the MVDR optimization problem, as described in appendix D, according to

$$\text{minimize} \quad \boldsymbol{w}_{\mathrm{hh}}^{\mathsf{T}} \boldsymbol{R}_{\mathrm{hh},v'} \boldsymbol{w}_{\mathrm{hh}}^{*} \tag{4.131}$$

$$\text{subject to} \quad \boldsymbol{w}_{\mathrm{hh}}^{\mathsf{T}} \mathbf{1} = 1 \,, \tag{4.132}$$

with the solution

$$\boldsymbol{w}_{\mathrm{hh}}^{*} = \frac{\boldsymbol{R}_{\mathrm{hh},\boldsymbol{v}'}^{-1}\mathbf{1}}{\mathbf{1}^{\top}\boldsymbol{R}_{\mathrm{hh},\boldsymbol{v}'}^{-1}\mathbf{1}} \,. \tag{4.133}$$

Of course the inner structure of $\boldsymbol{R}_{\mathrm{hh},\boldsymbol{v}'}$ is more complicated compared to the standard case. The ilth element $r_{\mathrm{hh},il}$ of $\boldsymbol{R}_{\mathrm{hh},\boldsymbol{v}'}$ equates

$$\begin{aligned} r_{\mathrm{hh},il} &= \frac{1}{\det \boldsymbol{R}_i} \cdot \frac{1}{\det \boldsymbol{T}_i} \cdot \frac{1}{(\det \boldsymbol{R}_l)^*} \cdot \frac{1}{(\det \boldsymbol{T}_l)^*} \\ &\quad \cdot \mathcal{E}\{(r_{\mathrm{co,v}} v_{\mathrm{h}} t_{\mathrm{co,v}} - r_{\mathrm{cx,v}} v_{\mathrm{v}} t_{\mathrm{co,v}} - r_{\mathrm{co,v}} v_{\mathrm{h}} t_{\mathrm{cx,h}} + r_{\mathrm{cx,v}} v_{\mathrm{v}} t_{\mathrm{cx,h}})_i \\ &\quad \cdot (r_{\mathrm{co,v}} v_{\mathrm{h}} t_{\mathrm{co,v}} - r_{\mathrm{cx,v}} v_{\mathrm{v}} t_{\mathrm{co,v}} - r_{\mathrm{co,v}} v_{\mathrm{h}} t_{\mathrm{cx,h}} + r_{\mathrm{cx,v}} v_{\mathrm{v}} t_{\mathrm{cx,h}})_l^*\} \qquad (4.134) \\ &= \frac{1}{|\det \boldsymbol{R}|^2} \cdot \frac{1}{|\det \boldsymbol{T}|^2} \\ &\quad \cdot (|r_{\mathrm{co,v}}|^2 \sigma_{v_{\mathrm{h}}}^2 |t_{\mathrm{co,v}}|^2 + |r_{\mathrm{cx,v}}|^2 \sigma_{v_{\mathrm{v}}}^2 |t_{\mathrm{co,v}}|^2 \\ &\quad + |r_{\mathrm{co,v}}|^2 \sigma_{v_{\mathrm{h}}}^2 |t_{\mathrm{cx,h}}|^2 + |r_{\mathrm{cx,v}}|^2 \sigma_{v_{\mathrm{v}}}^2 |t_{\mathrm{cx,h}}|^2)\big|_{i=l} \,, \qquad (4.135) \end{aligned}$$

if uncorrelated noise is assumed. This procedure applies in an analogous way to the three other polarization combinations vh, hv and vv.

Figure 4.19 shows a block diagram of this polarimetric beamforming concept. Usually, within the feed array of a reflector SAR system, the h- and v-antenna feed elements are combined in a single radiator, as for example with a patch antenna. Principally, this beamforming method is applicable to both elevation feed arrays and to azimuth arrays. Clearly, the efficiency of such a concept is based on an accurate knowledge of the cross-pol patterns, which might be, as stated in the beginning, substantially larger compared to the planar array case. In any case, due to the focusing effect of reflector antennas, the cross-polarized patterns will be of very low gain compared to the co-polarized patterns. Therefore, one might restrict this spatial processing principle to a few sidelobes. Another consequence is, that the application of the LCMV algorithm taking into account the cross-pol patterns to suppress ambiguities far away from the main beam, is likely not possible at all, simply because these cross-polarized patterns cannot be measured accurately enough.

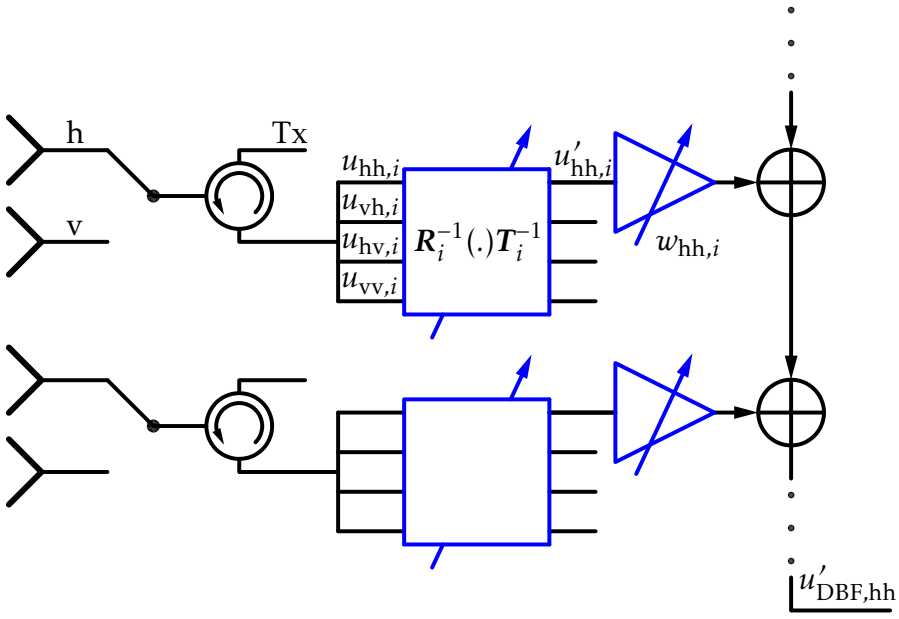

Figure 4.19: Polarimetric beamforming scheme on receive. The polarization switch toggles between the h-antenna and the v-antenna. All four polarization combinations are recorded and multiplied with the inverse transmit- and receive pattern transfer functions $\boldsymbol{T}_i$ and $\boldsymbol{R}_i$, respectively, in order to decouple the scattering coefficients. Finally, to minimize the thermal receiver noise, MVDR weights $\boldsymbol{w}$ are applied on each polarization channel.

5 Reflector SAR System Design Example

In chapter 4 the concept of multi-channel reflector SAR systems has been introduced. General signal processing schemes have been discussed, applicable to multi-channel reflector SAR systems, on the basis of selected beamforming algorithms. In the following, these signal processing methods shall be demonstrated on a concrete reflector design example. However, before demonstrating the performances of such reflector SAR systems, compact design equations, allowing to derive the size of the reflector antenna as well as the size of feed array, shall be given. These equations establish the link to the SAR imaging geometry which are finally necessary to design a SAR mission with reflector antenna systems.

5.1 Reflector Design Equations

The design of a SAR system and specifically the dimensioning of the SAR antenna can be regarded as an optimization process where most parameters depend on each other in a nonlinear way. Instead of solving a complicated mathematical problem here simple design formulas for a paraboloidal reflector antenna in offset configuration with elliptical aperture area shall be provided. As in the case of planar array antennas, it is useful to separate the design process in azimuth and elevation. A possible set of input parameters, distinguished into instrument related parameters, geometrical conditions and antenna characteristics, is listed in Table 5.1 for a specific design example.

Among the instrument parameters the pulse duty cycle dc is not required in the design process itself but it is important for the timing considerations. Probably the most critical parameter for a SAR design is the pulse repetition frequency PRF. Generally, the PRF affects the azimuth ambiguity-to-signal ratio $AASR$ and the range ambiguity-to-signal ratio $RASR$ in the opposite direction. Increasing the PRF improves the $AASR$ while the range ambiguity level will rise and vice versa. Since wide-swath SAR operation requires low PRFs, the $AASR$ will put a lower bound to potential PRFs. In terms of SAR antenna dimensions, the minimum PRF as well as the maximum PRF are constrained by what is called in [18] the antenna diffraction limit which refers to the half-power beamwidth, or 3 dB beamwidth, respectively. As introduced with equa-

	parameter	symbol	value
geometry	orbit height	h_s	745 km
	minimum incident angle	$\theta_{i,min}$	25.2 °
	swath width	X	90 km
	azimuth resolution	Δy	0.8 m
inst.	center frequency	f_c	9.65 GHz
	pulse duty cycle	dc	0.1
	minimum PRF	PRF_{min}	2800 Hz
antenna	maximum antenna gain	G_{max}	57.12 dB
	feed element spacing in elevation	Δx_f	$0.6\,\lambda$
	feed element spacing in azimuth	Δy_f	$0.6\,\lambda$
	F-over-D ratio	α_f	0.7
	design factor	α	1.38
	aperture efficiency	η_{ap}	0.8

Table 5.1: Input parameters for the design of a multi-channel reflector antenna SAR system.

tion (3.12), the 3 dB beamwidth for center fed parabolic reflector antennas is

$$\Theta_{3dB} \approx 1.22\frac{\lambda}{D}\,, \tag{5.1}$$

with D the reflector diameter in elevation or in azimuth, respectively. This formula is valid if the reflector is properly illuminated by the feed, as outlined in chapter 3.1.2.

The azimuth signal, which is naturally a discrete signal, will have its ambiguous spectra spaced integer multiples of the PRF apart. Since the signal of interest is contained inside the 3 dB domain of the antenna beam, it has to be ensured that the PRF is chosen such that the ambiguous azimuth spectra are at least this 3 dB beamwidth spaced apart. Using equations (2.44), (2.46) and (5.1) this can be stated as

$$PRF \geq \frac{4v_y}{\lambda} \cdot \sin\left(\alpha \cdot \frac{\Theta_{3dB,az}}{2}\right) \gtrsim \alpha \cdot \frac{2.44v_y}{D_{az}}\,, \tag{5.2}$$

with the relative velocity v_y between the sensor and a target on ground. For spaceborne SAR systems an acceptable azimuth ambiguity-to-signal ratio is less then -20 dB. Therefore, the half-power beamwidth might be too optimistic as criterion for the PRF choice. Additionally, off-focus patterns will be inherently defocused. All these effects are accounted for with the factor α, $\alpha \geq 1$.

A similar consideration on range ambiguities leads to an upper bound for the PRF depending on the antenna diameter in elevation D_{el}. Here, the critical

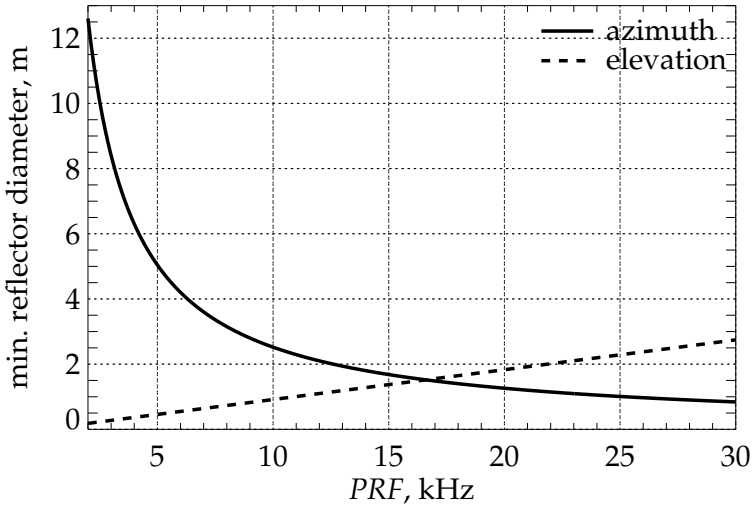

Figure 5.1: Minimal reflector diameters in azimuth and elevation versus *PRF*. These curves are computed from inequalities (5.4) based on the parameters given in Table 5.1.

situation occurs in far range, where the direction of the range ambiguities are closer to the direction of the signal than in near range. The upper bound can be found to be

$$PRF \lesssim \frac{c}{4r_{\max}\sin(\alpha\cdot\Theta_{3\mathrm{dB,el}}/4)\tan\theta_{\mathrm{i,max}}} \approx \frac{c\cdot D_{\mathrm{el}}}{1.22r_{\max}\cdot\alpha\cdot\lambda\cdot\tan\theta_{\mathrm{i,max}}}\,, \quad (5.3)$$

where $\theta_{\mathrm{i,max}}$ is the maximum incident angle in far range and $r_{\max}$ the corresponding maximum distance (see Fig. 3.11). Note, for pulsed SAR systems the timing puts a much stronger constraint, since a to high *PRF* would allow to acquire very narrow swaths. Rewriting both inequalities (5.2) and (5.3) according to

$$\alpha\cdot\frac{2.44v_y}{D_{\mathrm{az}}} \lesssim PRF \lesssim \frac{c\cdot D_{\mathrm{el}}}{1.22r_{\max}\cdot\alpha\cdot\lambda\cdot\tan\theta_{\mathrm{i,max}}} \quad (5.4)$$

makes clear that the usable *PRF*s are physically constrained by the reflector dimensions and the imaging geometry. These inequalities are illustrated graphically in Fig. 5.1 based on the example system specified in Table 5.1.

Concerning the antenna related input parameters in Table 5.1 the theoretical maximum gain

$$G_{\max} = 4\pi\frac{A_{\mathrm{eff}}}{\lambda^2} \approx \eta_{\mathrm{ap}}\pi^2\frac{D_{\mathrm{az}}D_{\mathrm{el}}}{\lambda^2} \quad (5.5)$$

can be used to balance the reflector design. Here, the effective antenna area A_{eff} is approximated with the physical projected aperture area for an elliptical reflector cross section. The aperture efficiency η_{ap} accounts for spillover and taper effects, as described by equations (3.8) and (3.9). To derive a useful value for the focal length F, the diameter D of an equivalent circular aperture reflector could be taken simply by setting $D = D_{\mathrm{az}} = D_{\mathrm{el}}$ in equation 5.5 and solving for D

$$D = \frac{\lambda}{\pi}\sqrt{\frac{G_{\max}}{\eta_{\mathrm{ap}}}}\,. \tag{5.6}$$

Then for a given focal ratio α_{f}

$$\alpha_{\mathrm{f}} \equiv \frac{F}{D}\,, \tag{5.7}$$

the focal length F for an elliptic aperture reflector can be calculated. A larger focal ratio means a flatter reflector shape, which is generally better suited in conjunction with feed arrays, since here the impact of the defocusing effect for border area elements will be moderate.

The angular Doppler domain in azimuth $\Theta_{\mathrm{3dB,az,Tx}}$ and the scan range in elevation $\Theta_{\mathrm{3dB,el,Tx}}$ determine the overall feed array size Y_{f} and X_{f}, respectively, as illustrated in Fig. 5.2. The spacing between feed elements Δx_{f} and Δy_{f} should be so small that adjacent channel patterns have a sufficient angular overlap, but large enough that coupling effects can be tolerated. As rule of thumb the element spacing is such that the electrical size of the apertures of adjacent feed elements touch each other.

The SAR imaging geometry can be described by the orbit height h_{s}, the minimum incident angle $\theta_{\mathrm{i,min}}$ and the swath width X. More precisely, the swath width is the arc length, assuming a spherical Earth model. Especially the orbit height and the swath width are of importance, since they determine the repeat cycle. Shorter revisit times can be achieved with higher orbits, if the elevation scan range is kept constant, which in turn requires larger antennas or a higher transmit power in order to compensate the loss of signal power due to the larger distance between sensor and swath. The spatial resolutions in azimuth Δy and ground range Δr_{g} are principally independent. However, a quadratic resolution cell is often advantageous.

In the following two chapters, simple reflector and feed array design equations based on ray optical considerations are derived. These equations allow to arrive at a first rough reflector SAR antenna design.

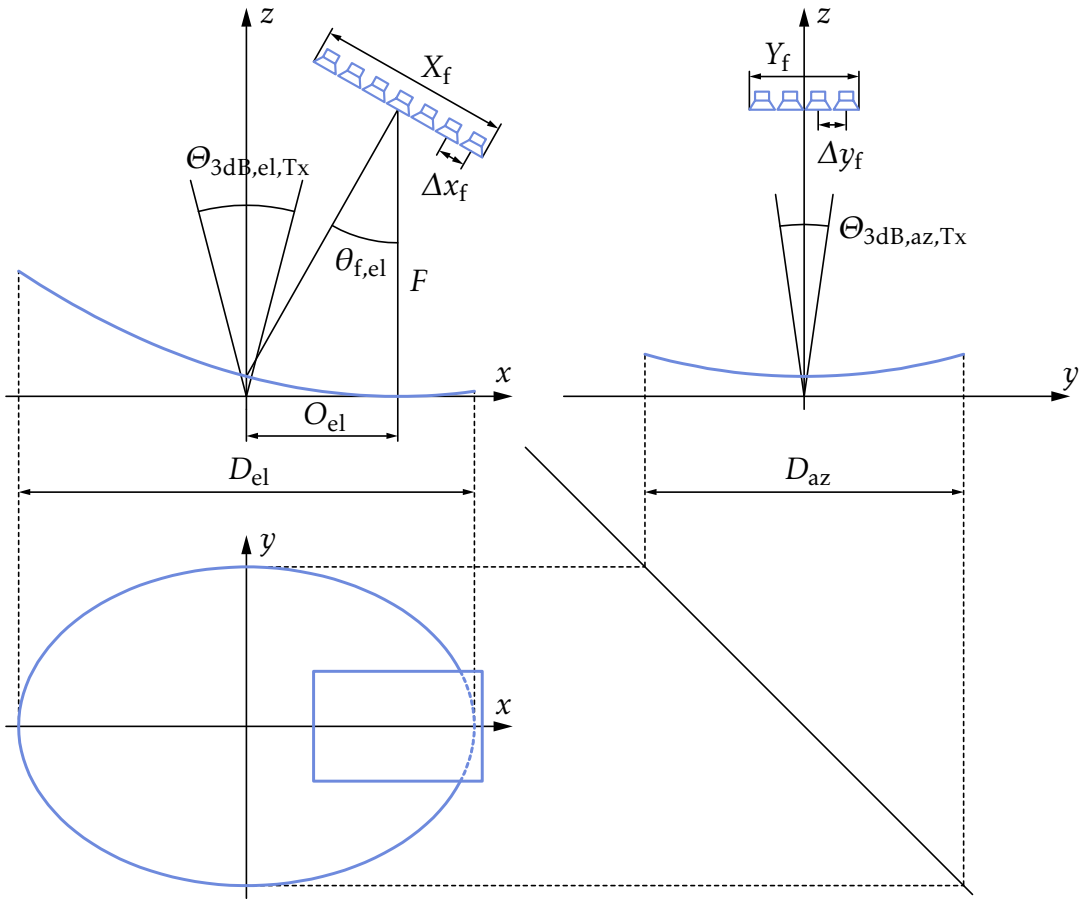

Figure 5.2: Cut drawing of an elliptic aperture reflector antenna with feed array in three normal projections. Here, an offset configuration in elevation is depicted.

5.1.1 Reflector and Feed Array Design in Azimuth

From a SAR mission perspective, the *AASR* and indirectly the swath width pose the main requirements on the size of the reflector in azimuth. However, at the same time other constraints, which limit the size of the antenna, need to be taken into account. The launcher puts an upper limit on the diameter of the reflector, which can be delivered to space. Another constraint is put by the data communication link from space to ground, determining the maximal data rate. Here, an approach is chosen which supports wide-swath acquisitions with a large number of azimuth channels sampled at a minimum *PRF*. In this case, the antenna aperture diameter in azimuth can be computed from equation (5.2)

yielding

$$D_{\mathrm{az}} = \alpha \cdot \frac{2.44 v_y}{PRF_{\mathrm{min}}} \,. \tag{5.8}$$

Note, the factor α relates to the broadening of the off-focus patterns which in turn affects the *AASR*. Depending on the frequency band, this diameter can be more than 100 wavelengths. The azimuth resolution yields the Doppler wavenumber domain to be processed according to

$$K_y' = \frac{2\pi}{\Delta y} \,. \tag{5.9}$$

Then the corresponding 3 dB azimuth angular domain can be computed according to

$$\Theta_{\mathrm{3dB,az,Tx}} = 2 \arcsin\left(\frac{K_y'}{4k}\right) \approx \frac{\lambda}{2\Delta y} \,, \tag{5.10}$$

with $k = 2\pi/\lambda$. Reflector antennas with feeds in offset configuration are widely used. These concepts are more immune to multipath effects occurring between the reflector and the feed array structure as well as the satellite bus. Although the gain loss due to blockage is negligible, these multipath effects can modulate the pattern over the frequency band of interest. Consequently, these effects can be reduced by moving the feed array out of this 3 dB transmit beamwidth. This can be realized by an offset in azimuth

$$O_{\mathrm{az}} \gtrsim 2F \tan\left(\frac{\Theta_{\mathrm{3dB,az,Tx}}}{2}\right) = \frac{2F}{\sqrt{(4\Delta y/\lambda)^2 - 1}} \,. \tag{5.11}$$

This formula represents rather a lower limit for the offset. However, too large offsets will result in a broadening of the patterns and an increase of the sidelobes. Using a ray optics approximation, the feed width in azimuth can then be expressed as

$$\begin{aligned} Y_{\mathrm{f}} \approx \sqrt{O_{\mathrm{az}}^2 + F^2} \cdot \sin\left(\frac{\Theta_{\mathrm{3dB,az,Tx}}}{2}\right) \\ \cdot \left(\frac{1}{\cos\left(\Delta\theta + \frac{\Theta_{\mathrm{3dB,az,Tx}}}{2}\right)} + \frac{1}{\cos\left(\Delta\theta - \frac{\Theta_{\mathrm{3dB,az,Tx}}}{2}\right)} \right) \,, \end{aligned} \tag{5.12}$$

with $\Delta\theta$ according to

$$\Delta\theta = 2 \arctan\left(\frac{O_{\mathrm{az}}}{2F}\right) - \arctan\left(\frac{O_{\mathrm{az}}}{F}\right) \,. \tag{5.13}$$

Formula (5.12) is relatively precise for center fed configurations, that is $O_{\mathrm{az}} = 0\,\mathrm{m}$, but becomes increasingly inaccurate for larger offsets and wide half-power beamwidths due to the defocusing effect. The feed is usually tilted towards the center of the reflector [84] by an angle of

$$\theta_{\mathrm{f,az}} = 2\arctan\left(\frac{O_{\mathrm{az}}}{2F}\right). \tag{5.14}$$

Concerning the number of feed elements there are several aspects to be considered. From an electrical point of view it might be sufficient to simply divide the feed length Y_{f} by the element spacing Δy_{f}, because due to the defocusing effect the patterns at the feed border will broaden and therefore grant a wider field of view. From a beamforming perspective it is, however, beneficial to have as many feed elements as possible in order to suppress ambiguities more efficiently and to avoid performance degradation in terms of *SNR*. Insofar a good starting value for the number of feed elements in azimuth is

$$N_y \approx \left\lceil \frac{Y_{\mathrm{f}} + \Delta y_{\mathrm{f}}}{\Delta y_{\mathrm{f}}} \right\rceil, \tag{5.15}$$

where $\lceil . \rceil$ denotes the ceiling operator. With respect to the feed array complexity and the data rate, one would keep the number of channels as low as possible by choosing a larger element spacing. Clearly this number can only be a first guess in the design process.

5.1.2 Reflector and Feed Array Design in Elevation

The diameter of the projected reflector aperture in elevation D_{el} must obey inequality (5.3), where the largest intended *PRF* has to be taken into account. Typically, there will be a formidable margin for the diameter, that means for any reasonable *PRF* choice the permitted elevation diameter will be larger than the azimuth diameter (see Fig. 5.1). An exception can be operation modes employing full polarization, where the *PRF* needs to be doubled. With the maximum antenna gain G_{max} as input parameter, equation (5.5) can be solved for the elevation diameter

$$D_{\mathrm{el}} \approx \frac{G_{\mathrm{max}}\lambda^2}{\eta_{\mathrm{ap}}\pi^2 D_{\mathrm{az}}}. \tag{5.16}$$

The beamwidth on transmit in elevation is determined by the imaging geometry. Assuming again a spherical Earth model with radius r_{e}, the half-power

beamwidth covering the swath on ground can be shown to be

$$\Theta_{\mathrm{3dB,el,Tx}} = \arctan\left(\frac{\sqrt{2}r_{\mathrm{e}}\sqrt{1-\cos\left(\frac{X}{r_{\mathrm{e}}}\right)}\cos\left(\frac{X}{2r_{\mathrm{e}}}+\theta_{\mathrm{i,min}}\right)}{r_{\mathrm{min}}+\sqrt{2}r_{\mathrm{e}}\sqrt{1-\cos\left(\frac{X}{r_{\mathrm{e}}}\right)}\sin\left(\frac{X}{2r_{\mathrm{e}}}+\theta_{\mathrm{i,min}}\right)}\right), \tag{5.17}$$

with $\theta_{\mathrm{i,min}}$ and r_{min} the minimum incident angle and slant range distance in near range, respectively (see Fig. 3.11). Equivalently an offset in elevation can be derived as

$$O_{\mathrm{el}} = 2F\tan\left(\frac{\Theta_{\mathrm{3dB,el,Tx}}}{2}\right), \tag{5.18}$$

as indicated in Fig. 5.2. It is important to note that for a given antenna design either an azimuth offset or an elevation offset is introduced. The subsequent feed array length is then

$$\begin{aligned} X_{\mathrm{f}} \approx{}& \sqrt{O_{\mathrm{el}}^2+F^2}\cdot\sin\left(\frac{\Theta_{\mathrm{3dB,el,Tx}}}{2}\right) \\ &\cdot\left(\frac{1}{\cos\left(\Delta\theta+\frac{\Theta_{\mathrm{3dB,el,Tx}}}{2}\right)}+\frac{1}{\cos\left(\Delta\theta-\frac{\Theta_{\mathrm{3dB,el,Tx}}}{2}\right)}\right), \end{aligned} \tag{5.19}$$

with $\Delta\theta$ according to

$$\Delta\theta = 2\arctan\left(\frac{O_{\mathrm{el}}}{2F}\right)-\arctan\left(\frac{O_{\mathrm{el}}}{F}\right). \tag{5.20}$$

The elevation feed tile angle is

$$\theta_{\mathrm{f,el}} = 2\arctan\left(\frac{O_{\mathrm{el}}}{2F}\right). \tag{5.21}$$

Finally, the number of feed elements in elevation should take into account performance degradation effects at the swath border, induced for instance due to defocusing. This justifies a larger number of elevation elements in the order of

$$N_x \approx \left\lceil\frac{X_{\mathrm{f}}+4\Delta x_{\mathrm{f}}}{\Delta x_{\mathrm{f}}}\right\rceil. \tag{5.22}$$

Again, this number requires revision during a thorough design process.

This set of compact equations allows to design the reflector antenna including the feed array for a spaceborne SAR mission. In the following, the SAR performance in the context of digital beamforming shall be presented on the basis of an example reflector system.

5.2 System Performance

The performance of a SAR system is assessed by means of the *SNR*, the *AASR*, the *RASR* and, depending on the SAR application, other parameters. Regarding the sensitivity of a SAR system, here the *SNR* shall be evaluated in a comparative way. This means, the *SNR* of beamforming method 'x' is related to a reference *SNR*

$$\Delta SNR_{\mathrm{x}} = \frac{SNR_{\mathrm{x}}}{SNR_{\mathrm{ref}}} \,, \tag{5.23}$$

where 'x' stands for the unity-, MVDR- or LCMV-beamforming approach, alternatively. As already mentioned, the complex reflector antenna patterns are computed using TICRA GRASP9 [118].

The performance is simulated on the basis of a X-band reflector SAR system orbiting 745 km above the Earth surface. The input parameters important for the antenna design are listed in Table 5.1. In this design example the SAR system shall cover a swath width X of 90 km. The swath is acquired at the minimum *PRF* of 2800 Hz as indicated in the timing diagram in Fig. 5.3. Transmit pulses are marked in blue and nadir returns are drawn in green. Without proper suppression nadir returns usually impose a restriction for planar array antennas. However, in the reflector antenna case, these radar echoes do not strictly prevent an acquisition of those areas. This is because of the inherent focusing capability of parabolic reflectors. Acquiring with different *PRF*s, it is in principle possible to extend the total coverable ground range region up to several hundred kilometers. Nevertheless for the purpose of demonstration a single swath shall be considered. For all geometrical computations an spherical Earth model is assumed, conform with the WGS-84 definitions [90].

With these inputs, using the design equations in the previous section, the result is a reflector SAR antenna, with the geometrical parameters summarized in Table 5.2. The reflector diameter in azimuth has been computed on the basis of equation (5.8). The elevation diameter is derived using equation (5.16), where the maximum gain has been used to balance the ratio of azimuth diameter to elevation diameter. With regard to the feed element design it might proof reasonable to avoid overly elliptical reflectors, since the illumination of such shapes would become more difficult. The transmit beamwidth in elevation and azimuth is guaranteed with 33 and 7 elements, respectively. In a scenario with multiple subswaths, simply additional feed elements in elevation would be required to cover a wider region on ground. Depending on the feed element spacing this number can be quite large. One strategy to reduce the hardware cost is to combine always two or even more adjacent feed elements, likewise in elevation or azimuth, in a single TR-module. The disadvantage of this approach

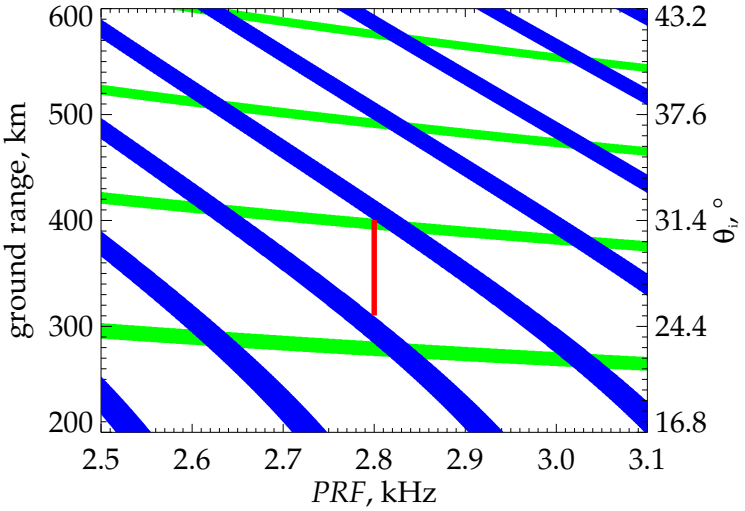

Figure 5.3: The timing diagram is plotted versus *PRF* and ground range, or incident angle θ_i on the right side, respectively. Here, the blue colored stripes indicate transmit events, while nadir returns are marked in green and the swath is drawn in red.

is that spatial diversity is sacrificed, reducing the effectiveness of digital beamforming. The other option would be to increase the feed element spacing itself, with the same negative effect on the flexibility of beamforming.

The performances are presented in elevation and azimuth separately, in concordance with chapters 4.4.1 and 4.4.2, respectively.

parameter	**symbol**	**value**
boresight angle wrt. nadir	θ_bore	25.13 °
transmit *HPBW* in elevation	$\Theta_\mathrm{3dB,el,Tx}$	5.44 °
transmit *HPBW* in azimuth	$\Theta_\mathrm{3dB,az,Tx}$	1.11 °
azimuth reflector diameter	D_az	9 m
elevation reflector diameter	D_el	7 m
focal length	F	5.55 m
elevation offset	O_el	0.6 m
no of elevation feed elements	N_x	33
no of azimuth feed elements	N_y	7

Table 5.2: Reflector and feed array design parameters.

5.2.1 Elevation Performance

In principle two sources for *SNR* degradation in the elevation beamforming process can be identified. The first source is spatial mismatch. Interpreting the array as a spatial filter, this kind of mismatch occurs if the array coefficients are not matched to the incident field. The second source is temporal mismatch, which refers to the waveform itself. In this case the received waveform after digital beamforming is not matched to the range compression filter, which is usually the time-inverted conjugate complex of the transmitted waveform. As outlined in chapter 4.4.1 a realtime beamforming concept needs to take into account the properties of the antenna, the spatial filter, as well as the characteristics of finite duration pulses, via temporal filter concepts.

Nevertheless, to gain insight in the spatial characteristics of a reflector antenna, it is useful to exclude real waveforms for the moment and instead assume Dirac-like pulses. This scenario can be understood as ideal reference case, or equivalently, as a beamforming approach with range compression before digital beamforming as sketched in chapter 4.2.2. In this case the *SNR* formula according to equation (4.89) writes

$$SNR(\vartheta) \sim \frac{|\boldsymbol{a}^{\mathsf{T}}(\vartheta)\boldsymbol{w}(\vartheta)|^2}{\boldsymbol{w}^{\mathsf{T}}\boldsymbol{R}_v\boldsymbol{w}^*} , \tag{5.24}$$

and with $\boldsymbol{R}_v \sim \mathbf{I}$ the *SNR* expressions for the three beamforming approaches given with equations (4.90), (4.91) and (4.92), neglecting all constant terms, reduce to

$$SNR_{\text{unity}}(\vartheta) \sim \frac{|\boldsymbol{a}^{\mathsf{T}}(\vartheta)\boldsymbol{w}(\vartheta)|^2}{N_{\text{act}}} , \tag{5.25}$$

$$SNR_{\text{MVDR}}(\vartheta) \sim \frac{1}{(\boldsymbol{a}^{\mathsf{H}}(\vartheta)\boldsymbol{a}(\vartheta))^{-1}} , \tag{5.26}$$

$$SNR_{\text{LCMV}}(\vartheta) \sim \frac{|\boldsymbol{a}^{\mathsf{T}}(\vartheta)\boldsymbol{w}(\vartheta)|^2}{\boldsymbol{c}^{\mathsf{T}}(\boldsymbol{A}^{\mathsf{H}}(\vartheta)\boldsymbol{A}(\vartheta))^{-1}\boldsymbol{c}^*} . \tag{5.27}$$

For a clear presentation the time variable n has been replaced by the elevation angle ϑ. Moreover, frequency independent antenna patterns $\boldsymbol{a} \neq f(k)$ are assumed. Since the pattern on transmit in equation (4.3) is synthesized such that it illuminates the complete swath, it does not contribute much to the beamformers. Insofar here only the patterns on receive $\boldsymbol{a} = \boldsymbol{a}_{\text{Rx}}$ shall be considered for the purpose of beamforming demonstration.

Relative *SNR* for Dirac-like Pulses

Figure 5.4 shows the elevation performance in terms of the relative *SNR* according to equation (5.23). The reference *SNR* is computed using the MVDR

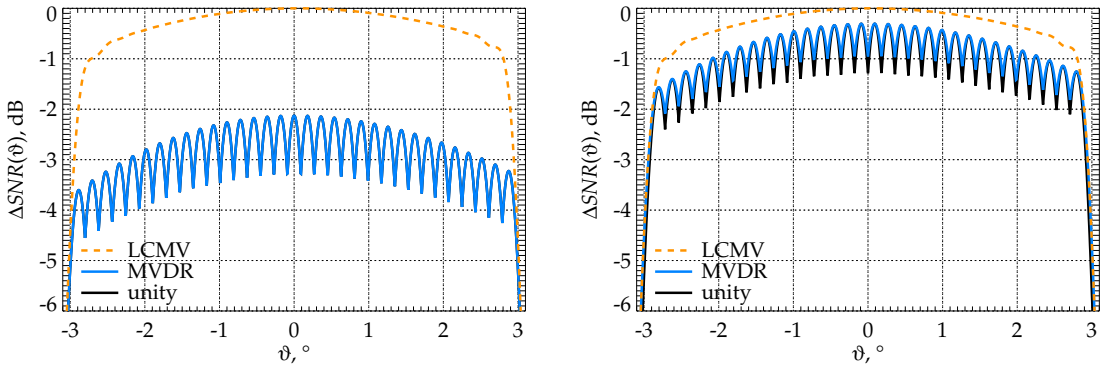

(a) $N_{\text{act}} = 1$

(b) $N_{\text{act}} = 2$

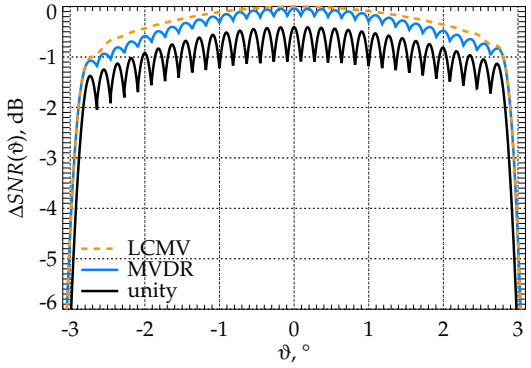

(c) $N_{\text{act}} = 3$

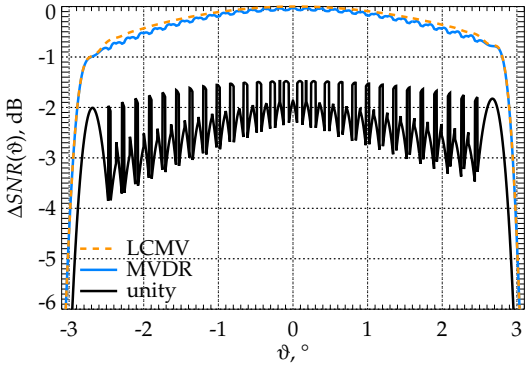

(d) $N_{\text{act}} = 4$

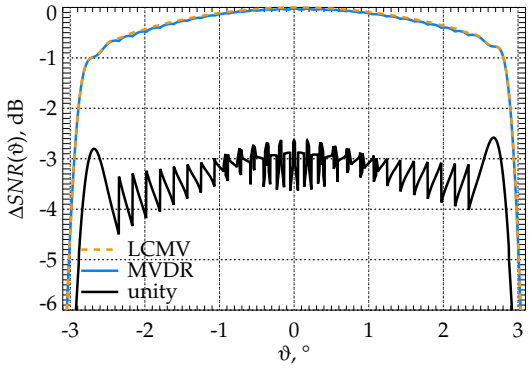

(e) $N_{\text{act}} = 5$

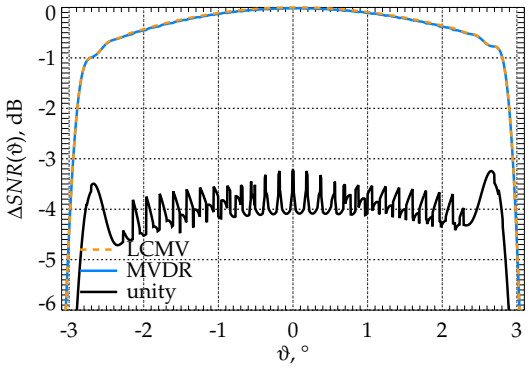

(f) $N_{\text{act}} = 6$

Figure 5.4: *SNR* for the individual beamformers normalized to the maximum *SNR* of the MVDR beamformer (all channels active), according to equation (5.23). In case of the LCMV method all channels are required in order to suppress range ambiguities effectively. Here, the effect of an increasing number of activated channels N_{act} is presented, assuming Dirac-like pulses ($dc = 0$).

beamformer with all elevation elements activated

$$SNR_{\text{ref}} = \max\left\{ \frac{1}{(\boldsymbol{a}^{\text{H}}(\vartheta)\boldsymbol{a}(\vartheta))^{-1}}\bigg|_{N_{\text{act}}=N_x} \right\} . \tag{5.28}$$

The parameter varied in the individual plots is the number of activated channels N_{act} ranging from a single channel in Fig. 5.4a to six activated elevation channels as presented in Fig. 5.4f. The exception is the LCMV beamformer which requires per definition as much channels as possible in order to damp range ambiguities successfully. As expected in the single-channel case in Fig. 5.4a the relative *SNR* for the unity beamformer is identical to the one of the MVDR beamformer being approximately 2 dB below the maximum. This is clearly not the optimal number of channels to be used for both concepts, unity beamforming as well as the MVDR beamforming. The optimum number of activated channels for the unity beamformer seems to be in the order of two or three as can be seen from the plots in Fig. 5.4b and 5.4c. Increasing the number of activated channels further results in successively lower *SNR* values as predicted by equation (5.25). Since the unity beamformer does use neither phase nor amplitude information, an objectionable effect are these characteristic discontinuities in the ΔSNR curves as can be observed in Fig. 5.4d to 5.4f. A further reason for these jumps is the channel activation law, whereby the channels with the highest gain in a specific direction are chosen. A consequence of this approach is that the activated channels need not necessarily be adjacent. In contrast the MVDR beamformer profits progressively by activating more channels due to its coherent nature. Another welcome effect is that the MVDR beamformer tends to smoothen the ripple like envelope of the antenna patterns resulting in flat relative *SNR* curves. The relative *SNR* curve for the LCMV beamformer has been computed to suppress range ambiguities occurring with a *PRF* of 2800 Hz as specified in Table 5.1.

Range Ambiguity-to-Signal Ratio

Even for larger *PRF*s LCMV beamforming in elevation might not be justified at all, when looking at the range ambiguity-to-signal ratios in Fig. 5.5. The *RASR* has been computed using equation (4.95) on the basis of a X-band soil & rock backscatter model [125] for vv-polarization as depicted in Fig. 5.5a. Although the LCMV beamformer is capable of reducing the range ambiguities on an average by another 15.2 dB compared to the MVDR beamformer and by 10.7 dB compared to unity beamforming, the worst case *RASR*, that means for large *PRF*s and in far range is already below -20 dB even for the unity beamformer. This is a consequence of the inherent focusing effect of reflector antennas, where

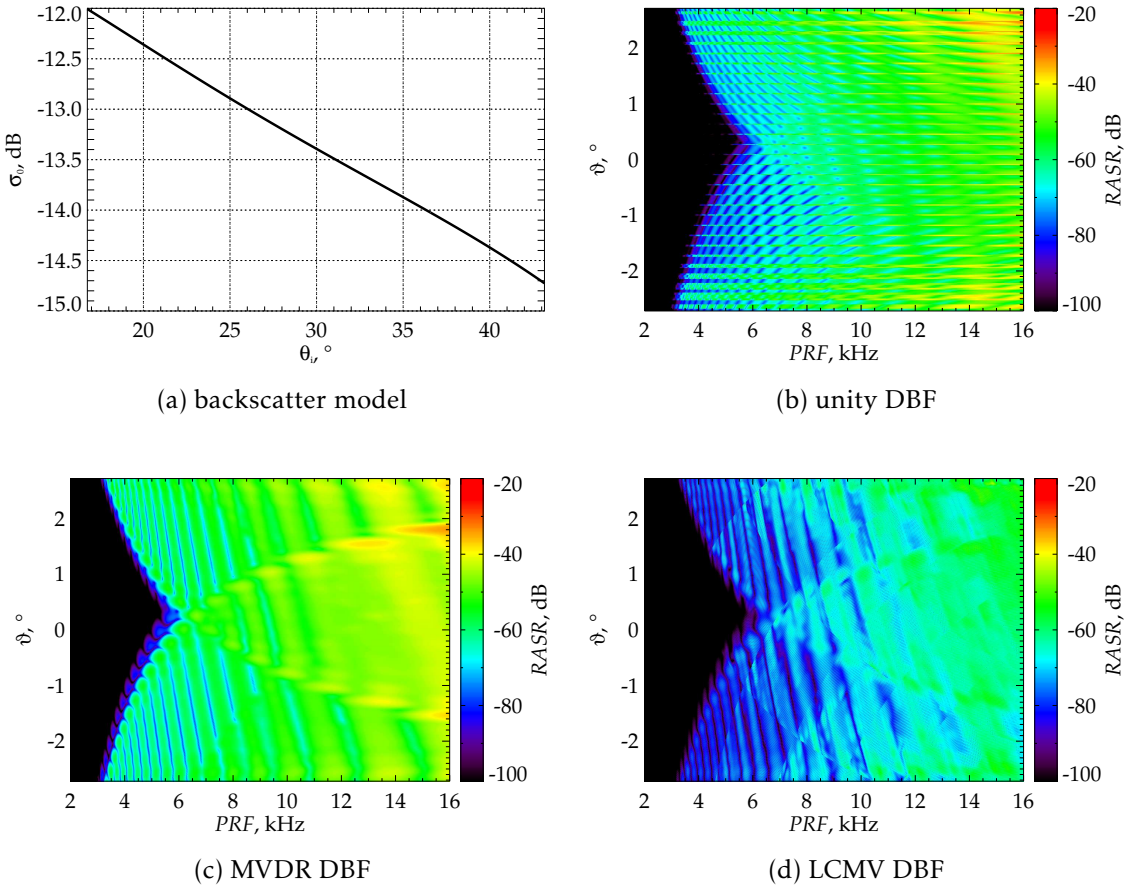

(a) backscatter model

(b) unity DBF

(c) MVDR DBF

(d) LCMV DBF

Figure 5.5: (a) soil & rock backscatter model for vv-polarization. (b)-(c) *RASR* for the three beamformers as function of the elevation scan angle ϑ and the *PRF*.

the sidelobes drop quickly, when moving away from the main beam. An example of patterns after digital beamforming for a *PRF* of 15.6 kHz is shown in Fig. 5.6 for unity, MVDR and LCMV beamforming. In the direction of the signal, indicated by the vertical green line, it can be observed that MVDR and LCMV beamforming outperform unity beamforming in terms of *SNR*. At the same time the LCMV beamformer suppresses range ambiguities, marked with red vertical lines. A scattering scenario not covered by this simple soil & rock model are nadir returns. If the signal is weak compared to the nadir echo the LCMV beamformer could proof useful for nadir suppression.

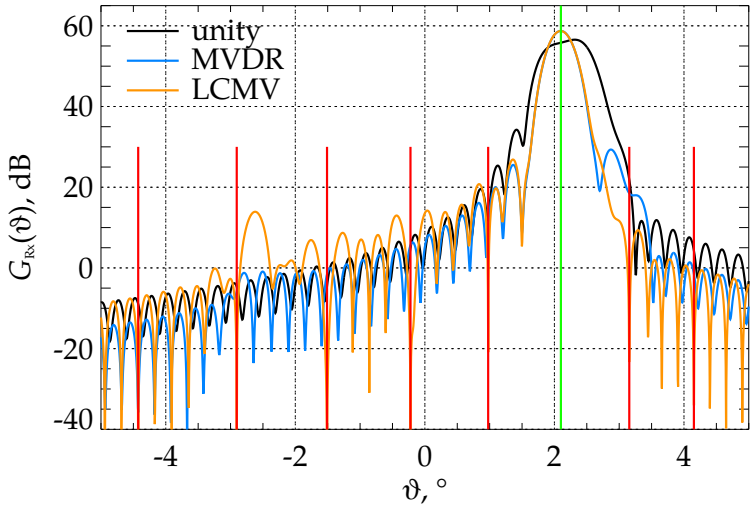

Figure 5.6: Patterns after digital beamforming. The direction of interest is indicated by the vertical green line, while range ambiguities are marked with red vertical lines. For demonstration purposes a relatively high *PRF* of 15.6 kHz has been chosen.

Performance with Extended Pulses

As initially mentioned, the second source of *SNR* degradation is temporal mismatch. This kind of degradation occurs if the temporal properties of the transmitted waveform are neglected in the beamforming process. With pulsed SAR systems typically the average transmit power is kept constant. This is the case if the pulse length τ_p relates to the *PRF* for a fixed pulse duty cycle *dc* according to

$$\tau_p = \frac{dc}{PRF} \,. \tag{5.29}$$

For the example system specified in Table 5.1 the pulse length is 35.7 µs. According to formula (3.23) this corresponds to an angular extent at the swath center of 0.68°, which is more then the double of the 3 dB elevation beamwidth of 0.31°. Insofar heavy losses can be expected if no waveform adaptive processing is applied. In the following simulations the channel activation law after equation (3.15), with $\alpha = 0.2$, has been utilized. At the swath center this results in a simultaneous activation of three channels, which proves to be optimal for the unity beamformer. The filter design $\boldsymbol{h}(n, n')$ in the time-variant beamforming operation (4.76) is mainly controlled by the number of subbands M and the number of FIR filter coefficients N_{coef}. For the unity beamformer the perfor-

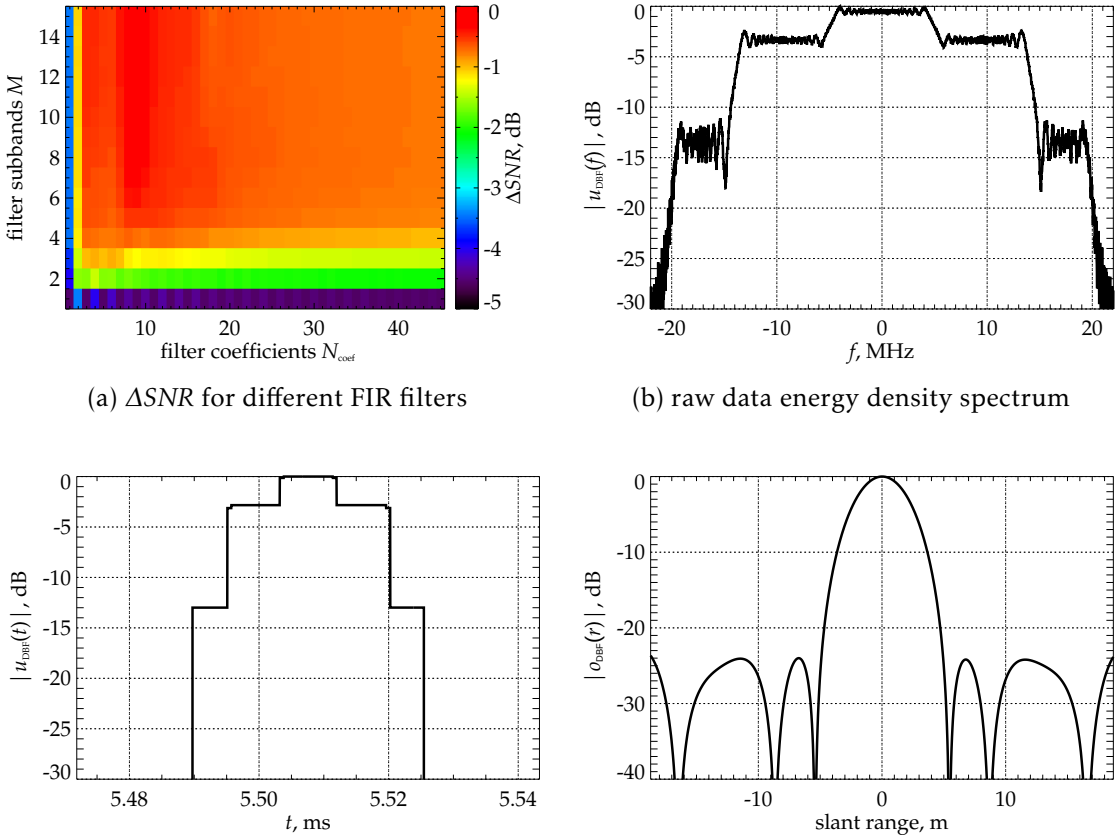

(a) ΔSNR for different FIR filters

(b) raw data energy density spectrum

(c) magnitude of the raw data signal

(d) SAR impulse response function

Figure 5.7: Performance for a time-variant unity beamforming approach using FIR filters. The point target is located at the swath center at $\vartheta = 0°$. (b), (c) Elevation beamformer output for $M = 1$ and $N_{\text{coef}} = 1$. (d) Corresponding range compressed SAR signal.

mance, taking into account the waveform, is shown in Fig. 5.7. This analysis is based on a point target simulation in the center of the swath at elevation angle $\vartheta = 0°$. The relative *SNR* is computed according to equation (4.87), where $\boldsymbol{R_v} = \sigma_v^2 \mathbf{I}$, with respect to the ideal MVDR beamforming approach, naturally producing the best *SNR*. Figure 5.7a shows the loss of *SNR*, induced by temporal and spatial mismatch. In the worst case, that is for a filter with a single subband M and a single filter coefficient N_{coef}, which is by definition a Dirac-like filter, the *SNR* loss is maximal. Figure 5.7c shows the magnitude of the normalized point target raw data signal for this case. Here, the amplitude modulation effect due to the channel switching, as outlined in chapter 3.3, becomes

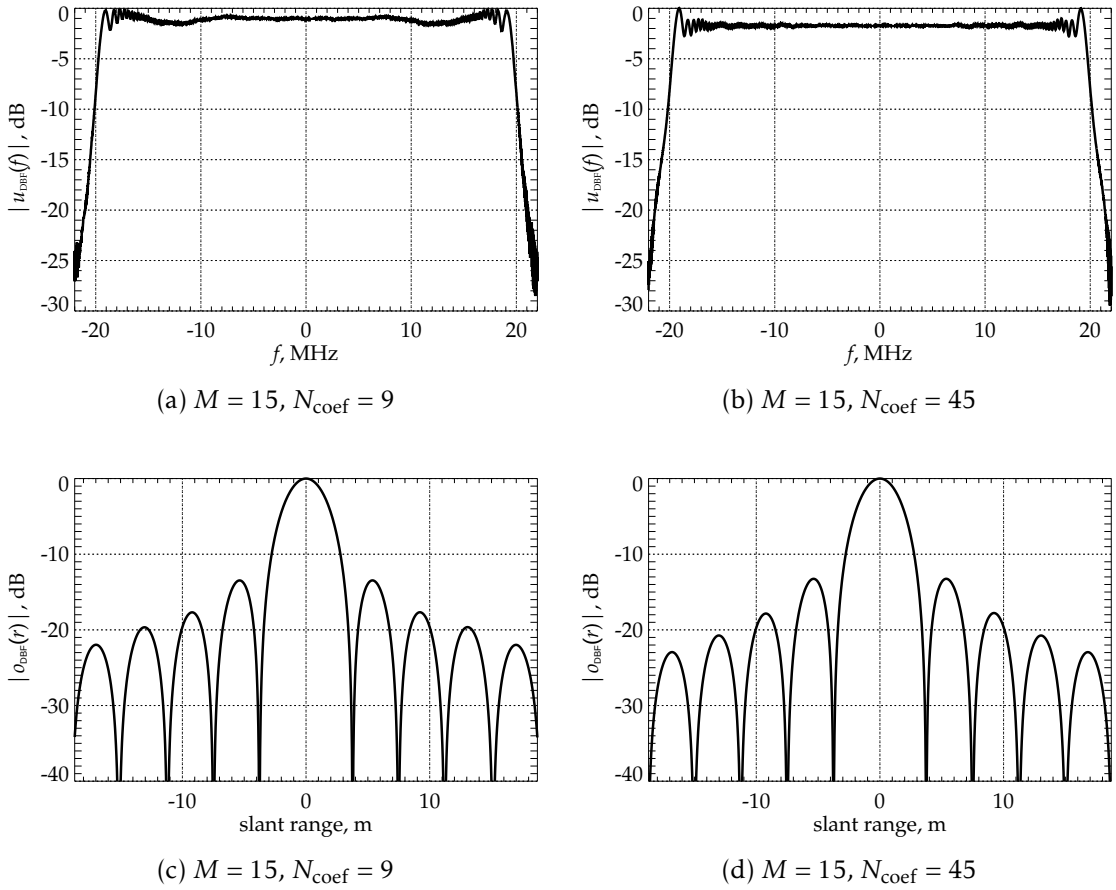

(a) $M = 15$, $N_{\text{coef}} = 9$

(b) $M = 15$, $N_{\text{coef}} = 45$

(c) $M = 15$, $N_{\text{coef}} = 9$

(d) $M = 15$, $N_{\text{coef}} = 45$

Figure 5.8: (a), (b) Point target spectra for two different FIR filter designs with unity beamforming. (c), (d) Corresponding range compressed SAR raw data signals.

evident. In this filter configuration the *SNR* loss is inevitable, since the only options are to broaden the receive beam, causing gain loss, or using a narrow beam, with the consequence of a loss of signal energy, as presented in Fig. 5.7c. Due to the linear time-frequency relationship of chirp waveforms, this modulation can also be observed in the energy density spectrum in Fig. 5.7b. This amplitude taper manifests in the corresponding range compressed point target signal, given in Fig. 5.7d, in a reduced sidelobe level and an increased mainlobe width. The solution to this problem is a FIR filter structure with several coefficients and multiple subbands. As can be observed in Fig. 5.7a, in terms of small *SNR* losses, there is a trend towards filter designs with a larger number of subbands and rather few filter coefficients in the order of ten to 20. Figure 5.8 shows two

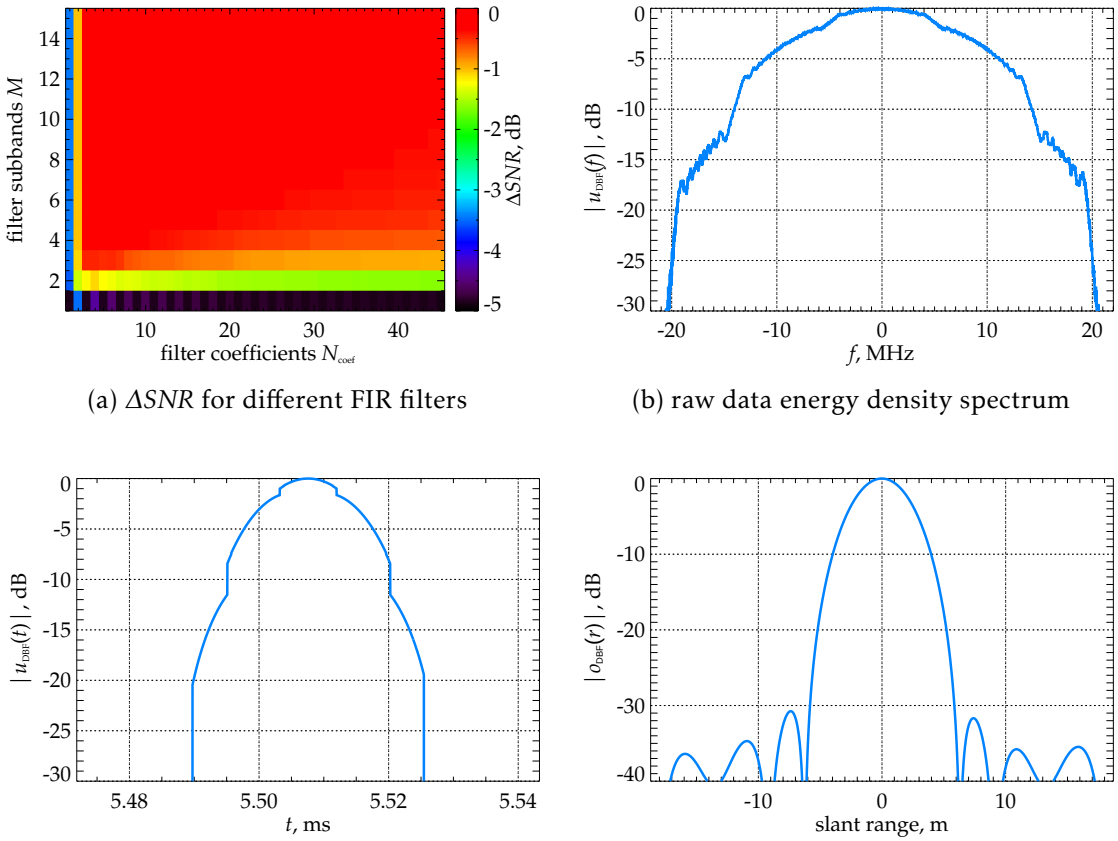

(a) ΔSNR for different FIR filters

(b) raw data energy density spectrum

(c) magnitude of the raw data signal

(d) SAR impulse response function

Figure 5.9: Performance for a time-variant MVDR beamforming approach using FIR filters. The point target is located at the swath center at $\vartheta = 0\,°$. (b)-(c) Elevation beamformer output for $M = 1$ and $N_{\text{coef}} = 1$. (d) Corresponding range compressed SAR signal.

examples of filter designs, using 15 subbands and nine filter coefficients in Fig. 5.8a, and 5.8c, which is optimal in terms of *SNR* loss, and with 45 coefficients in Fig. 5.8b and 5.8d. Although the solution with less filter coefficients provides a slightly better *SNR*, the filter design with 45 coefficients is capable of preserving the rectangular shape of the chirp spectrum almost perfectly. The ripple on the spectrum in Fig. 5.8b is induced by the individual subbands. The point target SAR impulse response functions exhibit both the sinc-like shape, although the solution for $N_{\text{coef}} = 9$ shows a larger ripple on the spectrum.

Time-variant beamforming in elevation employing the MVDR principle uses phase and amplitude information. MVDR beamforming can be understood as

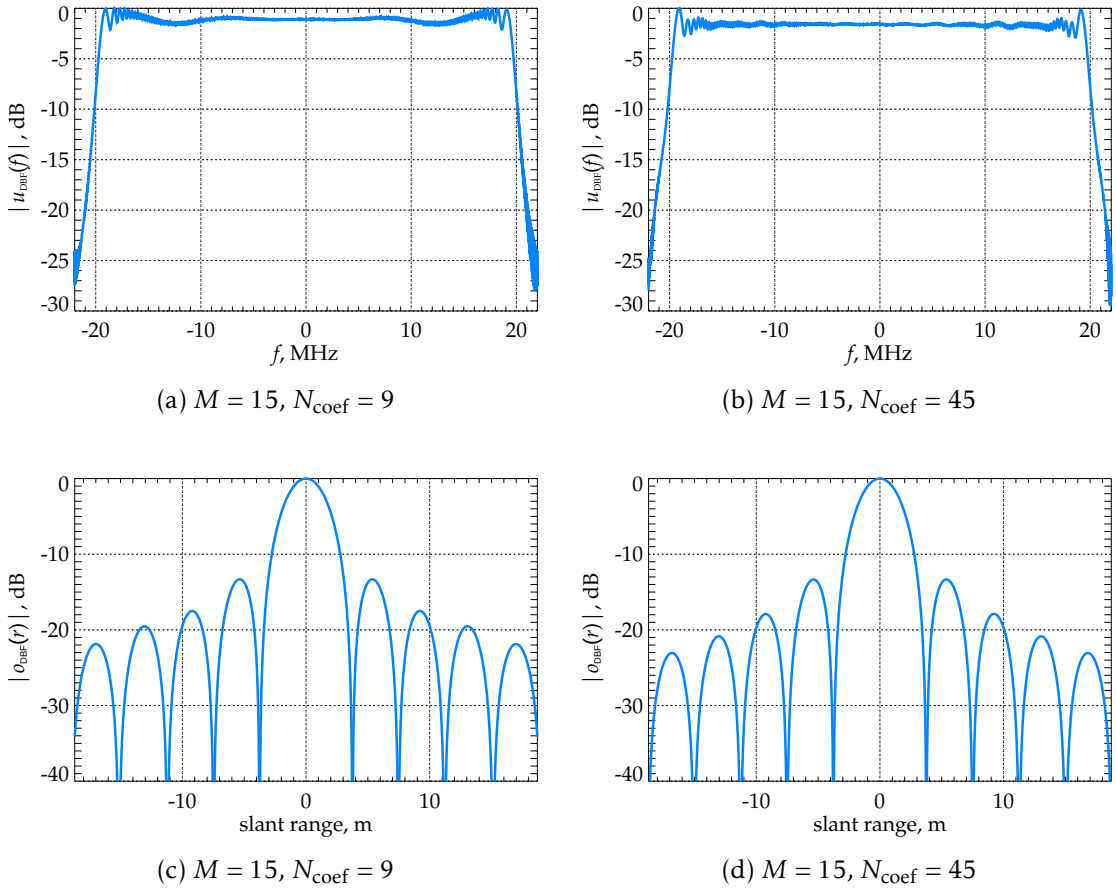

(a) $M = 15$, $N_{\text{coef}} = 9$

(b) $M = 15$, $N_{\text{coef}} = 45$

(c) $M = 15$, $N_{\text{coef}} = 9$

(d) $M = 15$, $N_{\text{coef}} = 45$

Figure 5.10: (a), (b) Point target spectra for two different FIR filter designs with MVDR beamforming. (c), (d) Corresponding range compressed SAR raw data signals.

spatial matched filtering and as such produces a unique signature in the point target spectrum, which deviates fundamentally from spectra generated with unity beamforming. This can be observed in Fig. 5.9. Besides the performance in terms of the relative *SNR*, presented in Fig. 5.9a, the beamformer output signal for Dirac-like filtering is shown in Fig. 5.9b to 5.9d. The weight vector is matched to the pulse center and consequently all other parts of the chirp suffer from a severe mismatch of the spatial filter coefficients. In contrast to unity beamforming this results in a rather continuous modulation of the point target spectrum as can be seen in Fig. 5.9b. Of course slight discontinuities due to the limited number of activated channels remain, as becomes apparent in the time domain signal in Fig. 5.9c. Figure 5.10 shows the MVDR counterpart to

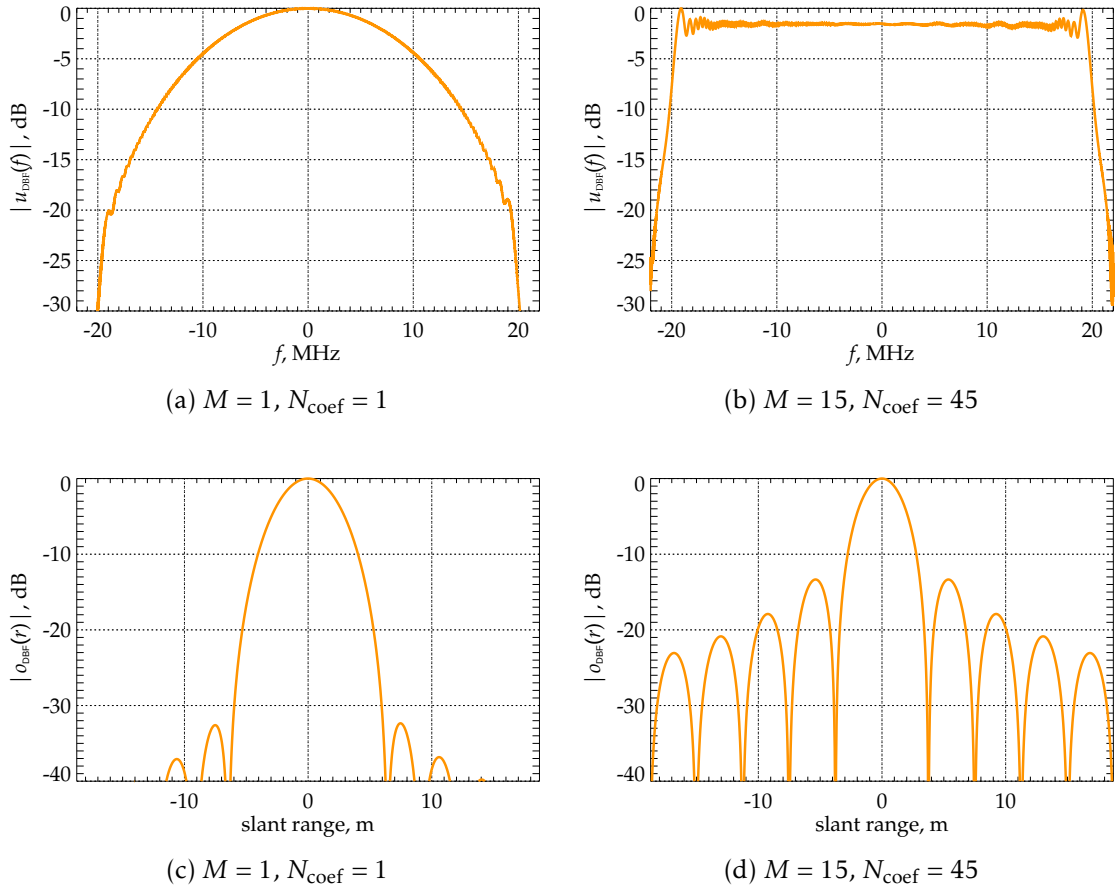

(a) $M = 1$, $N_{\text{coef}} = 1$

(b) $M = 15$, $N_{\text{coef}} = 45$

(c) $M = 1$, $N_{\text{coef}} = 1$

(d) $M = 15$, $N_{\text{coef}} = 45$

Figure 5.11: (a), (b) Point target spectra for two different FIR filter designs with LCMV beamforming. (c), (d) Corresponding range compressed SAR raw data signals.

Fig. 5.8. The shapes of the normalized spectra as well as the normalized point target impulse responses seem identical. Consequently, the difference in *SNR* resulting from spatial mismatch cannot be observed here. An important result from this analysis is that the temporal filter design is almost independent from the spatial filter design. This means that any spatial weights can be used with a fixed FIR filter.

Finally, the LCMV beamformer shows performances comparable to the MVDR beamforming approach. The results would be almost identical if the directions to be suppressed are far away from the direction of interest, which is the case for low *PRF*s. Using all available elevation channels the point target spectrum for Dirac-like filtering in Fig. 5.11a features no discontinuities at all. Accord-

DBF	**unity**		**MVDR**		**LCMV**	
M/N_{coef}	1/1	15/45	1/1	15/45	1/1	15/45
PSLR, dB	-24.195	-13.251	-31.684	-13.337	-32.370	-13.343
ISLR, dB	-15.426	-9.650	-25.715	-9.771	-30.951	-9.780
Δr, m	4.258	3.305	4.565	3.305	4.633	3.339
ΔSNR, dB	-4.544	-0.760	-4.856	-0.350	-4.940	-0.355

Table 5.3: Performance comparison for the three beamforming approaches and two FIR filter design examples.

ingly this strong taper produces very low sidelobes in the point target impulse response in Fig. 5.11c. The filter design with 15 subbands and 45 FIR filter coefficients practically coincides with the results using MVDR beamforming.

Table 5.3 summarizes the performance figures for the three beamforming approaches at the example of two FIR filter designs. The first example is the Dirac-like approach and in the second example 15 subbands and 45 FIR filter coefficients are used. The performance is compared by means of the relative *SNR*, the peak-sidelobe ratio *PSLR*, the integrated sidelobe ratio *ISLR*, as given in appendix G, and the slant range resolution Δr. Looking at the relative *SNR*, the numbers suggest, that the *SNR* loss is mainly driven by temporal mismatch. Beamforming techniques in conjunction with temporal filtering preserves almost ideal sinc-like SAR impulse response functions. It is important to mention that these investigations are based on a parameterized scenario, with a certain imaging geometry, certain radar parameters and a specific reflector antenna design, which might impact the results to a certain degree. For instance, LCMV beamforming depends on the *PRF*, since this parameter determines the ambiguous directions to be suppressed. Moreover, the simulations are performed for a point target in the center of the swath. Nevertheless, these performance results demonstrate the principal behavior of these three selected beamforming methods and illustrate the trend in terms of *SNR* loss and ambiguity suppression.

5.2.2 Azimuth Performance

The main criterion allowing to assess the usability of a reflector SAR system for wide-swath high-resolution operation is the *AASR*. This performance parameter, computed for a multi-channel SAR system with equation (4.113), sets a lower bound for usable *PRF*s and with this an upper bound for achievable swath widths. In analogy to beamforming in elevation, in azimuth the performance is analyzed for the three beamforming methods, unity, MVDR and LCMV beamforming. As in the elevation performance case, important for the judgement of a specific beamformer is the *SNR*, evaluated on the basis of equation

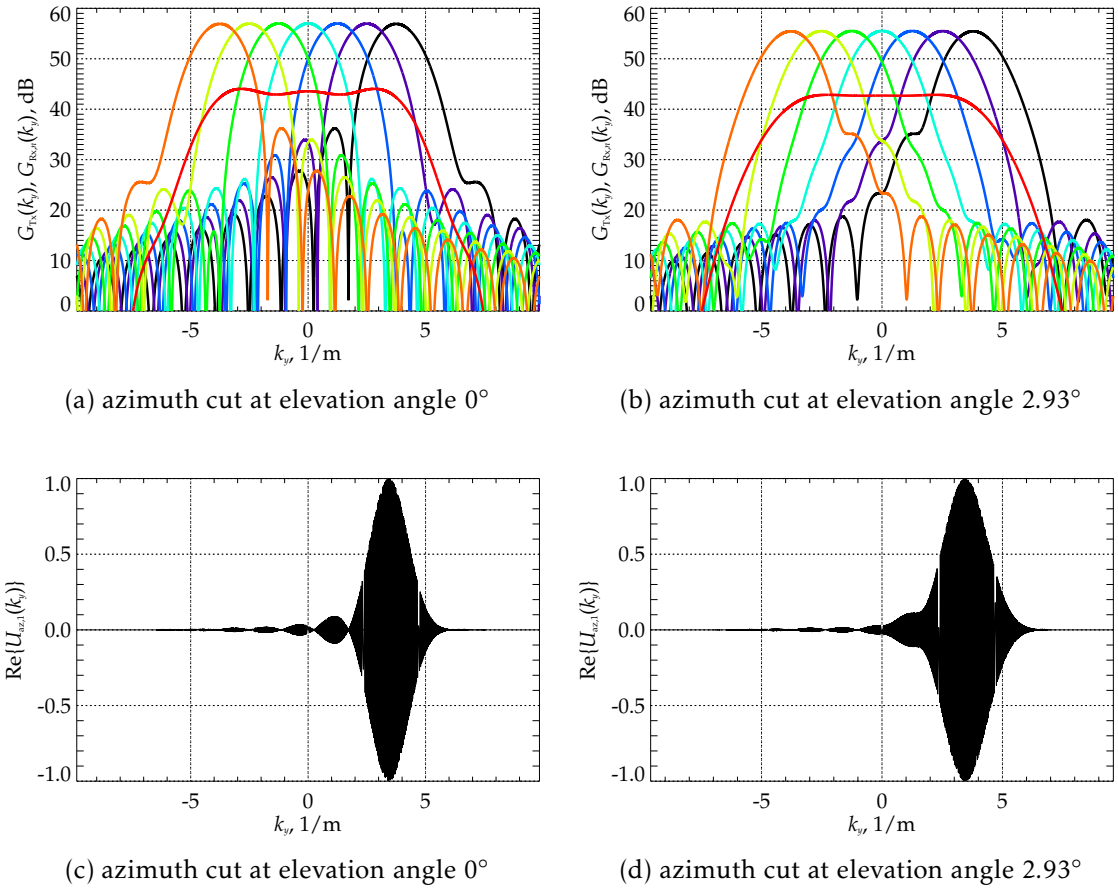

(a) azimuth cut at elevation angle 0°

(b) azimuth cut at elevation angle 2.93°

(c) azimuth cut at elevation angle 0°

(d) azimuth cut at elevation angle 2.93°

Figure 5.12: (a), (b) Antenna gain patterns in two different azimuth cut planes, where each pattern belongs to an individual feed element. The broad low gain patterns represent the transmit case with all elements active. (c), (d) Corresponding normalized raw data signals for the most right feed pattern.

(4.103), which is again measured with respect to the optimum *SNR* generated with MVDR beamforming. Instead of presenting the performance continuously versus the elevation angle, two dedicated azimuth cuts shall be investigated, the first being at the swath center at $\vartheta = 0°$ and the second at the swath border at $\vartheta = 2.93°$. Additionally, the performance is computed versus the *PRF* for these two cut planes. In the following simulations the azimuth signal has been filtered according to equation (4.111), where for the array manifold $\boldsymbol{a}_{\mathrm{az}}$ the receive patterns have been taken into account. This means, after filtering of the azimuth spectrum, the envelope of the transmit pattern remains.

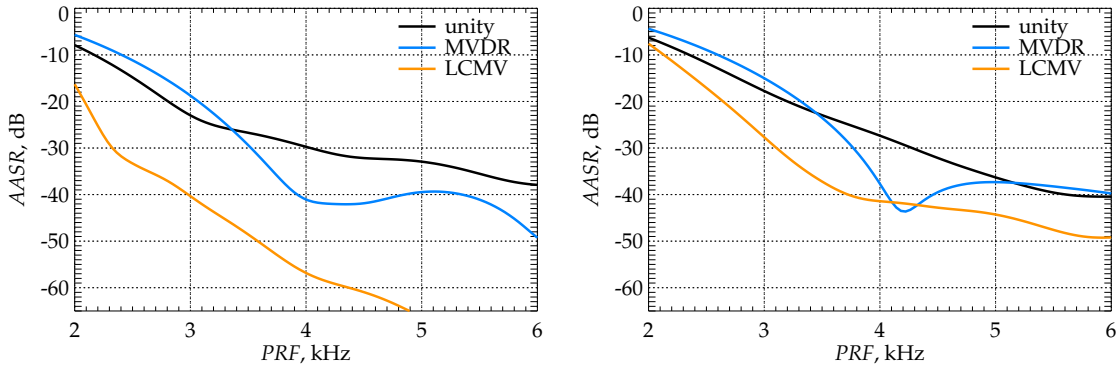

(a) azimuth cut at elevation angle 0°

(b) azimuth cut at elevation angle 2.93°

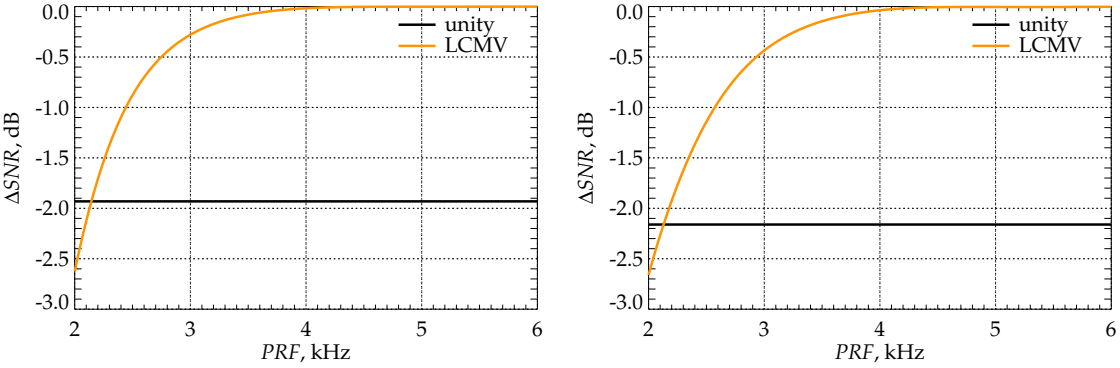

(c) azimuth cut at elevation angle 0°

(d) azimuth cut at elevation angle 2.93°

Figure 5.13: (a), (b) Azimuth ambiguity-to-signal ratio for the three beamforming approaches as function of the *PRF*. (c), (d) Corresponding *SNR* relative to the MVDR beamformer *SNR*.

The azimuth cuts of the antenna gain patterns, plotted for the elevation angles 0 ° in Fig. 5.12a and 2.93 ° in Fig. 5.12b versus azimuth wavenumber k_y, show, that the feed array design is suitable for acquiring a Doppler wavenumber spectrum with a width of $K_y' = 7.85\,\mathrm{m}^{-1}$ yielding the desired azimuth resolution Δy of 0.8 m (see equation (2.35)). Especially the pattern plot in Fig. 5.12b makes clear that the off-focus feed element patterns impose constraints in terms of azimuth ambiguity suppression due to the broadening of the mainlobes. The red curves represent the transmit patterns where all seven azimuth feed elements are active simultaneously. Figures 5.12c and 5.12d show single azimuth raw data channels corresponding to the most right patterns in Fig. 5.12a and 5.12b, respectively. Each azimuth channel is sampled with a low *PRF*, or wavenumber

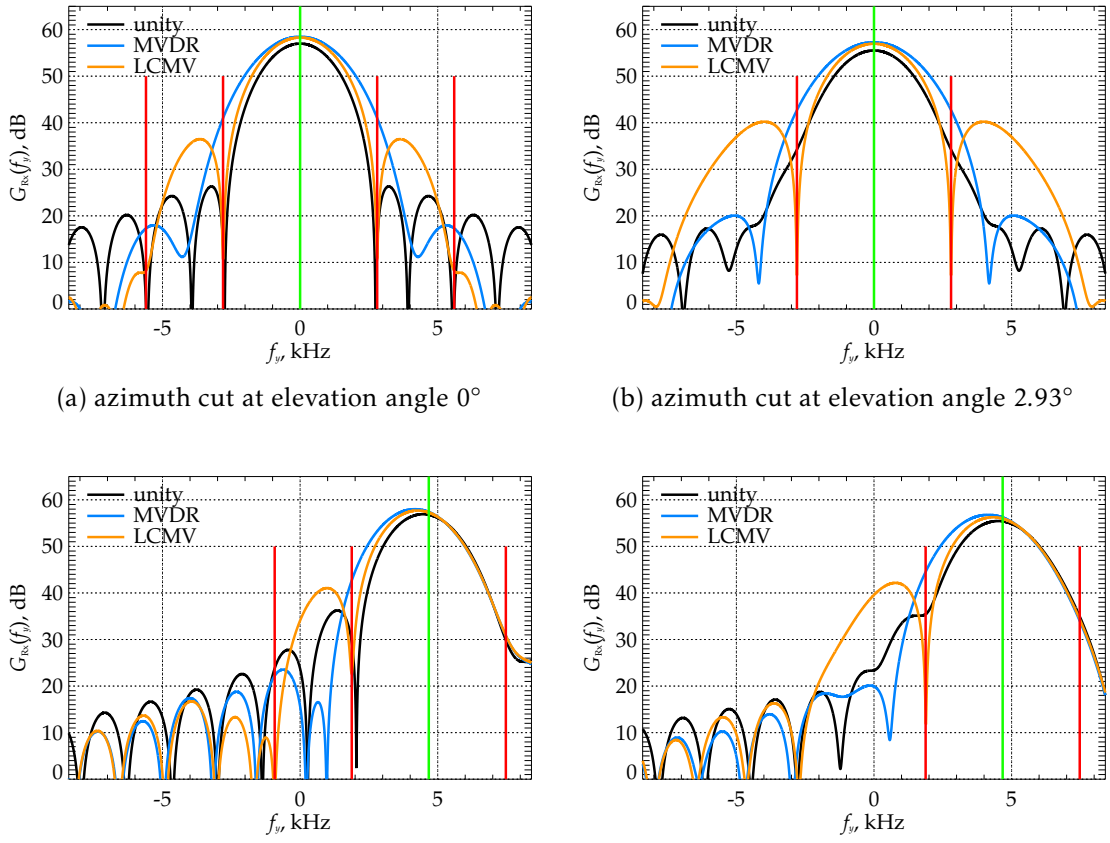

(a) azimuth cut at elevation angle 0°

(b) azimuth cut at elevation angle 2.93°

(c) azimuth cut at elevation angle 0°

(d) azimuth cut at elevation angle 2.93°

Figure 5.14: Individual patterns after digital beamforming for the center Doppler frequency (a), (b), and an off-center Doppler frequency (c), (d) indicated by the vertical green line. The ambiguous Doppler frequencies are marked with vertical red lines for a *PRF* of 2.8 kHz.

K_y, respectively, satisfying inequality (5.2). This means that the off-focus azimuth channels will suffer most from aliasing, since the corresponding patterns are broader compared to those at the array center. The effect of undersampling can be clearly observed at those ambiguous zero-Doppler positions spaced integer multiples of the sampling wavenumber K_y of 2.35 m^{-1}, corresponding to the *PRF* of 2.8 kHz via equation (2.46).

The performance in terms of the *AASR* is presented in Fig. 5.13a for the center cut plane and in Fig. 5.13b for an off-focus cut. In the center azimuth cut plane the unity beamformer performs with an *AASR* of -20.0 dB acceptable at the desired *PRF* of 2.8 kHz. The MVDR beamformer tends to amplify azimuth

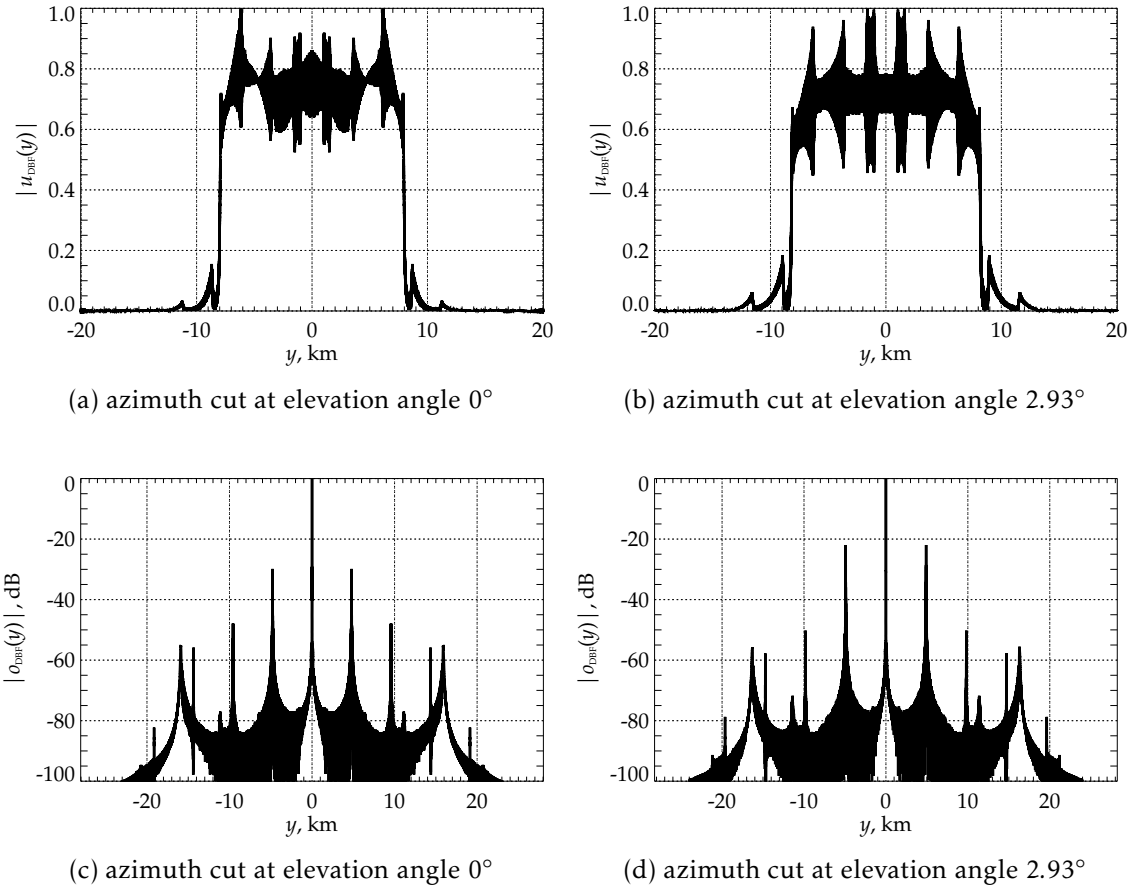

(a) azimuth cut at elevation angle 0°

(b) azimuth cut at elevation angle 2.93°

(c) azimuth cut at elevation angle 0°

(d) azimuth cut at elevation angle 2.93°

Figure 5.15: (a), (b) Azimuth raw data signals after unity beamforming. (c), (d) Corresponding azimuth compressed raw data signals.

ambiguities for *PRF*s below 3.35 kHz compared to unity beamforming. This is plausible, since MVDR beamforming maximizes the *SNR* or the gain pattern, respectively, for the wavenumber of interest and with this also the mainlobe becomes more accentuated. The consequence is that the first azimuth ambiguities move inside this mainlobe. For larger *PRF*s, MVDR beamforming produces smaller azimuth ambiguities compared to the unity beamformer, because more signal power is concentrated in the mainlobe, which in turn is absent in the sidelobes. In contrast with LCMV beamforming azimuth ambiguities are damped by more than 15 dB compared to the other two beamforming approaches almost over the entire *PRF* range. As mentioned above, the critical regions are in the near- and far-end of the swath, corresponding to the off-focus feed element patterns. The *AASR* curves for the azimuth cut at elevation angle 2.93 ° in Fig.

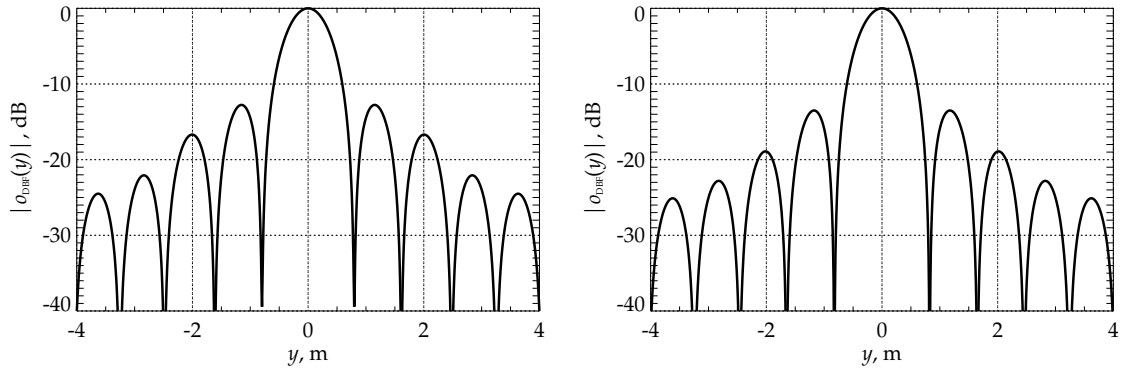

(a) azimuth cut at elevation angle 0°

(b) azimuth cut at elevation angle 2.93°

Figure 5.16: Mainlobe region of the azimuth impulse response functions shown in Fig. 5.15c and 5.15d, respectively.

5.13b illustrate that only LCMV beamforming maintains a sufficient ambiguity suppression in the order of -23.5 dB at 2.8 kHz *PRF*. Both, unity and MVDR beamforming collect large amounts of ambiguous signal energy with the mainlobes due to the defocusing effect. As in the elevation case unity and LCMV beamforming involve losses in *SNR*. This is plotted in Fig. 5.13c and 5.13d for the two cut planes. The *SNR* is related to the MVDR *SNR*, which corresponds to the zero dB level. For the unity beamformer always a single channel per Doppler wavenumber is utilized for all *PRF*s, resulting in a constant *SNR* loss in the order of 1.9 dB. For larger *PRF*s it might be possible to use more than one channel under the condition that the ambiguous Doppler wavenumbers are located apart far enough from the main beam. In contrast to unity beamforming LCMV and MVDR beamformers employ all channels simultaneously, with the consequence that the LCMV beamformer *SNR* converges to the *SNR* with MVDR beamforming for large *PRF*s. However, the lower the *PRF* the closer the ambiguous wavenumbers are located with respect to the wavenumber of interest, preventing the LCMV beamformer to efficiently suppress ambiguities. This means, a reflector antenna design should also be robust against *SNR* losses, which can be already quite large even if the *AASR* is still within the requirements. In the case of this design example the ΔSNR is with -0.4 dB at the swath center and -0.6 dB at the swath edge better than with unity beamforming for the desired *PRF* of 2.8 kHz.

To illustrate the beamforming concepts, examples of patterns after digital beamforming are presented in Fig. 5.14. The plots in Fig. 5.14a and 5.14b show such DBF patterns for the two azimuth cut planes, where the beam is

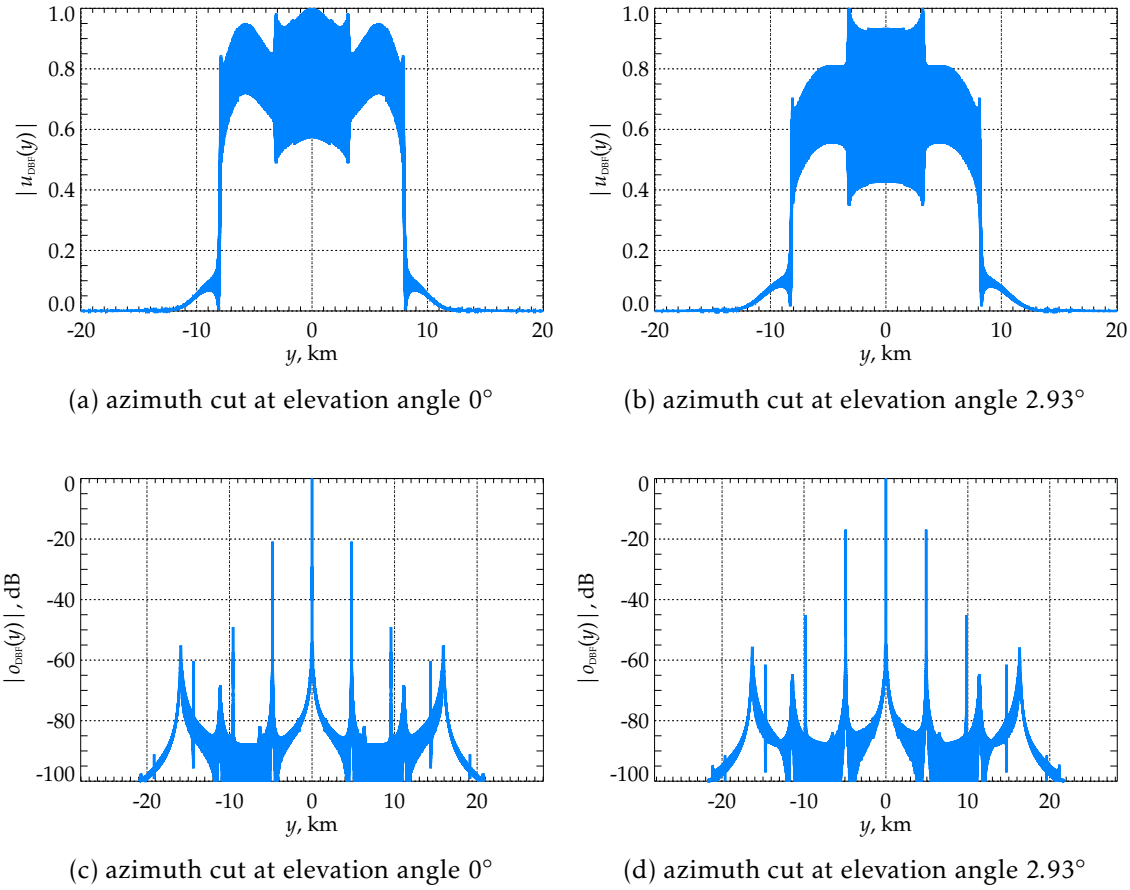

(a) azimuth cut at elevation angle 0°

(b) azimuth cut at elevation angle 2.93°

(c) azimuth cut at elevation angle 0°

(d) azimuth cut at elevation angle 2.93°

Figure 5.17: (a), (b) Azimuth raw data signals after MVDR beamforming. (c), (d) Corresponding azimuth compressed raw data signals.

optimized with respect to the center Doppler frequency $f_y = 0\,\text{kHz}$, indicated by the vertical green line. The ambiguous Doppler frequencies are spaced integer multiples of a *PRF* apart and marked with red lines. In both cut planes the unity DBF pattern is below the patterns with MVDR and LCMV beamforming. Concerning the MVDR beamformer the afore mentioned effect of mainlobe broadening and the resulting amplification of the first two azimuth ambiguities can be observed. For robustness reasons LCMV beamforming is performed using eigenvalue thresholding, as introduced in chapter 4.3.4, with $\mu = 0.05$. The effect from this technique can be seen in Fig. 5.14a. Here, the first two ambiguities on both sides of the frequency of interest have been suppressed, while the ambiguities at $\pm 5.6\,\text{kHz}$ are not as clearly damped as the ambiguities at $\pm 2.8\,\text{kHz}$. In the off-focus case in Fig. 5.14b the LCMV beamforming strat-

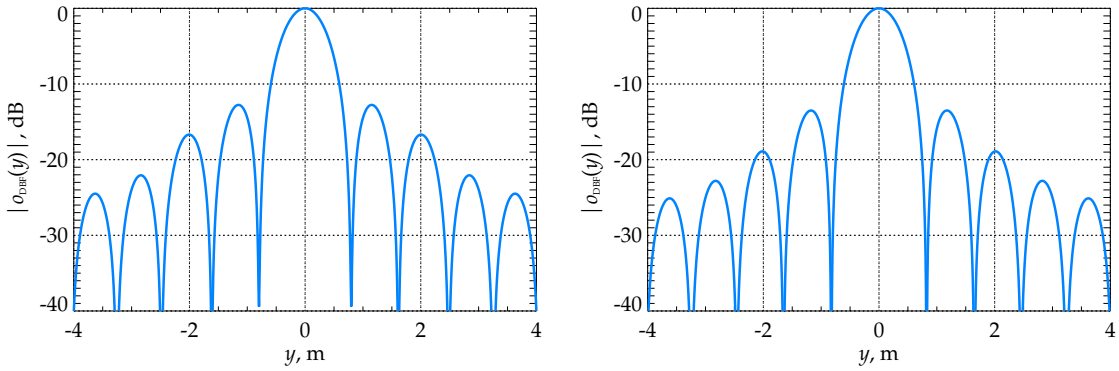

(a) azimuth cut at elevation angle 0°

(b) azimuth cut at elevation angle 2.93°

Figure 5.18: Mainlobe region of the azimuth impulse response functions shown in Fig. 5.17c and 5.17d, respectively.

egy has been adapted such that only the first two ambiguities are suppressed. It shows that this scenario is more stable with respect to the induced *SNR* loss. Even more challenging is beamforming for Doppler frequencies at the border of the azimuth spectrum. This is demonstrated for the largest processed Doppler frequency $f_y = 4.676\,\mathrm{kHz}$ in Fig. 5.14c and 5.14d. In the center cut as well as in the off-focus cut LCMV beamforming is only capable of suppressing the ambiguities left to the main beam. The coma lobe phenomenon prevents placing a pattern zero at $f_y = 7.476\,\mathrm{kHz}$. In contrast, unity and especially MVDR beamforming collect large amounts of ambiguous signal energy on both sides of the mainlobe.

The performance in terms of the *AASR* so far has been evaluated on the basis of equation (4.113). In the following, the azimuth processing principles comprising multirate processing techniques followed by digital beamforming as outlined in chapter 4.4.2 shall be demonstrated by means of point targets. Focusing on the pure effects from beamforming, additive noise is disclaimed in this simulation. For this, a single point target is placed at the swath center in the cut plane at $0\,^\circ$ and at the swath border at $2.93\,^\circ$. The azimuth raw data signals in the spatial domain after applying the processing steps in equations (4.99), (4.102) and (4.112) with unity beamforming are presented for the two cut planes in Fig. 5.15a and 5.15b. Inserting the processed Doppler wavenumber width $K_y' = 7.85\,\mathrm{m}^{-1}$ into equation (2.49) yields as spatial support for the

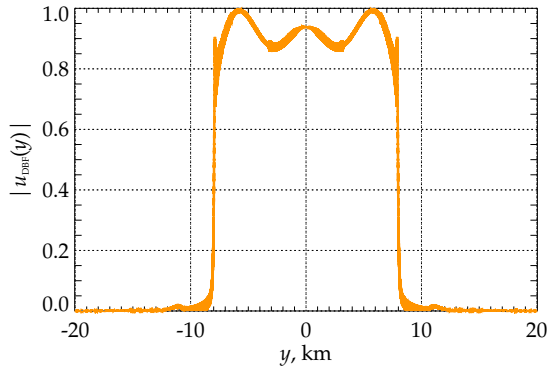

(a) azimuth cut at elevation angle 0°

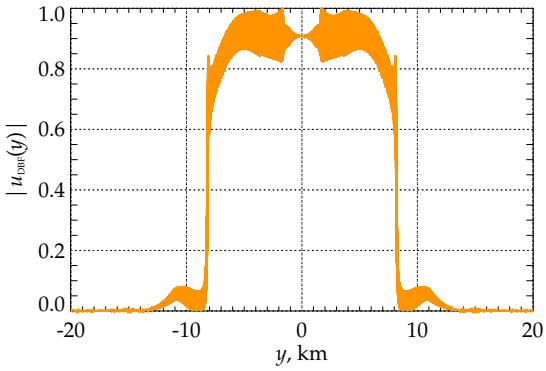

(b) azimuth cut at elevation angle 2.93°

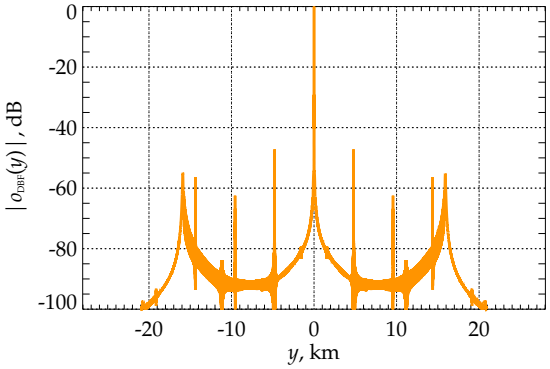

(c) azimuth cut at elevation angle 0°

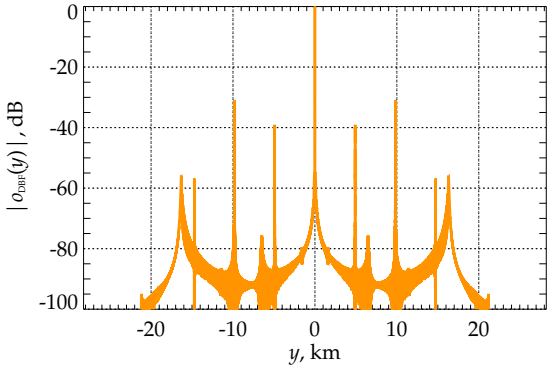

(d) azimuth cut at elevation angle 2.93°

Figure 5.19: (a), (b) Azimuth raw data signals after LCMV beamforming. (c), (d) Corresponding azimuth compressed raw data signals.

azimuth signal

$$y_B = \pm R_0 \left(\left(\frac{4k_c}{K_y'} \right)^2 - 1 \right)^{-\frac{1}{2}} = \begin{cases} \pm 7.989\,\mathrm{km} & , \quad 0° \\ \pm 8.196\,\mathrm{km} & , \quad 2.93° \end{cases} \tag{5.30}$$

As can be observed in both azimuth cuts, the signal is seriously contaminated with ambiguous signal energy. The corresponding azimuth compressed point targets are shown in Fig. 5.15c and 5.15d, respectively. Here, an azimuth compression filter h_{az} of rectangular shape according to

$$h_{\mathrm{az}}(y) = \mathrm{e}^{\mathrm{j}k_c \|\boldsymbol{r}_s(y) - \boldsymbol{r}\|}\,, \quad y \in [-y_B, y_B]\,, \tag{5.31}$$

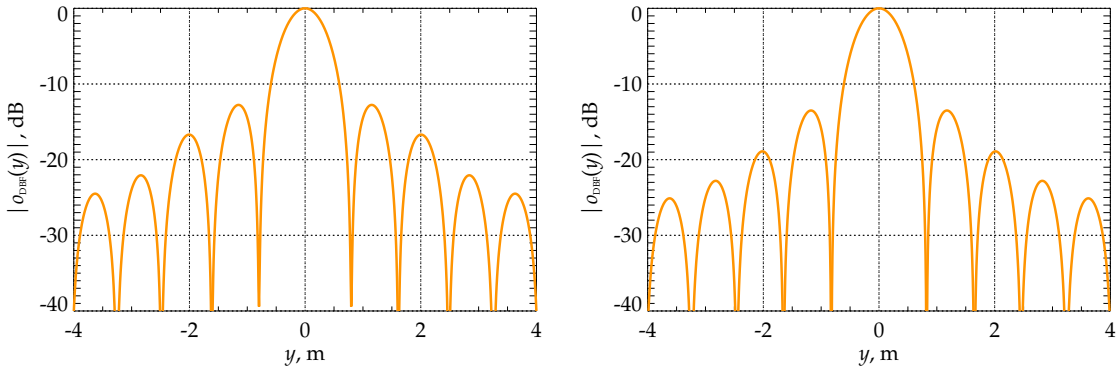

(a) azimuth cut at elevation angle 0°

(b) azimuth cut at elevation angle 2.93°

Figure 5.20: Mainlobe region of the azimuth impulse response functions shown in Fig. 5.19c and 5.19d, respectively.

has been applied. The azimuth compressed beamformer output is then

$$o_{\mathrm{DBF}}(y) = \int_{y'} u_{\mathrm{DBF}}(y - y')h_{\mathrm{az}}(y')\mathrm{d}y' \,. \tag{5.32}$$

Remember that u_{DBF} is the inversely filtered azimuth raw data signal after digital beamforming according using (4.111). As predicted by equation (2.49) for a zero-Doppler acquisition, the ambiguous azimuth point targets occur at

$$y_m = \pm[4.784, 9.568, 14.353, 19.139\,]\mathrm{km} \tag{5.33}$$

at the swath center and at

$$y_m = \pm[4.908, 9.816, 14.725, 19.636\,]\mathrm{km} \tag{5.34}$$

at the far end of the swath. There are two more ambiguities approximately at $\pm 2y_B$ which are the result of sampling the azimuth signal exactly with the same rate K'_y as the bandwidth of this azimuth signal. Although not of much importance, this artifact can be easily reduced by choosing a larger sampling rate K'_y in equation (4.100). The *AASR* directly measured from the compressed point target via a one-dimensional version of equation (2.47) is listed in Table 5.4 along with other performance parameters. A zoom into the region around the mainlobes is presented in Fig. 5.16, showing an almost sinc-like shape.

The analogous results for MVDR beamforming are presented in Fig. 5.17. As expected the azimuth signals in both azimuth cut planes in Fig. 5.17a and 5.17b are superimposed by a veritable amount of ambiguous signal energy, mainly

DBF	**unity**		**MVDR**		**LCMV**	
azimuth cut	0 °	2.93 °	0 °	2.93 °	0 °	2.93 °
PSLR, dB	-12.766	-13.504	-12.765	-13.506	-12.765	-13.506
ISLR, dB	-9.586	-10.720	-9.585	-10.721	-9.585	-10.721
Δy, m	0.712	0.728	0.712	0.728	0.712	0.728
ΔSNR (4.103), dB	-1.931	-2.161	0	0	-0.436	-0.639
ΔSNR sim., dB	-1.941	-2.135	0	0	-0.458	-0.636
AASR (4.113), dB	-20.002	-15.447	-15.522	-12.462	-37.150	-23.469
AASR sim., dB	-20.038	-15.698	-15.185	-12.317	-36.943	-23.132

Table 5.4: Performance comparison for the three beamforming approaches in two azimuth cut planes at $PRF = 2.8\,\text{kHz}$.

collected with the mainlobes. This manifests itself in the azimuth compressed point target signal in Fig. 5.17c and 5.17d as large mainlobe replicas. In contrast to unity beamforming the MVDR approach allows to utilize all available azimuth channels with the benefit of maximum gain and a flat signal spectrum. This results in almost perfect point target responses as indicated by the zoom plots in Fig. 5.18.

Finally, the results presented in Fig. 5.19 demonstrate the potentials with LCMV beamforming. At the swath center the point target signal in Fig. 5.19a shows almost no ambiguous azimuth signal energy, which also becomes evident from the corresponding focused signal in Fig. 5.19c. Also the envelope of the transmit pattern, remaining after inverse filtering, (see Fig. 5.12a) is clearly visible. At the swath border LCMV beamforming still offers a good ambiguity suppression as indicated in Fig. 5.19b and 5.19d. Remember, here the strategy was to suppress only the first left and right azimuth ambiguity.

The azimuth performance is summarized in Table 5.4 for the pulse repetition frequency of 2.8 kHz. The peak-sidelobe ratio as well as the integrated sidelobe ratio are close to the ideal performance of a sinc-like SAR impulse response. Also in terms of azimuth resolution Δy, no large differences can be observed. The *SNR*, computed via equation (4.103), is taken relative to the MVDR *SNR* making clear that unity beamforming causes a *SNR* loss in the order of 2 dB for this reflector and feed design. These *SNR* values show a good agreement with the *SNR* values computed from the simulated SAR impulse response. The *AASR* is computed using equation (4.113) and, for comparison, taken from the simulated SAR impulse response. Again, the *AASR* formula could be verified by the simulations. To get an impression on how the beamforming process shapes the signal and its ambiguities, the power expressions in equation (4.113) for the

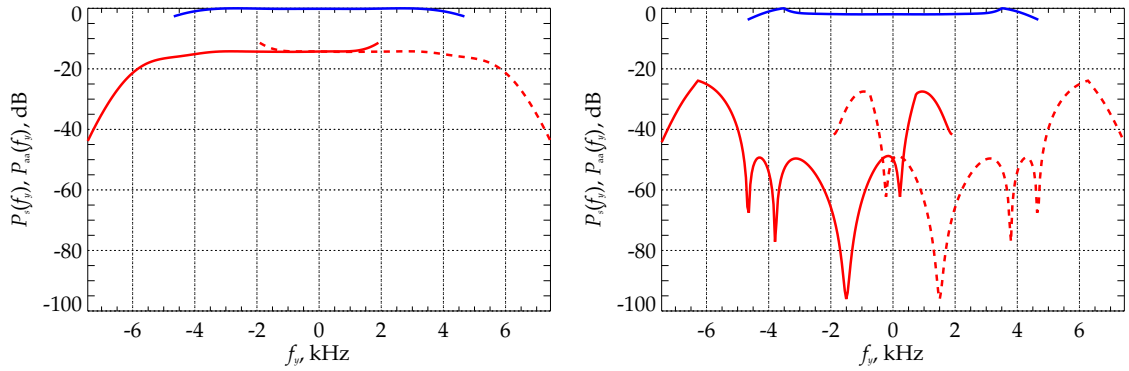

(a) MVDR DBF at elevation angle 2.93°

(b) LCMV DBF at elevation angle 2.93°

Figure 5.21: Signal power P_s (blue) and azimuth ambiguity power P_{aa} (red) versus Doppler frequency for MVDR beamforming (a) and LCMV beamforming (b) at a *PRF* of 2.8 kHz.

signal

$$P_s(k_y) = |g(k_y, \boldsymbol{r}) \cdot \boldsymbol{w}_{az}^T \boldsymbol{a}_{az}(k, \varphi, \vartheta)|^2 \tag{5.35}$$

and the azimuth ambiguities

$$P_{aa}(k_y + mK_y) = |g(k_y + mK_y, \boldsymbol{r}_m) \cdot \boldsymbol{w}_{az}^T \boldsymbol{a}_{az}(k, \varphi_m, \vartheta_m)|^2 \,, \quad m = \pm 1 \,, \tag{5.36}$$

have been plotted in Fig. 5.21. Here the signal power spectrum in blue color and the first left and first right power spectrum of the azimuth ambiguities in red color are shown. In case of MVDR beamforming, presented in Fig. 5.21a, the ambiguous spectra have a relatively high level compared to the LCMV beamformer in Fig. 5.21b, where the ambiguities are suppressed quite well. If one visually integrates the spectra for MVDR beamforming, it is evident that the *AASR* must be above -20 dB as given in Table 5.4. Interesting to observe is that the ambiguity suppression with LCMV beamforming performs not equally for all wavenumbers of interest. Particularly at the borders of the spectra, quite high levels of ambiguities can be observed. This is explained by the defocusing effect, whereupon the broader beams prevent a more efficient azimuth ambiguity suppression.

5.2.3 Polarimetric Performance

Fully polarimetric multi-channel SAR systems ask for dedicated processing concepts. Especially reflector antenna based polarimetric SAR systems can be ex-

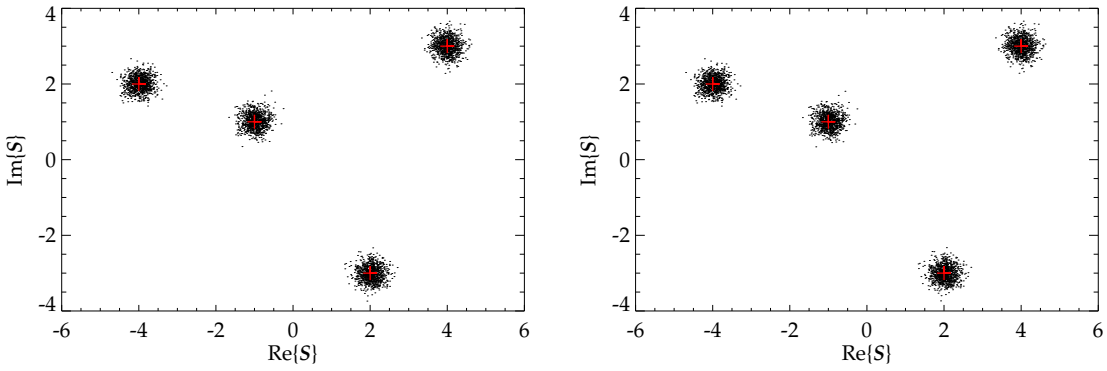

Figure 5.22: Monte Carlo simulation of a scattering matrix after conventional MVDR beamforming (a) and polarimetric MVDR beamforming (b), where the cross polar patterns are set to zero. The red crosses indicate the actual scattering matrix (5.37).

pected to radiate certain amounts of electromagnetic energy via their cross polarized far field patterns. In order to quantify the performances of such systems a Monte Carlo simulation has been conducted, where the conventional MVDR beamforming approach (4.53) is compared to the polarimetric MVDR beamforming technique (4.133). The signals according to equations (4.119) are simulated based on a single point target example, described by its scattering matrix

$$\boldsymbol{S} = \begin{bmatrix} 4+\mathrm{j}3 & -1+\mathrm{j} \\ 2-\mathrm{j}3 & -4+\mathrm{j}2 \end{bmatrix}. \tag{5.37}$$

The co- and cross-polar patterns are computed for an elevation branch in the center of the feed array, using all 33 channels, for the reflector system specified in Table 5.2. The point target is located at the direction $(\mathrm{el}, \mathrm{az}) = (0.42°, -0.08°)$.

In a first simulation the functionality of both beamforming approaches under the condition, when no cross polar patterns are present, is demonstrated in Fig. 5.22. Here, the red crosses denote the actual scattering coefficients and the dot clouds represent their realizations during the Monte Carlo simulation. As expected both procedures recover the actual scattering matrix $\boldsymbol{S}$, plotted in the complex plane, with a certain spread, induced by the thermal noise contributions. The performance changes, when cross-polar patterns become more dominant. To control the impact of the cross-polar patterns, they are weighted with a constant, such that the maximum gain of the co-polar patterns $G_{\mathrm{co,max}}$ keeps a fixed ratio, the so called *cross polarization isolation XPI*, with the maxi-

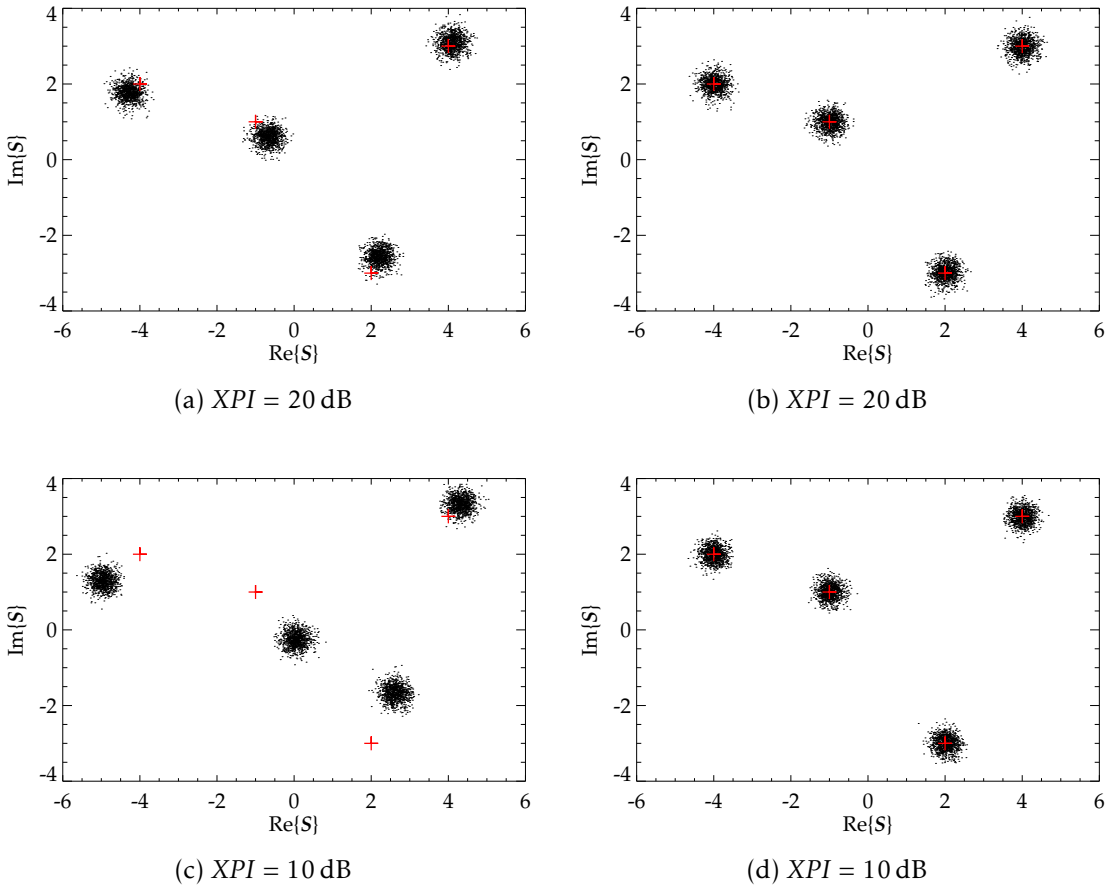

(a) $XPI = 20\,\mathrm{dB}$ (b) $XPI = 20\,\mathrm{dB}$

(c) $XPI = 10\,\mathrm{dB}$ (d) $XPI = 10\,\mathrm{dB}$

Figure 5.23: Polarimetric beamformer performance using the conventional MVDR approach (a) and (c) and with polarimetric MVDR beamforming (b) and (d), for different cross-polarization isolation levels XPI.

mum gain of the cross-polar patterns $G_{\mathrm{cx,max}}$[1] [110]

$$XPI = \frac{G_{\mathrm{co,max}}}{G_{\mathrm{cx,max}}} \,. \tag{5.38}$$

The results are presented for XPI levels of 10 dB and 20 dB in Fig. 5.23. Although an XPI of 10 dB represents an extreme case, the simulations with conventional MVDR beamforming according to equation (4.53) in Fig. 5.23a and

[1] For the actual reflector antenna the ratio of maximum co-polar gain to the maximum cross-polar gain in the direction of interest is approximately 40 dB. However, this is likely to be to optimistic, since cross-polar components of the feed antenna are not considered.

5.23c show that the estimated scattering matrix is prone to complex biases which increase with decreasing *XPI* level. The spread of the data points due to the thermal noise seems to be unaffected by the processing scheme. In either case, the polarimetric MVDR beamformer is capable of reconstructing the individual phasors of the scattering matrix distortionless, as can be observed in Fig. 5.23b and 5.23d, respectively.

As pointed out in the previous performance investigations, the most important factor for a successful implementation of beamforming routines is the precise knowledge of the antenna patterns. This is especially true for the cross-polar patterns in the frame of polarimetric beamforming. Arguably it is desirable to construct antennas with a good cross-polar isolation, in which case the measurement of the cross-polar patterns would become difficult. However, in such cases standard beamforming methods, ignoring these cross-polar patterns, would be sufficient to process the SAR raw data adequately. In contrast, with strong cross-polar field components, their measurement will be more precise, and consequently polarimetric DBF algorithms become applicable. Insofar, from a pure physical point of view, an antenna with distinct cross-polar patterns is not necessarily worse than its low cross-polar counterpart, since in both cases the available electromagnetic energy is combined in an optimal way, yielding comparable performances.

5.3 Error and Sensitivity Analysis

Up to now an ideal system with perfect knowledge of all parameters involved has been assumed. In practice, most parameters are subject to measurement errors or have to be estimated, if they are not directly accessible. Especially the analog and digital signal processing onboard the SAR satellite will be impacted by several error sources. This is illustrated with a system model for the ith elevation channel in Fig. 5.24. To demonstrate the impact of these error sources on the performance in terms of digital beamforming, infinite short pulses shall be assumed, which simplifies the FIR filter impulse response function to the Dirac-filter given in equation (4.88). Then the corresponding discrete time signal $u_{\mathrm{DBF},i}$ prior to summation for a point target is

$$u_{\mathrm{DBF},i}(n) = w_i(n) \cdot \mathcal{Q}\{\hat{o}g(\boldsymbol{k}, n)a_i(\boldsymbol{k}) + v_i(n) + e_i(\boldsymbol{k}, n)\}\,, \tag{5.39}$$

where $\mathcal{Q}\{.\}$ symbolizes the A/D conversion in operator notation. The term e_i represents not only range ambiguities but more generally spatio-temporal interference. Here, the wavenumber vector $\boldsymbol{k} = f(k, \vartheta, \varphi)$ is just written to underline the spatial dependency on the pattern a_i and the Green's function g and with this also the weights w_i. The spatial dimension is projected onto the tem-

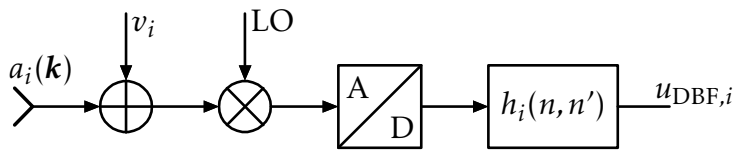

Figure 5.24: System model of the ith receiver path.

poral dimension. Without loosing generality $\hat{o}g$ can be set equal to one. Then equation (5.39) can be stated in the form

$$u_{\mathrm{DBF},i}(n) = w_i(n) \cdot [\delta(n) a_i(\boldsymbol{k}) + v_i(n) + e_i(\boldsymbol{k}, n) + q_i(\boldsymbol{k}, n)] \,, \tag{5.40}$$

where $q_i(\boldsymbol{k}, n)$ represents quantization errors. The most critical step in the digital beamforming process is the determination of the weights w_i. MVDR as well as LCMV beamforming utilize phase and amplitude information derived from measured and quantized antenna patterns $\widehat{a_i}(\boldsymbol{k})$

$$w_i = f(\widehat{a_i}(\boldsymbol{k} + \Delta\boldsymbol{k})) \tag{5.41}$$

$$= f(a_i(\boldsymbol{k} + \Delta\boldsymbol{k}) + \Delta a_i(\boldsymbol{k} + \Delta\boldsymbol{k})) \,. \tag{5.42}$$

These patterns can be decomposed into the true antenna patterns a_i superimposed by pattern measurement errors Δa_i. In addition, and even more severe for the beamforming, the direction of arrival is unknown or only known with a certain uncertainty $\Delta\boldsymbol{k}$. The effect of inaccurate knowledge of the DOA can be quantified with the simplified *SNR* expressions for the individual digital beamforming approaches given with equations (5.25) to (5.27). The *SNR* patterns are plotted in Fig. 5.25a for a DOA of $\vartheta = 0\,^\circ$ and in Fig. 5.25b at the swath border as a function of the DOA error $\Delta\vartheta$. Clearly the highest sensitivity with respect to DOA errors of the given reflector antenna, and generally of any antenna type, is in boresight direction, where the effective aperture area is maximal. With regard to the individual beamforming approaches the sensitivity is not significantly different, since all DBF methods are designed to maximize the gain in a certain DOA. For those classes of beamformers an appropriate error bound in the DOA error could be half the 3 dB beamwidth, given for reflector antennas with equation (3.12), yielding

$$\Delta\vartheta \leq 0.61 \frac{\lambda}{D} \,. \tag{5.43}$$

For the reflector antenna example in Table 5.2 this DOA error in elevation would approximately be $0.16\,^\circ$. Especially DOA errors can impact interference suppressing beamformers and decrease their effectiveness drastically.

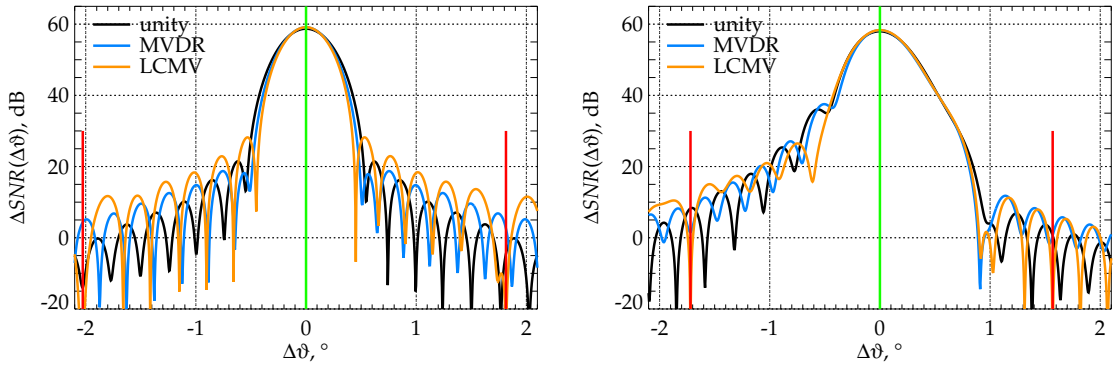

(a) $\vartheta = 0°$ (b) $\vartheta = 2.72°$

Figure 5.25: Sensitivity of the three beamformers with respect to direction of arrival errors $\Delta\vartheta$ for the example system specified in Table 5.2.

All other error sources, measurement and quantization errors Δa_i in the computation of the weights, additive noise v_i as well as quantization noise q_i in the received raw data signal can be summarized as random errors, which will basically lead to a mismatch between the weight vector $\boldsymbol{w}$ and the actual array manifold $\boldsymbol{a}$. The impact of this mismatch shall be investigated by means of a sensitivity analysis of the *SNR*

$$SNR(\vartheta) \sim \frac{|\boldsymbol{a}^{\mathsf{T}}\boldsymbol{w}|^2}{\boldsymbol{w}^{\mathsf{T}}\boldsymbol{R}_v\boldsymbol{w}^*} = \frac{\boldsymbol{w}^{\mathsf{T}}\boldsymbol{a}\boldsymbol{a}^{\mathsf{H}}\boldsymbol{w}^*}{\boldsymbol{w}^{\mathsf{T}}\boldsymbol{R}_v\boldsymbol{w}^*} = \frac{\boldsymbol{w}^{\mathsf{T}}\boldsymbol{R}_a\boldsymbol{w}^*}{\boldsymbol{w}^{\mathsf{T}}\boldsymbol{R}_v\boldsymbol{w}^*}\,, \tag{5.44}$$

and the signal-to-interference ratio

$$SIR(\vartheta) = \frac{\boldsymbol{w}^{\mathsf{T}}\boldsymbol{R}_a(\vartheta)\boldsymbol{w}^*}{\sum_i \boldsymbol{w}^{\mathsf{T}}\boldsymbol{R}_a(\vartheta_i)\boldsymbol{w}^*}\,, \tag{5.45}$$

with respect to variations in the weight vector $\boldsymbol{w}$. By taking the gradient with respect to $\boldsymbol{w}$ and $\boldsymbol{w}^*$ the *SNR* sensitivity is

$$\nabla_{\boldsymbol{w}} SNR = \frac{(\boldsymbol{R}_a - SNR\cdot\boldsymbol{R}_v)\boldsymbol{w}^*}{\boldsymbol{w}^{\mathsf{T}}\boldsymbol{R}_v\boldsymbol{w}^*}\,, \tag{5.46}$$

$$\nabla_{\boldsymbol{w}^*} SNR = \frac{\boldsymbol{w}^{\mathsf{T}}(\boldsymbol{R}_a - SNR\cdot\boldsymbol{R}_v)}{\boldsymbol{w}^{\mathsf{T}}\boldsymbol{R}_v\boldsymbol{w}^*} \tag{5.47}$$

and the signal-to-interference sensitivity is

$$\nabla_{\boldsymbol{w}} SIR = \frac{(\boldsymbol{R_a} - SIR \cdot \sum_i \boldsymbol{R_a})\boldsymbol{w}^*}{\sum_i \boldsymbol{w}^\mathsf{T} \boldsymbol{R_a} \boldsymbol{w}^*} , \tag{5.48}$$

$$\nabla_{\boldsymbol{w}^*} SIR = \frac{\boldsymbol{w}^\mathsf{T}(\boldsymbol{R_a} - SIR \cdot \sum_i \boldsymbol{R_a})}{\sum_i \boldsymbol{w}^\mathsf{T} \boldsymbol{R_a} \boldsymbol{w}^*} . \tag{5.49}$$

These gradients span a $2N_\mathrm{c}$-dimensional space and are therefore difficult to assess.

A more practicable approach is to add an error vector $\Delta\boldsymbol{a}$ to the true array manifold $\boldsymbol{a}$ and compute from this disturbed array manifold $\widehat{\boldsymbol{a}}$ a new weight vector $\widehat{\boldsymbol{w}}$ which is used in the *SNR* and *SIR* formulae

$$\widehat{SNR}(\vartheta) \sim \frac{\widehat{\boldsymbol{w}}^\mathsf{T} \boldsymbol{R_a} \widehat{\boldsymbol{w}}^*}{\widehat{\boldsymbol{w}}^\mathsf{T} \boldsymbol{R_v} \widehat{\boldsymbol{w}}^*} , \tag{5.50}$$

$$\widehat{SIR}(\vartheta) = \frac{\widehat{\boldsymbol{w}}^\mathsf{T} \boldsymbol{R_a}(\vartheta) \widehat{\boldsymbol{w}}^*}{\sum_i \widehat{\boldsymbol{w}}^\mathsf{T} \boldsymbol{R_a}(\vartheta_i) \widehat{\boldsymbol{w}}^*} . \tag{5.51}$$

In order to measure the relative degradation, the $\widehat{SNR}$-expression is normalized to the undistorted *SNR* formula (5.44) with MVDR beamforming yielding

$$\Delta SNR(\vartheta) = \frac{\widehat{SNR}(\vartheta)}{SNR_{\mathrm{MVDR}}(\vartheta)} . \tag{5.52}$$

The interference suppression performance using LCMV beamforming is taken with respect to the *SIR* with ideal MVDR beamforming

$$\Delta SIR(\vartheta) = \frac{\widehat{SIR}_{\mathrm{LCMV}}(\vartheta)}{SIR_{\mathrm{MVDR}}(\vartheta)} . \tag{5.53}$$

The performance is then evaluated by means of Monte-Carlo simulations resulting in *probability density functions* (PDF) for the $\Delta SNR(\vartheta)$ and the $\Delta SIR(\vartheta)$. Finally, from these PDFs the expectations [94]

$$\mu_{\Delta SNR} = \mathcal{E}\{\Delta SNR\} = \int_{\Delta\boldsymbol{a}} \Delta SNR(\Delta\boldsymbol{a}) p(\Delta\boldsymbol{a}) \mathrm{d}\Delta\boldsymbol{a} , \tag{5.54}$$

$$\mu_{\Delta SIR} = \mathcal{E}\{\Delta SIR\} = \int_{\Delta\boldsymbol{a}} \Delta SIR(\Delta\boldsymbol{a}) p(\Delta\boldsymbol{a}) \mathrm{d}\Delta\boldsymbol{a} , \tag{5.55}$$

where the real and imaginary parts of the complex antenna pattern error vector $\Delta\boldsymbol{a}$ are modeled as Gaussian random variables with zero mean ($\mu_{\Delta a} = 0$) and

	a_{rel}, dB	0	10	20	30	40	50	60
M.	$\mu_{\Delta SNR}$, dB	-3.262	-0.482	-0.085	-0.045	-0.04	-0.04	-0.04
	$\sigma_{\Delta SNR}$, dB	3.000	0.333	0.032	$3 \cdot 10^{-3}$	$3 \cdot 10^{-4}$	$3 \cdot 10^{-5}$	$3 \cdot 10^{-6}$
LCMV	$\mu_{\Delta SNR}$, dB	-12.49	-4.358	-0.668	-0.070	$7 \cdot 10^{-3}$	$8 \cdot 10^{-3}$	$1 \cdot 10^{-3}$
	$\sigma_{\Delta SNR}$, dB	4.317	1.046	0.126	0.013	$1 \cdot 10^{-3}$	$1 \cdot 10^{-4}$	$2 \cdot 10^{-5}$
	$\mu_{\Delta SIR}$, dB	-46.99	-36.30	-26.94	-17.47	-7.535	2.461	12.45
	$\sigma_{\Delta SIR}$, dB	5.682	3.732	3.516	3.493	3.485	3.491	3.488

Table 5.5: Relative sensitivity, subject to random errors, with MVDR beamforming at a DOA of $\vartheta = 0°$ and with LCMV beamforming at $\vartheta = 2.72°$ with interferences at $\vartheta = \{-2.03, 1.82\}°$, for different relative errors a_{rel}.

equal standard deviations $\sigma_{\Delta a}$, are computed. The standard deviations $\sigma_{\Delta SNR}$ and $\sigma_{\Delta SIR}$ of the corresponding PDFs are the square roots of the variances

$$\sigma^2_{\Delta SNR} = \mathcal{E}\{(\Delta SNR - \mu_{\Delta SNR})^2\} = \int_{\Delta \boldsymbol{a}} (\Delta SNR(\Delta \boldsymbol{a}) - \mu_{\Delta SNR})^2 p(\Delta \boldsymbol{a}) \mathrm{d}\Delta \boldsymbol{a} \,, \quad (5.56)$$

$$\sigma^2_{\Delta SIR} = \mathcal{E}\{(\Delta SIR - \mu_{\Delta SIR})^2\} = \int_{\Delta \boldsymbol{a}} (\Delta SIR(\Delta \boldsymbol{a}) - \mu_{\Delta SIR})^2 p(\Delta \boldsymbol{a}) \mathrm{d}\Delta \boldsymbol{a} \,. \quad (5.57)$$

Here, as error measure, the relative error a_{rel} is defined as ratio of the maximum antenna pattern magnitude $a_{\max}$, which corresponds to the maximum antenna gain, to the error standard deviation $\sigma_{\Delta a}$

$$a_{\mathrm{rel}} = 20 \lg a_{\max} - 20 \lg(\sqrt{2}\sigma_{\Delta a}) \,. \quad (5.58)$$

This means, if for instance the maximum antenna gain $a_{\max}$ is 60 dB and the relative error a_{rel} is 0 dB, then the error standard deviation $\sigma_{\Delta a}$ would be in the same order as the maximum antenna pattern magnitude $a_{\max}$.

The results of the Monte-Carlo simulation are listed in Table 5.5. The first two rows summarize the results with MVDR beamforming for different relative errors a_{rel} between 0 dB and 60 dB. For $a_{\mathrm{rel}} = 0$ dB the magnitude of the error is in the same order as the pattern maximum, consequently resulting in the largest *SNR* loss in the average of roughly 3.3 dB. However, if the error magnitude drops only 10 dB below the pattern maximum, the *SNR* loss becomes already very small. The PDF for the ΔSNR for this error scenario is presented is Fig. 5.26a. The corresponding results with LCMV beamforming are presented in rows three and four. However, a DOA at the swath border in far range at $\vartheta = 2.72°$ has been chosen, since here ambiguity suppression is more challenging. In terms of *SNR* loss principally the LCMV beamformer shows a higher sensitivity in the

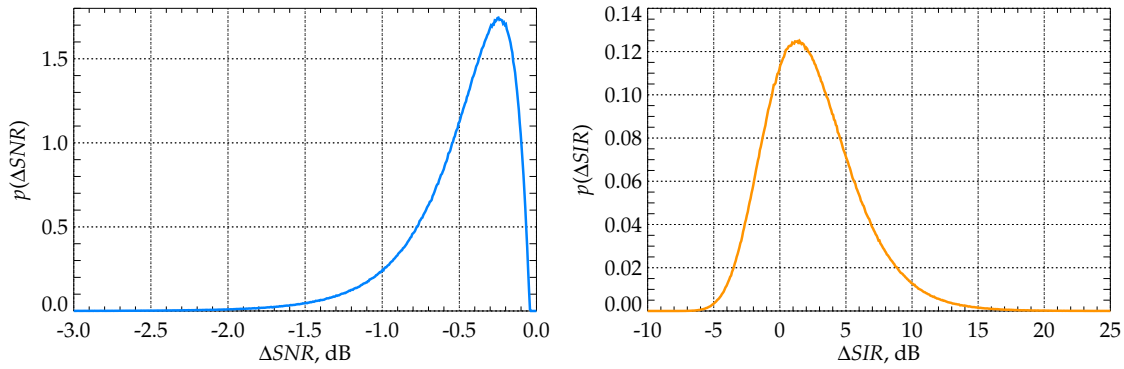

(a) $\vartheta = 0°$ (b) $\vartheta = 2.72°$

Figure 5.26: (a) PDF of the ΔSNR with MVDR beamforming for a relative error a_{rel} of 10 dB at the swath center ($\vartheta = 0°$). (b) PDF of the ΔSIR with LCMV beamforming for a relative error a_{rel} of 50 dB at the swath border.

presence of large random errors. The interference suppression performance is presented in rows five and six. A negative sign in front of the average relative signal-to-interference ratio $\mu_{\Delta SIR}$ means that the interference is actually larger compared to the MVDR beamformer (see equation (5.53)). Not until the error is 50 dB below the pattern maximum the LCMV beamformer produces a slight improvement in interference suppression in the order of 2.5 dB compared to the MVDR beamformer. The corresponding PDF is shown in Fig. 5.26b, where the 0 dB point marks the *SIR* level with MVDR beamforming. The quintessence of the analysis summarized in Table 5.5 is that the magnitude of the errors should not exceed the magnitude of the pattern in the respective direction. That means if for instance an interferer to be suppressed with LCMV beamforming occurs in the first sidelobe of channel pattern a_i, the additive errors Δa_i in the ith channel must not be larger in magnitude than this sidelobe. In contrast MVDR beamforming tolerates much larger errors since here only the mainlobe region is relevant.

6 Optimization Strategies

The performance analysis in chapter 5 demonstrates the potentials of reflector based SAR systems in conjunction with digital beamforming techniques under ideal conditions. However, in practice SAR systems are affected by a variety of systematic as well as random error sources. The influence of some of these errors have been investigated in chapter 5.3. In this chapter optimization strategies shall be introduced which offer the opportunity to mitigate or eliminate the impact of specific errors. In a first assessment alternative beamforming constraints shall be discussed which are more robust with DOA errors. Finally, a very important case is the failure of an entire T/R module, likewise in the transmit or receive path. This error scenario will lead to an innovative reflector concept.

6.1 Digital Beamforming with Robust Constraints

As outlined in chapter 5.3, the error sources can be divided into deterministic errors, like uncertainties in the direction of arrival, and random errors which also result in spatial mismatch. Robust beamforming concepts are for instance introduced in [75], where both random errors in the array manifold as well as DOA errors are covered. Here, the focus shall be laid on uncertainties in the direction of arrival. The basic idea is to formulate robust constraints which tolerate an imprecise knowledge in the direction of arrival to a certain degree. A well known technique in the context of spatial filtering is the application of window functions which suppress the pattern sidelobes. Talking about robust beamforming methods, it should be mentioned that the price of robustness is always a loss of gain or *SNR*. In case of windowing this means that the mainlobe becomes broader while loosing maximum gain at the same time. However, here a more general pattern synthesis optimization approach shall be utilized.

6.1.1 The Digital Sidelobe Canceller

An optimization problem, where the sidelobes are to be minimized while maintaining a maximum in the main beam, can be formulated according to

$$\boldsymbol{A}^{\mathsf{T}}(\vartheta_{\mathrm{t}})\boldsymbol{w} = 1 \,, \tag{6.1}$$

$$\boldsymbol{A}^{\mathsf{T}}(\vartheta_{\mathrm{s}})\boldsymbol{w} \leq \boldsymbol{c} \,, \tag{6.2}$$

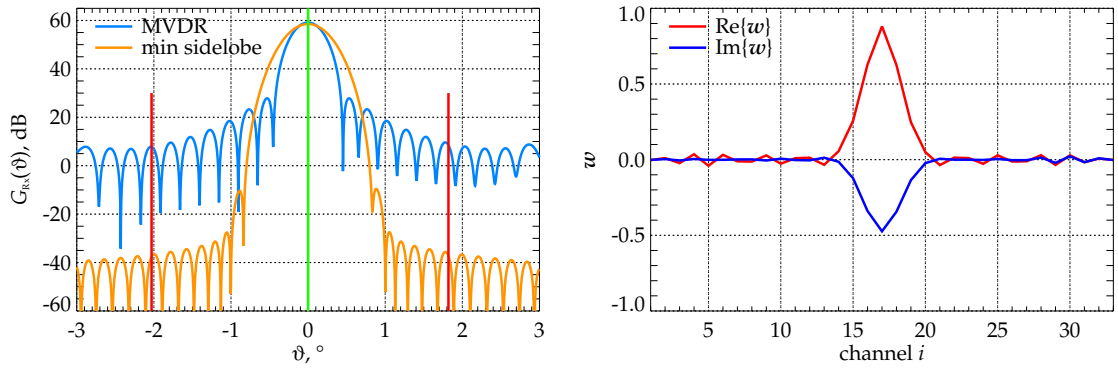

(a) (b)

Figure 6.1: (a) Gain patterns in elevation using MVDR beamforming (blue) and convex optimization (orange), where the sidelobes are to be minimized. The green vertical line indicates the signal of interest and the red vertical lines mark the directions of interference. (b) Complex weight vector corresponding to the DBF pattern with convex optimization.

where $\boldsymbol{A}$ represents the array response matrix, as defined in (D.4), $\boldsymbol{w}$ the unknown complex coefficient vector and $\boldsymbol{c}$ denotes a constraint vector. Note, within a numerical solver the angles ϑ_t and ϑ_s are discrete variables. Here, for the main beam constraint a single angle $\vartheta_t = 0\,°$ is considered, while the stop-band ϑ_s is defined over the angular domains $[-3,-1\,]° \wedge [1,3\,]°$, which are uniformly discretised with 20 angles in each domain. Here, the choice of the stop-band serves as demonstration example. In a real SAR system, for instance, the first two range ambiguities on both sides of the main beam could be suppressed in this way. This set of inequalities can be solved efficiently using the *disciplined convex programming* toolbox `cvx` [34], developed for MATLAB [81], as a so called *feasibility problem*. The result for the reflector antenna example given in Tables 5.1 and 5.2 is presented in Fig. 6.1a. Here, essentially the same interference scenario, as in the error analysis in Fig. 5.25a, is considered. Again indicated in green is the direction of interest and in red the directions of the interferers, respectively. Compared to the reference case with MVDR beamforming the sidelobes are reduced significantly over a wide range of elevation angles ϑ. Clearly, in a case where the directions to be suppressed are not too close to the main beam, this approach could be an interesting alternative, where no accurate knowledge of the directions of the interferers is required. The gain loss in comparison to MVDR beamforming is with -0.627 dB moderate. In Fig. 6.1b the correspond-

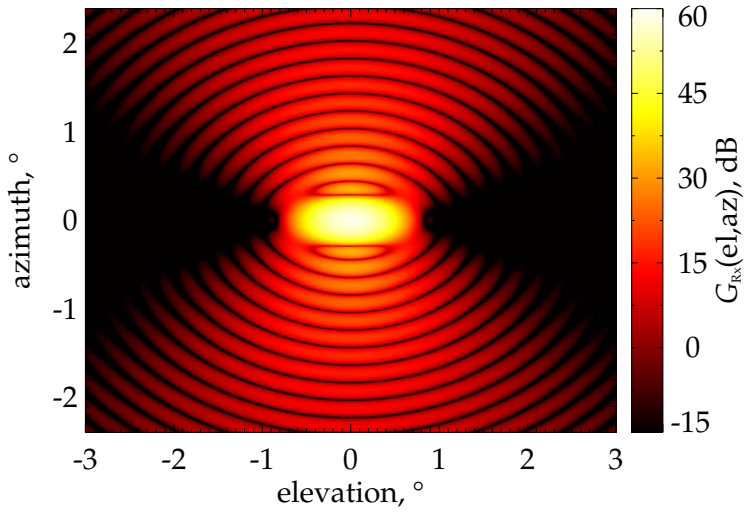

Figure 6.2: Two-dimensional representation of the gain pattern with sidelobes minimized in elevation.

ing imaginary- and real parts of the complex weight vector are presented. The main contribution in terms of electromagnetic power is delivered by elevation feed channels 14 to 19. Due to the broadening of the mainlobe this beamformer is also more robust with respect to errors in the direction of the signal. That means larger DOA errors can be tolerated. However, the directions of the interferences put a limit on the maximum mainlobe width. The two-dimensional gain pattern plot in Fig. 6.2 shows a distinct cancellation of the sidelobes in elevation, while the sidelobes in azimuth are almost unaffected.

6.1.2 LCMV Beamforming as Spatial Band-Stop Filter

The logical continuation of the LCMV method, where single nulls are placed within the interferer directions, as introduced with (4.58) and (4.59), is to widen these nulls, such that errors in the estimation of these interferer directions do not affect the SAR performance in terms of range ambiguity suppression. For the use within cvx this optimization problem can be stated according to

$$\text{minimize} \quad \boldsymbol{w}^{\mathsf{T}} \boldsymbol{R}_v \boldsymbol{w}^{*} \tag{6.3}$$

$$\text{subject to} \quad \boldsymbol{A}^{\mathsf{T}}(\vartheta)\boldsymbol{w} = \boldsymbol{c}\,, \quad \boldsymbol{A} \in \mathbb{C}^{N_c \times N_{\text{dir}}} \tag{6.4}$$

Here, again perfectly balanced channels $\boldsymbol{R}_v = \sigma_v^2 \mathbf{I}$ are assumed. The constraint vector $\boldsymbol{c}$ now contains a single '1' in the direction of interest, but in contrast to

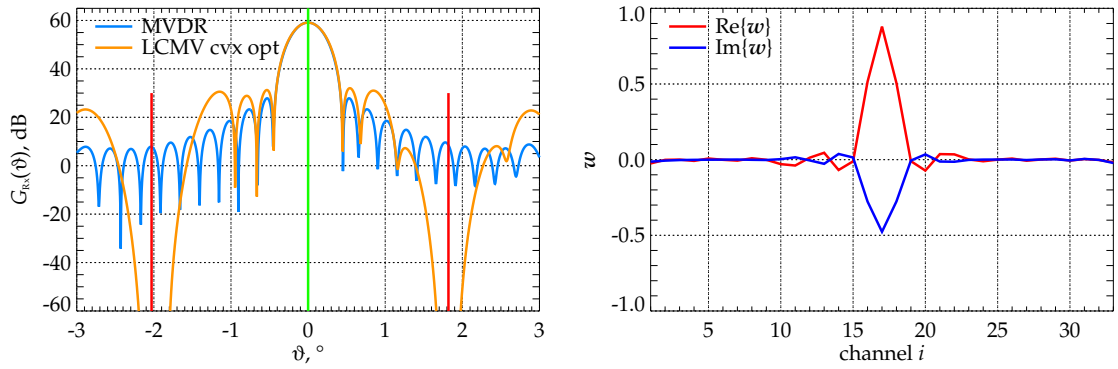

(a) (b)

Figure 6.3: (a) Gain patterns in elevation using MVDR beamforming and with convex optimization, where a domain around the interferences is suppressed. The green vertical line indicates the signal of interest and the red vertical lines mark the directions of interference. (b) Complex weight vector corresponding to the DBF pattern with convex optimization.

the initial approach, several nulls for each individual interferer direction

$$\boldsymbol{c}^{\mathsf{T}} = \begin{bmatrix} 1 & 0 & \dots & 0 \end{bmatrix}. \tag{6.5}$$

In the beamforming example in Fig. 6.3 21 zeroes are placed uniformly in an interval $\pm 0.1\,^{\circ}$ around each interference direction. As can be observed in Fig. 6.3a the effectively damped angular domain is well beyond this $0.2\,^{\circ}$ interval, making this DBF approach very robust in terms of interference suppression. This approach would even allow to suppress nadir returns. These kind of natural interferers might behave rather like large-scale targets so that the point target hypothesis might not hold. In comparison to the MVDR beamformer the main beam is well preserved with a slight gain loss of -0.043 dB. The two-dimensional pattern plot in Fig. 6.4 demonstrates that the suppressed domains around the interferers are of circular shape, although the constraints in equation (6.4) have been set for an azimuth angle of $0\,^{\circ}$. This means that such an approach would be robust against DOA errors in the two-dimensional spherical coordinate system (ϑ, φ).

In the context of range ambiguity suppression another benefit concerning such a beamforming strategy should be mentioned. Typically the SAR pulse duration is several ten microseconds, for the design example in tables 5.1 and 5.2 it is 35.7 µs. Consequently, for this imaging geometry, the projection of the

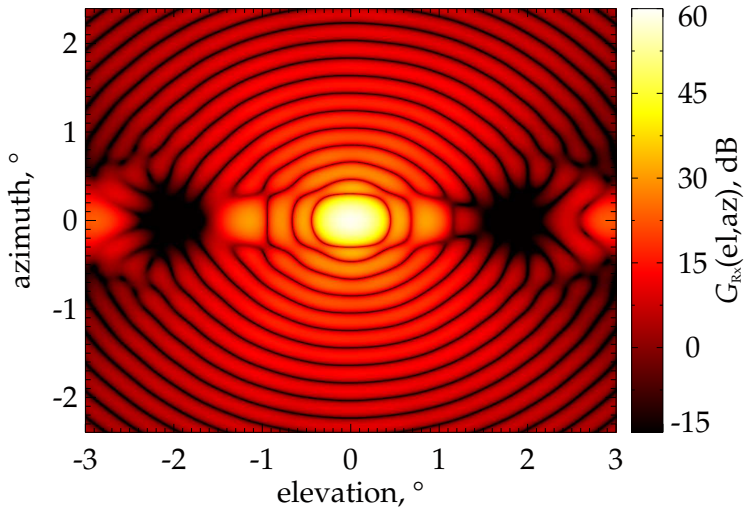

Figure 6.4: Two-dimensional representation of the gain pattern with convex optimization.

pulse on ground occupies an angular domain of 0.68 ° (see equation (3.23)). It is evident that if the angular domain where range ambiguities are to be expected is large enough, the temporal FIR filters $\overline{h}$ in (4.77) of the complex realtime beamformer hardware might be dispensable. This is because the complete pulse would fall into such an extended pattern zero. Instead the simple SCORE operation principle would be sufficient. Of course in terms of *SNR* a loss will be present, as demonstrated in chapter 5. The range ambiguity ratios taking into account the pulse duration, using a simplified version of equation (4.93) writes

$$RASR(\vartheta) = \frac{\sum\limits_{l\in\{-1,1\}} \sum_{N_\mathrm{p}} |\boldsymbol{a}^\mathsf{T}(\vartheta_l)\boldsymbol{w}(n)|^2}{\sum_{N_\mathrm{p}} |\boldsymbol{a}^\mathsf{T}(\vartheta)\boldsymbol{w}(n)|^2} \,. \tag{6.6}$$

For $\vartheta = 0°$ this results in a *RASR* of -47.058 dB for the MVDR beamformer, -45.235 dB for the conventional LCMV beamformer placing a strict zero at the directions of the two range ambiguities and -80.682 dB for LCMV beamforming with broader ambiguity suppression. The fact that here the conventional LCMV beamformer performs worse compared to the MVDR beamformer is not surprising. Forcing a zero in a sidelobe often involves an overshooting of adjacent sidelobes. This can for instance be observed in Fig. 5.6 at the ambiguity position at approximately $\vartheta = -3°$. Here, on the right side of the ambiguous direction a strong sidelobe appears. Clearly with a long duration pulse a larger amount of ambiguous signal energy would be collected with this sidelobe. How-

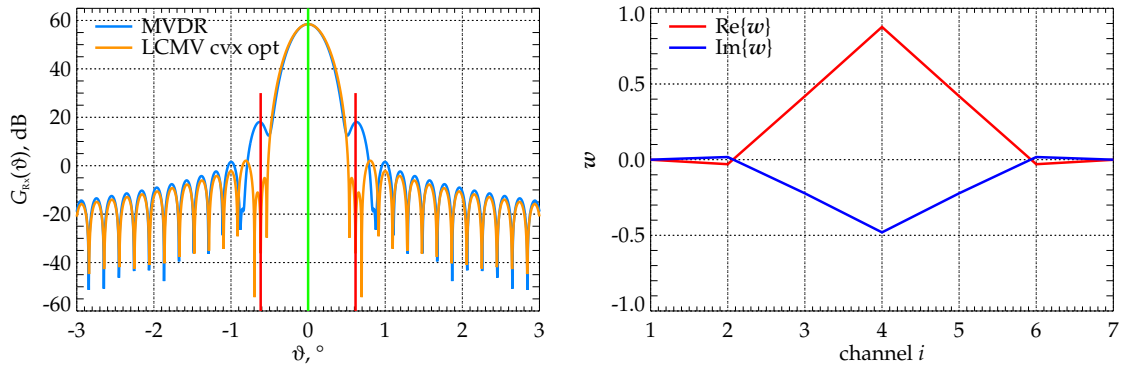

(a) (b)

Figure 6.5: (a) Gain patterns in azimuth using MVDR beamforming (blue) and convex optimization (orange), where a small region around the first two azimuth ambiguities is damped. The green vertical line indicates the signal of interest and the red vertical lines mark the directions of the ambiguities. (b) Complex weight vector corresponding to the DBF pattern with convex optimization.

ever, one should keep in mind that the price of this approach is a gain loss due to temporal mismatch, as investigated in chapter 5.2.1, in the order of four to five decibels. Insofar a combination of temporal waveform adaptive filtering techniques and robust weight selection provides the best performance.

Finally, an example is investigated, where the DBF approach defined via equations (6.3) and (6.4) is applied to the azimuth case. Concerning the definition of the constraints, it turns out that the number of directions N_{dir} should not be much larger than the number of available channels N_{c}. Otherwise the numerical solver might not converge. For our reflector example the number of channels in azimuth is seven. In a high-resolution wide-swath SAR scenario the azimuth case is of special interest, since the azimuth ambiguities occur in close vicinity to the main beam. In Fig. 6.5a an azimuth pattern with ambiguities at $\pm 0.615\,^{\circ}$ is presented. Compared to the MVDR beam the gain loss is -0.014 dB, while the improvement in ambiguity suppression is significant. Due to the small number of azimuth channels, the number of constraint directions is also in this order. Here, three directions for each azimuth ambiguity have been chosen, which can be well observed in the pattern plot. Equally, the corresponding 2-D pattern image in Fig. 6.6 suggests that such an approach is beneficial for beamforming in azimuth.

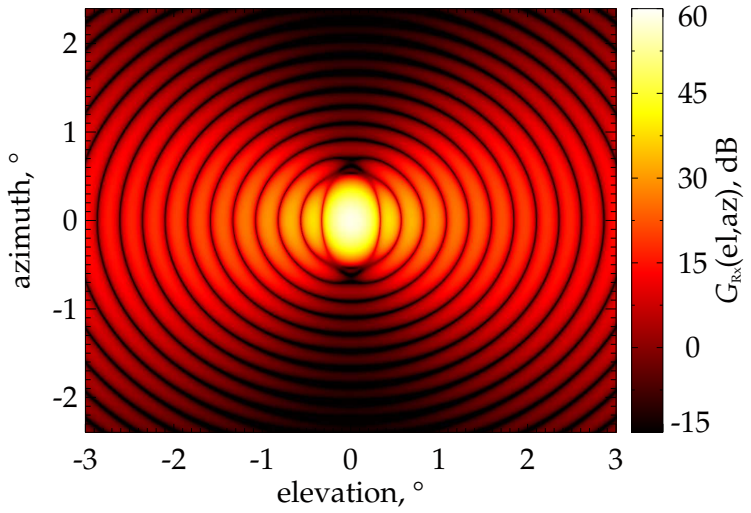

Figure 6.6: Two-dimensional representation of the gain pattern using convex optimization.

6.2 A Reflector Concept Robust against Feed Failures

Reflector antennas generate a shaped beam due to the mechanical molding of the reflector dish. That means, for any given feed position, only a certain solid angle can be illuminated. Therefore, a set of multiple feed elements is required in order to cover the complete angular domain of interest. It is evident that such systems are severely handicapped in case of a feed element failure. A dropped out element would cause a 'blind' spot in the antenna footprint. Therefore, state-of-the-art systems are planed with redundant receiver hardware. Clearly this option poses a considerable increase of the costs for satellite SAR systems. Moreover, the redundant electronics, as for example additionally required switches, will produce losses.

The most widely established spaceborne SAR antenna is the planar array antenna. This kind of antenna is robust against a single or even multiple element failures in terms of beam shape stability. The reason for this is that the element patterns have almost perfect overlap in the angular domain. The drawback is clearly that the antenna size required to realize a high-resolution wide-swath SAR system can render a SAR mission infeasible concerning the costs. Consequently, an antenna design is needed, which combines the robustness against element failure of a planar array antenna with the high gain of a large unfoldable low-weight reflector antenna. This concept involves a defocusing of the individual element beams by utilizing a modified reflector surface.

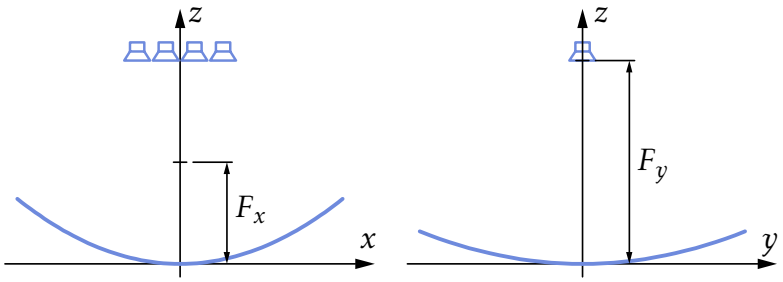

Figure 6.7: Cut drawings of a parabolic reflector with two foci. The linear feed array, indicated by the antenna symbols, is placed at the upper focal point at $[0, 0, F_y]$.

6.2.1 One-dimensionally Defocused Reflector Antennas

The concept of defocusing a reflector antenna is not new. Publications like [14, 91, 133] achieve a defocusing by moving the feed out of the focal point, $(x_f, y_f, z_f) = (0, 0, 0)$ in Fig. 3.3, and leave the shape of the reflector antenna unaltered. The advantage is that conventional reflectors with paraboloidal or cylindrical surfaces can be utilized. If, however, a defocusing is desired in only one dimension, for example in elevation, a simple displacement of the feed array would not be satisfying, since the pattern tends to symmetrically defocus in all dimensions. For example a paraboloidal reflector with an axially shifted feed will, compared to the focused case, generate a broader rotationally symmetric Bessel-like beam.

The favored method to defocus a reflector antenna is to shape the reflector surface itself [43]. The starting point is a parabolic reflector. Such a shape is generated by rotating a parabola for example around the z-axis, as in Fig. 3.3. Characteristic for such shapes is that a plane wave incident anti-parallel to the z-axis is focused in the so called focal point. A simple method to defocus a parabolic reflector is to construct a reflector with two focal points. Such a geometry can be described in cartesian coordinates as

$$z = \frac{x^2}{4F_x} + \frac{y^2}{4F_y}\,, \tag{6.7}$$

where F_x and F_y denote the focal lengths in the x- and y-dimension, respectively, as given in the cut drawings in Fig. 6.7. Figure 6.8 shows a perspective view of the dual focus reflector antenna with a circular projected aperture. The linear feed array is placed in the upper focal plane parallel to the x-axis in a centered position. Here, the feed elements radiate in negative z-direction. In a real SAR system, the outer feed elements could be tilted slightly, in order to provide a more homogeneous illumination of the reflector. Also bent feed array structures

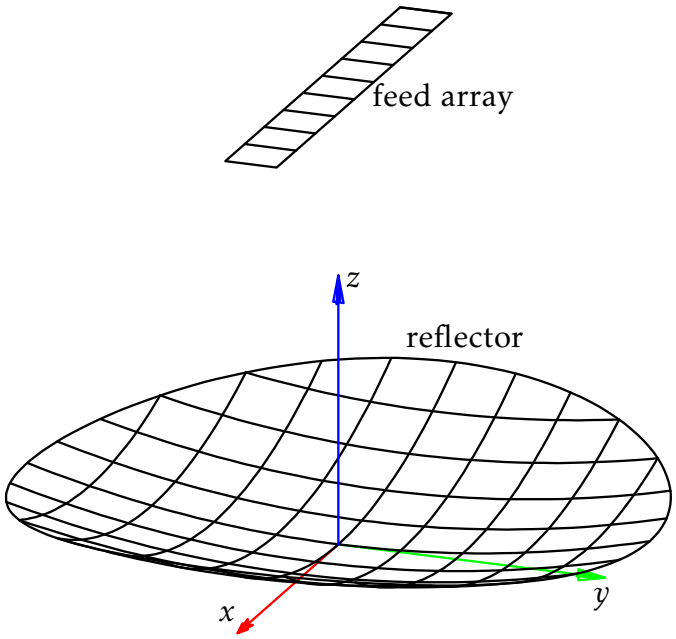

Figure 6.8: Perspective presentation of the dual focus reflector antenna with feed array in the upper focal point.

might be of interest. The defocusing effect has been analyzed by simulation of the two-dimensional electromagnetic field distribution in the focal plane $z = F_y$. Figure 6.9a shows the z-component of the power flux density or Poynting vector

$$\boldsymbol{S} = \boldsymbol{E} \times \boldsymbol{H}\,, \tag{6.8}$$

as a function of the Cartesian coordinates x and y. Recall, here the x-direction shall be associated with elevation and the y-direction with azimuth. This power density distribution is the result of a plane wave propagating anti-parallel to the z-direction and being scattered by the dual focus reflector. Clearly one can observe that the power density is concentrated in azimuth direction and distributed over a larger domain in the elevation direction, as desired by design. The squares shall represent the elements of the linear feed array. Here, black squares denote feed elements which receive the electromagnetic field above a given threshold. Consequently, those feed elements 'see' the afore mentioned plane wave and serve as 'redundant' elements in case of a drop out. For comparison, the power density distribution for a conventional single-focus reflector is depicted in Fig. 6.9b. The power density is concentrated around the focal point as expected. In case of a failure of the center element, the neighboring elements are not able to catch enough field energy to compensate the gain loss.

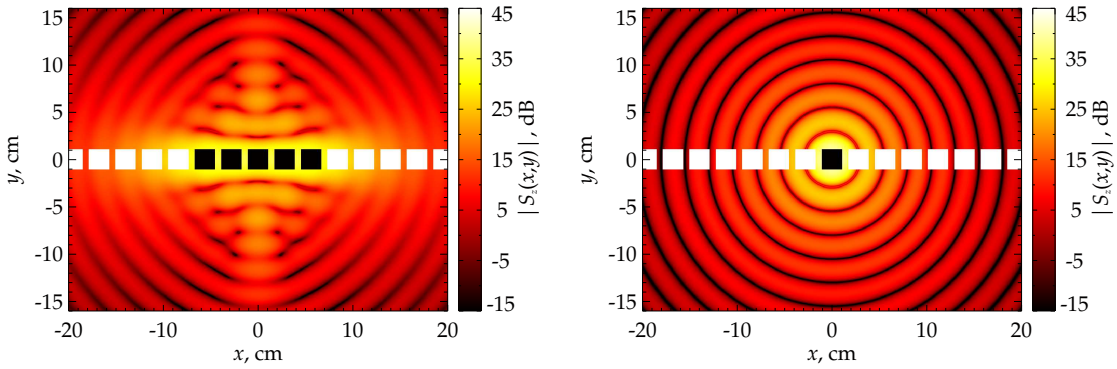

(a) dual-focus (b) single-focus

Figure 6.9: Power density distribution in the upper focal plane for a defocused reflector (a) with two foci and for a conventional single-focus parabolic reflector (b) in the focal plane. The squares represent feed array elements, of which the black ones denote elements receiving the field above a certain threshold.

6.2.2 Performance

The more common way to examine an antenna's performance is to look at the gain patterns. Therefore, the co- and cross-polar components of the electric far field for a reflector antenna with the specifications given in Table 6.1 have been simulated, using the EM simulation software TICRA GRASP [118]. Here, each feed element pattern is simulated by a linearly polarized Gaussian beam. For reciprocity reasons from the power density distribution shown in Fig. 6.9a it can be expected that the individual antenna patterns will also broaden and suffer a

parameter	**value**
frequency	9.65 GHz
reflector diameter	7 m
focal length (single-focus)	5 m
focal lengths (dual-focus)	$F_x = 4.95$ m, $F_y = 5.05$ m
number of feed elements	35
feed element spacing (single-focus)	0.9λ
feed element spacing (dual-focus)	$0.8 \ldots 0.9\,\lambda$

Table 6.1: Antenna parameters for a single-focus reflector and a reflector with two foci.

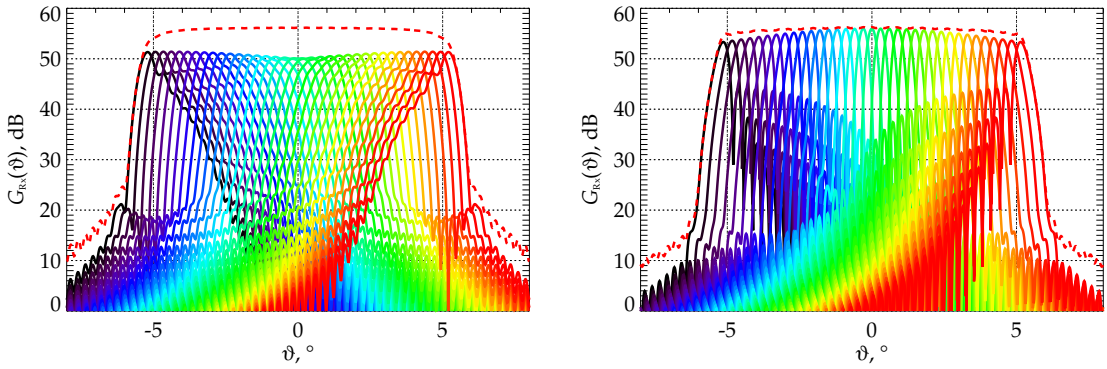

(a) dual-focus

(b) single-focus

Figure 6.10: Co-polar gain patterns for the dual-focus reflector (a) and the single-focus reflector (b) with 35 feed elements. The solid lines represent the individual patterns while the dashed line shows the pattern after digital beamforming on receive.

gain loss. This can be observed in the elevation cut plot in Fig. 6.10a. Each gain pattern corresponds to a feed element, or channel. The most right pattern in Fig. 6.10a belongs to the most left feed element in Fig. 6.9a (not visible in this plot). Again, for comparison, the analogous plot for a conventional single-focus reflector antenna is shown in Fig. 6.10b. Here, the sharp angular separation between the individual channel patterns can be recognized.

Clearly, the defocused reflector antenna unfolds its full potential in conjunction with digital beamforming techniques. Especially under failure conditions it is reasonable to rely on beamforming techniques which balance the gain loss, or optimize the *SNR*, respectively. Predestined for such a task is the MVDR beamformer, as introduced in chapter 4.3.3, with its analytical solution

$$\boldsymbol{w}^*(\vartheta) = \frac{\boldsymbol{R}_v^{-1}\boldsymbol{a}(\vartheta)}{\boldsymbol{a}^{\mathsf{H}}(\vartheta)\boldsymbol{R}_v^{-1}\boldsymbol{a}(\vartheta)} \,. \tag{6.9}$$

Here, for the purpose of illustration the noise has been neglected ($\boldsymbol{R}_v \sim \mathbf{I}$) and the signal has been set to one. For the array manifold $\boldsymbol{a}$ simply the co-polar electric field is inserted, yielding

$$\boldsymbol{a}(\vartheta) = \left[E_1(\vartheta) \quad E_2(\vartheta) \quad \dots \quad E_{N_x}(\vartheta)\right]^{\mathsf{T}}_{\mathrm{co-pol}} \,, \tag{6.10}$$

with the number of elevation channels N_x being 35 in this case. This results in gain patterns on receive, as plotted with dashed red lines in Figs. 6.10a and

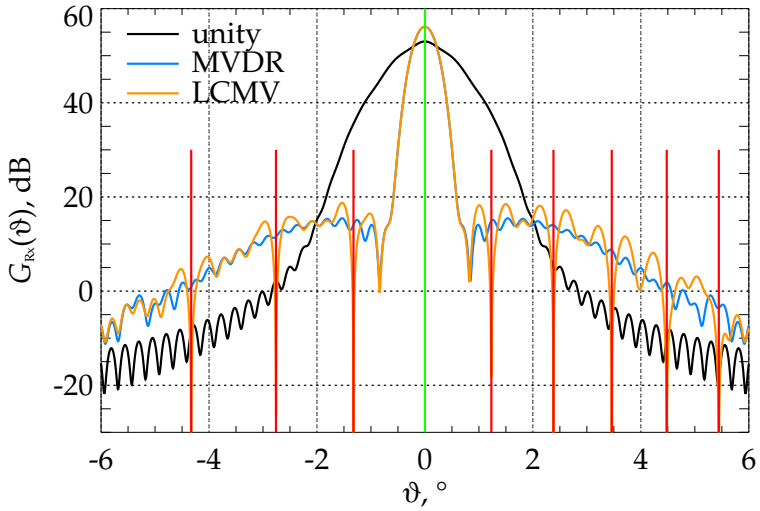

Figure 6.11: Gain pattern after digital beamforming with the dual-focus antenna for the three approaches unity, MVDR and LCMV beamforming. The vertical green line represents the signal direction and the vertical red lines denote the directions of range ambiguities.

6.10b, according to

$$G_{\mathrm{Rx}}(\vartheta) = \boldsymbol{a}^{\mathrm{H}}(\vartheta)\boldsymbol{a}(\vartheta)\,. \tag{6.11}$$

Figure 6.11 shows gain patterns after digital beamforming in elevation for the dual-focus antenna with unity, MVDR and LCMV beamforming. The main beam is directed towards the angle $\vartheta = 0\,°$, indicated by the vertical green line, while the range ambiguities are marked by vertical red lines. Here the imaging geometry defined in Table 5.1 at a *PRF* of 15 kHz has been taken as basis. This result shows that the dual-focus antenna has no different restrictions compared to the single-focus case in terms of interference suppression. With respect to the maximum gain, MVDR and LCMV beamforming are almost identical, whereas the unity approach, with five activated channels in this example, produces a significantly lower gain in the direction of the signal. Even more problematic is the broad pattern after unity beamforming, which would capture large amounts of ambiguous signal energy. Insofar this simple beamforming approach is inappropriate for most SAR imaging scenarios using dual-focus reflector antennas.

Generally, for any choice of the weight vector $\boldsymbol{w}$, the precise knowledge of the embedded complex array patterns $\boldsymbol{a}$ is relevant. That means, effects from multipath propagation or reflector surface imperfections, which potentially deteriorate the single-channel characteristic, will not impact severely the beam shape

after applying the complex weights. Insofar digital beamforming allows to tolerate even unknown error sources to a certain degree, as long as the array manifold is known accurately enough. In practice, this knowledge can be obtained via a calibration campaign over rain forest.

6.2.3 Performance under Failure Conditions

The initial question was how such a defocused reflector SAR system performs when a feed element fails. Basically two failure scenarios can be distinguished, a disruption in the transmit paths, for example caused by a loss of high power amplifiers, and failures in the receive chain. Figure 6.12a shows the normalized transmit gain pattern G_{Tx} when elements 18, 24 and 33, counting from right to left, fail. Such a large number of lost elements is an unrealistic scenario and serves here only for illustration purposes. For instance, the German SAR satellite TerraSAR-X uses phased array antenna technology with 384 transmit/receive modules. Since the launch of the satellite five years ago, all T/R modules are working properly. The single-focus system sustains a 12 dB gain loss at the center of the pattern, decreasing towards the border of the pattern. The defocused reflector is able to keep the gain loss on a constant level of roughly 3 dB. Indicated by the dashed red line is the result of a phase-only pattern synthesis, taking into account the four elements 22, 23, 25 and 26 around the failed element 24. This attempt shows that there might be the potential to further reduce the effects from a lost element on transmit for defocused reflector systems by a proper weight selection.

On receive the situation is different. Here, at every time instance, or at every elevation angle ϑ, respectively, a new beam is formed. However, even with the MVDR beamformer the single-focus reflector is prone to large gain losses in the order of 12 dB at the pattern center, as indicated in Fig. 6.12b. The potential of the defocused reflector in combination with digital beamforming techniques becomes evident, when looking at the solid red curve in Fig. 6.12b. With MVDR beamforming the gain loss can be significantly reduced. As reference the pattern, where no special DBF techniques are applied, is plotted (dashed red curve and denoted with unity). In this case only the five elements receiving the highest power (compare to Fig. 6.9a) are activated on receive.

6.2.4 Discussion

As stated in the beginning, a major cost driver for a reflector based SAR system is the feed array, including feed antennas and electronics. In order to minimize the number of feed elements a relatively large feed element spacing of $0.8\,\lambda$ to $0.9\,\lambda$ (see Table 6.1) has been chosen. As can be observed in Fig. 6.12b

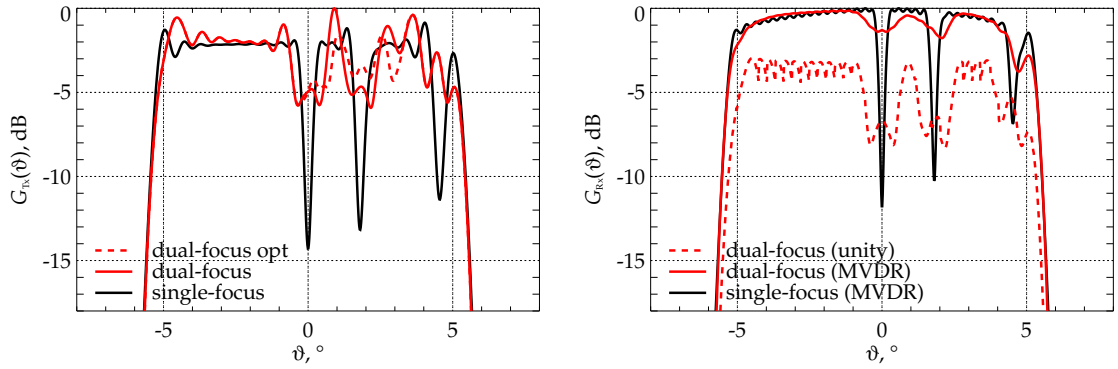

(a) transmit case (b) receive case

Figure 6.12: (a) The solid lines represent the normalized gain patterns on transmit for the single- and the dual-focus reflector, with failed elements 18, 24 and 33. Indicated by the dashed line is a heuristically optimized pattern, using phase-only synthesis methods. (b) Normalized gain pattern after digital beamforming on receive, with elements 18, 24 and 33 dropped out. The dashed line shows the receive pattern without DBF techniques, when only five elements are turned on at a time instance.

this causes a basically unwanted ripple on the gain pattern after digital beamforming for the conventional single-focus reflector system. With the dual-focus system the ripple vanishes and a smooth gain pattern over the entire swath can be realized. Despite the defocusing it shows that reflector SAR systems in general suffer from gain loss, if an element at the edge of the array fails. The consequence is a reduced swath width, which can be illuminated adequately. A possible strategy is to add two or three feed elements on both sides, which serve as redundant elements. This is still a more cost efficient solution than doubling the whole number of transmit-receive modules. A more general approach could be to optimize the reflector surface together with the feed array. This might involve feed arrays with new geometrical shapes. As demonstrated in the previous section, defocused reflector SAR systems unfold their full potential only in conjunction with DBF techniques.

Of special importance for polarimetric SAR applications is the polarization purity. Reflector antennas can introduce cross-polarized signal power, contaminating the co-polar signal, in two ways, first by the reflector itself and second by the feed antenna. Here, the focus has been laid on the effects induced by the reflector assuming ideal feed antennas. Field simulations of the cross-polar

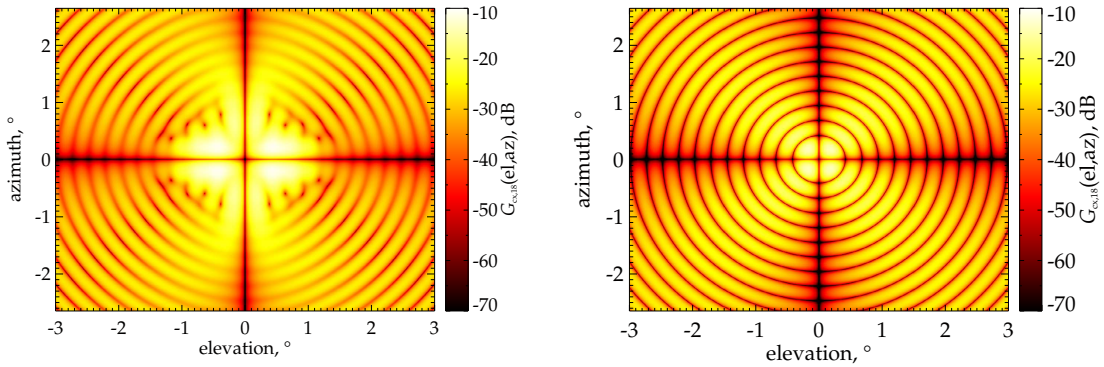

(a) dual-focus (b) single-focus

Figure 6.13: Cross-polar gain pattern for the center element for the defocused reflector (a) and the single-focus reflector (b).

patterns (see Fig. 6.13) show in case of the single-focus reflector, that the gain maximum varies between -13.9 dB for the center element and 13.0 dB at the feed array edges, while in the dual-focus case the gain maximum for the same feed elements varies between -10.8 dB and 10.4 dB, respectively. Although the cross-polar levels for the center feed element of the dual-focus reflector rises, this analysis shows that the defocusing seems to balance the peak cross-polar levels and therefore does not effect polarimetric operation negatively. However, in case of stronger cross-polar pattern components the DBF technique presented in chapter 4.4.3 might become relevant.

In real SAR systems essentially two types of feed antennas, depending on the frequency band, are of interest. For example, L-band or P-band systems commonly use patch antennas, while in X-band also horn antennas are an alternative. Due to the dense packing of the feed antennas, effects from coupling become more pronounced compared to direct radiating arrays with large inter-element spacings. However, with the same reasoning as in chapter 6.2.2, the performance after digital beamforming will be impacted only marginally, assuming a precise knowledge of the complex patterns.

7 Digital Beamforming Demonstrator

Spaceborne SAR systems based on large unfoldable mesh reflector antenna technology in conjunction with digital signal processing onboard the spacecraft represent a quantum jump in next generation Earth observation systems. Therefore, it is imperative to study the feasibility of such concepts by means of demonstrators. The demonstrator developed at the Microwaves and Radar Institute of the German Aerospace Center is a stationary ground-based system operated in X-band. The conceptual idea was to create a design, which mimics a scaled version of a potential spaceborne reflector SAR system as close as possible. The main parts of the demonstrator are the transmit and receive hardware block, with the specifications summarized in Table 7.1 and the reflector combined with a linear feed array [95]. The parabolically shaped reflector with elliptic aperture is faced by eight standard gain horns, as depicted in Fig. 7.1. Each gain horn represents a receive channel, whose signal is individually amplified, down converted, digitized and recorded for further processing on a personal computer. Not shown in Fig. 7.1 is the transmit antenna. The transmit horn antenna, is installed below the receive array and points directly to the scene to be illuminated. Due to the large spacing of the receive feed horns of 4.4 cm, which is dictated by the base plate dimensions of the horns (see Fig. 7.1b), the mutual pattern overlap between adjacent channels is relatively small, as can be observed in Fig. 7.2a. This plot shows the individual far field patterns after deflection at the reflector. The corresponding phase patterns are presented in Fig. 7.2b, where the phases in the mainlobe region above a minimum gain of 15 dB

parameter	**value**	**parameter**	**value**
RF frequency range	9.43 … 9.73 GHz	large apert. diam.	1.0 m
RF center frequency	9.58 GHz	small apert. diam.	0.7 m
LO frequency	9.375 GHz	focal length	0.5 m
IF center frequency	205 MHz	offset	0.35 m
max. bandwidth	300 MHz	number of chan.	8
max. output power	15 dBm	feed spacing	4.4 cm
max. ADC sampl. r.	2 GS/s per ch.	polarizations	hh, hv, vh, hh
ADC resolution	10 bit	height above gr.	12.8 m

Table 7.1: Specification of the ground-based reflector DBF demonstrator in X-band configuration.

(a) (b)

Figure 7.1: (a) Parabolic reflector with elliptic aperture and attached feed array. (b) Feed array comprising eight 10 dB standard gain horns spaced 4.4 cm.

are shown. Although the reflector antenna is designed such, that the symmetry plane runs through zero degree in Fig. 7.2, both plots reveal a certain asymmetry, which is explained partly by imperfections in the mechanical construction process. These complex patterns have been acquired in the anechoic chamber of DLR's TechLab and serve as input for all a priori knowledge based digital beamforming experiments presented in the following. The experiments are intended to verify selected digital beamforming concepts introduced in chapter 4

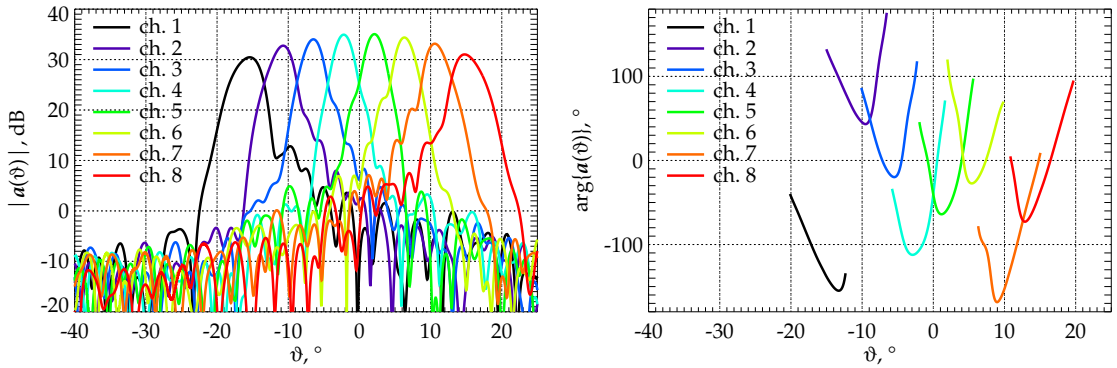

(a) (b)

Figure 7.2: (a) Principal H-cut of the vv co-polar channel patterns, measured in the anechoic chamber at 9.58 GHz. (b) Corresponding phase patterns inside the mainlobe regions above a threshold of 15 dB.

at least in their core functionalities.

7.1 Data Preprocessing

The multi-channel radar data are recorded as really sampled signals $u_{\mathrm{IF,r},i}(t)$ in the intermediate frequency (IF) band. That means in the first preprocessing step the analytic signal needs to be generated. The ith analytic channel signal $u_{\mathrm{IF},i}(t)$ is found with the Hilbert transform $\mathcal{H}\{.\}$ (see appendix H) according to

$$u_{\mathrm{IF},i}(t) = u_{\mathrm{IF,r},i}(t) + \mathrm{j}\mathcal{H}\{u_{\mathrm{IF,r},i}(t)\} \,. \tag{7.1}$$

Note, the Hilbert transformer is a non-causal *infinite impulse response* (IIR) filter and has therefore to be approximated by a FIR filter. Consequently, small artifacts might be present in the analytic signal.

The second preprocessing step is the down conversion of the intermediate frequency band signal $u_{\mathrm{IF},i}(t)$ to baseband

$$u_i(t) = u_{\mathrm{IF},i}(t) \cdot \mathrm{e}^{-\mathrm{j}2\pi f_{\mathrm{IF}} t} \,. \tag{7.2}$$

With this, the data are available for the further digital processing.

7.2 Demonstration of Principle: Unity and MVDR Beamforming

The very basic digital beamforming concept, common to the investigated processing schemes in elevation or azimuth, is the application of weights to SAR data according to equations (4.20), (4.29) or (4.76) and (4.77). Therefore, the first DBF experiment aims at a verification of the expected improvement in gain or *SNR*, respectively, of these linear combinations. For this, the multi-channel radar demonstrator has been mounted on top of DLR's TechLab building as schematically indicated in Fig. 7.3. The reflector with feed array is aligned horizontally and pointing to the target object, a corner reflector. The corner reflector has been placed on ground in a distance of $r_0 = 47.5\,\mathrm{m}$ such, that it is seen under the horizontal angle $\vartheta = 0\,^\circ$ between channel patterns four and five (see Fig. 7.2). The placement in the intersection of two adjacent channel patterns shall guarantee the largest benefit with digital beamforming in terms of gain or *SNR*, respectively. Ideally this gain improvement should be roughly 3 dB for MVDR beamforming, since all other channels will not contribute significantly.

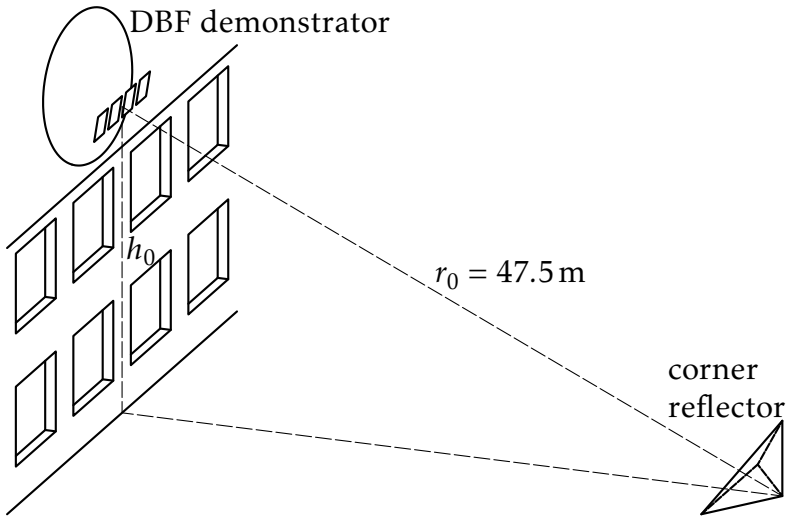

Figure 7.3: Simple measurement setup with a single corner reflector. The digital beamforming demonstrator is mounted on the roof of DLR's TechLab building (height $h_0 = 12.8\,\mathrm{m}$).

For this basic experiment it proofs useful to range compress the channel signals, as introduced in chapter 4.2.2, prior to digital beamforming[1]. This method collects most of the signal energy reflected by the trihedral in a single range resolution cell of size 0.5 m, resulting in a signal with optimal *SNR*. The normalized range compressed channel signals $\boldsymbol{u}_{\mathrm{rc}}(r)$ as function of slant range r are shown in Fig. 7.4a. Already from this plot it becomes evident that the trihedral had been placed with a slight horizontal angular offset, since the echo of the corner reflector in channel five is weaker compared to the one in channel four. The exact angular offset can be estimated using the well known *multiple signal classification* (MUSIC) algorithm [106], showing a peak at $\vartheta_0 = -0.36\,^\circ$ (see Fig. 7.4b). Given the direction of arrival, the array manifold $\boldsymbol{a}$, shown in Fig. 7.2, at angle ϑ_0 can be assigned to the target location in the range compressed data $\boldsymbol{u}_{\mathrm{rc}}$, depicted in Fig. 7.4a, at slant range distance r_0. The performance in terms of *SNR* can then be evaluated with the help of equation (5.24) at the position of the trihedral according to

$$SNR_{\boldsymbol{u}_{\mathrm{rc}}}(r_0) = \frac{|\boldsymbol{u}_{\mathrm{rc}}^{\mathsf{T}}(r_0)\boldsymbol{w}(\vartheta_0)|^2}{\boldsymbol{w}^{\mathsf{T}}(\vartheta_0)\boldsymbol{R}_{\boldsymbol{v}}(r_0)\boldsymbol{w}^{*}(\vartheta_0)} - 1\,. \tag{7.3}$$

[1] Here the measured channel replica serve as range compression filters, performing a basic calibration of the internal signal paths of the hardware unit. Also an amplitude calibration of the range compressed signal, based on the replicas, is introduced in order to equalize channel imbalances.

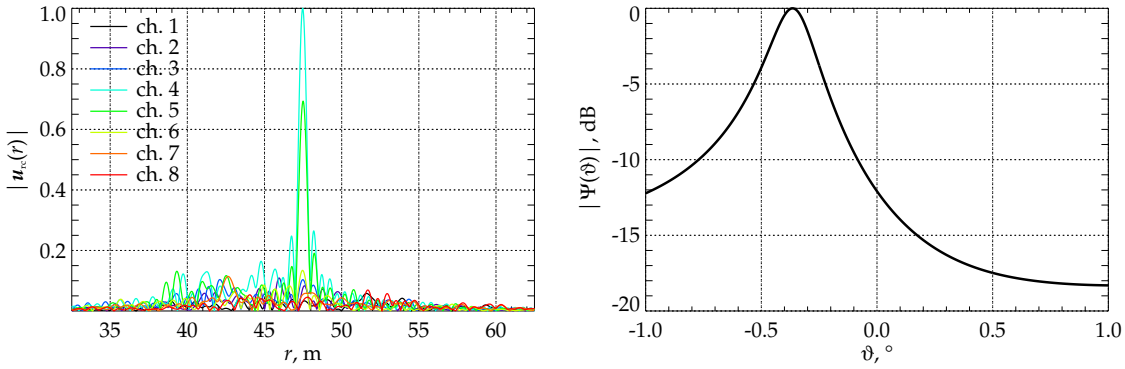

(a) (b)

Figure 7.4: (a) Received signals after range compression for the individual channels. (b) MUSIC spectrum $\Psi(\vartheta)$ with a maximum at the direction of the corner reflector at $\vartheta_0 = -0.36°$.

Note, the term '-1' is required since $\boldsymbol{u}_{\mathrm{rc}}$ contains signal as well as noise. As reference, for comparison purposes, also the DBF gain is computed, which can be interpreted likewise as *SNR*

$$SNR_{\boldsymbol{a}}(r_0) = \frac{|\boldsymbol{a}^{\mathsf{T}}(\vartheta_0)\boldsymbol{w}(\vartheta_0)|^2}{\boldsymbol{w}^{\mathsf{T}}(\vartheta_0)\boldsymbol{R}_{\boldsymbol{v}}(r_0)\boldsymbol{w}^{*}(\vartheta_0)} \,. \tag{7.4}$$

The results are plotted in Fig. 7.5 as function of the number of activated channels N_{act} for unity as well as MVDR beamforming. Here, the *SNR* values have been normalized according to

$$\Delta SNR_{\boldsymbol{u}_{\mathrm{rc}}} = \frac{SNR_{\boldsymbol{u}_{\mathrm{rc}}}}{SNR_{\boldsymbol{u}_{\mathrm{rc}},\mathrm{MVDR}}(N_{\mathrm{act}} = 1)} \,, \tag{7.5}$$

$$\Delta SNR_{\boldsymbol{a}} = \frac{SNR_{\boldsymbol{a}}}{SNR_{\boldsymbol{a},\mathrm{MVDR}}(N_{\mathrm{act}} = 1)} \,, \tag{7.6}$$

where the respective *SNR* values for unity or MVDR beamforming are inserted in the numerator. The noise covariance matrices in equations (7.3) and (7.4) have been estimated from the range compressed data in far range. Here, the signal contributions are damped enough due to reflector pattern sidelobes, so that the noise only assumption holds true. A first observation in Fig. 7.5 is that the gain improvement with two activated channels is approximately 2 dB with MVDR beamforming, instead of the ideally expected 3 dB. The reason for this is that the slight horizontal displacement of the trihedral caused channel five

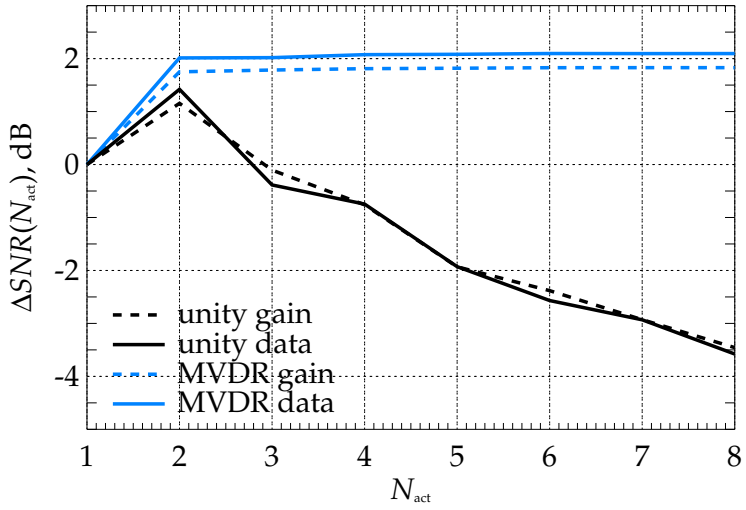

Figure 7.5: Relative *SNR* after digital beamforming at the location of the corner reflector at $r_0 = 47.5\,\mathrm{m}$ as function of the number of activated channels N_{act}.

to contribute with less signal power. Unity beamforming in contrast to MVDR beamforming is a method which uses no complex pattern information. Insofar the smaller *SNR* value for two activated channels is explained by the fact, that the complex patterns at ϑ_0 have different phases, as can be seen in Fig. 7.2b. If more than two channels are activated, the *SNR* for unity beamforming drops as expected, while MVDR beamforming allows to keep the *SNR* at a more or less constant level. This is clearly a consequence of the large feed element spacing.

7.3 A DBF Experiment in Elevation

The following experiment is intended to demonstrate time-variant digital beamforming in elevation, as discussed in section 4.4.1, which would be implemented using FPGAs onboard the satellite in a spaceborne SAR scenario. For this the reflector is rotated such, that the feed array is aligned in the elevation plane as depicted in Fig. 7.6. Five corner reflectors, placed at slant range distances 23.6 m, 28.0 m, 34.7 m, 44.1 m and 57.0 m, shall mark the region of interest. To have an impression of the measured scene, the range compressed signals for the individual channels are shown in Fig. 7.7. The transmitted waveform is a chirp signal with a duration of 10 µs and 300 MHz bandwidth. This pulse duration corresponds to a distance of 1.5 km, which would, according to formula (3.23), require a minimal receive beam width of 173.6 ° for the first target in near range.

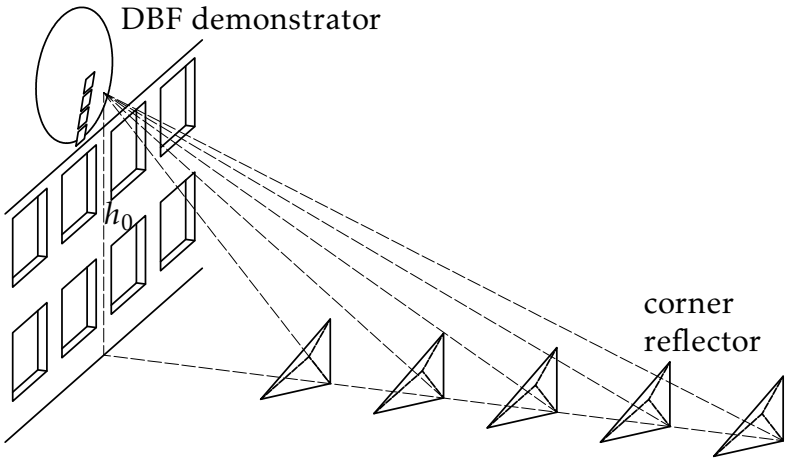

Figure 7.6: Measurement setup with five corner reflectors. The corners reflectors are aligned with the feed array in the elevation plane.

Since this beam width exceeds by far the visible range of all feed patterns (see Fig. 7.2), the immediate consequence is that all feed elements need to be active in order to receive the echoes of all the targets on ground. Therefore, as outlined in chapter 3.3, the gain would drop significantly compared to the case when just a single feed element would be active on receive. In that sense this experiment could be regarded as an extreme case, which is not encountered in spaceborne

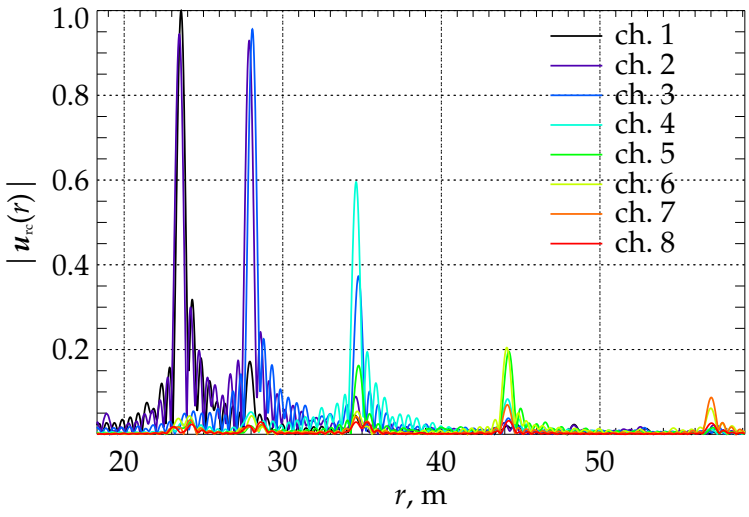

Figure 7.7: Individual channel signals after range compression with their respective replicas.

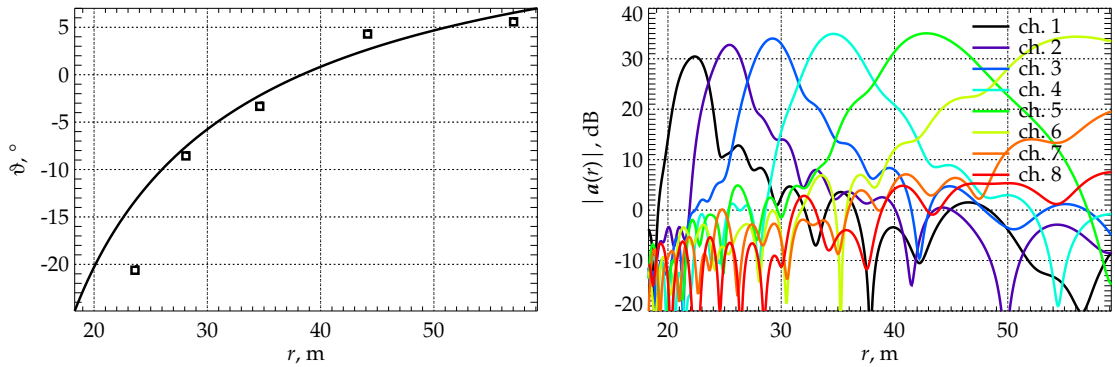

(a) (b)

Figure 7.8: (a) Relation between the scan angle ϑ and slant range r (solid curve). DOA estimates of the five corner reflectors (squares). (b) Reflector patterns projected on slant range.

Earth observation scenarios and, as such, represents the ideal test case.

A crucial step, before any processing can start, is to find the relation between delay time t, or slant range r and the elevation angle ϑ defined in the local antenna coordinate system. For a given imaging geometry this relation is defined via equations (4.12), (4.13) and (4.15). In case of this demonstrator experiment it is justified to establish a simplified model based on a rectangular geometry. Then the scan angle ϑ depends on the slant range r according to

$$\vartheta = \arccos\left(\frac{h_0}{r}\right) - \theta_{\text{bore}} \,. \tag{7.7}$$

The boresight angle θ_{bore} is 70.5 ° and the height h_0 is 12.8 m. Equation (7.7) is graphically illustrated by the solid line in Fig. 7.8a. Indicated by the squares are the MUSIC estimates of the directions of the five corner reflectors. What this mapping means for the antenna patterns is shown in Fig. 7.8b. Here the measured patterns are projected onto the slant range axis r. The near range patterns seem to be squeezed while the far range patterns observe a wide slant range domain.

Having now defined the mapping of the complex weights in the time-variant beamforming process, a second question concerns the FIR filter design according to equation (4.82). The main parameters of interest here are the number of subbands M and the number of filter coefficients N_{coef}. In consideration of the fact that the pulse length is very long, it is obvious that M should rather be a large number in order to divide the waveform into short segments. The number

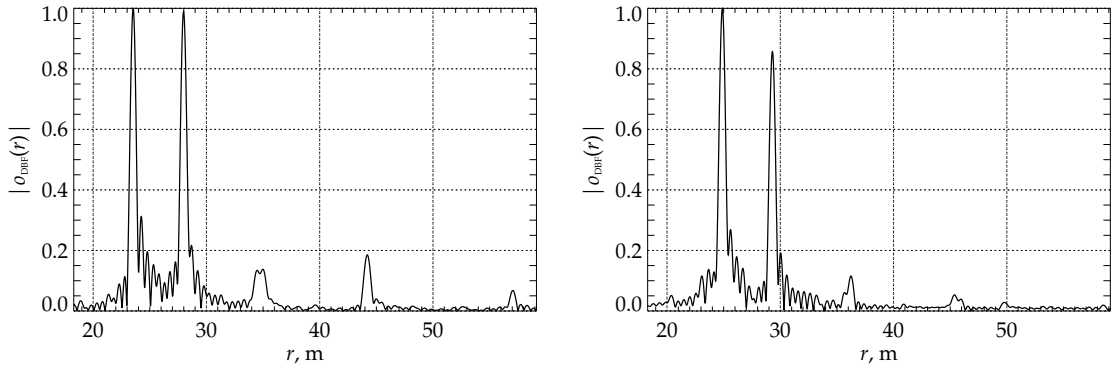

Figure 7.9: (a) Sum of the range compressed channel signals as presented in Fig. 7.7. (b) Range compressed signal after time-variant unity beamforming using a FIR filter with 500 subbands and seven filter coefficients.

of filter coefficients, in contrast, should not be too large in order to avoid a too rough temporal resolution of the chirp frequencies (see uncertainty principle (2.33)). Figure 7.9b shows the range compressed signal after digital beamforming using the unity principle. The FIR filter is designed with seven filter coefficients and 500 subbands, dividing the chirp into subpulses of 3 m length. As reference the sum of the range compressed channel signals, as presented in Fig. 7.7, is shown in Fig. 7.9a.

7.3.1 Discussion

Comparing the signal from Fig. 7.9a with the result after digital beamforming and range compression in Fig. 7.9b reveals a misalignment of the signals. This delay is caused by the FIR filters and is approximately proportional to half the filter length, which corresponds to 1.5 m slant range displacement. Although this additional delay is not much of an issue, since it can be corrected, increasing the length of FIR filter results in a progressive degradation of the signal because of the poorer temporal resolution of the chirp frequencies. Moreover, the targets seem to suffer from a damping. An explanation for this might lie in the fact, that the signals in Fig. 7.7 have been range compressed with their individual replicas before they have been summed in order to generate the final result in Fig. 7.9a. In contrast, in the time-variant approach, beamforming is applied in the raw data domain and the final beamformer raw data output is range compressed with an ideal filter. A conclusion to be drawn from this observation is that the individual receive channels should have similar transfer character-

istics. Otherwise the FIR filters possibly could be designed such that channel imbalances can be compensated. Clearly, in the spaceborne case the FIR filter design would not require so many subbands and therefore these demonstration result shows that time-variant beamforming using FIR filters has the potential to be implemented onboard a SAR satellite.

8 Conclusions

Spaceborne SAR systems with digital beamforming present a powerful technique to map large areas with high spatial and temporal resolution. This high-resolution wide-swath concept is the direct consequence of future demanding applications like disaster monitoring, Earth system dynamics monitoring, moving target indication (MTI), or in the military field of reconnaissance and surveillance. The general problem with such applications is to direct a sufficient amount of electromagnetic energy to the surface, in order to keep a certain sensitivity. From a SAR antenna design point of view two parameters principally allow to tune a SAR system in terms of *SNR*, that are the transmit power and the antenna gain. Since increasing the output power of T/R modules always is a significant cost driver, here in this work the innovative concept of combining a digital feed array with a large aperture unfoldable mesh reflector is investigated. This reflector antenna concept, already a mature technique in satellite communications, adopted to SAR applications, is a promising technology in terms of cost saving due to the lighter weight of the antenna structure compared to classical planar array antennas. At the same time, very large aperture areas can be realized exceeding those of the largest planar array antenna SAR systems currently in orbit.

This work contributes to current research activities in the field of synthetic aperture radar with a generalized and consistent description of digital beamforming for SAR systems using wavenumber calculus. Special emphasis is laid on a separation of SAR specific processing steps and digital beamforming, with the result that conventional SAR focusing routines can be applied to the raw data output after beamforming. The two main criteria for beamforming were to maintain the maximal system sensitivity in terms of *SNR* and the capability of suppressing interferences in terms of range- and azimuth ambiguities as well as artificial interferers.

The necessity of realtime processing motivated a separation of the 3-D wavenumber domain beamforming concepts into a two-dimensional beamforming in elevation and a one-dimensional beamforming in azimuth. In elevation, the temporal characteristics of the transmitted waveform have been incorporated in a spatio-temporal processing scheme which allows to overcome restrictions of long duration pulse SAR systems with high gain antennas. The beamforming procedures in azimuth aim at a system operation with low pulse repetition frequencies in order to map large swath widths and to maintain low downlink

data rates. Further, existing beamforming principles have been extended to polarimetric SAR applications, and a processing scheme has been introduced which allows to deal with polarimetric multichannel reflector SAR systems. In this context the postulation of a high degree of polarization purity of the SAR antenna must be questioned, since multichannel beamforming systems principally allow to combine co- and cross-polarized electromagnetic energy in an optimal way.

In order to ease the process of constructing a reflector antenna in the context of a SAR mission, simple design equations have been derived based on a few instrument, antenna and geometrical input parameters. The performance is demonstrated using the example of a spaceborne reflector SAR system, by means of numerical simulations. In this context it was a major goal to provide compact performance figures for the signal-to-noise ratio, the azimuth ambiguity-to-signal ratio and the range ambiguity-to-signal ratio, which displays the time-variant beamforming principles for multichannel SAR systems correctly. In the limit these formulas are also valid for single-channel systems.

Finally, a major weak point of array-fed reflector SAR systems is identified, which is the loss of sensitivity in case of a feed element failure. For this, the novel conceptual idea of creating a defocused reflector antenna, which can be regarded as a hybrid between a planar array antenna and a conventional reflector antenna, has been analyzed. It shows that the main advantage of planar array antennas, the robustness against antenna element drop outs, can be successfully combined with the large aperture areas of reflector antennas. In conjunction with digital beamforming techniques such an antenna type has the potential to outperform conventional planar array SAR systems in terms of performance as well as costs.

The beamforming concepts introduced in this thesis have been verified by means of numerical simulations, where the predictions of the compact performance figures could be confirmed. The availability of real measurement data, generated by a reflector based multi-channel demonstrator, allowed to test selected beamforming algorithms. These experiments show promising results, which help to understand the challenges of reflector based SAR systems with digital beamforming in terms of calibration requirements, as well as pattern and pointing accuracy.

8.1 Outlook

The trend in future SAR development is clearly towards digital beamforming systems. In this work emphasis has been laid on beamforming techniques on receive for reflector SAR systems. These innovative concepts shall find applica-

tion for the first time on Tandem-L [70, 87], a spaceborne SAR mission proposal for Earth dynamics monitoring. For future SAR systems the novel idea of multi-dimensional waveform encoding [61, 67] foresees the use of spatio-temporally coupled waveforms, which allows, following the *multiple-input multiple-output* (MIMO) concept of communication systems, to explore a larger information space. Under consideration are for instance waveforms based on *orthogonal frequency-division multiplexing* (OFDM), a multi-carrier modulation technique adopted from communication engineering, and recently more SAR-affine waveform concepts [57, 65, 66]. Such techniques will lead to a new generation of highly advanced and highly flexible SAR systems and new SAR imaging modes [64]. Looking ahead, the opportunity of an Earth spanning network of *low Earth orbit* (LEO), *medium Earth orbit* (MEO) and *geostationary Earth orbit* (GEO) radar satellites will permit a quasi-continuous monitoring of dynamic processes [86]. Here the potential lies in the fusion of multi-sensor data and with this the exploration of a larger information content, even across different frequency bands, allowing defacto 'color' vision.

These concepts necessarily drive new developments of digital electronics, as well as sophisticated RF front-ends. One antenna concept recently discussed for future SAR systems are *reflectarrays*. Antennas of this kind have been studied since more than 40 years [42, 105, 119] and might prove to be an alternative to large unfoldable lightweight reflector antennas. Especially dual-reflectarrays could enhance the beam scanning abilities by phase control, both on the sub-reflector as well as on the main reflector [22]. Also from a mechanical point of view this type of antenna might be folded more easily and stowed in a smaller volume, therefore permitting even larger antennas to be brought to space. In this context also hybrid solutions are thinkable, where classic parabolic reflectors could be combined with reflectarrays.

A Electromagnetic Scattering

The basic approach to the electromagnetic scattering problem is to linearly decompose the total electric and magnetic field, $\boldsymbol{E}(\boldsymbol{r},t)$ and $\boldsymbol{H}(\boldsymbol{r},t)$, into an incident field component and a scattered field component, as given in equations (2.8) and (2.9). For stationary, linear and isotropic media the total field complies with Maxwell's equations (2.1) and (2.2) in the form

$$\nabla \times \boldsymbol{E}(\boldsymbol{r},t) = -\mu(\boldsymbol{r})\frac{\partial \boldsymbol{H}(\boldsymbol{r},t)}{\partial t}\,, \tag{A.1}$$

$$\nabla \times \boldsymbol{H}(\boldsymbol{r},t) = \epsilon(\boldsymbol{r})\frac{\partial \boldsymbol{E}(\boldsymbol{r},t)}{\partial t} + \boldsymbol{J}(\boldsymbol{r},t)\,. \tag{A.2}$$

By definition, the incident field is generated by the same sources without the scattering body present [20], yielding

$$\nabla \times \boldsymbol{E}^{\mathrm{i}}(\boldsymbol{r},t) = -\mu_0\frac{\partial \boldsymbol{H}^{\mathrm{i}}(\boldsymbol{r},t)}{\partial t}\,, \tag{A.3}$$

$$\nabla \times \boldsymbol{H}^{\mathrm{i}}(\boldsymbol{r},t) = \epsilon_0\frac{\partial \boldsymbol{E}^{\mathrm{i}}(\boldsymbol{r},t)}{\partial t} + \boldsymbol{J}(\boldsymbol{r},t)\,. \tag{A.4}$$

Then, by subtracting (A.3) from (A.1) and (A.4) from (A.2), the Maxwell equations for the scattered fields write

$$\nabla \times \boldsymbol{E}^{\mathrm{s}}(\boldsymbol{r},t) = -\boldsymbol{J}_{\mathrm{m}}(\boldsymbol{r},t) - \mu_0\frac{\partial \boldsymbol{H}^{\mathrm{s}}(\boldsymbol{r},t)}{\partial t}\,, \tag{A.5}$$

$$\nabla \times \boldsymbol{H}^{\mathrm{s}}(\boldsymbol{r},t) = \boldsymbol{J}_{\mathrm{e}}(\boldsymbol{r},t) + \epsilon_0\frac{\partial \boldsymbol{E}^{\mathrm{s}}(\boldsymbol{r},t)}{\partial t}\,, \tag{A.6}$$

with the *equivalent* electric and magnetic current densities

$$\boldsymbol{J}_{\mathrm{e}}(\boldsymbol{r},t) = (\epsilon(\boldsymbol{r}) - \epsilon_0)\frac{\partial \boldsymbol{E}(\boldsymbol{r},t)}{\partial t}\,, \tag{A.7}$$

$$\boldsymbol{J}_{\mathrm{m}}(\boldsymbol{r},t) = (\mu(\boldsymbol{r}) - \mu_0)\frac{\partial \boldsymbol{H}(\boldsymbol{r},t)}{\partial t}\,. \tag{A.8}$$

The consequence of this approach is, that the divergence of the magnetic flux density is no more zero, but equivalent to a magnetic charge density $\rho_{\mathrm{m}}(\boldsymbol{r},t)$, so

that the divergence laws (2.3) and (2.4) for the scattered fields write

$$\nabla \cdot \boldsymbol{E}^{\mathrm{s}}(\boldsymbol{r},t) = \frac{\rho_{\mathrm{e}}(\boldsymbol{r},t)}{\epsilon_0} \,, \tag{A.9}$$

$$\nabla \cdot \boldsymbol{H}^{\mathrm{s}}(\boldsymbol{r},t) = \frac{\rho_{\mathrm{m}}(\boldsymbol{r},t)}{\mu_0} \,. \tag{A.10}$$

A.1 Field Solutions

Solutions for the field equations (A.5) and (A.6) can be found by a so called *mixed potential* ansatz. For this, a scalar electric and magnetic potential, ϕ_{e} and ϕ_{m}, as well as vectorial potentials $\boldsymbol{A}_{\mathrm{e}}$ and $\boldsymbol{A}_{\mathrm{m}}$, for electric and magnetic current sources, respectively, are introduced. Then, omitting the space-time dependency $(\boldsymbol{r},t)$, the ansatz for the scattered fields in time domain is [1]

$$\boldsymbol{E}^{\mathrm{s}}_{\mathrm{e}} = -\nabla\phi_{\mathrm{e}} - \frac{\partial \boldsymbol{A}_{\mathrm{e}}}{\partial t} \quad , \quad \boldsymbol{E}^{\mathrm{s}}_{\mathrm{m}} = -\frac{1}{\epsilon_0}\nabla \times \boldsymbol{A}_{\mathrm{m}} \,, \tag{A.11}$$

$$\boldsymbol{H}^{\mathrm{s}}_{\mathrm{m}} = -\nabla\phi_{\mathrm{m}} - \frac{\partial \boldsymbol{A}_{\mathrm{m}}}{\partial t} \quad , \quad \boldsymbol{H}^{\mathrm{s}}_{\mathrm{e}} = \frac{1}{\mu_0}\nabla \times \boldsymbol{A}_{\mathrm{e}} \,. \tag{A.12}$$

The scalar potentials can be replaced using the *Lorenz condition* [107]

$$\nabla \cdot \boldsymbol{A} + \epsilon_0\mu_0\frac{\partial \phi}{\partial t} = 0 \,. \tag{A.13}$$

This partial differential equation can be formally integrated over t, yielding

$$\phi = -\frac{1}{\epsilon_0\mu_0}\int_t \nabla \cdot \boldsymbol{A} \,. \tag{A.14}$$

With this, the total scattered field ansatz becomes

$$\boldsymbol{E}^{\mathrm{s}} = \boldsymbol{E}^{\mathrm{s}}_{\mathrm{e}} + \boldsymbol{E}^{\mathrm{s}}_{\mathrm{m}} = \frac{1}{\epsilon_0\mu_0}\nabla\Big(\int_t \nabla \cdot \boldsymbol{A}_{\mathrm{e}}\Big) - \frac{\partial \boldsymbol{A}_{\mathrm{e}}}{\partial t} - \frac{1}{\epsilon_0}\nabla \times \boldsymbol{A}_{\mathrm{m}} \,, \tag{A.15}$$

$$\boldsymbol{H}^{\mathrm{s}} = \boldsymbol{H}^{\mathrm{s}}_{\mathrm{m}} + \boldsymbol{H}^{\mathrm{s}}_{\mathrm{e}} = \frac{1}{\epsilon_0\mu_0}\nabla\Big(\int_t \nabla \cdot \boldsymbol{A}_{\mathrm{m}}\Big) - \frac{\partial \boldsymbol{A}_{\mathrm{m}}}{\partial t} + \frac{1}{\mu_0}\nabla \times \boldsymbol{A}_{\mathrm{e}} \,. \tag{A.16}$$

Now wave equations for the vectorial potential functions $\boldsymbol{A}_{\mathrm{e}}$ and $\boldsymbol{A}_{\mathrm{m}}$ can be derived, inserting (A.15) and (A.16) into (A.5) and (A.6) yielding

$$\epsilon_0\mu_0\frac{\partial^2 \boldsymbol{A}_{\mathrm{e}}(\boldsymbol{r},t)}{\partial t^2} - \Delta\boldsymbol{A}_{\mathrm{e}}(\boldsymbol{r},t) = \mu_0\boldsymbol{J}_{\mathrm{e}}(\boldsymbol{r},t) \,, \tag{A.17}$$

$$\epsilon_0\mu_0\frac{\partial^2 \boldsymbol{A}_{\mathrm{m}}(\boldsymbol{r},t)}{\partial t^2} - \Delta\boldsymbol{A}_{\mathrm{m}}(\boldsymbol{r},t) = \epsilon_0\boldsymbol{J}_{\mathrm{m}}(\boldsymbol{r},t) \,, \tag{A.18}$$

where Δ represents the *Laplace operator*. Here, the identities $\nabla \times \nabla\phi = \mathbf{0}$ and $\nabla \times \nabla \times \boldsymbol{A} = \nabla(\nabla \cdot \boldsymbol{A}) - \Delta \boldsymbol{A}$ have been exploited. These equations are of the D'Alembert type

$$\Box \boldsymbol{V}(\boldsymbol{r}, t) = \boldsymbol{Q}(\boldsymbol{r}, t) \,, \quad \text{with} \quad \Box = \epsilon_0 \mu_0 \frac{\partial^2}{\partial t^2} - \Delta \,, \tag{A.19}$$

with the solution based on Green's second identity according to

$$\boldsymbol{V}(\boldsymbol{r}, t) = \int_{t'} \iiint_{\boldsymbol{r}'} \boldsymbol{Q}(\boldsymbol{r}', t') g(\boldsymbol{r} - \boldsymbol{r}', t - t') \mathrm{d}\boldsymbol{r}' \mathrm{d}t' \,, \tag{A.20}$$

and the Green's function

$$g(\boldsymbol{r}, t) = \frac{\delta(t - \|\boldsymbol{r}\|/c)}{4\pi \|\boldsymbol{r}\|} \,, \quad c = \frac{1}{\sqrt{\epsilon_0 \mu_0}} \,. \tag{A.21}$$

This solution, obeying causality, is also known as *retarded*, since the cause of any effect, leaving quantum mechanical considerations aside, must lie in whose past. Note, here in the context of radar scattering, the surface boundary integral $\partial \boldsymbol{r}'$ is neglected, since the fields are assumed to vanish for large distances from the scatterer. The solution for the vector potentials then are

$$\boldsymbol{A}_{\mathrm{e}}(\boldsymbol{r}, t) = \mu_0 \int_{t'} \iiint_{\boldsymbol{r}'} \boldsymbol{J}_{\mathrm{e}}(\boldsymbol{r}', t') \frac{\delta(t - \|\boldsymbol{r} - \boldsymbol{r}'\|/c - t')}{4\pi \|\boldsymbol{r} - \boldsymbol{r}'\|} \mathrm{d}\boldsymbol{r}' \mathrm{d}t' \,, \tag{A.22}$$

$$\boldsymbol{A}_{\mathrm{m}}(\boldsymbol{r}, t) = \epsilon_0 \int_{t'} \iiint_{\boldsymbol{r}'} \boldsymbol{J}_{\mathrm{m}}(\boldsymbol{r}', t') \frac{\delta(t - \|\boldsymbol{r} - \boldsymbol{r}'\|/c - t')}{4\pi \|\boldsymbol{r} - \boldsymbol{r}'\|} \mathrm{d}\boldsymbol{r}' \mathrm{d}t' \,. \tag{A.23}$$

Finally, the scattered electric and magnetic fields are found by inserting equations (A.22) and (A.23) into (A.15) and (A.16), resulting in

$$\begin{aligned} \boldsymbol{E}^{\mathrm{s}}(\boldsymbol{r}, t) = \frac{1}{\epsilon_0} \nabla \Big(& \int_t \nabla \cdot \int_{t'} \iiint_{\boldsymbol{r}'} \boldsymbol{J}_{\mathrm{e}}(\boldsymbol{r}', t') \frac{\delta(t - \|\boldsymbol{r} - \boldsymbol{r}'\|/c - t')}{4\pi \|\boldsymbol{r} - \boldsymbol{r}'\|} \mathrm{d}\boldsymbol{r}' \mathrm{d}t' \Big) \\ & - \mu_0 \frac{\partial}{\partial t} \int_{t'} \iiint_{\boldsymbol{r}'} \boldsymbol{J}_{\mathrm{e}}(\boldsymbol{r}', t') \frac{\delta(t - \|\boldsymbol{r} - \boldsymbol{r}'\|/c - t')}{4\pi \|\boldsymbol{r} - \boldsymbol{r}'\|} \mathrm{d}\boldsymbol{r}' \mathrm{d}t' \\ & - \nabla \times \int_{t'} \iiint_{\boldsymbol{r}'} \boldsymbol{J}_{\mathrm{m}}(\boldsymbol{r}', t') \frac{\delta(t - \|\boldsymbol{r} - \boldsymbol{r}'\|/c - t')}{4\pi \|\boldsymbol{r} - \boldsymbol{r}'\|} \mathrm{d}\boldsymbol{r}' \mathrm{d}t' \,, \end{aligned} \tag{A.24}$$

$$\begin{aligned} \boldsymbol{H}^{\mathrm{s}}(\boldsymbol{r}, t) = \frac{1}{\mu_0} \nabla \Big(& \int_t \nabla \cdot \int_{t'} \iiint_{\boldsymbol{r}'} \boldsymbol{J}_{\mathrm{m}}(\boldsymbol{r}', t') \frac{\delta(t - \|\boldsymbol{r} - \boldsymbol{r}'\|/c - t')}{4\pi \|\boldsymbol{r} - \boldsymbol{r}'\|} \mathrm{d}\boldsymbol{r}' \mathrm{d}t' \Big) \\ & - \epsilon_0 \frac{\partial}{\partial t} \int_{t'} \iiint_{\boldsymbol{r}'} \boldsymbol{J}_{\mathrm{m}}(\boldsymbol{r}', t') \frac{\delta(t - \|\boldsymbol{r} - \boldsymbol{r}'\|/c - t')}{4\pi \|\boldsymbol{r} - \boldsymbol{r}'\|} \mathrm{d}\boldsymbol{r}' \mathrm{d}t' \\ & + \nabla \times \int_{t'} \iiint_{\boldsymbol{r}'} \boldsymbol{J}_{\mathrm{e}}(\boldsymbol{r}', t') \frac{\delta(t - \|\boldsymbol{r} - \boldsymbol{r}'\|/c - t')}{4\pi \|\boldsymbol{r} - \boldsymbol{r}'\|} \mathrm{d}\boldsymbol{r}' \mathrm{d}t' \,. \end{aligned} \tag{A.25}$$

To emphasize this again, the integration $\int_t$ does not consume the time variable t, but formally denotes the antiderivative. If the observation space $(\boldsymbol{r}, t)$ does not coincide with the source space ($\boldsymbol{r}$',t') the non-primed operators may be drawn into the source integral [103], so that these equations can be cast in the compact form

$$\begin{aligned}\boldsymbol{E}^{\mathrm{s}}(\boldsymbol{r},t) = \int_{t'}\iiint_{\boldsymbol{r}'}\left[\frac{1}{\epsilon_0}(\boldsymbol{J}_{\mathrm{e}}(\boldsymbol{r}',t')\cdot\nabla)\nabla\int_t -\mu_0\boldsymbol{J}_{\mathrm{e}}(\boldsymbol{r}',t')\frac{\partial}{\partial t}+\boldsymbol{J}_{\mathrm{m}}(\boldsymbol{r}',t')\times\nabla\right]\\ \cdot\frac{\delta(t-\|\boldsymbol{r}-\boldsymbol{r}'\|/c-t')}{4\pi\|\boldsymbol{r}-\boldsymbol{r}'\|}\mathrm{d}\boldsymbol{r}'\mathrm{d}t' \,, \qquad (A.26)\\ \boldsymbol{H}^{\mathrm{s}}(\boldsymbol{r},t) = \int_{t'}\iiint_{\boldsymbol{r}'}\left[\frac{1}{\mu_0}(\boldsymbol{J}_{\mathrm{m}}(\boldsymbol{r}',t')\cdot\nabla)\nabla\int_t -\epsilon_0\boldsymbol{J}_{\mathrm{m}}(\boldsymbol{r}',t')\frac{\partial}{\partial t}-\boldsymbol{J}_{\mathrm{e}}(\boldsymbol{r}',t')\times\nabla\right]\\ \cdot\frac{\delta(t-\|\boldsymbol{r}-\boldsymbol{r}'\|/c-t')}{4\pi\|\boldsymbol{r}-\boldsymbol{r}'\|}\mathrm{d}\boldsymbol{r}'\mathrm{d}t' \,. \qquad (A.27)\end{aligned}$$

This result is obtained using $\nabla\times(\boldsymbol{J}g) = g(\nabla\times\boldsymbol{J}) - \boldsymbol{J}\times(\nabla g)$ and $\nabla(\nabla\cdot(\boldsymbol{J}g)) = (\nabla\cdot\boldsymbol{J})\nabla g + g\nabla(\nabla\cdot\boldsymbol{J}) + (\boldsymbol{J}\cdot\nabla)\nabla g + (\nabla g\cdot\nabla)\boldsymbol{J} + \nabla g\times(\nabla\times\boldsymbol{J})$. Finally, these scattered fields can be expressed in terms of the total fields, substituting equations (A.7) and (A.8) for the electric and magnetic current densities

$$\begin{aligned}\boldsymbol{E}^{\mathrm{s}}(\boldsymbol{r},t) = \int_{t'}\iiint_{\boldsymbol{r}'}\left[\frac{1}{\epsilon_0}((\epsilon(\boldsymbol{r}')-\epsilon_0)\boldsymbol{E}(\boldsymbol{r}',t')\cdot\nabla)\nabla-\mu_0(\epsilon(\boldsymbol{r}')-\epsilon_0)\boldsymbol{E}(\boldsymbol{r}',t')\frac{\partial^2}{\partial t^2}\right.\\ \left.+(\mu(\boldsymbol{r}')-\mu_0)\boldsymbol{H}(\boldsymbol{r}',t')\frac{\partial}{\partial t}\times\nabla\right]\frac{\delta(t-\|\boldsymbol{r}-\boldsymbol{r}'\|/c-t')}{4\pi\|\boldsymbol{r}-\boldsymbol{r}'\|}\mathrm{d}\boldsymbol{r}'\mathrm{d}t' \,, \qquad (A.28)\\ \boldsymbol{H}^{\mathrm{s}}(\boldsymbol{r},t) = \int_{t'}\iiint_{\boldsymbol{r}'}\left[\frac{1}{\mu_0}((\mu(\boldsymbol{r}')-\mu_0)\boldsymbol{H}(\boldsymbol{r}',t')\cdot\nabla)\nabla-\epsilon_0(\mu(\boldsymbol{r}')-\mu_0)\boldsymbol{H}(\boldsymbol{r}',t')\frac{\partial^2}{\partial t^2}\right.\\ \left.-(\epsilon(\boldsymbol{r}')-\epsilon_0)\boldsymbol{E}(\boldsymbol{r}',t')\frac{\partial}{\partial t}\times\nabla\right]\frac{\delta(t-\|\boldsymbol{r}-\boldsymbol{r}'\|/c-t')}{4\pi\|\boldsymbol{r}-\boldsymbol{r}'\|}\mathrm{d}\boldsymbol{r}'\mathrm{d}t' \,. \qquad (A.29)\end{aligned}$$

For the sake of completeness here also the temporal frequency domain versions of equations (A.24) and (A.25) shall be given, since they often appear in the literature (see for example [1]). Evaluating the temporal convolution integral t' and taking the Fourier transform on both sides with respect to the vari-

able t, these equations can be stated according to

$$\begin{aligned}
\boldsymbol{E}^{\mathrm{s}}(\boldsymbol{r},\omega) = &-\frac{\mathrm{j}}{\omega\epsilon_0}\nabla(\nabla\cdot\iiint_{\boldsymbol{r}'}\boldsymbol{J}_{\mathrm{e}}(\boldsymbol{r}',\omega)\frac{\mathrm{e}^{-\mathrm{j}k\|\boldsymbol{r}-\boldsymbol{r}'\|}}{4\pi\|\boldsymbol{r}-\boldsymbol{r}'\|}\mathrm{d}\boldsymbol{r}') \\
&-\mathrm{j}\omega\mu_0\iiint_{\boldsymbol{r}'}\boldsymbol{J}_{\mathrm{e}}(\boldsymbol{r}',\omega)\frac{\mathrm{e}^{-\mathrm{j}k\|\boldsymbol{r}-\boldsymbol{r}'\|}}{4\pi\|\boldsymbol{r}-\boldsymbol{r}'\|}\mathrm{d}\boldsymbol{r}' \\
&-\nabla\times\iiint_{\boldsymbol{r}'}\boldsymbol{J}_{\mathrm{m}}(\boldsymbol{r}',\omega)\frac{\mathrm{e}^{-\mathrm{j}k\|\boldsymbol{r}-\boldsymbol{r}'\|}}{4\pi\|\boldsymbol{r}-\boldsymbol{r}'\|}\mathrm{d}\boldsymbol{r}'\,, \qquad \text{(A.30)} \\
\boldsymbol{H}^{\mathrm{s}}(\boldsymbol{r},\omega) = &-\frac{\mathrm{j}}{\omega\mu_0}\nabla(\nabla\cdot\iiint_{\boldsymbol{r}'}\boldsymbol{J}_{\mathrm{m}}(\boldsymbol{r}',\omega)\frac{\mathrm{e}^{-\mathrm{j}k\|\boldsymbol{r}-\boldsymbol{r}'\|}}{4\pi\|\boldsymbol{r}-\boldsymbol{r}'\|}\mathrm{d}\boldsymbol{r}') \\
&-\mathrm{j}\omega\epsilon_0\iiint_{\boldsymbol{r}'}\boldsymbol{J}_{\mathrm{m}}(\boldsymbol{r}',\omega)\frac{\mathrm{e}^{-\mathrm{j}k\|\boldsymbol{r}-\boldsymbol{r}'\|}}{4\pi\|\boldsymbol{r}-\boldsymbol{r}'\|}\mathrm{d}\boldsymbol{r}' \\
&+\nabla\times\iiint_{\boldsymbol{r}'}\boldsymbol{J}_{\mathrm{e}}(\boldsymbol{r}',\omega)\frac{\mathrm{e}^{-\mathrm{j}k\|\boldsymbol{r}-\boldsymbol{r}'\|}}{4\pi\|\boldsymbol{r}-\boldsymbol{r}'\|}\mathrm{d}\boldsymbol{r}'\,, \qquad \text{(A.31)}
\end{aligned}$$

as function of the equivalent electric and magnetic current densities in frequency domain

$$\boldsymbol{J}_{\mathrm{e}}(\boldsymbol{r},\omega) = \mathrm{j}\omega(\epsilon(\boldsymbol{r})-\epsilon_0)\boldsymbol{E}(\boldsymbol{r},\omega)\,, \qquad \text{(A.32)}$$

$$\boldsymbol{J}_{\mathrm{m}}(\boldsymbol{r},\omega) = \mathrm{j}\omega(\mu(\boldsymbol{r})-\mu_0)\boldsymbol{H}(\boldsymbol{r},\omega)\,. \qquad \text{(A.33)}$$

B Linearly Filtered Processes

Commonly the signal-to-noise ratio of a SAR system is estimated based on some variant of the radar equation. Here, typically power expressions, derived from the spectral properties of the SAR system, are incorporated. In the rare cases when SAR focusing is taken into account, the filters are often assumed to be of rectangular shape and consequently do not explicitly appear in the radar equation. Here, the attempt shall be undertaken to derive the power $P_y(t)$ of a filtered process

$$y(t) = x(t) * h(t) = \int_{-\infty}^{\infty} x(t')h(t-t')\mathrm{d}t' \,, \tag{B.1}$$

modeling the SAR focusing operation. The filter $h(t)$, as shown in Fig. B.1, shall be the impulse response function of a linear time invariant (LTI) system. The class of filters considered here are optimal filters, so called matched filters. Concerning the input process $x(t)$, principally two cases can be distinguished. In the first case $x(t)$ is a deterministic signal, as for example a chirp waveform. The second case refers to stochastic signals, so called random processes.

The *SNR* in a SAR image typically refers to the quotient of signal and noise power contained within an individual resolution cell. Insofar the concept of instantaneous power is required. Starting with deterministic signals $x(t)$ the instantaneous power at the filter output is

$$P_y(t) = \lim_{T\to 0} \frac{1}{2T} \int_{t-T}^{t+T} |y(t')|^2 \mathrm{d}t' \,. \tag{B.2}$$

This, however, is for matched filters

$$h(t) = x^*(-t) \,, \tag{B.3}$$

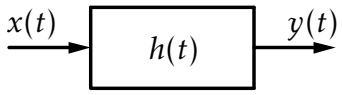

Figure B.1: Linear time invariant system, modeling SAR focusing in one dimension.

substituting $y(t)$ with equation (B.1), exactly equal to the autocorrelation function evaluated at $t' = 0$

$$\begin{aligned} P_y &= \lim_{T\to 0} \frac{1}{2T} \int_{t-T}^{t+T} \left| \int_{-\infty}^{\infty} x(t'')x^*(t''-t')\mathrm{d}t'' \right|^2 \mathrm{d}t' \Bigg|_{t'=0} \\ &= \left| \int_{-\infty}^{\infty} |x(t'')|^2 \mathrm{d}t'' \right|^2 . \end{aligned} \tag{B.4}$$

Using Parseval's theorem this can be easily transferred into the spectral domain yielding

$$P_y = \left| \int_{-\infty}^{\infty} |X(f)|^2 \mathrm{d}f \right|^2 . \tag{B.5}$$

To clarify the impact of the filter the last equation can be stated according to

$$P_y = \left| \int_{-\infty}^{\infty} X(f)H(f)\mathrm{d}f \right|^2 , \quad H(f) = X^*(f) . \tag{B.6}$$

This equation can be interpreted such that the individual spectral components of the signal $X(f)$ multiplied with the filter transfer function $H(f)$ are combined coherently. It is important to stress that this consideration is only valid for matched filters. A simplification can be introduced if a constant signal spectrum and with this a constant filter spectrum, respectively, is assumed. By setting $|H(f)| = 1$ the output power is

$$P_y = \left| \int_{-\infty}^{\infty} |X(f)|\mathrm{d}f \right|^2 . \tag{B.7}$$

In time domain this is equivalent to coherently integrate the signal components

$$P_y = \left| \int_{-\infty}^{\infty} |x(t)|\mathrm{d}t \right|^2 . \tag{B.8}$$

Now let the process $x(t)$ be characterized by its second-order statistics, assuming zero mean. The output power is then equivalent to the variance of $|y(t)|^2$ [35]

$$\begin{aligned} P_y(t) &= \mathcal{E}\left\{|y(t)|^2\right\} \\ &= \mathcal{E}\left\{ \int_{-\infty}^{\infty} x(t')h(t-t')\mathrm{d}t' \int_{-\infty}^{\infty} x^*(t'')h^*(t-t'')\mathrm{d}t'' \right\} \\ &= \int_{-\infty}^{\infty}\int_{-\infty}^{\infty} h(t-t')h^*(t-t'')\mathcal{E}\left\{x(t')x^*(t'')\right\}\mathrm{d}t'\mathrm{d}t'' \end{aligned} \tag{B.9}$$

Expression (B.9) can be simplified if a white noise process is assumed. This gives

$$P_y(t) = \int_{-\infty}^{\infty} |h(t-t')|^2 \mathcal{E}\left\{|x(t')|^2\right\} \mathrm{d}t' = \int_{-\infty}^{\infty} |h(t-t')|^2 \sigma_x^2(t') \mathrm{d}t' \tag{B.10}$$

A final simplification can be introduced by considering a stationary process with variance σ_x^2 yielding

$$P_y = \sigma_x^2 \int_{-\infty}^{\infty} |h(t')|^2 \mathrm{d}t' = \sigma_x^2 \int_{-\infty}^{\infty} |H(f)|^2 \mathrm{d}f = \sigma_x^2 E_h \,. \tag{B.11}$$

From this last result it becomes clear that the power of a filtered stationary random process is given by its variance multiplied with the filter energy E_h.

Finally, if the input process $x(t)$ consists of a signal $s(t)$, superimposed by a noise process $v(t)$

$$x(t) = s(t) + v(t) \,, \tag{B.12}$$

the signal-to-noise ratio of the output process $y(t)$, assuming uncorrelated signal and noise, can be computed with the time domain representations (B.8) and (B.11) according to

$$SNR = \frac{\left|\int_{-\infty}^{\infty} |s(t)| \mathrm{d}t\right|^2}{\sigma_v^2 \int_{-\infty}^{\infty} |h(t)|^2 \mathrm{d}t} = \frac{\left|\int_{-\infty}^{\infty} \sqrt{P_s(t)} \mathrm{d}t\right|^2}{\int_{-\infty}^{\infty} P_v(t) \mathrm{d}t} \,. \tag{B.13}$$

Remember, this *SNR* assessment is strictly valid only under the hypothesis of matched filters with constant envelope. In a real application the integrations are performed over a finite domain, so that these integrals exist. In the frequency domain the constant envelope requirement can be dropped (but not the matched filter precondition), and computes with equations (B.6) and (B.11) as

$$SNR = \frac{\left|\int_{-\infty}^{\infty} S(f) H(f) \mathrm{d}f\right|^2}{\sigma_v^2 \int_{-\infty}^{\infty} |H(f)|^2 \mathrm{d}f} \,. \tag{B.14}$$

Here, again, the integrals exist, assuming bandlimited signal and noise processes.

C Matched Filtered Chirp Signals

Consider a linearly frequency modulated signal $x(t)$ of the form

$$x(t) = \mathrm{rect}\left(\frac{t}{\tau_\mathrm{p}}\right) \mathrm{e}^{\mathrm{j}at^2}\,, \quad a = \pi\frac{B}{\tau_\mathrm{p}}\,, \tag{C.1}$$

with bandwidth B and duration τ_p. The convolution operation according to equation (B.1) using a matched filter (B.3) is the autocorrelation function of the chirp waveform

$$y(t) = x(t) \star x(t) = \int_{-\infty}^{\infty} x(t')x^*(t'-t)\mathrm{d}t'\,. \tag{C.2}$$

Evaluating this integral over two distinct domains yields for the first domain

$$\begin{aligned} y_1(t) &= \int_{-\tau_\mathrm{p}/2}^{t+\tau_\mathrm{p}/2} \mathrm{e}^{\mathrm{j}at'^2}\mathrm{e}^{-\mathrm{j}a(t'-t)^2}\mathrm{d}t' \\ &= \mathrm{e}^{-\mathrm{j}at^2}\int_{-\tau_\mathrm{p}/2}^{t+\tau_\mathrm{p}/2} \mathrm{e}^{\mathrm{j}a2tt'}\mathrm{d}t' \\ &= \mathrm{e}^{-\mathrm{j}at^2}\cdot\frac{\mathrm{e}^{\mathrm{j}a2tt'}}{\mathrm{j}a2t}\bigg|_{-\tau_\mathrm{p}/2}^{t+\tau_\mathrm{p}/2} \\ &= (\tau_\mathrm{p}+t)\cdot\mathrm{sinc}(at(\tau_\mathrm{p}+t))\,, \quad t\in[-\tau_\mathrm{p},0]\,. \end{aligned} \tag{C.3}$$

The second integral equates

$$\begin{aligned} y_2(t) &= \int_{t-\tau_\mathrm{p}/2}^{\tau_\mathrm{p}/2} \mathrm{e}^{\mathrm{j}at'^2}\mathrm{e}^{-\mathrm{j}a(t'-t)^2}\mathrm{d}t' \\ &= (\tau_\mathrm{p}-t)\cdot\mathrm{sinc}(at(\tau_\mathrm{p}-t))\,, \quad t\in[0,\tau_\mathrm{p}]\,. \end{aligned} \tag{C.4}$$

Outside the domain $[-\tau_\mathrm{p},\tau_\mathrm{p}]$ the integral is zero. In compact form this result can be written as

$$y(t) = (\tau_\mathrm{p}-|t|)\cdot\mathrm{sinc}(at(\tau_\mathrm{p}-|t|))\cdot\mathrm{rect}\left(\frac{t}{2\tau_\mathrm{p}}\right)\,. \tag{C.5}$$

D Quadratic Optimization

A common optimization problem encountered in array processing refers to the minimization of quadratic norms subject to linear constraints

$$\text{minimize} \quad \boldsymbol{w}^{\mathsf{T}}\boldsymbol{R}_{\boldsymbol{v}}\boldsymbol{w}^{*} \tag{D.1}$$

$$\text{subject to} \quad \boldsymbol{A}^{\mathsf{T}}\boldsymbol{w} = \boldsymbol{c}\,. \tag{D.2}$$

Let the matrix $\boldsymbol{R}_{\boldsymbol{v}}$ be the result of

$$\boldsymbol{R}_{\boldsymbol{v}} = \mathcal{E}\left\{\boldsymbol{v}\boldsymbol{v}^{\mathsf{H}}\right\} \in \mathbb{C}^{N\times N}\,, \tag{D.3}$$

implying $\boldsymbol{R}_{\boldsymbol{v}} = \boldsymbol{R}_{\boldsymbol{v}}^{\mathsf{H}}$ and the array manifold $\boldsymbol{a}$ for different directions collected in the matrix $\boldsymbol{A}$

$$\boldsymbol{A} = \left[\boldsymbol{a}(k_1,\varphi_1,\vartheta_1) \quad \boldsymbol{a}(k_2,\varphi_2,\vartheta_2) \quad \ldots \quad \boldsymbol{a}(k_M,\varphi_M,\vartheta_M)\right] \in \mathbb{C}^{N\times M}\,. \tag{D.4}$$

The vector $\boldsymbol{c} \in \mathbb{C}^{M\times 1}$ defines a constraint vector. This optimization problem can be solved with the method of *Lagrange multipliers* using complex analysis [6]. The Lagrange function

$$\Lambda(\boldsymbol{w},\boldsymbol{w}^{*}) = \boldsymbol{w}^{\mathsf{T}}\boldsymbol{R}_{\boldsymbol{v}}\boldsymbol{w}^{*} + \boldsymbol{\lambda}^{\mathsf{T}}(\boldsymbol{A}^{\mathsf{T}}\boldsymbol{w} - \boldsymbol{c}) + \boldsymbol{\lambda}^{\mathsf{H}}(\boldsymbol{A}^{\mathsf{H}}\boldsymbol{w}^{*} - \boldsymbol{c}^{*}) \tag{D.5}$$

is differentiated with respect to the unknowns $\boldsymbol{w}$ and $\boldsymbol{\lambda}^{*}$ and set to zero

$$\nabla_{\boldsymbol{w}}\Lambda(\boldsymbol{w},\boldsymbol{w}^{*}) = \boldsymbol{R}_{\boldsymbol{v}}\boldsymbol{w}^{*} + \boldsymbol{A}\boldsymbol{\lambda} = \boldsymbol{0}\,, \tag{D.6}$$

$$\nabla_{\boldsymbol{\lambda}^{*}}\Lambda(\boldsymbol{w},\boldsymbol{w}^{*}) = \boldsymbol{A}^{\mathsf{H}}\boldsymbol{w}^{*} - \boldsymbol{c}^{*} = \boldsymbol{0}\,. \tag{D.7}$$

Solving equations (D.6) for $\boldsymbol{w}^{*}$

$$\boldsymbol{w}^{*} = -\boldsymbol{R}_{\boldsymbol{v}}^{-1}\boldsymbol{A}\boldsymbol{\lambda} \tag{D.8}$$

and inserting this result into equations (D.7) and solving for $\boldsymbol{\lambda}$ yields

$$\boldsymbol{\lambda} = -(\boldsymbol{A}^{\mathsf{H}}\boldsymbol{R}_{\boldsymbol{v}}^{-1}\boldsymbol{A})^{-1}\boldsymbol{c}^{*} \tag{D.9}$$

The final result for the vector $\boldsymbol{w}^{*}$ is then obtained by substituting equations (D.9) into equations (D.8)

$$\boldsymbol{w}^{*} = \boldsymbol{R}_{\boldsymbol{v}}^{-1}\boldsymbol{A}(\boldsymbol{A}^{\mathsf{H}}\boldsymbol{R}_{\boldsymbol{v}}^{-1}\boldsymbol{A})^{-1}\boldsymbol{c}^{*}\,. \tag{D.10}$$

In the literature this solution is known as *Linear Constraint Minimum Variance* (LCMV) beamformer [123]. A special case of this beamformer is the *Minimum Variance Distortionless Response* (MVDR) beamformer, that is obtained for $M = 1$, giving

$$\boldsymbol{w}^* = \frac{c^* \boldsymbol{R}_v^{-1} \boldsymbol{a}}{\boldsymbol{a}^{\mathsf{H}} \boldsymbol{R}_v^{-1} \boldsymbol{a}} \,, \tag{D.11}$$

with a scalar constraint $c \in \mathbb{C}$.

E *SNR* for Time-Variant Beamformers

The *SNR* shall be derived in time domain with the discrete time variable n. Rewriting the beamformer output (4.76) for a point target gives

$$u_{\mathrm{DBF}}(n) = \sum_{n'=0}^{N_{\mathrm{coef}}-1} \boldsymbol{u}^{\mathsf{T}}(n-n')\boldsymbol{h}(n,n') \tag{E.1}$$

$$= \sum_{n'} o(\vartheta)\boldsymbol{a}^{\mathsf{T}}(\vartheta)g(\vartheta,n-n')\boldsymbol{h}(n,n') + \sum_{n'} \boldsymbol{v}^{\mathsf{T}}(n-n')\boldsymbol{h}(n,n') \,. \tag{E.2}$$

Note that o as well as v_i are complex random processes. If we assume uniform and independent Gaussian random variables for the real part and the imaginary part with zero mean, respectively, the processes are characterized by their variances σ_o^2 and $\sigma_{v_i}^2$. Assuming uncorrelated noise and signal the power of the beamformer output is

$$P_{u_{\mathrm{DBF}}}(n) = \mathcal{E}\{|u_{\mathrm{DBF}}(n)|^2\} \tag{E.3}$$

$$= \mathcal{E}\{|\sum_{n'} o(\vartheta)\boldsymbol{a}^{\mathsf{T}}(\vartheta)g(\vartheta,n-n')\boldsymbol{h}(n,n')|^2\}$$

$$+ \mathcal{E}\{|\sum_{n'} \boldsymbol{v}^{\mathsf{T}}(n-n')\boldsymbol{h}(n,n')|^2\} \tag{E.4}$$

$$= P_s(n) + P_v(n) \,, \tag{E.5}$$

with $\mathcal{E}\{.\}$ the expectation operator. In principle the *SNR* can be already computed. However this expression is difficult to interpret in the traditional sense of digital beamforming. Rearranging the terms in the sum and evaluating the expectation operator, the signal power $P_s(n)$ can be written as

$$P_s(n) = \mathcal{E}\{|\sum_{n'} o(\vartheta)g(\vartheta,n-n')\boldsymbol{a}^{\mathsf{T}}(\vartheta)\boldsymbol{h}(n,n')|^2\}$$

$$= \sigma_o^2(\vartheta)|\boldsymbol{a}^{\mathsf{T}}(\vartheta)\sum_{n'} g(\vartheta,n-n')\boldsymbol{h}(n,n')|^2 \,. \tag{E.6}$$

The noise power $P_v(n)$ is

$$P_v(n) = \mathcal{E}\{|\sum_{n'} \boldsymbol{h}^{\mathsf{T}}(n,n')\boldsymbol{v}(n-n')|^2\} \,. \tag{E.7}$$

In order to account for all combinations when evaluating the squared expression $|.|^2$ in equation (E.7) another variable $m' \in [0, N_{\text{coef}} - 1]$ is introduced. This gives

$$P_v(n) = \sum_{n'} \sum_{m'} \boldsymbol{h}^{\mathsf{T}}(n, n') \mathcal{E}\{\boldsymbol{v}(n - n') \boldsymbol{v}^{\mathsf{H}}(n - m')\} \boldsymbol{h}^*(n, m') \tag{E.8}$$

$$= \sum_{n'} \sum_{m'} \boldsymbol{h}^{\mathsf{T}}(n, n') \boldsymbol{R}_{\boldsymbol{v}}(n - n', n - m') \boldsymbol{h}^*(n, m') \,. \tag{E.9}$$

A simplification can be introduced if one assumes that the samples of the random processes are mutually independent. Then the covariance matrices become the zero matrices for $n' \neq m'$ and the noise power is

$$P_v(n) = \sum_{n'} \boldsymbol{h}^{\mathsf{T}}(n, n') \boldsymbol{R}_{\boldsymbol{v}}(n - n') \boldsymbol{h}^*(n, n') \,. \tag{E.10}$$

For a Dirac impulse response function $h_i(n, n') = w_i(n)\delta(n')$ this is the well known expression of the noise power for a multi-channel beamformer. Finally, this expression can be further simplified, if channels with cross powers zero are assumed, yielding

$$P_v(n) = \sum_i \sigma_{v_i}^2 \sum_{n'} |h_i(n, n')|^2 \,. \tag{E.11}$$

The signal-to-noise ratio for the compressed SAR signal can then be computed as (see equation (B.13) in appendix B for a detailed theoretic derivation)

$$SNR(n) \approx \frac{\left| \sum_n^{n+N_{\text{p}}} \sqrt{P_s(n)} \right|^2}{\sum_n^{n+N_{\text{p}}} P_v(n)} \,, \tag{E.12}$$

substituting (E.6) for the signal power and either (E.9), (E.10) or (E.11) for the noise power.

It is important to mention that the *SNR* expression (E.12) is only valid if the sampling frequency f_{s} is smaller than the signal bandwidth B. If the sampling frequency is larger than the bandwidth the noise samples become dependent and combine therefore coherently as it is the case for the signal samples. Principally the *SNR* cannot be improved by oversampling.

F Optimal Time-Variant Beamforming

We start again from the discrete version of the space-time beamformer given in equation (4.76). With the results derived in appendix E the noise power according to equation (E.10) is to be minimized under a linear constraint on the signal power similar to equation (E.6). The optimization problem can then be stated as

$$\text{minimize} \quad \sum_{n'=0}^{N_{\text{coef}}-1} \boldsymbol{h}^{\mathsf{T}}(n,n')\boldsymbol{R}_{\boldsymbol{v}}(n-n')\boldsymbol{h}^{*}(n,n') \tag{F.1}$$

$$\text{subject to} \quad \boldsymbol{A}^{\mathsf{T}} \sum_{n'=0}^{N_{\text{coef}}-1} g(n-n')\boldsymbol{h}(n,n') = \boldsymbol{c}\,. \tag{F.2}$$

Here, the array response matrix shall have the same structure as given in (D.4). Then the summation can be transferred to a vectorial notation giving

$$\begin{bmatrix}\boldsymbol{h}^{\mathsf{T}}(n,0) & \boldsymbol{h}^{\mathsf{T}}(n,1) & \dots\end{bmatrix}\begin{bmatrix}\boldsymbol{R}_{\boldsymbol{v}}(n-0) & \boldsymbol{0} & \dots \\ \boldsymbol{0} & \boldsymbol{R}_{\boldsymbol{v}}(n-1) & \dots \\ \vdots & \vdots & \ddots\end{bmatrix}\begin{bmatrix}\boldsymbol{h}^{*}(n,0) \\ \boldsymbol{h}^{*}(n,1) \\ \vdots\end{bmatrix} \tag{F.3}$$

$$\begin{bmatrix} g(n-0)\boldsymbol{a}^{\mathsf{T}}(k,\varphi_1,\vartheta_1) & g(n-1)\boldsymbol{a}^{\mathsf{T}}(k,\varphi_1,\vartheta_1) & \dots \\ g(n-0)\boldsymbol{a}^{\mathsf{T}}(k,\varphi_2,\vartheta_2) & g(n-1)\boldsymbol{a}^{\mathsf{T}}(k,\varphi_2,\vartheta_2) & \dots \\ \vdots & \vdots & \ddots\end{bmatrix}\begin{bmatrix}\boldsymbol{h}(n,0) \\ \boldsymbol{h}(n,1) \\ \vdots\end{bmatrix} = \begin{bmatrix}c_1 \\ c_2 \\ \vdots\end{bmatrix}, \tag{F.4}$$

or short

$$\text{minimize} \quad \widehat{\boldsymbol{h}}^{\mathsf{T}}(n,n')\widehat{\boldsymbol{R}}_{\boldsymbol{v}}(n-n')\widehat{\boldsymbol{h}}^{*}(n,n') \tag{F.5}$$

$$\text{subject to} \quad \widehat{\boldsymbol{A}}^{\mathsf{T}}(\vartheta,n-n')\widehat{\boldsymbol{h}}(n,n') = \boldsymbol{c}\,. \tag{F.6}$$

One can observe that this optimization problem is of the same structure as given in (D.1) and leads to the LCMV beamformer solution analogous to equation (D.10) as

$$\widehat{\boldsymbol{h}}^{*} = \widehat{\boldsymbol{R}}_{\boldsymbol{v}}^{-1}\widehat{\boldsymbol{A}}\left(\widehat{\boldsymbol{A}}^{\mathsf{H}}\widehat{\boldsymbol{R}}_{\boldsymbol{v}}^{-1}\widehat{\boldsymbol{A}}\right)^{-1}\boldsymbol{c}^{*}\,. \tag{F.7}$$

Remember, the new array response matrix $\widehat{\boldsymbol{A}}$ contains the transmitted waveform $p(n)$ via equation (4.4). Inspecting the solution, the question arises how many delayed versions $g(n-n')$ are required.

Having available N_c independent channels to suppress N_{dir} directions, $N_{dir} < N_c$, the size of the matrices and vectors are

$$\left[1 \times N_c \cdot N_{coef}\right]\left[N_c \cdot N_{coef} \times N_c \cdot N_{coef}\right]\left[N_c \cdot N_{coef} \times 1\right] , \tag{F.8}$$

$$\left[N_{dir} \times N_c \cdot N_{coef}\right]\left[N_c \cdot N_{coef} \times 1\right] = \left[N_{dir} \times 1\right] . \tag{F.9}$$

Since N_c and N_{dir} are in the order of a few ten, the size of the system of equations might be heavily impacted by the number of coefficients N_{coef}. The reason is, that this beamformer solution contains a range compression via the conjugate complex kernel g^*. Essentially this approach is similar to the beamforming after range compression method as introduced in chapter 4.2.2, except that here the frequency dependency of the antenna patterns is accounted for in the array response matrix $\widehat{\boldsymbol{A}}$. This implies that the number of coefficients equals the number of samples per pulse N_p for a given sampling frequency f_s and pulse length τ_p

$$N_{coef} = N_p = \text{nint}\{\tau_p f_s\} . \tag{F.10}$$

This can easily yield several thousands of coefficients rendering such a DBF approach infeasible. Insofar the value of this solution lies not in its practical application, but in a theoretical approach where beamforming and SAR focusing are combined in a single step. Such a concept might be generalized taking into account azimuth focusing. Insofar this solution could serve as limit to be compared with other DBF techniques of this kind.

G Integrated and Peak-Sidelobe Ratio

Two common performance figures characterizing SAR impulse response functions are the integrated sidelobe ratio *ISLR* and the peak-sidelobe ratio *PSLR*. These performance measures, for instance also applied on antenna diagrams, are only meaningful if a single main beam and from the main beam distinguishable sidelobes are present. Following the definition in [112] the *ISLR* is given as the ratio of the energy in the sidelobes to the energy in the mainlobe

$$ISLR = \frac{\int_{-\infty}^{x_1} |y(x)|^2 \mathrm{d}x + \int_{x_2}^{\infty} |y(x)|^2 \mathrm{d}x}{\int_{x_1}^{x_2} |y(x)|^2 \mathrm{d}x} \,, \tag{G.1}$$

where x_1 and x_2 are the first left and right local minima of $|y(x)|^2$ with respect to the mainlobe maximum, respectively. Note, these integrals always exist, since natural waveforms are of finite duration. The peak-sidelobe ratio is the quotient of the first left or right sidelobe maximum and the mainlobe maximum of $|y(x)|^2$

$$PSLR = \frac{|y(x_{\mathrm{SL}})|^2}{|y(x_{\mathrm{ML}})|^2} \,, \tag{G.2}$$

with x_{SL} the position of the first left or right sidelobe maximum and x_{ML} of the mainlobe maximum. Since in this work always the first right sidelobe is taken, in some cases the *PSLR*s using the first left sidelobe deviate due to asymmetries in the impulse response function.

H Hilbert Transform Relations

An important integral transformation in functional analysis is the Hilbert transform. Considering a real or complex valued function $x(t)$ of the real variable t, its Hilbert transform $\mathcal{H}\{.\}$ is defined according to

$$\mathcal{H}\{x(t)\} = \frac{1}{\pi} \int_{-\infty}^{\infty} \frac{x(t)}{t' - t} \mathrm{d}t \,. \tag{H.1}$$

This integral is interpreted in the sense of the Cauchy principal value. The Hilbert transform is invertible and the original function is obtained by applying the negative Hilbert transform

$$x(t) = \mathcal{H}^{-1}\{\mathcal{H}\{x(t)\}\} = -\mathcal{H}\{\mathcal{H}\{x(t)\}\} \,. \tag{H.2}$$

In information and communication theory this integral transform constitutes important relations of signals. Let $x(t) = x_\mathrm{r}(t) + \mathrm{j}x_\mathrm{i}(t)$ be a complex signal, with the real part $x_\mathrm{r}(t),\ x_\mathrm{r} \in \mathbb{R}$ and the imaginary part $x_\mathrm{i}(t),\ x_\mathrm{i} \in \mathbb{R}$. Then for an *analytic* signal $x(t)$, whose spectrum $X(f)$ has by definition no negative parts $X(f) = 0,\ f < 0$, real and imaginary part are related via

$$x_\mathrm{r}(t) = -\mathcal{H}\{x_\mathrm{i}(t)\} = -\frac{1}{\pi t} * x_\mathrm{i}(t) \,, \tag{H.3}$$

$$x_\mathrm{i}(t) = \mathcal{H}\{x_\mathrm{r}(t)\} = \frac{1}{\pi t} * x_\mathrm{r}(t) \,. \tag{H.4}$$

A similar relation exists for the real and imaginary part of the spectrum $X(f) = X_\mathrm{r}(f) + \mathrm{j}X_\mathrm{i}(f)$ of a *causal* signal $x(t),\ x(t) = 0,\ t < 0$.

$$X_\mathrm{r}(f) = \mathcal{H}\{X_\mathrm{i}(f)\} = -\mathrm{j} \cdot \mathrm{sgn}(f) \cdot X_\mathrm{i}(f) \,, \tag{H.5}$$

$$X_\mathrm{i}(f) = -\mathcal{H}\{X_\mathrm{r}(f)\} = \mathrm{j} \cdot \mathrm{sgn}(f) \cdot X_\mathrm{r}(f) \,. \tag{H.6}$$

Bibliography

[1] C. Balanis, *Antenna Theory: Analysis and Design*. John Wiley & Sons, Inc., 1997.

[2] J. Bartow, D. Jacoby, and G. Krassner, "Progressive Communication Satellite Systems Design," *IRE Transactions on Military Electronics*, vol. MIL-4, no. 2, pp. 208–215, Apr 1960.

[3] J. H. Blythe, "Radar systems," U.S. Patent 4,253,098, Feb, 1981.

[4] N. N. Bojarski, "The far field in terms of the spatial Fourier transform of the sources and its implications on the inverse problem," *Journal of Applied Physics*, vol. 58, no. 1, pp. 1–4, Jul 1985.

[5] F. Bordoni, M. Younis, E. Varona, and G. Krieger, "Adaptive SCan-On-REceive based on Spatial Spectral Estimation for High-Resolution, Wide-Swath Synthetic Aperture Radar," in *IEEE International Geoscience and Remote Sensing Symposium (IGARSS)*, vol. 1, Jul 2009, pp. 64–67.

[6] D. Brandwood, "A complex gradient operator and its application in adaptive array theory," *IEE Proceedings F Communications, Radar and Signal Processing*, vol. 130, no. 1, pp. 11–16, Feb 1983.

[7] L. Brule, J. Smyth, and H. Baeggli, "RADARSAT-2 Program Update," in *IEEE International Geoscience and Remote Sensing Symposium (IGARSS)*, vol. 2, Sep 2004, pp. 1186–1189.

[8] O. Bucci and G. D'Elia, "Power synthesis of reconfigurable conformal arrays with phase-only control," *IEE Proceedings - Microwaves, Antennas and Propagation*, vol. 145, no. 1, pp. 131–136, Feb 1998.

[9] O. Bucci, G. D'Elia, and G. Romito, "Synthesis technique for scanning and/or reconfigurable beam reflector antennas with phase-only control," *IEE Proceedings - Microwaves, Antennas and Propagation*, vol. 143, no. 5, pp. 402–412, Oct 1996.

[10] S. Buckreuss, R. Werninghaus, and W. Pitz, "The German Satellite Mission TerraSAR-X," in *IEEE Radar Conference RADAR '08*, May 2008, pp. 1–5.

[11] J. Capon, "High-Resolution Frequency-Wavenumber Spectrum Analysis," *Proceedings of the IEEE*, vol. 57, no. 8, pp. 1408–1418, Aug 1969.

[12] N. Chamberlain, H. Ghaemi, L. Giersch, L. Harcke, R. Hodges, J. Hoffman, W. J. R., Jordan, B. Khayatian, P. Rosen, G. Sadowy, S. Shaffer, Y. Shen, L. Veilleux, and P. Wu, "The DESDynI Synthetic Aperture Radar Array-Fed Reflector Antenna," in *IEEE International Symposium on Phased Array Systems and Technology (ARRAY)*, Oct 2010, pp. 381–386.

[13] M. Cheney and B. Borden, "Problems in synthetic-aperture radar imaging," *Inverse Problems*, vol. 25, no. 12, pp. 1–18, Nov 2009.

[14] D. Cheng and S. Moseley, "On-Axis Defocus Characteristics of the Paraboloidal Reflector," *IRE Transactions on Antennas and Propagation*, pp. 214–216, Oct 1955.

[15] J. Cimino and C. Elachi, *Shuttle Imaging Radar-A (SIR-A) Experiment*, ser. JPL publication. National Aeronautics and Space Administration, Jet Propulsion Laboratory, California Institute of Technology, 1982, vol. 82, no. 77.

[16] J. Cimino, C. Elachi, and M. Settle, "SIR-B - The Second Shuttle Imaging Radar Experiment," *IEEE Transactions on Geoscience and Remote Sensing*, vol. GE-24, no. 4, pp. 445–452, Jul 1986.

[17] J. C. Curlander and R. N. McDonough, *Synthetic Aperture Radar Systems and Signal Processing*. John Wiley & Sons, Inc., 1991.

[18] A. Currie and M. Brown, "Wide-swath SAR," *IEE Proceedings-F Radar and Signal Processing*, vol. 139, no. 2, pp. 122–135, Apr 1992.

[19] J. Detlefsen, "The Resolution Limits of the Imaging of Conducting Bodies using Multistatic Scattering," *IEEE Transactions on Antennas and Propagation*, vol. 28, no. 3, pp. 377–380, May 1980.

[20] ——, "Numerische Methoden in der Hochfrequenztechnik," Fachgebiet HFS des Lehrstuhls für Hochfrequenztechnik der Technischen Universität München, Vorlesungsskript, 2002.

[21] D. Dudley, *Mathematical Foundations for the Electromagnetic Theory*, ser. Electromagnetic Waves. IEEE Press, 1994.

[22] J. Encinar, C. Tienda, E. Carrasco, M. Arrebola, and G. Toso, "Design of Dual-Reflectarray Antenna for Beam Scanning," in *IEEE Antennas and Propagation Society International Symposium (APSURSI)*, 2010, pp. 1–4.

[23] P. P. Ewald, "Introduction to the dynamical theory of X-ray diffraction," *Acta Crystallographica Section A*, vol. 25, no. 1, pp. 103–108, Jan 1969.

[24] C. Fischer, C. Schaefer, and C. Heer, "Technology Development for the HRWS (High Resolution Wide Swath) SAR," in *International Radar Symposium (IRS)*, Sep 2007.

[25] ——, "Frontend Development for the High Resolution Wide Swath SAR," in *European Conference on Synthetic Aperture Radar (EUSAR)*, Jun 2008.

[26] A. Freeman, "SAR Calibration: An Overview," *IEEE Transactions on Geoscience and Remote Sensing*, vol. 30, no. 6, pp. 1107–1121, Nov 1992.

[27] A. Freeman, W. Johnson, B. Huneycutt, R. Jordan, S. Hensley, P. Siqueira, and J. Curlander, "The 'Myth' of the Minimum SAR Antenna Area Constraint," *IEEE Transactions on Geoscience and Remote Sensing*, vol. 38, no. 1, pp. 320–324, Jan 2000.

[28] A. Freeman, G. Krieger, P. Rosen, M. Younis, W. Johnson, S. Huber, R. Jordan, and A. Moreira, "SweepSAR: Beam-forming on Receive using a Reflector-Phased Array Feed Combination for Spaceborne SAR," in *IEEE Radar Conference (RadarCon)*, May 2009.

[29] T. Fujisaka and Y. Oh-Hashi, "Synthetic Aperture Radar System," U.S. Patent 5,059,966, Oct, 1991.

[30] N. Gebert, G. Krieger, and A. Moreira, "Digital Beamforming for HRWS-SAR imaging: System Design, Performance and Optimization Strategies," in *IEEE International Geoscience and Remote Sensing Symposium (IGARSS)*, Aug 2006, pp. 1836–1839.

[31] ——, "Digital Beamforming on Receive: Techniques and Optimization Strategies for High-Resolution Wide-Swath SAR Imaging," *IEEE Transactions on Aerospace and Electronic Systems*, vol. 45, no. 2, pp. 564–592, Apr 2009.

[32] B. Grafmüller, A. Herschlein, and C. Fischer, "The TerraSAR-X Antenna System," in *IEEE International Radar Conference*, May 2005, pp. 222–225.

[33] C. Granet, I. Davis, J. Kot, and G. Pope, "A Deployable Reflector Antenna with a Simplified X/Ka Simultaneous Feed-System," in *European Conference on Antennas and Propagation (EuCAP)*, Mar 2009, pp. 1176–1178.

[34] M. Grant and S. Boyd, "CVX: Matlab software for disciplined convex programming, version 1.21," http://cvxr.com, Apr 2011.

[35] R. M. Gray and L. D. Davisson, *An Introduction to Statistical Signal Processing*. Cambridge University Press, 2004.

[36] A. Haar, "Zur Theorie der orthogonalen Funktionensysteme," *Mathematische Annalen*, vol. 69, no. 3, pp. 331–371, 1910.

[37] R. C. Hansen, *Phased Array Antennas*. John Wiley & Sons, Inc., 1998.

[38] C. Heer and P. Shutie, "Digital Beam Forming Synthetic Aperture Radar," in *IEEE MTT-S International Microwave Symposium Digest*, Jun 2005.

[39] H. R. Hertz, "Über sehr schnelle elektrische Schwingungen," *Annalen der Physik*, vol. 267, pp. 421–448, 1887.

[40] C. Hülsmeyer, "Verfahren, um entfernte metallische Gegenstände mittels elektrischer Wellen einem Beobachter zu melden," Deutschland Patent 165 546, Apr, 1904.

[41] ——, "Verfahren zur Bestimmung der Entfernung von metallischen Gegenständen (Schiffen o. dgl.), deren Gegenwart durch das Verfahren nach Patent 165546 festgestellt wird," Deutschland Patent 169 154, Nov, 1904.

[42] J. Huang, "Analysis of a Microstrip Reflectarray Antenna for Microspacecraft Applications," in *Telecommunications and Data Acquisition Report*, Feb 1995, pp. 153–173.

[43] S. Huber, M. Younis, G. Krieger, and A. Moreira, "A Dual-Focus Reflector Antenna for Spaceborne SAR Systems with Digital Beamforming," *IEEE Transactions on Antennas and Propagation*, vol. 61, no. 3, pp. 1461–1465, 2013.

[44] S. Huber, M. Younis, and G. Krieger, "Reflektorantenne für ein Radar mit synthetischer Apertur," European Patent WO2 013 011 023 (A1), 2013.

[45] S. Huber, M. Younis, A. Patyuchenko, and G. Krieger, "A Novel Digital Beam-Forming Concept for Spaceborne Reflector SAR Systems," in *European Radar Conference (EuRAD)*, Oct 2009, pp. 238–241.

[46] ——, "Digital Beam Forming Concepts with Application to Spaceborne Reflector SAR Systems," in *International Radar Symposium (IRS)*, Jun 2010, pp. 1–4.

[47] ——, "Digital Beam Forming Techniques for Spaceborne Reflector SAR Systems," in *8th European Conference on Synthetic Aperture Radar (EUSAR)*, Jun 2010, pp. 962–965.

[48] S. Huber, M. Younis, A. Patyuchenko, G. Krieger, and A. Moreira, "Spaceborne Reflector SAR Systems with Digital Beamforming," *IEEE Transactions on Aerospace and Electronic Systems*, vol. 48, no. 4, pp. 3473–3493, Oct 2012.

[49] C. C. Hung and R. Mittra, "Secondary Pattern and Focal Region Distribution of Reflector Antennas Under Wide-Angle Scanning," *IEEE Transactions on Antennas and Propagation*, vol. 31, no. 5, pp. 756–763, Sep 1983.

[50] P. Ingerson and W. Wong, "The Analysis of Deployable Umbrella Parabolic Reflectors," *IEEE Transactions on Antennas and Propagation*, vol. 20, no. 4, pp. 409–414, Jul 1972.

[51] Y. Jin, J. Moura, N. O'Donoughue, M. Mulford, and A. Samuel, "Time Reversal Synthetic Aperture Radar Imaging In Multipath," in *Conference Record of the Forty-First Asilomar Conference on Signals, Systems and Computers (ACSSC)*, Nov 2007, pp. 1812–1816.

[52] W. Johnson, P. Rosen, S. Hensley, and A. Freeman, "Radar designs for the desdyni mission," in *IEEE Radar Conference*, May 2009.

[53] R. Jordan, "The Seasat-A Synthetic Aperture Radar System," *IEEE Journal of Oceanic Engineering*, vol. 5, no. 2, pp. 154–164, Apr 1980.

[54] J. T. Kare, "Moving receive beam method and apparatus for synthetic aperture radar," U.S. Patent US 6,175,326 B1, Jan, 2001.

[55] U. Kiencke and M. Schwarz, "Methoden der Signalverarbeitung," Institut für Industrielle Informationstechnik der Universität Karlsruhe, Vorlesungsskript, 2005.

[56] J.-H. Kim, M. Younis, and W. Wiesbeck, "Experimental Performance Investigation of Digital Beamforming on Synthetic Aperture Radar," in *IEEE International Geoscience and Remote Sensing Symposium (IGARSS)*, vol. 5, Jul 2008, pp. 176–179.

[57] J.-H. Kim, M. Younis, A. Moreira, and W. Wiesbeck, "A Novel OFDM Chirp Waveform Scheme for Use of Multiple Transmitters in SAR," *IEEE Geoscience and Remote Sensing Letters*, vol. 10, no. 3, pp. 568–572, 2013.

[58] R. Klemm, *Principles of Space-Time Adaptive Processing*. The Institution of Engineering and Technology, London, United Kingdom, 2006.

[59] D. Koebel, C. Tobehn, and B. Penné, "OHB Platforms for Constellation Sattelites," in *5th IAA Symposium on Small Satellites for Earth Observation*, Apr 2005.

[60] K. Küpfmueller, "Über Einschwingvorgänge in Wellenfiltern," *Elektrische Nachrichtentechnik*, vol. 1, pp. 141–152, 1924.

[61] G. Krieger, N. Gebert, and A. Moreira, "Multidimensional Waveform Encoding for Synthetic Aperture Radar Remote Sensing," in *IET International Conference on Radar Systems*, Oct 2007.

[62] G. Krieger, I. Hajnsek, K. Papathanassiou, M. Eineder, M. Younis, F. D. Zan, P. Prats, S. Huber, M. Werner, H. Fiedler, A. Freeman, P. Rosen, S. Hensley, W. Johnson, L. Veilleux, B. Grafmüller, R. Werninghaus, R. Bamler, and A. Moreira, "The Tandem-L Mission Proposal: Monitoring Earth's Dynamics with High Resolution SAR Interferometry," in *IEEE Radar Conference*, May 2009.

[63] G. Krieger, M. Younis, N. Gebert, S. Huber, F. Bordoni, A. Patyuchenko, and A. Moreira, "Advanced Digital Beamforming Concepts for Future SAR Systems," in *IEEE International Geoscience and Remote Sensing Symposium (IGARSS)*, Jul 2010, pp. 245–248.

[64] G. Krieger, M. Younis, S. Huber, F. Bordoni, A. Patyuchenko, J. Kim, P. Laskowski, M. Villano, T. Rommel, P. Lopez-Dekker, and A. Moreira, "Digital Beamforming and MIMO SAR: Review and New Concepts," in *European Conference on Synthetic Aperture Radar (EUSAR)*, Apr 2012, pp. 11–14.

[65] ——, "MIMO-SAR and the Orthogonality Confusion," in *IEEE International Geoscience and Remote Sensing Symposium (IGARSS)*, 2012, pp. 1533–1536.

[66] G. Krieger, "MIMO-SAR: Opportunities and Pitfalls," *IEEE Transactions on Geoscience and Remote Sensing*, pp. 1–18, 2013.

[67] G. Krieger, N. Gebert, and A. Moreira, "Multidimensional Waveform Encoding: A New Digital Beamforming Technique for Synthetic Aperture Radar Remote Sensing," *IEEE Transactions on Geoscience and Remote Sensing*, vol. 46, no. 1, pp. 31–46, Jan 2008.

[68] G. Krieger, N. Gebert, M. Younis, F. Bordoni, A. Patyuchenko, and A. Moreira, "Advanced Concepts for Ultra-Wide-Swath SAR Imaging," in *European Conference on Synthetic Aperture Radar (EUSAR)*, vol. 2, Jun 2008, pp. 31–34.

[69] G. Krieger, N. Gebert, M. Younis, and A. Moreira, "Advanced Synthetic Aperture Radar Based on Digital Beamforming and Waveform Diversity," in *IEEE Radar Conference (RADAR)*, May 2008, pp. 767–772.

[70] G. Krieger, I. Hajnsek, K. Papathanassiou, M. Eineder, M. Younis, F. D. Zan, S. Huber, P. Lopez-Dekker, P. Prats, M. Werner, Y. Shen, A. Freeman, P. Rosen, S. Hensley, B. Johnson, L. Villeux, B. Grafmüller, R. Werninghaus, R. Bamler, and A. Moreira, "Tandem-L: An Innovative Interferometric and Polarimetric SAR Mission to Monitor Earth System Dynamics with High Resolution," in *IEEE International Geoscience and Remote Sensing Symposium (IGARSS)*, Jul 2010, pp. 253–256.

[71] R. Lange, "Cassini-Huygens Mission Overview and Recent Science Results," in *IEEE Aerospace Conference*, Mar 2008.

[72] J. Li, P. Stoica, and Z. Wang, "On Robust Capon Beamforming and Diagonal Loading," *IEEE Transactions on Signal Processing*, vol. 51, no. 7, pp. 1702–1715, Jul 2003.

[73] Z. Li, Z. Bao, H. Wang, and G. Liao, "Performance Improvement for Constellation SAR using Signal Processing Techniques," *IEEE Transactions on Aerospace and Electronic Systems*, vol. 42, no. 2, pp. 436–452, Apr 2006.

[74] P. Lombardo, "A Multichannel Spaceborne Radar for the COSMO-Skymed Satellite Constellation," in *IEEE Aerospace Conference*, vol. 1, 2004, pp. 111–119.

[75] R. G. Lorenz and S. P. Boyd, "Robust Minimum Variance Beamforming," *IEEE Transactions on Signal Processing*, vol. 53, no. 5, pp. 1684–1696, May 2005.

[76] J. Louet and S. Bruzzi, "ENVISAT Mission and System," in *IEEE International Geoscience and Remote Sensing Symposium (IGARSS)*, vol. 3, 1999, pp. 1680–1682.

[77] M. Ludwig, S. D'Addio, and P. Saameno-Perez, "Ka-Band SAR for Spaceborne Applications based on Scan-on-Receive Techniques," in *European Conference on Synthetic Aperture Radar (EUSAR)*, Jun 2008.

[78] R. J. Mailloux, *Phased Array Antenna Handbook*, 2nd ed. Artech House, Inc., 1994.

[79] G. Marconi, "Improvements in Transmitting Electrical Impulses and Signals, and in Apparatus therefor," Great Britain Patent 12,039, Jun, 1896.

[80] J. Marquez-Martinez, J. Mittermayer, and M. Rodriguez-Cassola, "Radiometric Resolution Optimization for Future SAR Systems," in *IEEE International Geoscience and Remote Sensing Symposium (IGARSS)*, vol. 3, Sep 2004, pp. 1738–1741.

[81] "MATLAB, version R2012a," http://www.mathworks.com, The MathWorks Inc., Apr 2012.

[82] J. C. Maxwell, "A Dynamical Theory of the Electromagnetic Field," *Philosophical Transactions of the Royal Society of London*, vol. 155, pp. 459–512, 1865.

[83] J. McWhirter and T. Shepherd, "Adaptive algorithms in the space and time domains," *IEE Proceedings F Communications, Radar and Signal Processing*, vol. 130, no. 1, pp. 17–21, Feb 1983.

[84] T. A. Milligan, *Modern Antenna Design*, 2nd ed. John Wiley & Sons, Inc., 2005.

[85] A. Moreira, G. Krieger, I. Hajnsek, D. Hounam, M. Werner, S. Riegger, and E. Settelmeyer, "TanDEM-X: a TerraSAR-X Add-On Satellite for Single-Pass SAR Interferometry," in *IEEE International Geoscience and Remote Sensing Symposium (IGARSS)*, vol. 2, Sep 2004, pp. 1000–1003.

[86] A. Moreira, "The Earth seen from Space by Radar Remote Sensing - a Vision for 2025," in *IEEE Technology Time Machine Symposium (TTM)*, May 2012.

[87] A. Moreira, G. Krieger, M. Younis, I. Hajnsek, K. Papathanassiou, M. Eineder, and F. D. Zan, "Tandem-L: A Mission Proposal for Monitoring Dynamic Earth Processes," in *IEEE International Geoscience and Remote Sensing Symposium (IGARSS)*, Jul 2011, pp. 1385–1388.

[88] B. Murmann, "A/D Converter Trends: Power Dissipation, Scaling and Digitally Assisted Architectures," in *IEEE Custom Integrated Circuits Conference (CICC)*, Sep 2008, pp. 105–112.

[89] Y. Nemoto, H. Nishino, M. Ono, H. Mizutamari, K. Nishikawa, and K. Tanaka, "Japanese Earth Resources Satellite-1 Synthetic Aperture Radar," *Proceedings of the IEEE*, vol. 79, no. 6, pp. 800–809, Jun 1991.

[90] NIMA, "Department of Defense World Geodetic System 1984 - Its Definitions and Relationships with Local Geodetic Systems," National Imagery and Mapping Agency, Technical Report, Jan 2000.

[91] A. Olver and J. Syed, "Variable beamwidth reflector antenna by feed defocusing," *IEE Proceedings - Microwaves, Antennas and Propagation*, vol. 142, no. 5, pp. 394–398, Oct 1995.

[92] S. Ozawa, K. Shintate, and A. Tsujihata, "30m Class Lightweight Large Deployable Reflector," in *European Conference on Antennas and Propagation (EuCAP)*, Apr 2011, pp. 3354–3358.

[93] A. Papoulis, "Generalized Sampling Expansion," *IEEE Transactions on Circuits and Systems*, vol. 24, no. 11, pp. 652–654, Nov 1977.

[94] ——, *Probability, Random Variables, and Stochastic Processes*, 3rd ed., R. L. Howell and J. M. Morriss, Eds. McGraw-Hill, Inc., 1991.

[95] A. Patyuchenko, T. Rommel, P. Laskowski, M. Younis, and G. Krieger, "Digital Beam-Forming Reconfigurable Radar System Demonstrator," in *IEEE International Geoscience and Remote Sensing Symposium (IGARSS)*, 2012, pp. 1541–1544.

[96] A. Patyuchenko, M. Younis, S. Huber, and G. Krieger, "Performance Optimization of the Reflector Antenna for the Digital Beam-Forming SAR System," in *Proceedings of Advanced RF Sensors and Remote Sensing Instruments (ARSI)*, 2009.

[97] ——, "Optimization Aspects of the Reflector Antenna for the Digital Beam-Forming SAR System," in *European Conference on Synthetic Aperture Radar (EUSAR)*, Jun 2010.

[98] R. Petersson and P. Ingvarson, "The Planar Array Antennas for the European Remote Sensing Satellite ERS-1," in *18th European Microwave Conference (EUMA)*, Sep 1988, pp. 289–294.

[99] R. Raney, "SNR in SAR," in *IEEE International Geoscience and Remote Sensing Symposium (IGARSS)*, vol. 2, Oct 1985, pp. 994–999.

[100] R. Raney and R. Bamler, "Comments on SAR Signal and Noise Equations," in *IEEE International Geoscience and Remote Sensing Symposium (IGARSS)*, vol. 1, Aug 1994, pp. 298–300.

[101] M. Rast, "ESA's Future Plans for Earth Observation from Polar Orbit," in *IEEE International Geoscience and Remote Sensing Symposium (IGARSS)*, vol. 3, Aug 1994, pp. 1705–1708.

[102] A. Rosenqvist, M. Shimada, N. Ito, and M. Watanabe, "ALOS PALSAR: A Pathfinder Mission for Global-Scale Monitoring of the Environment," *IEEE Transactions on Geoscience and Remote Sensing (TGRS)*, vol. 45, no. 11, pp. 3307–3316, Nov 2007.

[103] E. J. Rothwell and M. J. Cloud, *Electromagnetics*. CRC Press, 2002.

[104] G. Sadowy, H. Ghaemi, B. Heavey, D. Perkovic, M. Zawadzki, and D. Moller, "Ka-band Digital Beamforming and SweepSAR Demonstration for Ice and Solid Earth Topography," in *European Conference on Synthetic Aperture Radar (EUSAR)*, Jun 2010.

[105] J. Salmon, R. Pierrot, and Y. Commault, "An X Band Reflect-Array with Integrated PIN Diodes," in *Antennas and Propagation Society International Symposium*, vol. 12, Jun 1974, pp. 376–378.

[106] R. O. Schmidt, "Multiple Emitter Location and Signal Parameter Estimation," *IEEE Transactions on Antennas and Propagation*, vol. 34, no. 3, pp. 276–280, 1986.

[107] U. Siart. Grundgleichungen der elektromagnetischen theorie. [Online]. Available: http://www.siart.de/lehre/maxwell.pdf

[108] L. Sibul and G. Sohie, "Structure of a Multibeam Adaptive Space-Time Processor," *Proceedings of the IEEE*, vol. 70, no. 3, pp. 303–304, Mar 1982.

[109] S. Silver, *Microwave Antenna Theory and Design*, 1st ed. McGraw-Hill Book Company, Inc., 1949.

[110] H. Sizun, *Radio Wave Propagation for Telecommunication Applications*, ser. Foundations of Engineering Mechanics. Springer, 2005.

[111] M. I. Skolnik, *Radar Handbook*, 2nd ed. McGraw-Hill, Inc., 1990.

[112] ——, *Radar Handbook*, 3rd ed. McGraw-Hill, Inc., 2008.

[113] M. Stangl, R. Werninghaus, and R. Zahn, "The TerraSAR-X Active Phased Array Antenna," in *IEEE International Symposium on Phased Array Systems and Technology (ARRAY)*, Oct 2003, pp. 70–75.

[114] W. L. Stutzman, *Antenna Theory and Design*. John Wiley & Sons, Inc., 1981.

[115] M. Suess, B. Grafmüller, and R. Zahn, "A novel high resolution, wide swath SAR," in *IEEE International Geoscience and Remote Sensing Symposium (IGARSS)*, vol. 3, 2001, pp. 1013–1015.

[116] M. Suess and W. Wiesbeck, "Side-looking Synthetic Aperture Radar System," European Patent EP 1 241 487 B1, Sep, 2002.

[117] M. Thomson, "The AstroMesh Deployable Reflector," in *IEEE Antennas and Propagation Society International Symposium*, vol. 3, Aug 1999, pp. 1516–1519.

[118] "General reflector and antenna farm analysis software," http://www.ticra.com, TICRA, Aug 2011.

[119] C. Tienda, M. Arrebola, J. Encinar, and G. Toso, "Analysis of a dual-reflect array antenna," *IET Microwaves, Antennas Propagation*, vol. 5, no. 13, pp. 1636–1645, Oct 2011.

[120] R. Touzi, W. Boerner, J. Lee, and E. Lueneburg, "A review of polarimetry in the context of synthetic aperture radar: concepts and information extraction," *IEEE Transactions on Geoscience and Remote Sensing*, vol. 30, no. 3, pp. 380–407, 2004.

[121] A. Trastoy and F. Ares, "Phase-only synthesis of continuous linear aperture distribution patterns with asymmetric side lobes," *Electronics Letters*, vol. 34, no. 20, pp. 1916–1917, Oct 1998.

[122] A. Trastoy, F. Ares, and E. Moreno, "Phase-Only Control of Antenna Sum and Shaped Patterns Through Null Perturbation," *IEEE Antennas and Propagation Magazine*, vol. 43, no. 6, pp. 45–54, Dec 2001.

[123] H. L. V. Trees, *Optimum Array Processing*. John Wiley & Sons, Inc., 2002.

[124] L. Tsang, J. A. Kong, and R. T. Shin, *Theory of Microwave Remote Sensing*. John Wiley & Sons, Inc., 1985.

[125] F. Ulaby and M. Dobson, *Handbook of Radar Scattering Statistics for Terrain*. Artech House, Inc., 1989.

[126] V. Verba, L. Neronskiy, and I. Osipov, "Russian Spaceborne Imaging Radars: Scientific and Technical Achievements and Priority Perspectives of Development," in *Proceedings of URSI GA Commission F08*, Oct 2005.

[127] F. Vincent and O. Besson, "Steering vector errors and diagonal loading," *IEE Proceedings - Radar, Sonar and Navigation*, vol. 151, no. 6, pp. 337–343, Dec 2004.

[128] S. Wall, "The Magellan Mission: High-Resolution Radar Mapping of Venus," in *IEEE International Geoscience and Remote Sensing Symposium (IGARSS)*, vol. 2, Sep 1988, pp. 729–730.

[129] J. Way, D. Evans, and C. Elachi, "The SIR-C/X-SAR Mission," in *IEEE International Geoscience and Remote Sensing Symposium (IGARSS)*, vol. 2, Aug 1993, p. 593.

[130] M. Werner, "Shuttle Radar Topography Mission (SRTM): Experience with the X-Band SAR Interferometer," in *Proceedings of CIE International Conference on Radar*, 2001, pp. 634–638.

[131] C. A. Wiley, "Pulsed doppler radar methods and apparatus," U.S. Patent 3,196,436, Aug, 1954.

[132] P. Wood, N. Sultan, and G. Seguin, "A Dual-Polarized Reconfigurable-Beam Antenna for the DSAR Synthetic Aperture Radar," in *AP-S Digest Antennas and Propagation Society International Symposium*, vol. 3, Jul 1996, pp. 1716–1719.

[133] R. Yang, "Illuminating curved passive reflector with defocused parabolic antenna," in *WESCON/58 Conference Record*, vol. 2, Aug 1958, pp. 260–265.

[134] M. Younis, C. Fischer, and W. Wiesbeck, "Digital Beamforming in SAR Systems," *IEEE Transactions on Geoscience and Remote Sensing*, vol. 41, no. 7, pp. 1735–1739, Jul 2003.

[135] M. Younis, S. Huber, A. Patyuchenko, F. Bordoni, and G. Krieger, "Performance Comparison of Reflector- and Planar-Antenna based Digital Beam-Forming SAR," *International Journal of Antennas and Propagation*, vol. 2009, pp. 1–14, Jun 2009.